AD-A243 471

REPORT DOCUMENTATION PAGE

Form Approved
OMB No. 0704-0188

...is estimated to average 1 hour per response, including the time for reviewing instructions, searching existing data sources, ...ing and reviewing the collection of information. Send comments regarding this burden estimate or any other aspect of this ...ing this burden, to Washington Headquarters Services, Directorate for Information Operations and Reports, 1215 Jefferson ...d to the Office of Management and Budget, Paperwork Reduction Project (0704-0188), Washington, DC 20503.

2. REPORT DATE

3. REPORT TYPE AND DATES COVERED
~~THESIS~~/DISSERTATION

4. TITLE AND SUBTITLE
Toward the Robust Control of High Bandwidth High Precision Flexible Optical Systems

5. FUNDING NUMBERS

6. AUTHOR(S)
Kenneth W. Barker, Major

7. PERFORMING ORGANIZATION NAME(S) AND ADDRESS(ES)
AFIT Student Attending: University of Washington

8. PERFORMING ORGANIZATION REPORT NUMBER
AFIT/CI/CIA-91-018D

9. SPONSORING/MONITORING AGENCY NAME(S) AND ADDRESS(ES)
AFIT/CI
Wright-Patterson AFB OH 45433-6583

10. SPONSORING/MONITORING AGENCY REPORT NUMBER

DTIC ELECTE DEC 16 1991 S C D

11. SUPPLEMENTARY NOTES

12a. DISTRIBUTION/AVAILABILITY STATEMENT
Approved for Public Release IAW 190-1
Distributed Unlimited
ERNEST A. HAYGOOD, Captain, USAF
Executive Officer

12b. DISTRIBUTION CODE

13. ABSTRACT (*Maximum 200 words*)

14. SUBJECT TERMS

15. NUMBER OF PAGES
80

16. PRICE CODE

17. SECURITY CLASSIFICATION OF REPORT

18. SECURITY CLASSIFICATION OF THIS PAGE

19. SECURITY CLASSIFICATION OF ABSTRACT

20. LIMITATION OF ABSTRACT

NSN 7540-01-280-5500

Standard Form 298 (Rev. 2-89)
Prescribed by ANSI Std Z39-18
298-102

180

University of Washington

Abstract

Toward the Robust Control of High Bandwidth High Precision Flexible Optical Systems

by Kenneth W. Barker

Chairperson of Supervisory Committee: Prof. Juris Vagners
Dept. of Aeronautics and Astronautics

It is well known that control-structure-interaction (CSI) phenomena limit the stability and performance of controlled flexible structures. Most CSI research focuses on rigid body control of flexible structures with relatively low closed loop control bandwidths. This research examines the CSI phenomena associated with high bandwidth high precision control of a reaction actuator mounted to a flexible support structure.

In particular, control-structure-interaction using a high gain porportional-integral-derivative (PID) controller is examined as it relates to certain design parameters. Rapid small angle line-of-sight repositioning and precision line-of-sight stabilization against a variety of disturbances are performed using both a single and multimode model. The single flexible mode model consists of a three-mass lightly damped translating system, referred to as the modified benchmark model. The multimode model consists of a single-axis reaction steering mirror mounted to the tip of a flexible truss-like support structure.

Control-structure-interaction analysis of the reaction actuator control problem is performed first on the single-mode model as a function of flexible mode location, then with the multimode model as a function of inertial and elastic coupling between the reaction steering mirror and the flexible support structure. The analysis describes the control-structure-interaction effects on both stability and performance of a high gain line-of-sight PID controller.

This research introduces the idea of bicollocated control of a reaction actuator. It also shows that control of a reaction actuator in the classical 'collocated' sense may

lead to nonminimum phase zeros in the plant model and may result in an unstable closed loop system. The critical parameters affecting both stability and performance of high gain reaction actuator controllers on flexible systems are shown to be actuator natural frequency, actuator inertia, and uncoupled flexible support structure modal inertia, and coupled system modal reaction inertia.

Toward the Robust Control of High Bandwidth High Precision Flexible Optical Systems

by

Kenneth W. Barker

A dissertation submitted in partial fulfillment
of the requirements for the degree of

Doctor of Philosophy

University of Washington

1991

Approved by____________________________________
(Chairperson of Supervisory Committee)

Program Authorized
to Offer Degree Aeronautics & Astronautics

Date 3 June, 1991

TABLE OF CONTENTS

LIST OF FIGURES

LIST OF TABLES

ACKNOWLEDGMENTS

Successful completion of this research was in the hands of just a few very special people. Deepest gratitude goes first to my best friend and wife, Debi. I'll never be able to adequately thank her for 18 years of committment and sacrifice. She, better than anyone I know, best exemplifies unconditional love and support to me and our three beautiful children. In all that is important in life, her accomplishments these past three years far surpass mine. Thanks also to my children, Brett, Aaron, and Jamie for understanding why 'dad has to study'. Hey, kids! School's over, let's go to Disneyland! I am also very grateful to Juris Vagners for guiding me through the research maze, for knowing which obstacles to let me negotiate and which to remove, and for giving the support I needed to complete this degree in the time allocated. Thanks also to the U.S. Air Force and the U.S. Air Force Academy for sponsoring me for these past three years. Finally and most importantly I want to acknowledge my Lord and Savior, Jesus Christ. He provided the strength and endurance I needed to proceed one day at a time.

Chapter 1

INTRODUCTION

1.1 Background

Flexible optical systems are used in a variety of space and ground applications including communications, astronomy, and directed energy. Though specific missions vary significantly, these systems share some design commonality. Most fundamentally they consist of an arrangement of optical elements (reflectors, mirrors, sensors, etc) mounted in some fashion on a flexible support structure.

The two primary tasks of flexible optical systems (FOS) are 1) to direct the line-of-sight (LOS) to an inertial point or along an inertial path and 2) to stabilize the LOS about an inertial point or about an inertial path against both internal and external disturbances. Often, both tasks will be performed simultaneously. An example of a FOS performing both tasks is a ground-based radar tracking an aircraft as wind buffets against the support structure. Other examples include an orbiting directed energy system rapidly undergoing small changes in LOS angle to pin-point individual targets within a cluster of targets or the Hubble Space Telescope (HST) quiescently focusing on a distant star while subjected to gravity gradients and other disturbance torques.

For purposes of this research, these systems are categorized into those with slow or fast dynamics and those with high or low precision requirements. The terms 'slow' and 'fast' describe the LOS re-positioning or retargeting time requirements. 'High' or 'low' precision refers to the degree to which LOS vibration can be tolerated. In this context, the HST is a slow dynamics high precision FOS. Scientists can afford to wait minutes or hours for the system to settle down to meet high performance requirements. The directed energy system is a fast dynamics high precision FOS. LOS re-positioning of a few degrees within a few tenths of a second while requiring LOS stability orders of magnitude better than ever before demonstrated is typical of this severe performance environment. For example, the HST can precision point at

.1 degrees per second; roughly the rate of a minute hand on a watch. In comparison, the directed energy system precision points at 5 degrees per second; roughly as fast as a second hand and two orders of magnitude faster than the HST [33]. An equally demanding performance requirement, unique to the directed energy fast dynamics flexible optical system is the small angle rapid retargeting between individual targets in a multi-target field. The fast dynamics FOS operation environment is inherently more severe due to short settling time requirements complicated by extremely small tolerances in LOS vibration and pointing error.

This research focuses on the philosophy surrounding the design of an LOS controller for a fast dynamics high precision FOS undergoing rapid retargeting and precision line-of-sight jitter stabilization. The FOS of interest consists of an optical actuator mounted at the tip of a flexible support structure. The optical actuator will be referred to as a fast steering mirror (FSM) throughout the remainder of this dissertation. The entire assembly can undergo rigid body rotation about the support structure hub using a rigid body torque actuator. Structural vibration can be suppressed by controlling structural actuators. The LOS controller uses available actuators and some pre-determined control policy to perform the tasks outlined in the opening paragraphs.

To date, no fast dynamics flexible optical system has been either built or designed to perform small angle rapid retargeting. Only the larger angle slewing maneuver with LOS stabilization has been addressed utilizing decentralized LOS controllers [33, 34, 42]. The LOS controller is designed to stabilize the FSM using LOS measurements taken from sensors mounted elsewhere on the flexible structure. LOS commands are augmented with tracking data for target following. Generally, SISO loops are designed for each of the two tip-tilt axes to control angular motion and one for the piston axis to control focus. The control loops are designed as though the FSM were mounted to a rigid body. Active structural vibration suppression, using some type of reaction mass actuator, is either localized or non-existent. Passive damping on the flexible support structure has been considered [33, 42]. Rigid body slew, it is envisioned, will be accomplished with torque commands shaped so as not to excite the structure's elastic modes in any significant manner. This design philosophy relies on the stiffness of the support structure, negligible FSM reaction into that support structure, and of course our ability to re-position the flexible support structure quickly and quietly. In other words, interaction between the flexible structure and the LOS controller is at least initially neglected. While the technologies required to build a controller of this type may exist, one is yet to be built that demonstrates the necessary performance. In light of the severe performance requirements it seems relevant to design the flexible optical system to minimize the control-structure-interaction phenomena resulting from support structure flexibility. To accomplish this, we must first understand how control-structure-interaction affects both stability and performance of the flexible optical system.

1.2 Problem Statement

The research goal is to identify critical control-structure-interaction parameters affecting high bandwidth high precision flexible optical system line-of-sight controller design and to determine the closed-loop effects of inertial and elastic coupling between the optical actuator (single axis fast steering mirror) and the flexible support structure.

1.3 The Present Work and its Relation to the Literature

Modeling, control, and design of flexible structures have been studied extensively over the past two decades. Advances have been made in the areas of modeling and model reduction, passive and active control, decentralized and hierachical control, integrated structural and control design, and sensor and actuator location and selection [41]. Recent trends in this area include research in system identification and experimental controller hardware validation.

Flexible optical systems comprise a unique subset of the overall class of large flexible structures. Though often not physically large when compared to space station or large deployable solar arrays, their models can consist of a comparably large number of degrees of freedom. This being so, all theoretical, computational, and practical methodologies of modeling, control, and design are relevant. Current research exploring LOS control of flexible optical systems can be broadly divided into two areas 1) segmented mirror control, and 2) actuator/structure interaction. Research in both areas reveals the importance of proper consideration of control-structure interaction when designing LOS controllers that have any hope of successful implementation in hardware.

Segmented mirror control has received much attention recently because several flexible optical systems require large (7-10 meter) diameter primary mirrors constructed from an array of smaller mirror segments. Primary mirror shape control becomes an exercise in controlling these smaller mirror segments. Due to the relatively low closed-loop bandwidth (< 20Hz) of the mirror segment controllers, these will be referred to as slow dynamics systems. NASA's Large Deployable Reflector and the University of California Berkley's Keck Ten Meter Telescope (TMT) are two such systems. Both have high precision requirements that demand the integration of both structural dynamics and active control design. Aubrun, Lorell, Havas, and Henninger [2] reported the dynamic analysis of the control system used to align the 36 hexagonal segments of the Keck TMT primary mirror. The interaction between the segment alignment control system and the telescope was shown to adversely impact the telescope's optical performance. Recent work by Aubrun, Carrier, and Ramakrishnan [3, 9, 40] explored shape control for the array of primary mirror segments on two different, yet similar, slow dynamics flexible optical systems. Aubrun and Lorell [3] demonstrated the control-structure interaction phenomena using the Lockheed Palo Alto Research Laboratory Advanced Structures/Controls Integrated Experiment (ASCIE) Testbed. They showed that, with a classical controller, achievable segment controller bandwidth decreases as the number of segments being controlled is increased. This tradeoff was attributed to controller interaction with the first critical vibration mode. Using worst case analysis and synthesis methods, Carrier [9] designed a 12-input/12–output segment controller for the ASCIE testbed and showed an increase (in simulation) in the achievable controller bandwidth from 4 to 12 times. Using a model of the Advanced Space Structures Technology Research Experiments (ASTREX) facility, a testbed with a segmented mirror system similar to ASCIE, Ramakrishnan, Byun, Skelton, and Cossey [40] applied the Output Variance Control (OVC) approach to design a LOS controller. The OVC approach minimizes input energy subject to inequality constraints on the output variances. OVC is basically a nonlinear mathematical programming problem with inequality contstraints.

The segmented mirror control work described above is primarily relevant to slow dynamics flexible optical systems. Other work more pertinent to the type of fast dynamics flexible optical system described in this research has been reported in recent literature. This work involves exploring the interaction between the dynamics of actuators, flexible beams, and the control laws uniting the two. Barbieri and Özgüner [5] developed the linear equations of motion for the unconstrained (pin-free) and constrained (inertia-free) mode expansions for a uniform flexible slewing beam. In this work, theoretical frequencies were verified with an experimental counterbalanced aluminum beam. E. Garcia and Inman [17] added the dynamics of a hub torquer, an armature controlled DC electric motor, and developed the equations of motion describing actuator-structure interaction for a slewing flexible structure. They also introduced the idea of selecting a 'best' ratio between the servo inertia and beam inertia to improve the controllability of the system's flexible modes. Working at the opposite end of the beam, Zimmerman and Inman [59] analyzed the actuator-structure interaction for a proof-mass actuator mounted to the tip of a cantilevered beam. They predicted the presence of potential instabilities and performance degradation if proper consideration is not given to interactions between the control law, the structure, and the actuator. In doing this, they dispelled the previously accepted view that simple rate-feedback is necessarily a stable control law. With added damping to the fundamental structural mode as a design criterion, it was shown that the break frequency of the actuator should be designed below the first natural frequency of the structure for best performance. In similar research, J. Garcia [18] investigated the stability of an actuated mirror mounted to the tip of a flexible beam. His control objective was not vibration suppression, as with the research discussed above, but instead to position the face of the mirror in inertial space. J. Garcia concluded that if the actuated mass is small compared to the mass of the structure, the flexibility of the structure can be ignored when controlling the mirror with proportional feedback including a first order roll-off filter. He referred to this as 'reckless' control. Because J. Garcia assumed the actuated mirror mass small, he was able to neglect its affect on the natural frequencies and mode shapes of the combined system. As a result, the transfer function between mirror inertial position and mirror actuation force did not reflect any change in combined system dynamics as a function of mirror mass. Shaw and Vu [47] investigated the dynamics of the same system analyzed by J. Garcia, but with non-negligible actuated mass. Their equations of motion reflect the coupling between the actuator and structure under closed-loop control as a function of actuated mass.

Recall that current fast dynamics FOS LOS controller designs can be referred to as decentralized and structurally uncoupled. They are decentralized in that LOS control is provided only to the FSM with only one source of information. This information is based upon LOS measurements from sensors mounted somewhere on the structure and isolated somewhat from the structure. These controller designs are structurally uncoupled in that during the controller design the mirror support structure is considered rigid. Our research suggests a different philosophy for the design for such a LOS controller.

Though generally related to the segmented mirror control research, our work is more specifically related to the actuator/structure/control interaction research applied to simple beams and actuated masses. The research is this area is similar to ours primarily in the types of systems considered: simple beams with hub torquers and tip actuated masses. The primary differences are in three areas

1) we are interested in controlling the system LOS within extremely small tolerances by controlling the inertial angle of a reaction fast steering mirror. In this regard, our research is most similar to that of J. Garcia.

2) we recognize the dynamic coupling between actuated mass (inertia) and the flexible support structure and have included these dynamics in our equations of motion. Recall, J. Garcia assumed negligibly small actuated mass. Though Shaw and Vu included actuated mass, their control objective was strictly vibration suppression.

3) we are interested in identifying the parameters required to minimize the interaction between the LOS controller and the flexible structure rather than designing a LOS controller to compensate for existing interaction.

1.4 Organization of this Dissertation

The development of a planar 65 degree of freedom flexible optical system is presented in chapter two. The finite element model as well as the dynamics of the optical and structural actuators are discussed. Dynamic characterizations are presented.

In chapter three, a method for classifying the structural flexibility types for the single-mode reaction actuator model is developed. The modified benchmark problem, a lightly damped translating three-mass model, is developed and cast in the context of the high bandwidth high precision flexible optical system. The modified benchmark problem is a dynamic simplification of the planar flexible optical system. Here the fundamental control-structure-interaction phenomena complicating the flexible optical system LOS controller design are explored.

In chapter four, the multi-mode flexible optical system LOS control problem is addressed. The impact of the control-structure-interaction phenomena on performance and robustness are discussed in terms of key system parameters describing mirror dynamics, support structure flexibility, and the degree of inertial coupling between the mirror and the flexible support structure.

In chapter five, the conclusions and recommendations for future work are presented.

1.5 Novel Contributions of this Work

This work presents the following new contributions and results in line-of-sight control of high bandwidth high precision flexible optical systems.

1) We have developed a 65 degree-of-freedom model of a planar flexible optical system incorporating both rigid body and elastic modes, reaction mass actuators, and a reactionless fast steering mirror for use in examining relevant control-structure-interaction phenomena and robust control techniques for the high bandwidth high precision line-of-sight control problem.

2) We have extended the work of J.T. Spanos [49] to the reaction actuator control problem. Specifically, we have developed a method of classifying structural flexibility for the single-mode reaction actuator control model.

3) We have introduced the concept of bicollocated reaction actuator control and have established guarantees for the existance of minimum phase structural modes.

4) We have formulated the modified benchmark problem, a simple physically realizable single-mode representation of the reaction actuator control problem.

5) We have defined key structural parameters and demonstrated their role in determining both the type and degree of control-structure-interaction phenomena affecting the stability and performance of line-of-sight controllers for the flexible optical system.

It would be easy to try to limit the results of this research to the specific flexible optical system configuration developed in chapter two and analyzed in chapter four.

Such a temptation should be avoided. The results of chapters three and four are clear–interaction between a reaction actuator and its flexible support structure can cause system instabilities and/or prohibitively limit performance. The common practice of designing a controller based upon the rigid support assumption and then adding the necessary 'structural filters' to handle troublesome lightly damped flexible modes will result in excessively high order controllers when many flexible modes reside inside the control loop crossover frequency. Though residues are small for these high order modes, we must keep in mind that line-of-sight pointing jitter tolerances may be smaller than these residues. In fact, our research shows significant LOS jitter from flexible modes even beyond loop crossover. While these can be treated with high order roll-off filters or by frequency shaping in the retargeting commands, we must still deal with the large number of modes inside loop crossover. Passive damping techniques will likely fall short in the amount of damping gained. Active damping techniques imply additional hardware, weight, and complexity. In light of these tradeoffs, it seems right that the physical mechanisms supporting adverse control-structure-interaction should be treated prior to controller design. If the flexible support structure and fast steering mirror are designed to minimize these adverse interactions with the LOS controller, payoffs will be realized in terms of controller simplicity and total system performance.

Chapter 2

THE FLEXIBLE OPTICAL SYSTEM MODEL

2.1 Overview

Too often we simply receive a system model along with the system performance requirements and charge off to design our controller. We're elated when simulations meet performance goals but befuddled when the real system doesn't. We then expend significant effort identifying our system with the hope of 'tuning' our model. We believe an equally significant effort should go toward the initial development and validation of a that model. When we understand the assumptions going into our model, only then will we have confidence in its prediction accuracy and then we will understand our system dynamics well enough to troubleshoot our controller failures.

This chapter is devoted to the development, validation, and dynamic characterization of the flexible optical system (FOS) model used in this research. The system can be correctly identified as high bandwidth and high precision only after the appropriate line-of-sight (LOS) controller is implemented (see chapter 4). The basic FOS is comprised of a fast steering mirror mounted to the tip of a flexible support structure. The flexible structure is pinned at the hub for rigid body rotation in the horizontal plane. The mirror is constrained to rotate in the same plane. Figure 2.1 shows the FOS with two reaction-mass actuators mounted to the tip and mid-point of the flexible structure.

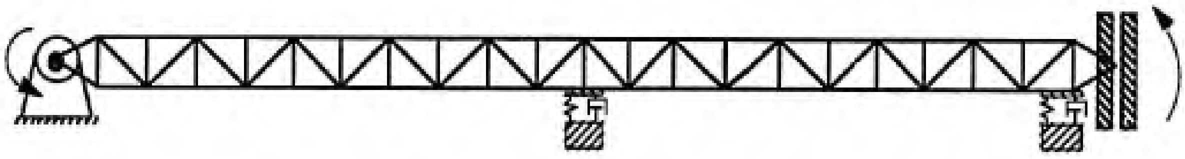

Figure 2.1: Planar Flexible Optical System

In section 2.2 we describe the development and validation of the finite element model for the planar flexible support structure. The model reduction procedure is described in section 2.3. In section 2.4, models for the reaction-mass actuators and reactionless fast steering mirror are developed and added to the flexible support structure model. In section 2.5 we describe the time and frequency domain dynamics of various FOS configurations.

2.2 The Flexible Support Structure

Flexible optical systems intended for use in space are constructed with light, flexible truss assemblies supporting the optical components. A typical cassegranian telescope consists of a primary mirror separated by some nominal distance from a secondary mirror. This separation is maintained by a flexible support structure, such as a tripod. The operational telescope can direct its LOS freely about two axes of rotation. In this research, the flexible support structure is modeled as a single planar truss; a simplification of the two-axis tripod. A finite element model (FEM) is first built describing an existing constrained-free hardware set-up. Experimental and theoretical model validation is performed on the constrained-free FEM. The boundary conditions are then modified and a pinned-free FEM is built, more suitable to this research. The undamped FEMs can be represented in the form of a matrix equation as

$$[M]\ddot{\mathbf{q}} + [K]\mathbf{q} = \mathbf{f} \tag{2.1}$$

where $\mathbf{q}$ is the vector of generalized coordinates and $\mathbf{f}$ is the vector of force and torque inputs corresponding to each coordinate. [M] and [K] are the consistent mass and stiffness matrices, respectively.

2.2.1 The 63-DOF Constrained-Free Finite Element Model

The planar truss modeled in this research is similar to that constructed by Hallauer and Lamberson at the U.S. Air Force Academy, in Colorado Springs, CO. [22]. A similar hardware experiment has been constructed at the University of Washington in the Department of Aeronautics and Astronautics Controls Laboratory. Since the finite element model and state-space model are derived from this hardware configuration, this section will begin with some details on its construction.

Figure 2.2 illustrates the 20-bay, 7.07 meter long planar truss. The diagonal and

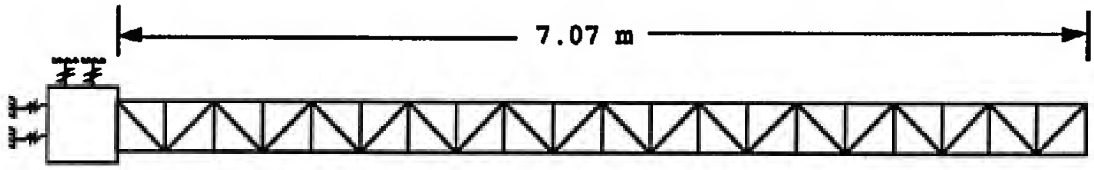

Figure 2.2: The Planar Truss

side dimensions of each square bay are 0.500 meters and 0.354 meters, respectively. Longitudinal positions along the truss, from the constrained end, are denoted by station numbers 0-20. The 240 lb. truss lies flat in the horizontal plane and is supported by 3/4 inch steel balls, rolling with very little friction. The longitudinal, diagonal, and chordwise members are constructed from aluminum and connected with threaded steel joints. Attached to the 21 chordwise truss members are rigid steel bars designed to lower the structure's natural frequencies and to prevent out-of-plane motion by ensuring positive contact between the structure and the steel balls [22]. The aluminum truss members and the steel joints are modular components of the Meroform Construction System M12, manufactured by the Mero Corporation. The truss members are tubular with cross-sectional dimensions of 22mm O.D. by 1mm thick. The ends of the truss members are fitted with steel bolt assemblies providing a rigid connection with the threaded steel joints. The joints are Mero standard M12 steel nodes.

Longitudinal stiffnesses of the truss members, including the effects of the terminal bolt assemblies were measured [22]. As indicated in figure 2.2, the root of the truss is not fixed, but constrained by a table, essentially another flexible structure. The table is constructed of steel and is bolted to the concrete floor. To approximate the effect of the table and floor in the mathematical model, the first two transverse vibration modes of the table alone were measured. Using the two measured natural frequencies, the known table geometry, and the calculated mass and rotational inertia of the table, the stiffness values for the transverse and longitudinal table springs were inferred.

The finite element model for the planar truss was developed using Matrix Algebra Package/Structural MODES (MAPMODES), a special purpose FORTRAN program written by Professor W.L. Hallauer of Virginia Polytechnic Institute [21].

MAPMODES performs standard matrix algebra operations, calculates stiffness and mass matrices for plane truss, frame, and grid structures consisting of straight one-dimensional structural elements, solves for static structural displacements by the matrix stiffness method, and solves the structural dynamics eigenvalue problem for natural frequencies, mode shapes, and generalized masses.

Each longeron and diagonal of the truss is modeled as a single planar truss element having no bending freedom using standard element stiffness and consistent mass matrices [37]. Each batten is modeled as a rigid bar (rectangular parallelopiped), and the masses of the concentrated steel joints, servo accelerometers, and reaction-mass actuator parasitic components are added appropriately to the inertias of the batten elements. Each steel joint is idealized to be rigid. The truss and the rigid bars are connected at the intersections of their axes. The support table is modeled as a spring restrained rigid mass connected to the batten at station 0. The resulting finite element model has 63 degrees-of-freedom (DOFs), three at each of the 21 battens: longitudinal translation x, lateral translation y, and rotation θ, all about the batten center-of-gravity. Figure 2.3 illustrates the relevant degrees-of-freedom of the planar truss. The relationship between degrees-of-freedom DOF, generalized coordinates $\mathbf{q}$, inputs $\mathbf{f}$, and physical truss stations for the undamped constrained-free truss finite-element model is provided in table 2.1.

The finite element model of the constrained–free planar truss is validated both experimentally via actual hardware measurements and analytically via Euler-Bernoulli beam theory. Results from these validations are presented in the following sections and summarized in table 2.2 and figure 2.4.

2.2.2 63-DOF Model Validation via Hardware

The finite element model natural frequencies and mode shapes were computed and compared to experimental data gathered from the U.S. Air Force Academy's planar truss. Computing the natural frequencies and mode shapes from the finite element model (i.e. solving the free vibration generalized eigenvalue problem) is discussed in section 2.3. The natural frequencies were obtained experimentally from a single accelerometer located at the truss tip, while the mode shapes were measured using a single portable non-contact displacement sensor at each truss station. The specific

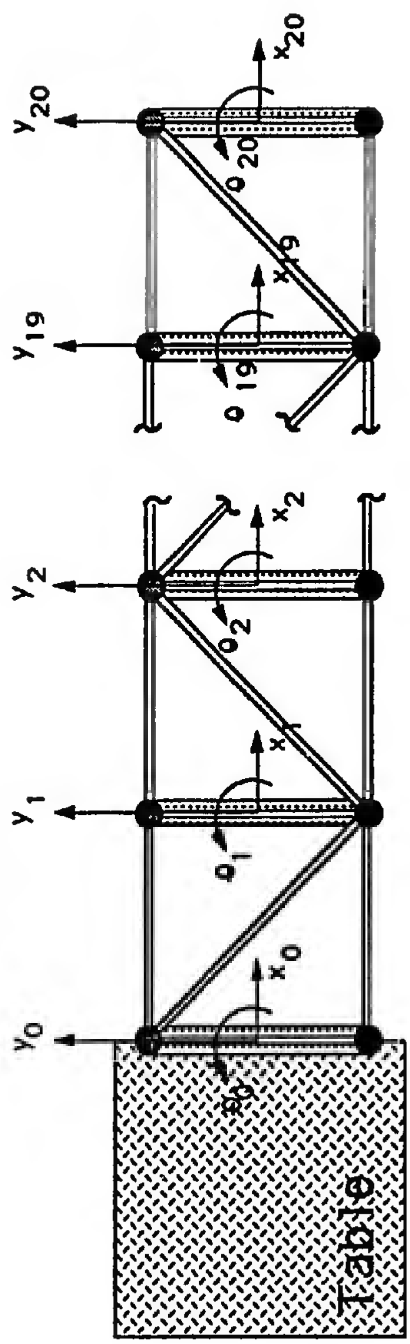

Figure 2.3: The Planar Truss and Its Degrees-of-Freedom

Table 2.1: Degrees-of-Freedom vs. Generalized Coordinates on the Planar Truss

$[M]\ddot{\mathbf{q}} + [K]\mathbf{q} = \mathbf{f}$ (equation 2.1)							
Station	$\mathbf{q}$	*DOF*	$\mathbf{f}$	*Station*	$\mathbf{q}$	*DOF*	$\mathbf{f}$
(tip) 20	x_{20}	1	fx_{20}	(mid) 10	x_{10}	31	fx_{10}
	y_{20}	2	fy_{20}		y_{10}	32	fy_{10}
	θ_{20}	3	t_{20}		θ_{10}	33	t_{10}
19	x_{19}	4	fx_{19}	9	x_9	34	fx_9
	y_{19}	5	fy_{19}		y_9	35	fy_9
	θ_{19}	6	t_{19}		θ_9	36	t_9
18	x_{18}	7	fx_{18}	8	x_8	37	fx_8
	y_{18}	8	fy_{18}		y_8	38	fy_8
	θ_{18}	9	t_{18}		θ_8	39	t_8
17	x_{17}	10	fx_{17}	7	x_7	40	fx_7
	y_{17}	11	fy_{17}		y_7	41	fy_7
	θ_{17}	12	t_{17}		θ_7	42	t_7
16	x_{16}	13	fx_{16}	6	x_6	43	fx_6
	y_{16}	14	fy_{16}		y_6	44	fy_6
	θ_{16}	15	t_{16}		θ_6	45	t_6
(3/4) 15	x_{15}	16	fx_{15}	(1/4) 5	x_5	46	fx_5
	y_{15}	17	fy_{15}		y_5	47	fy_5
	θ_{15}	18	t_{15}		θ_5	48	t_5
14	x_{14}	19	fx_{14}	4	x_4	49	fx_4
	y_{14}	20	fy_{14}		y_4	50	fy_4
	θ_{14}	21	t_{14}		θ_4	51	t_4
13	x_{13}	22	fx_{13}	3	x_3	52	fx_3
	y_{13}	23	fy_{13}		y_3	53	fy_3
	θ_{13}	24	t_{13}		θ_3	54	t_3
12	x_{12}	25	fx_{12}	2	x_2	55	fx_2
	y_{12}	26	fy_{12}		y_2	56	fy_2
	θ_{12}	27	t_{12}		θ_2	57	t_2
11	x_{11}	28	fx_{11}	1	x_1	58	fx_1
	y_{11}	29	fy_{11}		y_1	59	fy_1
	θ_{11}	30	t_{11}		θ_1	60	t_1
				(hub) 0	x_0	61	fx_0
					y_0	62	fy_0
					θ_0	63	t_0

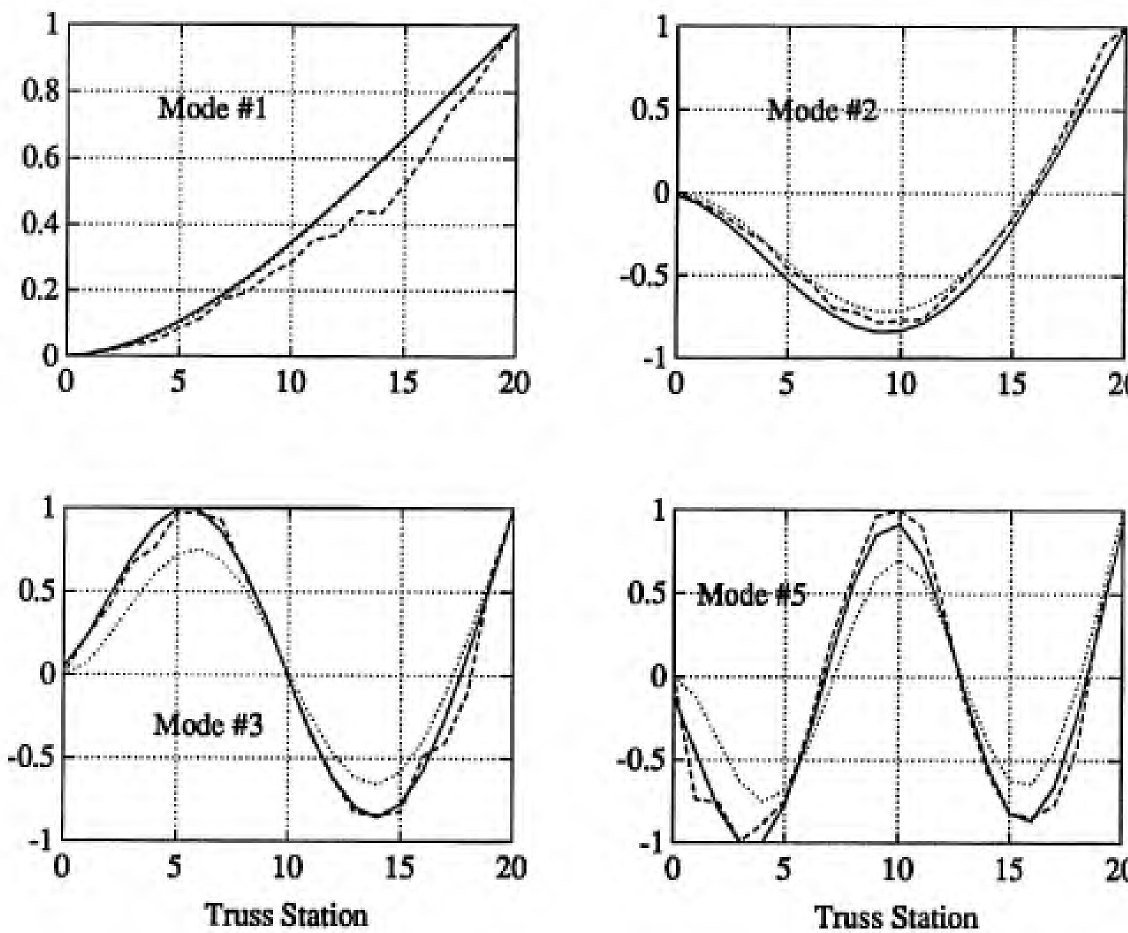

Figure 2.4: Normalized Bending Mode Shapes Comparison: Constrained-Free Finite Element Model (solid) & Experimental (dashed), Fixed-Free Analytical (dotted)

Table 2.2: Modal Frequencies Comparison: Constrained-Free Model Validation

	Natural Frequencies (Hz)			
	Constrained-Free		*Fixed-Free*	
Mode	*Hardware*	*FEM#1*	*FEM#2*	*Beam Theory*
1	1.60	1.61	1.65	1.53
2	10.00	9.50	9.71	9.62
3	24.70	24.71	25.34	26.92
4	30.00	29.32	30.47	30.93
5	43.00	43.43	44.85	52.76

sensor used was the Electro-Mike Displacement Transducer, Model PA12D03, a product of the Electro Corporation. The sensor functions by projecting a 200 kHz field in front of the sensor. When a conductive, metal object (target) enters this field, eddy currents are induced in the target. These eddy currents are detected by the sensor and its oscillator, which generates a command signal. This command signal can be used to activate a wide variety of outputs–relays, time delays, solid-state switches, or pulse outputs that can be used to activate control systems or microprocessors. In our case, we simply recorded the output signal (command signal).

As seen in table 2.2, the natural frequencies for the first five modes compare quite closely between the finite element model (FEM#1) and the hardware. Modes 1–3 and 5 are bending modes. Mode 4 is a longitudinal or 'pogo' mode. FEM#1 considers the table flexibility, which is realized in hardware. FEM#2 considers the table as truly rigid; a model most comparable to beam theory comparisons.

The first four bending mode shapes are constructed from discrete displacement measurements using the Electro-Mike Displacement Transducer. These shapes are compared with shapes computed from FEM#1 in figure 2.4. This figure also shows mode shapes predicted from simple Euler-Bernoulli beam theory, which will be discussed in the following section. The 'pogo' mode shape was not measured. The bending mode shapes shown in figure 2.4 were normalized to a maximum displacement of one. The vertical scale represents the normalized modal displacement along the length of the truss.

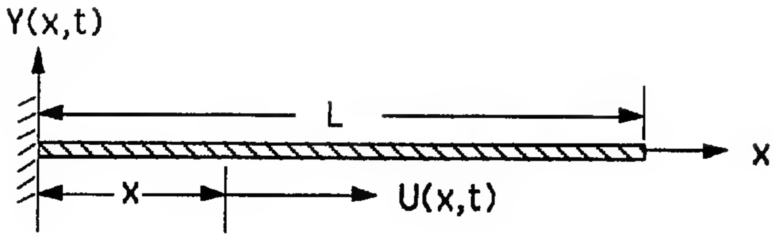

Figure 2.5: The Simple Fixed-Free Euler-Bernoulli Beam

In some cases measured modal amplitude data were smoothed between data points as physical obstructions interfered with these measurements. Measurement non-linearities were also encountered contributing to the less than ideal matching between measured and computed mode shapes. These non-linearities are most noticeable in the data collected on the first mode shape. The first mode undergoes the largest amplitude displacements, some of which were outside the sensor's one half inch linear range. Given the known shortcomings of the Electro-Mike, the measured mode shapes are considered quite accurate. However, because the Electro-Mike measurements were recorded without simultaneous recordings of the forcing function, phase information is considered unreliable. The differences in amplitude between measured and computed data is probably due to the 'rigid' joint assumption in the finite element model. Joint compliance would explain the higher measured amplitudes at modal anti-nodes. No attempt was made to validate modal frequencies or mode shapes for bending modes beyond the first four.

2.2.3 63-DOF Model Validation via Beam Theory

It is at least a matter of curiosity to determine how well simple Euler-Bernoulli beam theory predicts the first five modes of the hardware baselined finite element model. To this end, the Euler-Bernoulli lateral and longitudinal free vibration equations of motion are formulated and tailored to the planar truss. In this analysis, the plane truss assumes the form of the homogeneous, uniform, fixed-free slender beam shown in figure 2.5.

Lateral Vibration

Neglecting shear deformation and rotary inertia, the lateral free vibration partial differential equation of motion is

$$\frac{\partial}{\partial_x}\left[EI(x)\frac{\partial^2 y(x,t)}{\partial_x^2}\right] + m(x)\frac{\partial^2 y(x,t)}{\partial_t^2} = 0 \qquad (2.2)$$

where *EI(x)* is the bending stiffness and *m(x)* is the mass per unit length, both constant for the uniform beam. Assuming the solution to equation 2.2 to be separable in both time and space, $y(x,t) = Y(x)q(t)$, one obtains ordinary differential equations describing the mode shapes (equation 2.3), and natural frequencies (equation 2.4).

$$\frac{d^4Y(x)}{dx^4} - \beta^4 Y(x) = 0 \qquad (2.3)$$

$$\frac{d^2q(t)}{dt^2} + \omega^2 q(t) = 0 \qquad (2.4)$$

where,

$$\beta^4 = \frac{\omega^2 m(x)}{EI(x)} \qquad (2.5)$$

and where $q(t)$ is the vector of modal coordinates and ω is the vector or natural frequencies. The four boundary conditions describing the fixed-free beam configuration for equation 2.3 are

$$Y(0) = 0 \qquad (2.6)$$

$$\frac{dY(0)}{dx} = 0 \qquad (2.7)$$

$$-EI(x)\frac{d^2Y(L)}{dx^2} = 0 \qquad (2.8)$$

$$-\frac{d}{dx}\left[EI(x)\frac{d^2Y(L)}{dx^2}\right] = 0 \qquad (2.9)$$

where $x = 0$ and $x = L$ are the beam fixed and free ends, respectively. The problem of determining ω^2 for which equation 2.3 has a non-trivial solution satisfying the homogeneous boundary conditions (equations 2.6–2.9) is called the eigenvalue problem [29].

The general solution to equation 2.3 is of the form

$$Y(x) = c_1 \sin\beta x + c_2 \cos\beta x + c_3 \sinh\beta x + c_4 \cosh\beta x \tag{2.10}$$

After applying boundary conditions, the frequency and mode shape equations become

$$\cos\beta_n L \cosh\beta_n L = -1 \tag{2.11}$$

$$\begin{aligned} Y_n(x) \;=\; & A_n[(\sin\beta_n L - \sinh\beta_n L)(\sin\beta_n x - \sinh\beta_n x) \\ & +(\cos\beta_n L + \cosh\beta_n L)(\cos\beta_n x - \cosh\beta_n x)] \\ & \qquad n = 1, 2, \ldots, \infty \end{aligned} \tag{2.12}$$

where $Y_n(x)$ is the vector of non-normalized mode shapes, A_n is an arbitrary constant. It can be shown that the mode shapes $Y_n(x)$ are orthogonal and constitute a complete set of orthogonal eigenfunctions. The orthogonality condition, combined with the normalization statement, is given by

$$\int_0^L m(x)Y_r(x)Y_s(x)dx = \delta_{rs} \qquad r, s = 0, 1, 2, \ldots, \infty \tag{2.13}$$

The frequency equation 2.11 is trancendental and must be solved numerically.

The planar truss is 278 inches long and has a mass of 7.42 slugs, giving $m(x) = 2.227 \times 10^{-3}$ $(lbf - s^2)/in^2$. The problem of predicting frequencies and mode shapes becomes one of determining the equivalent bending stiffness *EI(x)*. A beam stiffness of 1×10^8 $lbf - in^2$ was used in computing the natural frequencies and mode shapes provided in table 2.2 and figure 2.4.

To provide a more valid comparison between beam theory and FEM results, the original FEM (FEM#1) was modified to represent a fixed-free rather than constrained-free boundary condition. This fixed-free FEM is referred to as FEM#2. The same values for *EI(x)* and *m(x)* are used between the two finite element models.

The frequency data in table 2.2 generated from FEM#2 and beam theory compares reasonably well through the first four modes. The larger discrepancy in the fifth mode natural frequency is primarily due to neglecting rotary inertia in the equations of motion for the simple beam. The weighty rigid bars attached to the truss at each of the 21 battens contribute significant rotary inertia at each successive truss station. Like the addition of mass to an otherwise uniform beam, rotary inertia tends to decrease lateral vibration natural frequencies. The mode shapes shown in figure 2.4 reflect similar conclusions regarding the absence of rotary inertia effects from beam theory.

Longitudinal Vibration

Using the same assumptions and notation of the previous section, the longitudinal free vibration partial differential equation of motion is

$$\frac{\partial}{\partial_x}\left[EA(x)\frac{\partial u(x,t)}{\partial_x}\right] - m(x)\frac{\partial^2 u(x,t)}{\partial_t^2} = 0 \tag{2.14}$$

where *EA(x)* is the longitudinal stiffness, constant for the uniform beam. For the fixed-free beam, the eigenvalue problem reduces to the ordinary differential equation

$$\frac{d^2U(x)}{dx^2} + \beta^2 U(x) = 0 \tag{2.15}$$

where,

$$\beta^2 = \frac{\omega^2 m(x)}{EA(x)} \tag{2.16}$$

The appropriate boundary conditions are

$$U(0) = 0 \tag{2.17}$$

$$-EA(x)\frac{dU(L)}{dx} = 0 \tag{2.18}$$

The solution to equation 2.15 is

$$U(x) = c_1 \sin\beta x + c_2 \cos\beta x \tag{2.19}$$

Application of the boundary conditions (equations 2.17 and 2.18) gives

$$\cos\beta_n L = 0 \tag{2.20}$$

which gives the eigenvalues

$$\beta_n = (2n-1)\frac{\pi}{2L} \tag{2.21}$$

Equation 2.21 can be written in terms of the natural frequencies ω_n such that

$$\omega_n = \beta_n \sqrt{\frac{EA(x)}{m(x)}} = (2n-1)\frac{\pi}{2}\sqrt{\frac{EA(x)}{m(x)L^2}} \tag{2.22}$$

When normalized against *m(x)* such that

$$\int_0^L m(x)U_r(x)U_s(x)dx = \delta_{rs} \qquad r,s = 0,1,2,\ldots,\infty \tag{2.23}$$

the corresponding orthonormal mode shapes can be written as

$$U_n(x) = \sqrt{\frac{2}{m(x)L}}\sin(2n-1)\frac{\pi x}{2L} \tag{2.24}$$

The longitudinal vibration equations for frequency and mode shapes can be used to validate the planar truss finite element model for only the fourth mode listed in table 2.2. Higher modes in the finite element models exhibit increasing coupling between lateral and longitudinal modes. Validating the fourth mode, which is almost exclusively longitudinal or 'pogo' translates into the simple exercise of selecting a longitudinal stiffness *EA(x)* such that ω_1, from equation 2.22, matches the natural frequency for the fourth mode associated with FEM#2 in table 2.2. An equivalent longitudinal stiffness *EA(x)* of 2.5×10^6 lbf was selected, however, no real validation takes place as only one natural frequency was matched.

2.2.4 The 61-DOF Pinned-Free Finite Element Model

In this research, we seek to examine the benefits of structural vibration suppression for the large angle rigid body slew. The FOS model must therefore include the appropriate dynamics for rigid body rotation about the hub. The 63 DOF finite element model developed in section 2.2.2 is modified to account for the rigid body rotational mode by fixing both x_0 and y_0 while leaving θ_0 free. This reduces the model from 63 to 61 DOF. The 61-DOF pinned-free finite element model is referred to as FEM#3.

The lateral vibration pinned-free beam natural frequencies and modes shapes are, of course, different than those of the fixed-free beam. The change in both natural frequencies and mode shapes is validated with Euler-Bernoulli beam theory. Results

Table 2.3: Modal Frequencies Comparison: Pinned-Free Model Validation

	Natural Frequencies (Hz)	
Mode	*FEM#3*	*Beam Theory*
1	0.00	0.00
2	7.20	6.73
3	21.93	21.80
4	30.79	30.79
5	41.92	45.49
6	64.80	77.79

from this validation are presented in the following section and summarized in table 2.3 and figure 2.6. Hardware validation was not performed since a pinned-free truss was not available.

2.2.5 61-DOF Model Validation via Beam Theory

The lateral and longitudinal free vibration equations of motion formulated in section 2.2.3 are tailored to the pinned-free truss configuration. Here, the plane truss assumes the form of the homogeneous, uniform, pinned-free slender beam shown in figure 2.7. Bending stiffness *EI(x)* and longitudinal stiffness *EA(x)* from the validations carried out on the fixed-free FEM are used in this analysis.

Lateral and Longitudinal Vibration

The general formulation for pinned-free lateral and longitudinal vibration problem is identical to that for the fixed-free problem, with the exception of the boundary conditions. For the lateral vibration problem, equations 2.2 – 2.5 apply, with the new boundary conditions given by

$$Y(0) = 0 \tag{2.25}$$

$$-EI(x)\frac{d^2Y(0)}{dx^2} = 0 \tag{2.26}$$

$$-EI(x)\frac{d^2Y(L)}{dx^2} = 0 \tag{2.27}$$

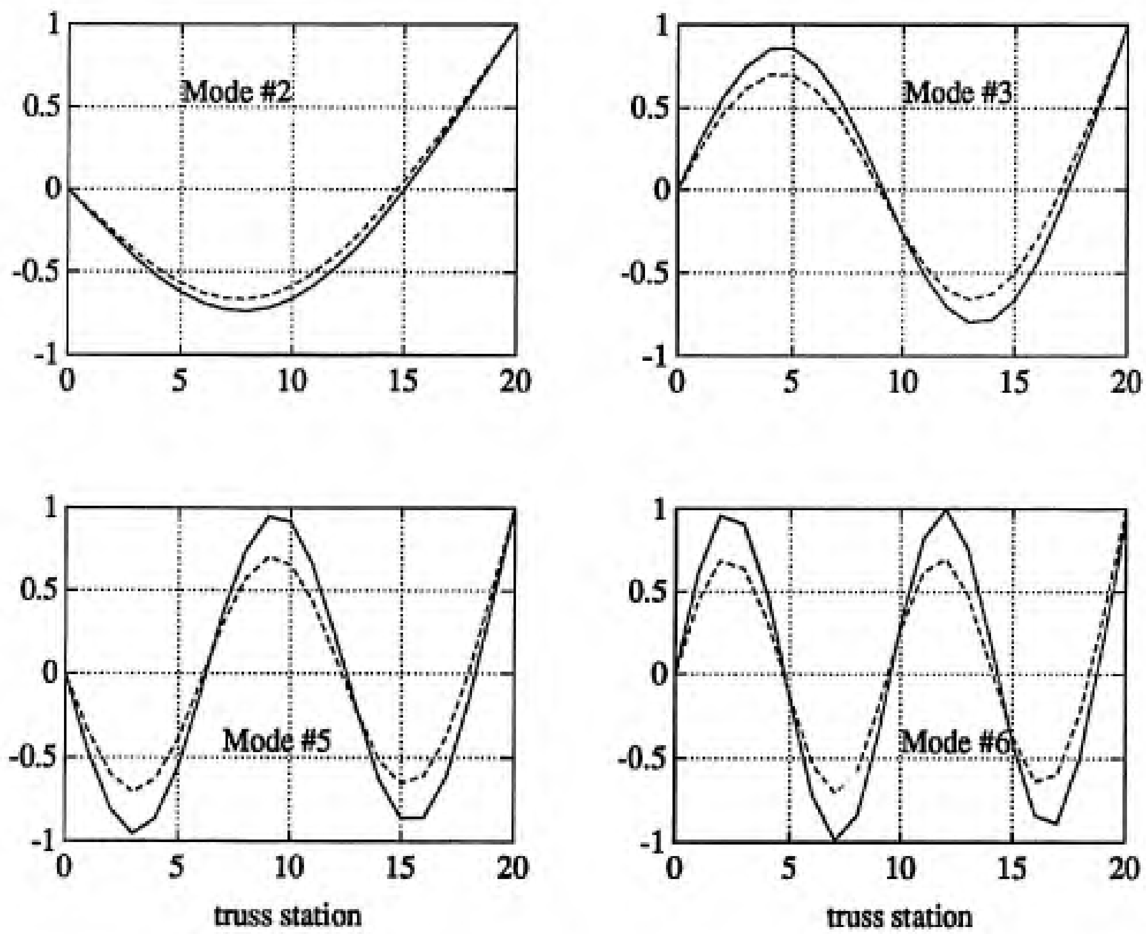

Figure 2.6: Normalized Bending Mode Shapes Comparison: Pinned-Free Finite Element Model (solid) vs. Analytical (dashed)

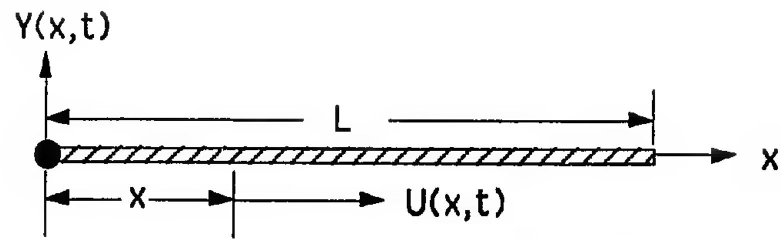

Figure 2.7: The Simple Pinned-Free Euler-Bernoulli Beam

$$-\frac{d}{dx}\left[EI(x)\frac{d^2Y(L)}{dx^2}\right] = 0 \tag{2.28}$$

The general solution to equation 2.3 is still given by equation 2.10. The new frequency and mode shape equations become

$$\sin\beta_n L \cosh\beta_n L = \cos\beta_n L \sinh\beta_n L \tag{2.29}$$

$$Y_n(x) = A_n[\sinh\beta_n L \sin\beta_n x + \sin\beta_n L \sinh\beta_n x] \tag{2.30}$$

Comparisons between beam theory and the finite element model of the pinned-free configuration lead to similar conclusions as with the fixed-free case. Lateral vibration natural frequencies (modes 2, 3, 5, 6) are predicted lower from beam theory due to neglecting rotary inertia. The longitudinal vibration natural frequency (mode 4) is exactly the same as the fixed-free case since the boundary conditions are identical. These validation results confirm the finite element modeling performed on the flexible support structure used as part of the overall flexible optical system in this research.

2.3 Model Reduction

The 61-DOF model (order $2n = 122$) is unnecessarily and impractically large for design and analysis of LOS and/or vibration suppression controllers. We will reduce the model to order $2n_r < 2n$ using a procedure which exactly preserves the dynamic response of the full model in n_r selected DOF and n_r selected modes. This procedure requires solving the generalized free vibration eigenvalue problem

$$[M]\ddot{\mathbf{q}} + [K]\mathbf{q} = \mathbf{0} \tag{2.31}$$

and obtaining the eigenvalue matrix Λ where

$$\Lambda = diag(\omega_1^2, \omega_2^2, \ldots, \omega_{n_r}^2)$$

and the mass normalized eigenvector matrix (modal matrix) Φ where

$$\Phi^T M \Phi = I$$

The model reduction procedure, referred to as 'modal truncation', extracts from the modal matrix Φ the $n_r \times n_r$ reduced modal matrix ϕ, whose rows correspond to the n_r selected DOFs and whose columns correspond to the n_r selected modes. It is necessary to choose DOFs and modes such that ϕ is nonsingular. Similarly, one extracts from Λ the reduced $n_r \times n_r$ diagonal eigenvalue matrix λ, whose diagonal elements correspond to the n_r selected modes. Then the reduced set of system equations becomes

$$[M_r]\ddot{\mathbf{q}}_\mathbf{r} + [K_r]\mathbf{q}_\mathbf{r} = \mathbf{f}_\mathbf{r} \tag{2.32}$$

where $\mathbf{f}_\mathbf{r}$ is the reduced vector of inputs corresponding to $\mathbf{q}_\mathbf{r}$. The reduced mass and stiffness matrices are given by

$$M_r = \phi^{-T}\phi^{-1} \tag{2.33}$$

$$K_r = \phi^{-T}\lambda\phi^{-1} \tag{2.34}$$

Viscous damping can be introduced into equation 2.32 by selecting viscous damping coefficients ζ_s for each mode in the reduced order model. These coefficients can be determined experimentally or by engineering judgment. The modal damping matrix is of the form

$$[2\zeta\omega] = \text{diag}(2\zeta_s\omega_s), \qquad s = 1, 2, \ldots, n_r$$

The reduced viscous damping matrix is

$$[C_r] = \phi^{-T}[2\zeta\omega]\phi^{-1} \tag{2.35}$$

The reduced order damped system of equations can now be described as

$$[M_r]\ddot{\mathbf{q}}_\mathbf{r} + [C_r]\dot{\mathbf{q}}_\mathbf{r} + [K_r]\mathbf{q}_\mathbf{r} = \mathbf{f}_\mathbf{r} \tag{2.36}$$

It is important to note that this method of estimating a reduced viscous damping matrix assumes that the damping does not couple the undamped vibration modes.

Once the model has been reduced, the various actuators can be added to the mathematical model. Section 2.4 describes the actuators of interest and the procedure to include them into the model.

2.4 The Structural and Optical Actuators

This section describes the development of both structural vibration suppression actuators and the reactionless fast steering mirror. Both types of actuators are integrated into various configurations of the flexible optical system model.

2.4.1 The Reaction-Mass Actuator

Active damping in any flexible structure requires some sort of force or displacement (stress or strain) control. The most typical force actuator is the reaction-mass actuator (RMA) and is illustrated in figure 2.8. The RMA relies on an electromagnetic interaction force f, between the proof mass m_a, and the system mass m_s, to 'resist' undesired system motion. The RMA in figure 2.8 can be realized in hardware with a permanent magnet and coil. The stiffness k and damping c (approximated as a viscous damping constant) are a consequence of the flexible suspension system within the actuator that connects the coil with the permanent magnet. The force f is the electromagnetic interaction force between the coil and the reaction mass. With

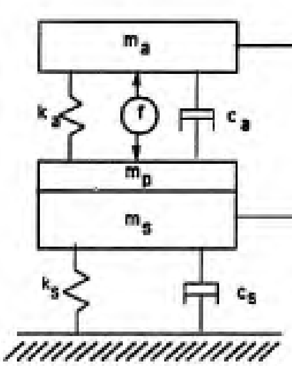

Figure 2.8: The Reaction-Mass Actuator

current through the coil proportional to input voltage e, the transfer function for the 'stand alone' RMA is

$$\frac{F_s(s)}{E(s)} = \frac{Gs^2}{s^2 + 2\zeta_a\omega_a s + \omega_a^2} \tag{2.37}$$

where G is an electromagnetic gain constant (*lbf/volt*), $E(s)$ is the Laplace transform of the input voltage, $F_s(s)$ is the Laplace transform of the total force output and

$$\begin{aligned} \omega_a &= \sqrt{\frac{k_a}{m_a}} = \text{RMA natural frequency (rad/sec)} \\ \zeta_a &= \frac{c_a}{2m_a\omega_a} = \text{RMA damping coefficient} \end{aligned}$$

In this context, 'stand alone' implies that the RMA is attached to a rigid support structure or $m_s + m_p \approx \infty$. Using a Lagrangian approach with inertial coordinates, the equations of motion for the RMA in figure 2.8 are

$$\begin{bmatrix} m_s + m_p & 0 \\ 0 & m_a \end{bmatrix} \begin{bmatrix} \ddot{x}_s \\ \ddot{x}_a \end{bmatrix} + \\ \begin{bmatrix} c_s + c_a & -c_a \\ -c_a & c_a \end{bmatrix} \begin{bmatrix} \dot{x}_s \\ \dot{x}_a \end{bmatrix} + \begin{bmatrix} k_s + k_a & -k_a \\ -k_a & k_a \end{bmatrix} \begin{bmatrix} x_s \\ x_a \end{bmatrix} = \begin{bmatrix} 1 \\ -1 \end{bmatrix} f \tag{2.38}$$

which gives symmetric mass, damping, and stiffness matrices with off-diagonal coupling in damping and stiffness. If equation 2.38 is subjected to a coordinate transformation T so that the second generalized coordinate is relative to the first

$$\underbrace{\begin{bmatrix} x_s & x_a \end{bmatrix}}_{X_T} \xrightarrow{T} \underbrace{\begin{bmatrix} x_s & x_{as} \end{bmatrix}}_{\tilde{X}_T}$$

where,

$$T = \begin{bmatrix} 1 & 0 \\ -1 & 1 \end{bmatrix}$$

such that $X = T^{-1}\tilde{X}$, the mass matrix remains symmetric while the damping and stiffness matrices are both symmetric and diagonal[1]. Performing this coordinate

[1] For very large systems a symmetric mass matrix is advantageous in solving the eigenvalue problem [30].

transformation on equation 2.38, the equations of motion become

$$\begin{bmatrix} m_s + m_p + m_a & m_a \\ m_a & m_a \end{bmatrix} \begin{bmatrix} \ddot{x}_s \\ \ddot{x}_{as} \end{bmatrix} +$$
$$\begin{bmatrix} c_s & 0 \\ 0 & c_a \end{bmatrix} \begin{bmatrix} \dot{x}_s \\ \dot{x}_{as} \end{bmatrix} + \begin{bmatrix} k_s & 0 \\ 0 & k_a \end{bmatrix} \begin{bmatrix} x_s \\ x_{as} \end{bmatrix} = \begin{bmatrix} 0 \\ -1 \end{bmatrix} f \tag{2.39}$$

While the three system matrices for both equations 2.38 and 2.39 are symmetric, the damping and stiffness matrices of equation 2.39 are considerably easier to form, especially for systems with large numbers of actuators. The inertially coupled mass matrix $[\tilde{m}]$ of equation 2.39 can be easily constructed by performing the coordinate transformation on the diagonal mass matrix $[m]$ of equation 2.38 as in

$$[\tilde{m}] = T^{-T}[m]T^{-1}$$

This procedure was used to augment the flexible structure's system matrices with the RMA's mass, damping, and stiffness parameters. These parameters are selected to meet specific vibration suppression requirements. Active research continues to enhance our understanding of RMA dynamics and its usefulness in both passive and active vibration suppression [14, 47, 52]. Figure 2.9 illustrates a tip-mounted RMA with relevant force and motion quantities.

The motion variable used for RMA active damping is the relative velocity $\dot{y}_{22} - \dot{y}_{20}$. The force quantity f_{22-20} is the RMA interaction force. A more general relationship for n RMAs operating as active dampers along the flexible structure is given by

$$\mathbf{f}_{\mathbf{i-j}} = -\overbrace{\begin{bmatrix} c_1 & & \\ & \ddots & \\ & & c_n \end{bmatrix}}^{\Delta} \dot{\mathbf{q}}_{\mathbf{ij}} \tag{2.40}$$

The vector of relative coordinates $\mathbf{q_{ij}} = \mathbf{q_i} - \mathbf{q_j}$ where $\mathbf{q_i}$ denote the RMA DOFs and $\mathbf{q_j}$ the flexible structure DOFs corresponding to each RMA attachment point. The force or torque interaction between $\mathbf{q_i}$ and $\mathbf{q_j}$ is denoted by $\mathbf{f_{i-j}}$. For the configuration shown in figure 2.9 with the single tip-mounted RMA, $n = 1$, $q_i = y_{22}$, and $q_j = y_{20}$.

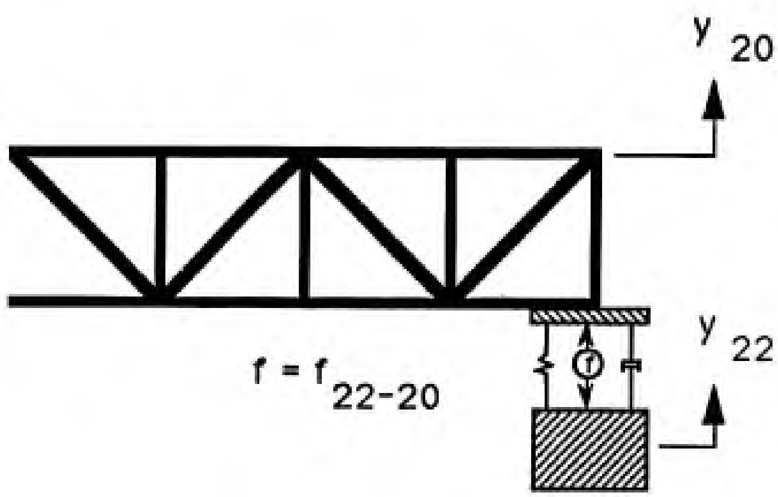

Figure 2.9: RMA Mounted to the Flexible Structure Tip

Damping constants $c_1, \ldots, c_n$ make up the $n \times n$ constant diagonal matrix $\mathbf{\Delta}$, which can be included in $[C_r]$ in equation 2.36.

Miller and Crawley [32] used similar relative velocities and interaction forces, respectively, as system outputs, $\mathbf{y}$, and system inputs $\mathbf{u}$, in output feedback control of the form $\mathbf{u} = -\mathbf{\Delta y}$. If $\mathbf{\Delta}$ is positive definite, and if there are no time delays or other hardware dynamic characteristics not already described by the mathematical model, then this form of output feedback can only increase system stability [32, 22]. There are many schemes available to select 'optimal' values for these velocity feedback constants. In this research, we are less interested in the specific 'optimal' algorithm used to select these values but more interested in the benefits of including them as design parameters in the control of high bandwidth flexible optical systems.

2.4.2 The Reactionless Fast Steering Mirror

A fast steering mirror is required in the design of an optical pointing and stabilization system in order to perform quick retargeting maneuvers and/or precision pointing in the midst of broadband disturbances. A steering mirror is simply a mirror (or other reflective surface) attached to a rigid mounting structure, called the substrate. A two-axis mirror can be articulated about two perpendicular axes, providing 'tip–tilt' motion. For this research, we consider only a single axis mirror as our LOS motion is confined to a plane. A steering mirror can be properly considered 'fast' only if it can be operated in a 'fast' or high bandwidth loop. Mirror substrate flexibility and sensor and actuator dynamics can both limit the operable closed-loop bandwidth. Fast steering mirrors operating in 300–500 Hz pointing or stabilization loops have been demonstrated [15].

A reactionless steering mirror is designed to reduce the amount of reaction torque generated during operation. This is done by including a 'reaction-mass' to the back of the steering mirror that operates in a nearly 'equal-but-opposite' fashion to the mirror. Figure 2.10 illustrates a typical reactionless steering mirror design mounted to the tip of the flexible support structure modeled in section 2.2. The quantities θ_m, θ_{rm}, t_m, and t_{rm} are rotation angles and driving torques of the mirror and reaction mass, respectively.

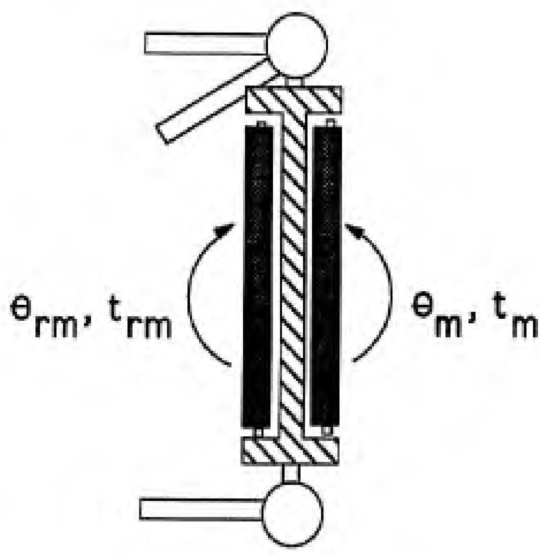

Figure 2.10: The Reactionless Fast Steering Mirror

State-of-the-art reactionless mirrors have demonstrated less than ten percent mismatch in perfect torque cancellation [36]. When the fast steering mirror is to be mounted on a space–borne flexible support structure, it would seem that the reactionless feature would be ideal. The CSI challenge would then be limited to the large angle slewing problem, since small angle retargeting or high bandwidth stabilization would be accomplished with no (ideally) reactive disturbance to the flexible support structure. While this appears to be the design method of choice by the practicing community, one must recognize the weight penalties that go along with the reactionless mirror design (i.e. a reactionless mirror can weigh twice as much as a non-reactionless mirror). This is particularly significant when the steering mirror comprises a large percentage of the total system weight or is mounted to the tip of a lightweight lightly damped flexible structure.

There are some fundamental similarities between the RMA and the non-reactionless fast steering mirror. The dynamics of both can be represented as lightly damped second order spring-mass(inertia)-damper systems and both will 'react' against the structure to which they are mounted. However, while the RMA is intended to react against the structure, the fast steering mirror is not. Its objective is simply to position the LOS of its reflected ray. The transfer function describing this operation is

$$\frac{\theta_m(s)}{t_m(s)} = \frac{\frac{1}{J_m}}{s^2 + 2\zeta_m\omega_m s + \omega_m^2} \tag{2.41}$$

where J_m is the mirror inertia, t_m is the applied mirror torque, ζ_m is the inherent mirror system damping coefficient, and ω_m is the mirror natural frequency. The same transfer function for the reactionless mirror includes two lightly damped closely spaced poles. The small separation in these natural frequencies is due to mismatches in inertia and spring constants.

To model the dynamic coupling between the reactionless steering mirror and its flexible support structure we need a relationship in the form of equation 2.36 that includes the mass (inertia), stiffness, and damping parameters characteristic of the reactionless mirror. This equation is derived in a manner similar to the RMA augmentation. First, the diagonal mass matrix is extracted from the kinetic energy equation for the 'stand alone' reactionless mirror system. The 'all-inertial' coordinate basis of this diagonal mass matrix is then transformed to one with relative mirror and reaction-mass angles. The damping and stiffness matrices are formed by simply adding diagonal elements to the pre-existing damping and stiffness matrices. For example, if we assume a zero-mass zero-inertia mirror mounting bracket (i.e. no parasitic mass or inertia) and a concentric pivot point for both the mirror and the reaction-mass, the kinetic energy of the mirror system in terms of all inertial coordinates is

$$\mathcal{K} = \frac{1}{2}[(m_m + m_{rm})(\dot{x}_m^2 + \dot{y}_m^2) + J_m\dot{\theta}_m^2 + J_{rm}\dot{\theta}_{rm}^2] \tag{2.42}$$

$$= \frac{1}{2}\underbrace{[\dot{x}_m\ \dot{y}_m\ \dot{\theta}_m\ \dot{\theta}_{rm}]}_{\dot{q}_4^T}\underbrace{\begin{bmatrix} (m_m + m_{rm}) & 0 & 0 & 0 \\ 0 & (m_m + m_{rm}) & 0 & 0 \\ 0 & 0 & J_m & 0 \\ 0 & 0 & 0 & J_{rm} \end{bmatrix}}_{M}\underbrace{\begin{bmatrix} \dot{x}_m \\ \dot{y}_m \\ \dot{\theta}_m \\ \dot{\theta}_{rm} \end{bmatrix}}_{\dot{q}_4} \tag{2.43}$$

$$= \frac{1}{2}\dot{q}_4^T M \dot{q}_4 \tag{2.44}$$

where the mass matrix M is 4×4 diagonal and referenced to all inertial coordinates. To include the elements of M with the elements of a larger system mass matrix, like $[M_r]$ of equation 2.36, with mirror and reaction-mass angles in terms of relative coordinates, a transformation must take place. This transformation not only converts mirror and reaction-mass angles from inertial to relative coordinates but also retains r generalized coordinates $\mathbf{q_r}$

$$\underbrace{[\ x_m\ y_m\ \theta_m\ \theta_{rm}\ ]}_{q_4^T} \xrightarrow{T} \underbrace{[\ \overbrace{\cdots\ x_{20}\ y_{20}\ \theta_{20}}^{q_r^T}\ \theta_{m20}\ \theta_{rm20}\ ]}_{q_{r+2}^T}$$

such that

$$q_{r+2} = T^{-1} q_4 \tag{2.45}$$

where the $4 \times (r+2)$ transformation matrix T is

$$T = \begin{bmatrix} 0 & \cdots & 0 & 1 & 0 & 0 & 0 & 0 \\ 0 & \cdots & 0 & 0 & 1 & 0 & 0 & 0 \\ 0 & \cdots & 0 & 0 & 0 & 1 & 1 & 0 \\ 0 & \cdots & 0 & 0 & 0 & 1 & 0 & 1 \end{bmatrix} \tag{2.46}$$

and $\theta_{m20} = \theta_m - \theta_{20}$ and $\theta_{rm20} = \theta_{rm} - \theta_{20}$. Since the mirror and reaction–mass are both assumed to pivot concentrically about the tip batten center-of-gravity, x_m and y_m are exactly x_{20} and y_{20} of table 2.1. Substituting equation 2.45 into equation 2.44, we get

$$\mathcal{K} = \frac{1}{2}\dot{q}_{r+2}^T \overbrace{T^T M T}^{[M_{r+2}]} \dot{q}_{r+2} \tag{2.47}$$

where $[M_{r+2}]$ is the system mass matrix that inertially couples the flexible structure (and any previously added RMA dynamics included in $[M_r]$) with the reactionless mirror.

To construct the system damping and stiffness matrices, one must only append the 2×2 diagonal reactionless mirror damping and stiffness matrices to $[C_r]$ and $[K_r]$ of equation 2.36. The augmented system damping and stiffness matrices are of the form

$$[C_{r+2}] = \begin{bmatrix} [C_r] & \\ & \begin{bmatrix} c_m & 0 \\ 0 & c_{rm} \end{bmatrix} \end{bmatrix} \tag{2.48}$$

$$[K_{r+2}] = \begin{bmatrix} [K_r] & \\ & \begin{bmatrix} k_m & 0 \\ 0 & k_{rm} \end{bmatrix} \end{bmatrix} \tag{2.49}$$

where c_m, c_{rm}, k_m, and k_{rm} are the damping and stiffness constants associated with mirror and reaction-mass motion relative to to the flexible structure attachment point.

The net reaction or 'torque leakage' T_L into the reactionless mirror support structure is the difference of the total torques acting on the mirror and reaction-mass or

$$T_L = J_m \ddot{\theta}_m - J_{rm} \ddot{\theta}_{rm} \tag{2.50}$$

Torque leakage is modeled as small mismatches in inertias J_m and J_{rm} and applied torques t_m and t_{rm}.

2.5 Dynamic Characterization of the Flexible Optical System

This section describes the dynamics of various configurations of the flexible optical system model. Each model allows us to examination a unique aspect of the CSI problem from the effects of torque leakage to the addition of vibration suppression control. We begin with the 61-DOF model of the flexible support structure developed in chapter 2 and reduce it to retain 7 descriptive system degrees-of-freedom. We add the 1-DOF fast steering mirror model to the 7-DOF structure model to obtain a reasonably low order (8-DOF) flexible optical system model useful for LOS controller design. To study the effects of active vibration suppression, single DOF reaction-mass actuators are added to the 8-DOF model creating 9-DOF and 10-DOF system models. The largest model consists of the 2-DOF reactionless mirror system mounted to the tip of the 61-DOF flexible support structure with two 1-DOF reaction-mass actuators, one at the tip and one at the mid-span. This 'full-up' 65-DOF configuration is illustrated in figure 2.1. These configurations are listed in table 2.4. It is important to note that any large flexible structure model can be reduced order with a corresponding reduction in modal fidelity. One must be careful not to remove those modes that will prove to be most troublesome to the particular controller. One hundred percent

Table 2.4: Flexible Optical System Configurations

Model #	*Flexible Structure DOFs*	*RMA*	*Mirror*	*Total System DOFs*
1	7-DOF	none	none	7-DOF
2	7-DOF	none	$T_L = 100\%$	8-DOF
3	7-DOF	tip/mid	$T_L = 100\%$	9-DOF
4	7-DOF	tip + mid	$T_L = 100\%$	10-DOF
5	61-DOF	tip + mid	$T_L = 100\%$	64-DOF

torque leakage ($T_L = 100\%$) implies a non-reactionless mirror. Models 2–5 can be augmented to include the reactionless mirror feature, adding one DOF.

The seven DOFs selected in the reduced flexible support structure model are

$$\{\ y_{20}\ y_{15}\ y_{10}\ y_5\ x_{20}\ \theta_{20}\ \theta_0\ \}$$

which represent all three DOFs at the truss tip, lateral DOFs along the truss quarter points, plus the rotational DOF at the truss hub (see table 2.1). The tip and mid-span RMA relative DOFs are y_{2220} and y_{2110}, respectively ($y_{2220} = y_{22} - y_{20}$, etc) with y_{22} and y_{21} representing the inertial RMA DOFs. The reactionless mirror DOFs are θ_{m20} and θ_{rm20}, respectively.

Dynamic characterizations of the FOS models are performed in the $2n_r$-order state-space. The state models are in the form

$$\begin{aligned}\dot{X}(t) &= AX(t) + BU(t) && (2.51)\\ Y(t) &= CX(t) && (2.52)\end{aligned}$$

where

$$X = \begin{bmatrix} \dot{\mathbf{q}}_r \\ \mathbf{q}_r \end{bmatrix} \qquad U = [\mathbf{f}_r]$$

and where $\mathbf{q}_r$ and $\dot{\mathbf{q}}_r$ are generalized coordinates and their velocities. The state vector X is order $2n_r \times 1$ and the input/disturbance vector U is order $n_r \times 1$. The transformation from the n_r system of equations (equation 2.36) to the $2n_r$ state-space representation is

$$A = \begin{bmatrix} -M_r^{-1}C_r & -M_r^{-1}K_r \\ I & 0 \end{bmatrix} \qquad (2.53)$$

$$B = \begin{bmatrix} M_r^{-1} \\ 0 \end{bmatrix} \qquad (2.54)$$

The C matrix of equation 2.52 is constructed by simply selecting as output the motion variable (degree-of-freedom) of interest.

Actuators Figures 2.11 and 2.12 are frequency response plots for a representative reaction-mass actuator and fast steering mirror for the transfer functions given in equations 2.37 and 2.41. Frequencies, f, are presented in Hertz which is related to frequencies, ω, by $f = \omega/2pi$.

61-DOF Flexible Support Structure Dynamics Figures 2.13–2.15 are frequency response plots for the 61-DOF flexible support structure described in section 2.2.4. Figures 2.13 and 2.14 show $\theta_0(j\omega)/t_0(j\omega)$ and $\theta_{20}(j\omega)/t_{20}(j\omega)$ which are examples of collocated systems (i.e. the sensor and actuator are collocated). Figure 2.15 shows $\theta_{20}(j\omega)/t_0(j\omega)$, a non-collocated system. Figures 2.16–2.18 are pole-zero maps for the two collocated and one non-collocated transfer functions. The pole-zero interlacing expected in collocated transfer functions of flexible systems is revealed in figures 2.16 and 2.18 [28]. Figure 2.18, the non-collocated transfer function, shows the non-minimum phase zeros which so often lead to 'tail-wags-dog' controller instability.

Of particular interest to the control designer are the transfer function zeros. Pole-zero separation dictates the amount of time a mode dwells at -180 degrees of phase and therefore must be considered when selecting closed-loop feedback gains. For certain types of structural flexibility, the smaller the pole-zero separation the faster phase loss from the pole is recovered, thereby limiting the potential instabilities[2]. Figures 2.19 and 2.20 illustrate the magnitude of pole-zero separation on a mode by mode basis for two collocated transfer functions expanded in 60 elastic modes. Pole-zero separation of the for k^{th} minimum phase elastic mode is described by parameter β_k where

$$\beta_k = \frac{\omega_k}{\Omega_k} \qquad k = 1, 2, \ldots, 60 \tag{2.55}$$

Pole-zero cancellation is implied by $\beta_k = 1$.

Model#1 Figures 2.21–2.23 are frequency response plots for the same transfer functions as in figures 2.13–2.15, but for the reduced 7-DOF Model#1. Pole-zero maps for the reduced 7-DOF model, similar to those shown in figures 2.16 and 2.17 show changes in the zero locations, but are most noticeable in figure 2.24–the non-collocated case. Zeros movement for the two collocated transfer functions is best shown by comparing β_k for the applicable six elastic modes. As seen in figures 2.25 and 2.26, the reduced order model under-estimates the pole-zero separation for the first few critical elastic modes. Figure 2.27 shows the lateral behavior of the flexible structure as it undergoes rigid body slew. The motion is induced by the shaped-torque command shown in figure 2.28. The four curves represent lateral motion at the truss tip, three-quarter point, mid-point, and one-quarter point (y_{20} y_{15} y_{10} y_5). The relative lack of oscillatory motion at y_{15} is due to the coincidence of that DOF with the first bending mode's anti-node. A sensor placed at y_{15} in a feedback loop

[2] Structural flexibility can be categorized into three basic types, each with unique implications to the design of feedback controllers [49]. These categories and control implications will be discussed in chapter 3 in the context of single mode expansions.

designed to control the first bending mode would sense little or no motion due to that mode. This is commonly referred to as modal unobservability.

Model#2 The steering mirror is added to the tip of the 7-DOF flexible structure model. The mirror can be described either as reactionless or non-reactionless (changing the degrees-of-freedom by one). The natural frequency of the mirror can also be varied, representing either of the two actuators described in section 2.4.2. For this research, the mirror mass is fixed at seventy percent of the total system mass which is two and one-third times the mass of the flexible support structure. Mirror inertia is varied between two tenths percent and fifty percent of support structure inertia. Figures 2.29 and 2.30 are frequency response plots for $\theta_0(j\omega)/t_0(j\omega)$ where the steering mirror natural frequency is 20 Hz (electromagnetic actuator) and 10 kHz (piezo-electric actuator), respectively. Figures 2.31 and 2.32 are frequency response plots for the mirror transfer function $\theta_m(j\omega)/t_m(j\omega)$. Figure 2.31 highlights the reversal in flexible mode pole-zero orientation as a function of actuator natural frequency. In figure 2.32 pole-zero separation is shown to be a function of the ratio between mirror and support structure inertia. Both effects shown in these two figures have significant implicactions in designing a line-of-sight controller.

Model#3 A single reaction-mass actuator is added, first to the tip, then to the mid-span of the flexible optical system model#2. Figure 2.33 shows the frequency response of the mirror transfer function $\theta_m(j\omega)/t_m(j\omega)$ for the system with a tip-mounted RMA and mirror natural frequency of 20 Hz. Figures 2.34 and 2.35 characterize the FOS for tip vs mid-span mounted RMA's. The transfer functions shown are $\dot{y}_{2110}(j\omega)/f_{2110}(j\omega)$ and $\dot{y}_{2220}(j\omega)/f_{2220}(j\omega)$, where f_{2110} and f_{2220} are the reaction forces acting between the RMA mass and the structure. The RMA mass in figure 2.35 is ten times that in figure 2.34. The mid-span RMA (left most plots) interacts much more with the system flexible modes whereas the tip RMA (right most plots) appears to be insensitive to any flexible mode. This 'insensitivity' is due to the large mirror mass lccated at the structure's tip, reducing the magnitude of the modal contribution at the tip. Another way of looking at this is to recognize that adding mass to the tip of a beam-like structure tends to fix the free end of the beam or cause it to behave more like an anti-node. Structural vibration tends to become 'uncontrollable' by way of a tip-mounted RMA, an important fact to recognize if FOS structural vibration control is to be attempted.

Model#4 and Model#5 Model#4 includes a 7-DOF reduced order flexible structure model, a non-reactionless steering mirror, plus both tip and mid-span mounted RMAs. Figure 2.36 shows the inertial non-reactionless mirror response to a step input in mirror torque. The model is then augmented with a mirror reaction-mass and driven at 110% of the mirror torque. This torque mismatch is in addition to the ten percent mismatch in mirror reaction-mass inertia. Figure 2.37 shows the mirror and the mirror reaction-mass response to a step input in mirror torque. Model#5 consists of the 61-DOF flexible support structure plus the same actuator elements found in model#4. Dynamic characterizations reveal only the presence of much higher frequency modes and will not be shown here. Model#5 will be used as the 'truth' model for LOS controllers designed using reduced order models.

In this chapter we have described the details of developing and validating models of the various elements of a flexible optical system. While the overall system model is specific in configuration, it is general in concept. If one looks at large space structures in general, one will find similar elements: flexible structures, actuation devices and disturbance sources. System uniqueness is found primarily in the mission and mission dictates controller bandwidth. The models developed in this chapter reveal various aspects of the control-structure-interaction problem facing the line-of-sight controller designer.

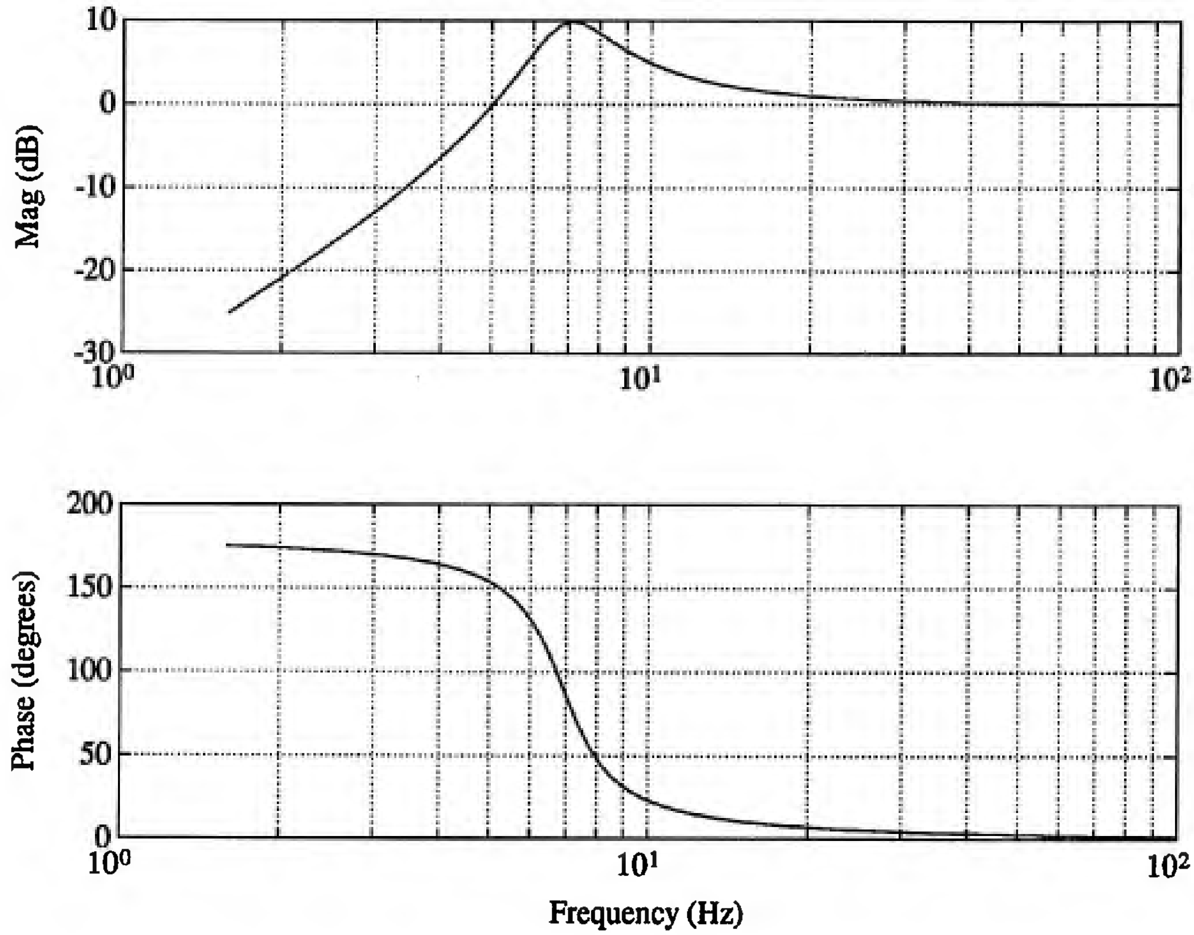

Figure 2.11: Reaction-Mass Actuator Frequency Response $F_s(j\omega)/E(j\omega)$

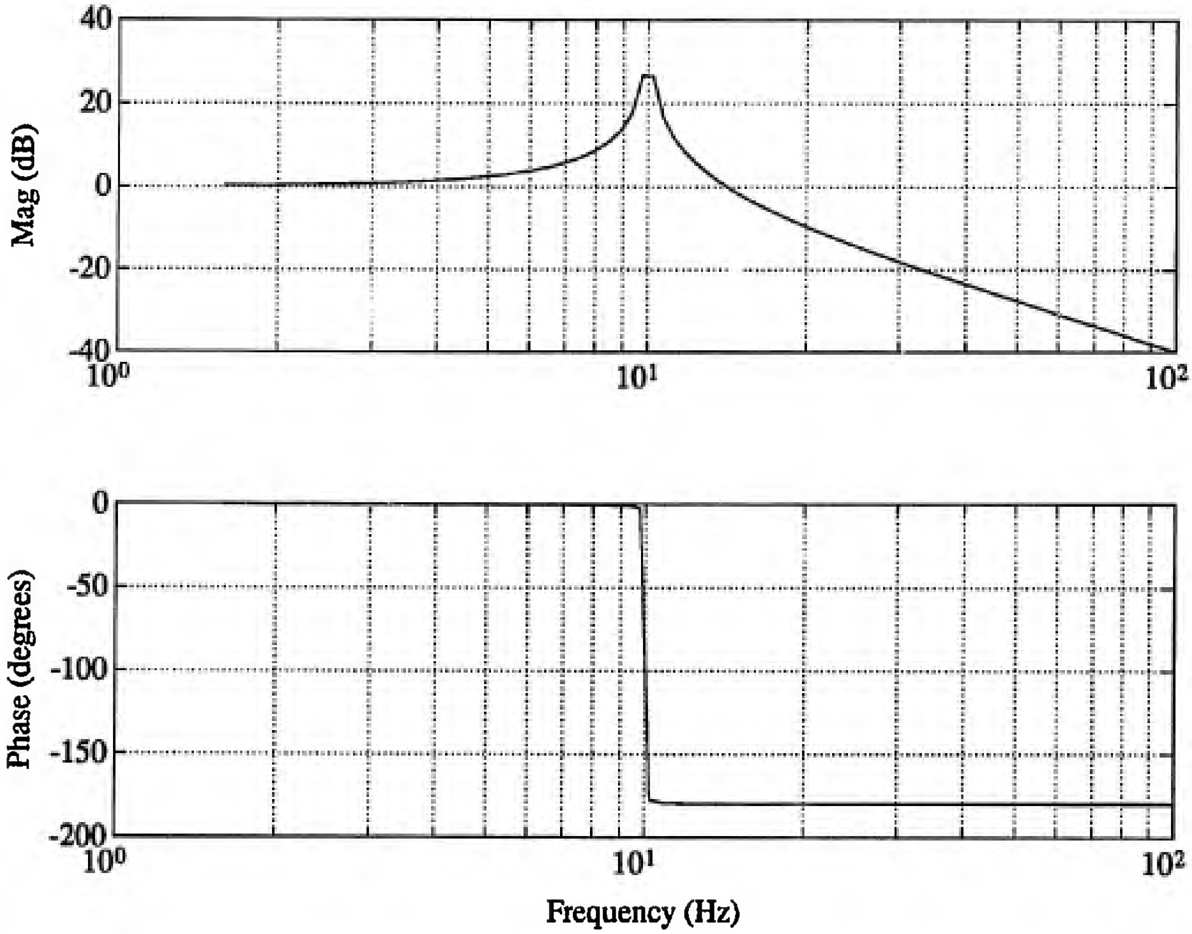

Figure 2.12: Fast Steering Mirror Frequency Response $\theta_m(j\omega)/t_m(j\omega)$

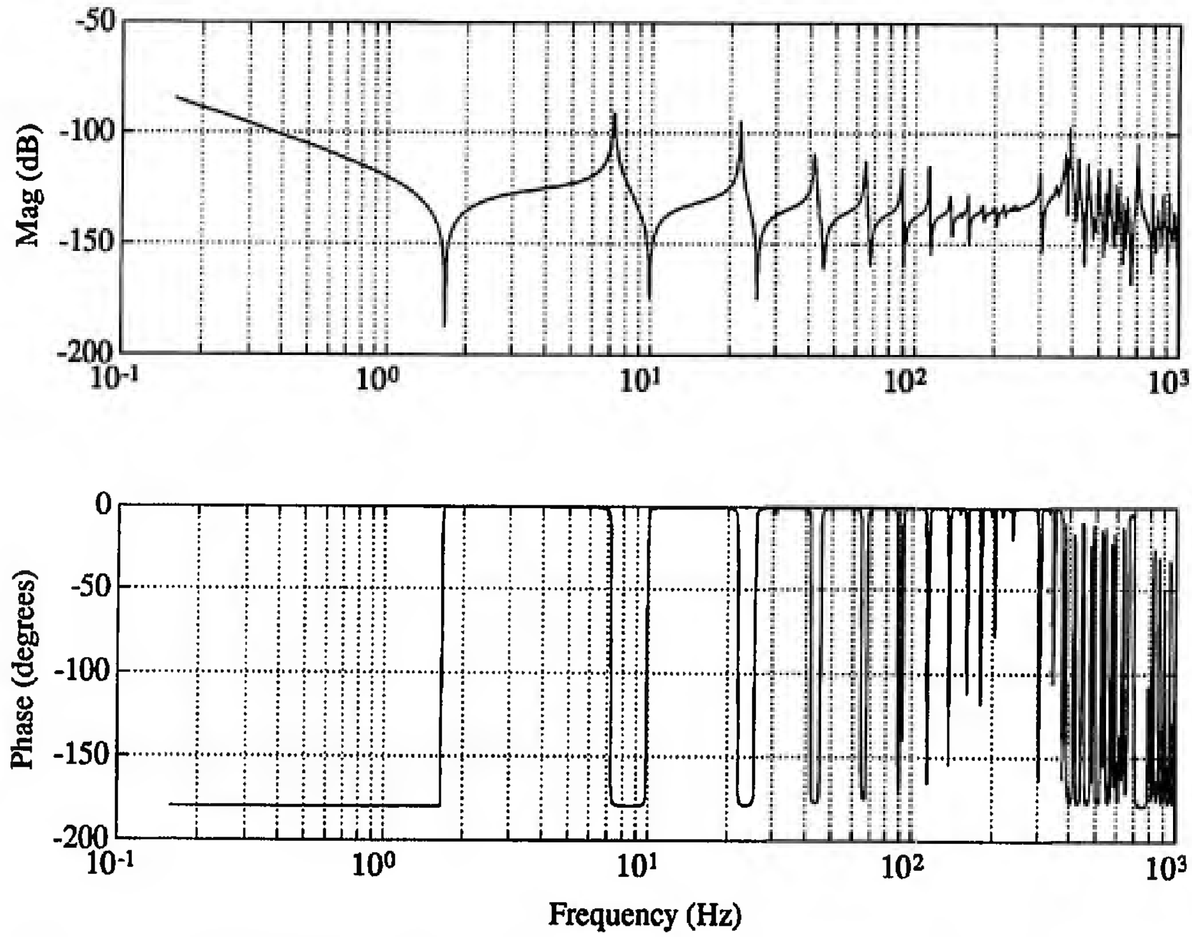

Figure 2.13: Flexible Support Structure Frequency Response $\theta_0(j\omega)/t_0(j\omega)$, 61-DOF Model

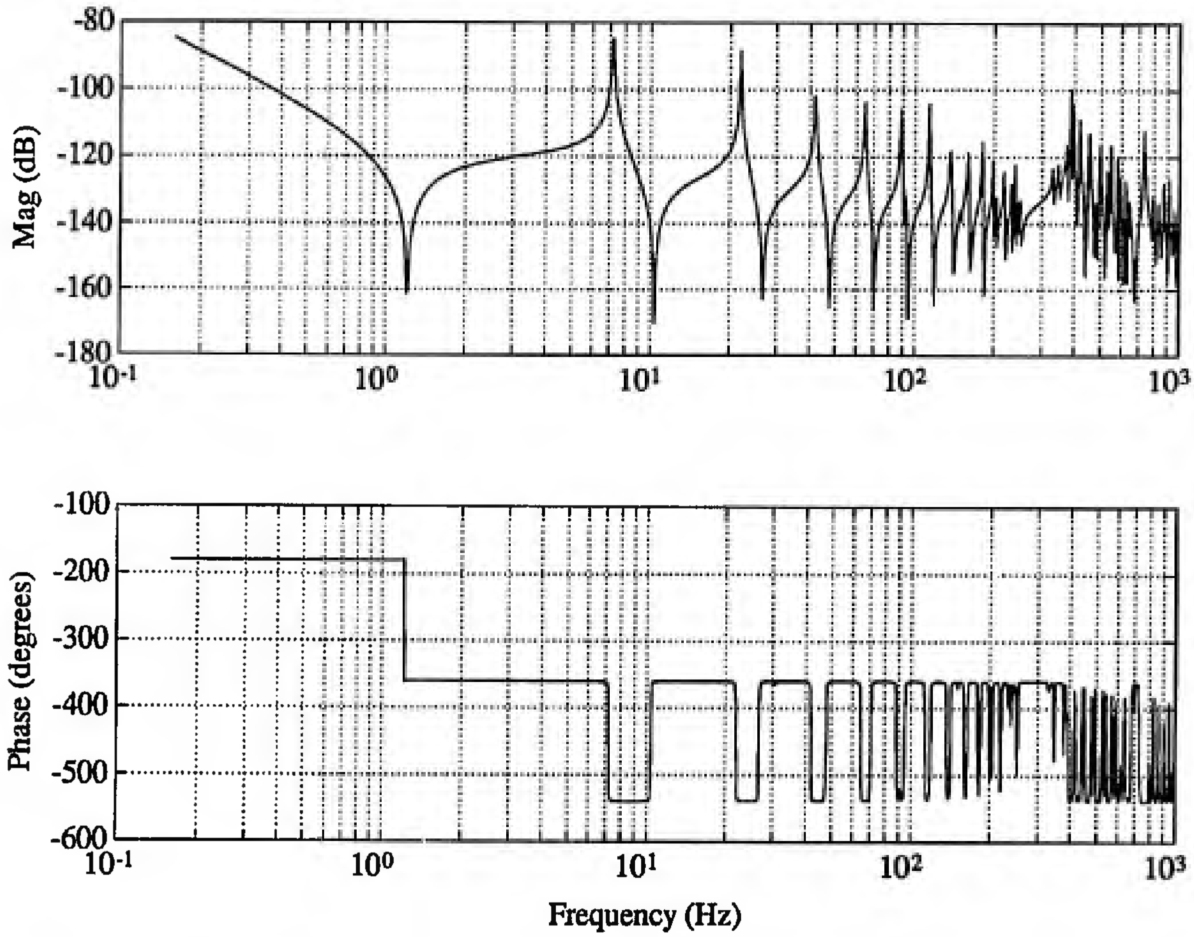

Figure 2.14: Flexible Support Structure Frequency Response $\theta_{20}(j\omega)/t_{20}(j\omega)$, 61-DOF Model

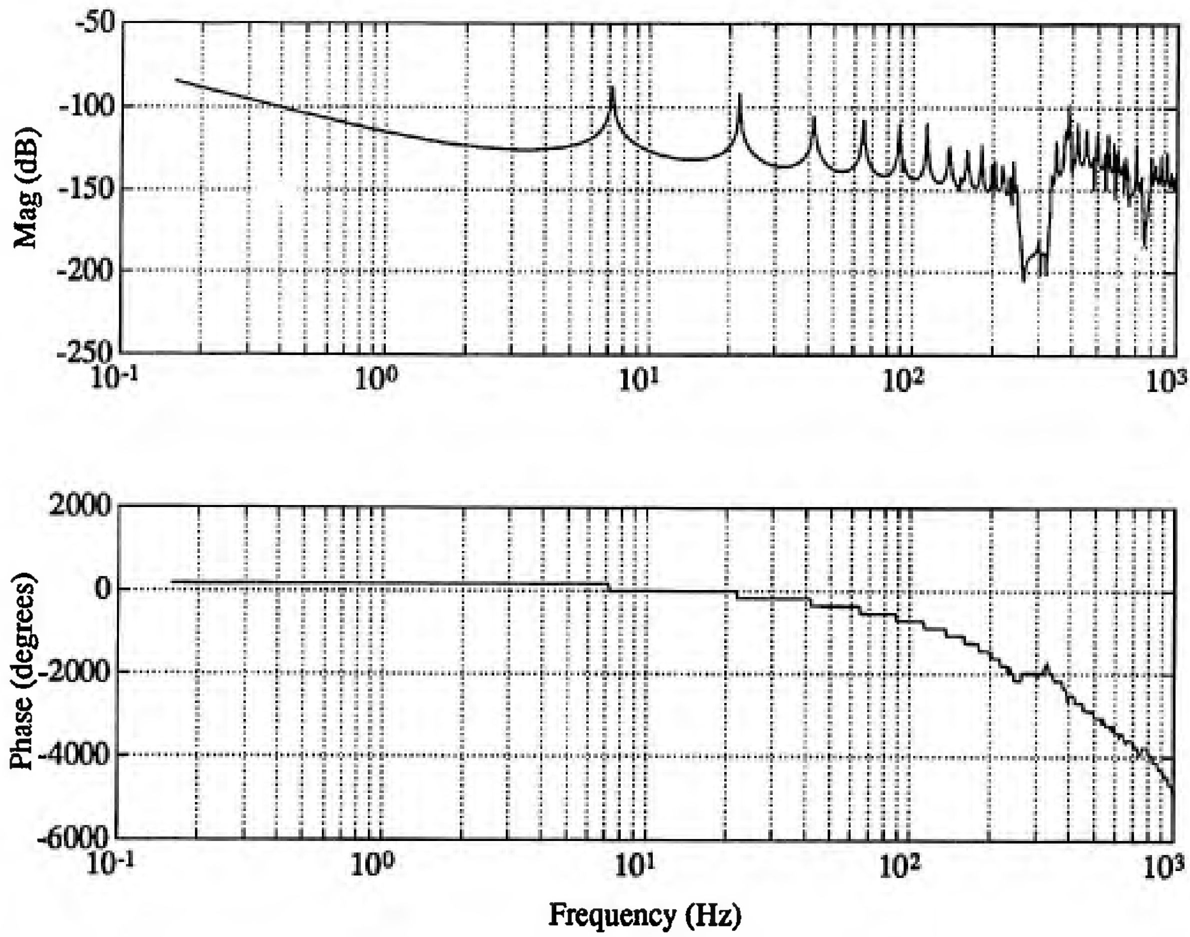

Figure 2.15: Flexible Support Structure Frequency Response $\theta_{20}(j\omega)/t_0(j\omega)$, 61-DOF Model

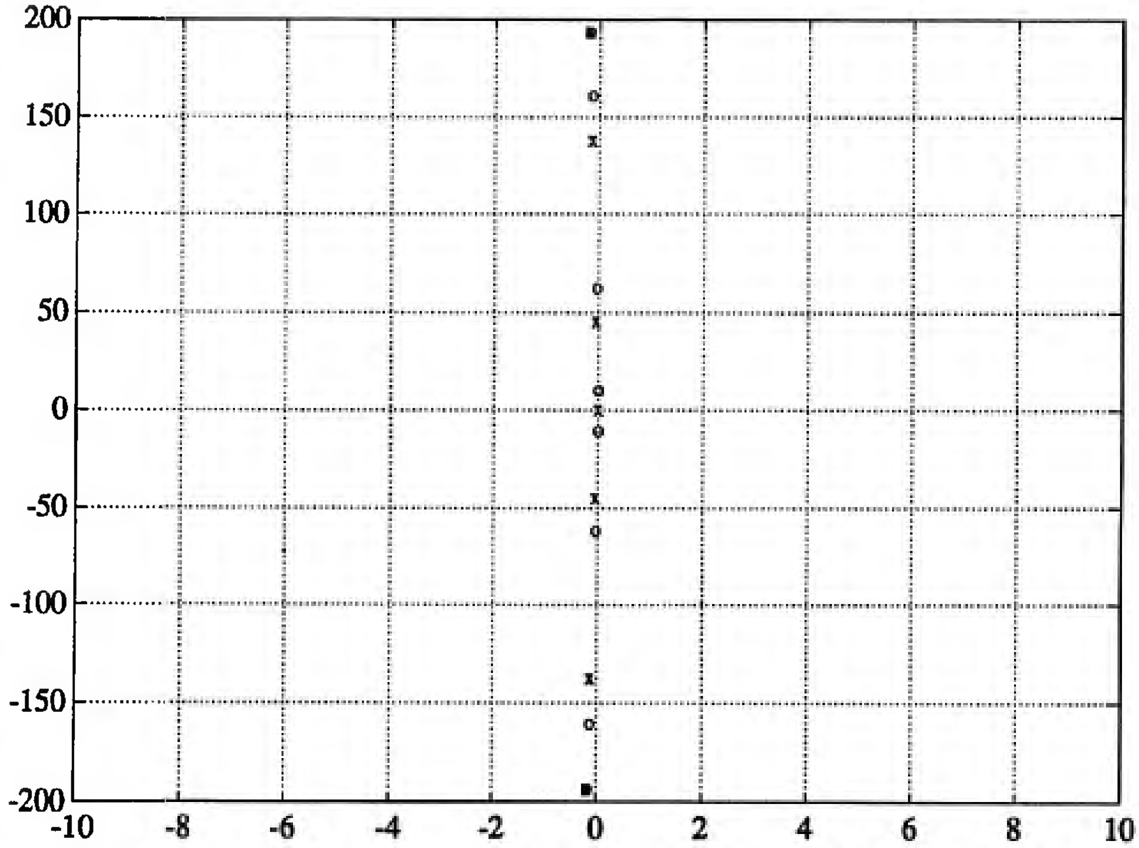

Figure 2.16: Pole-Zero Map for $\theta_0(s)/t_0(s)$: 60 Elastic Mode Expansion, 61-DOF Model

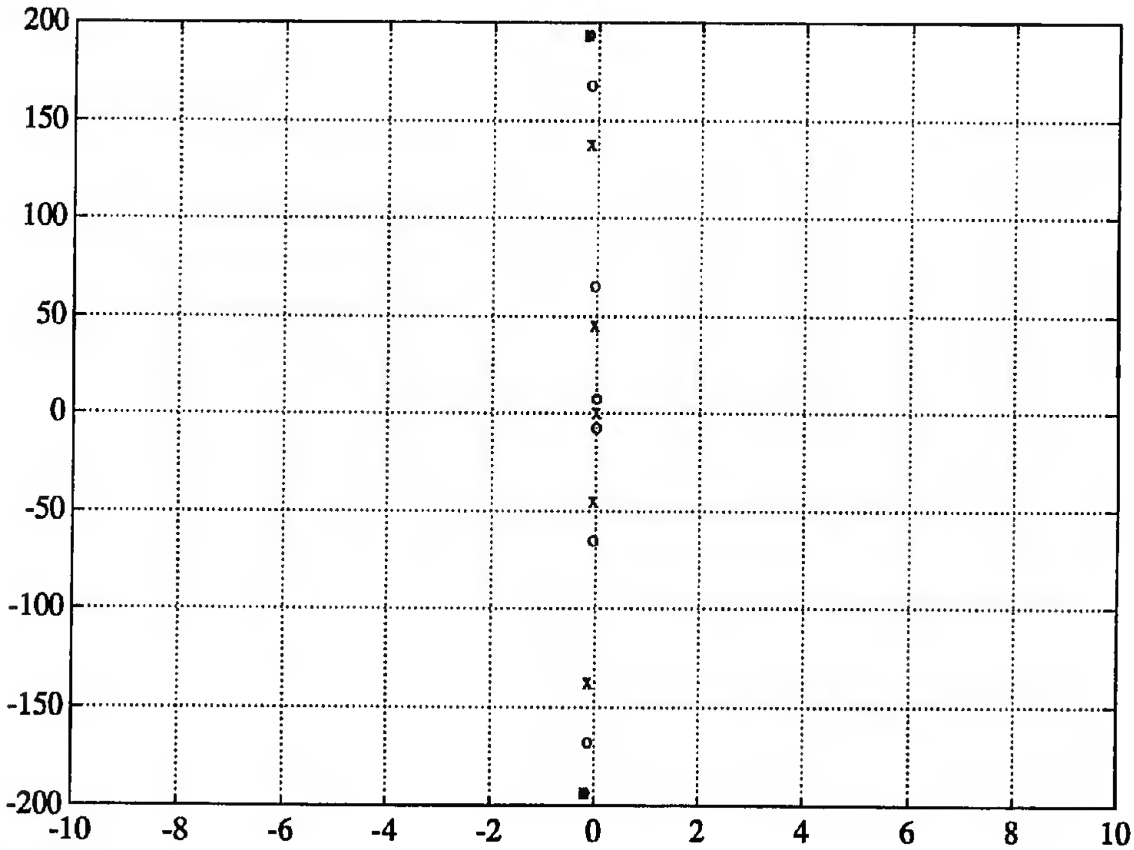

Figure 2.17: Pole-Zero Map for $\theta_{20}(s)/t_{20}(s)$: 60 Elastic Mode Expansion, 61-DOF Model

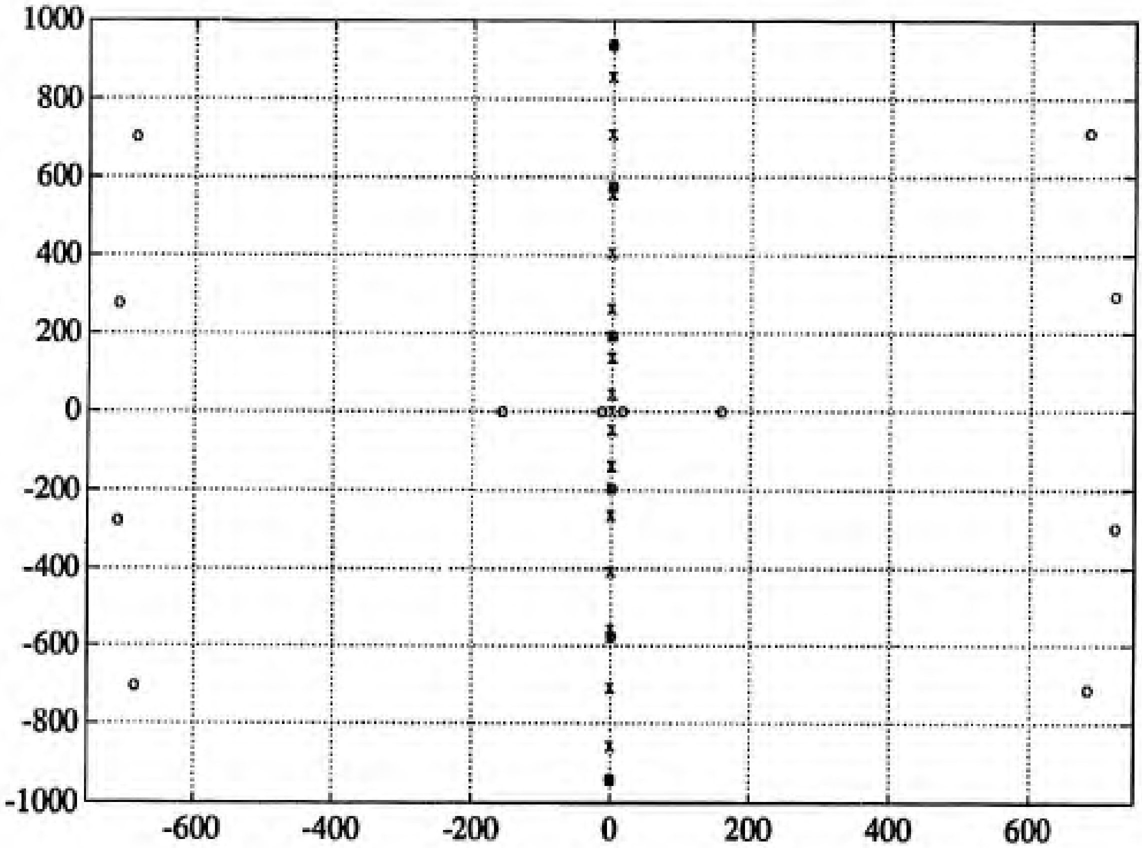

Figure 2.18: Pole-Zero Map for $\theta_{20}(s)/t_0(s)$: 60 Elastic Mode Expansion, 61-DOF Model

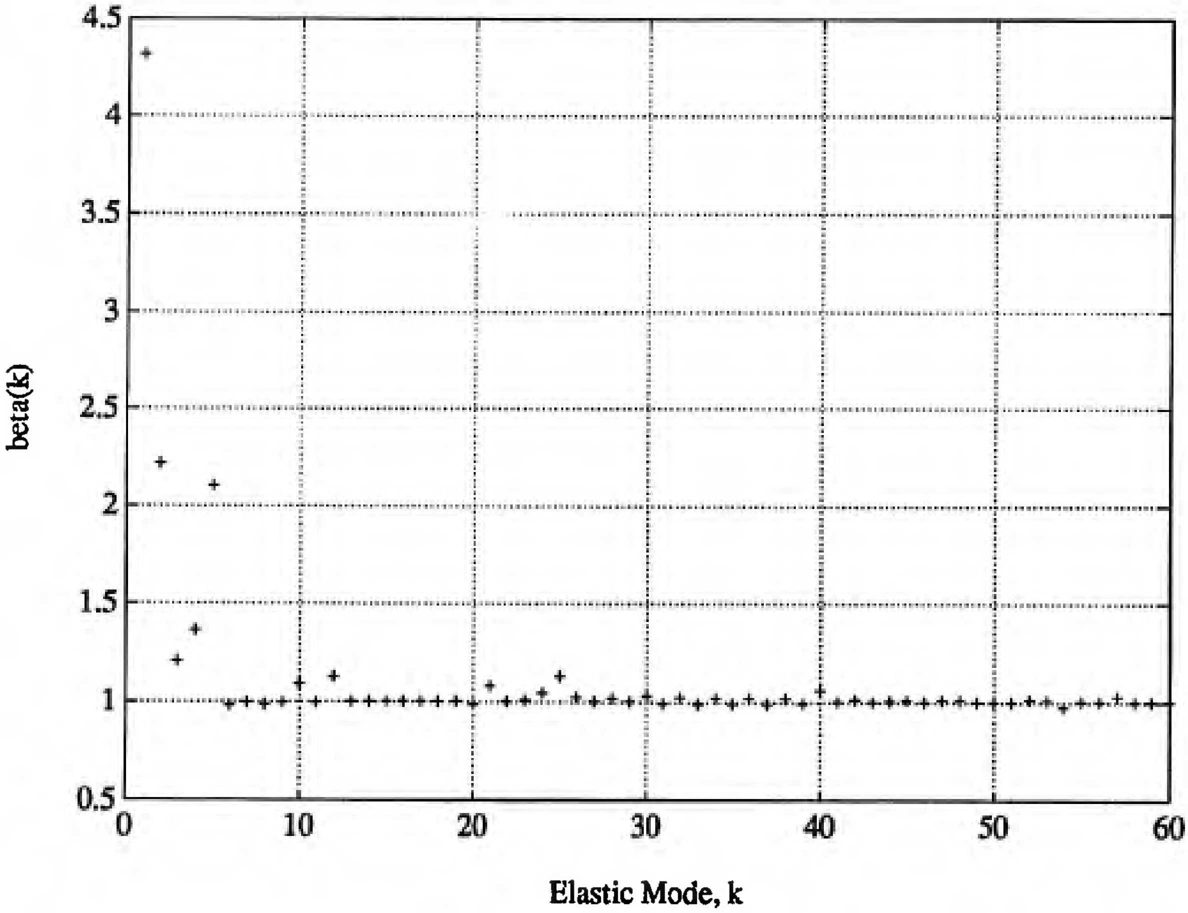

Figure 2.19: Pole-Zero Separation for $\theta_0(s)/t_0(s)$: 60 Elastic Mode Expansion, 61-DOF Model

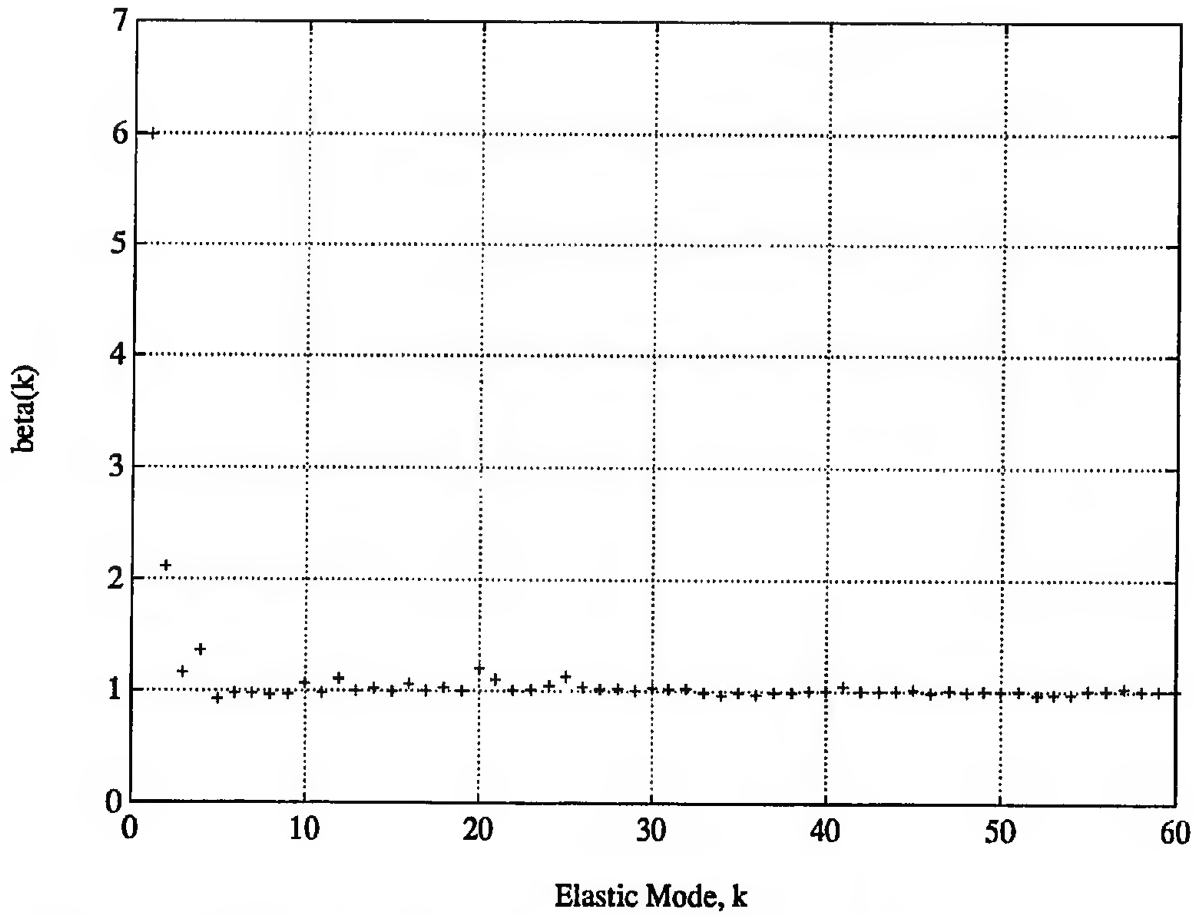

Figure 2.20: Pole-Zero Separation for $\theta_{20}(s)/t_{20}(s)$: 60 Elastic Mode Expansion, 61-DOF Model

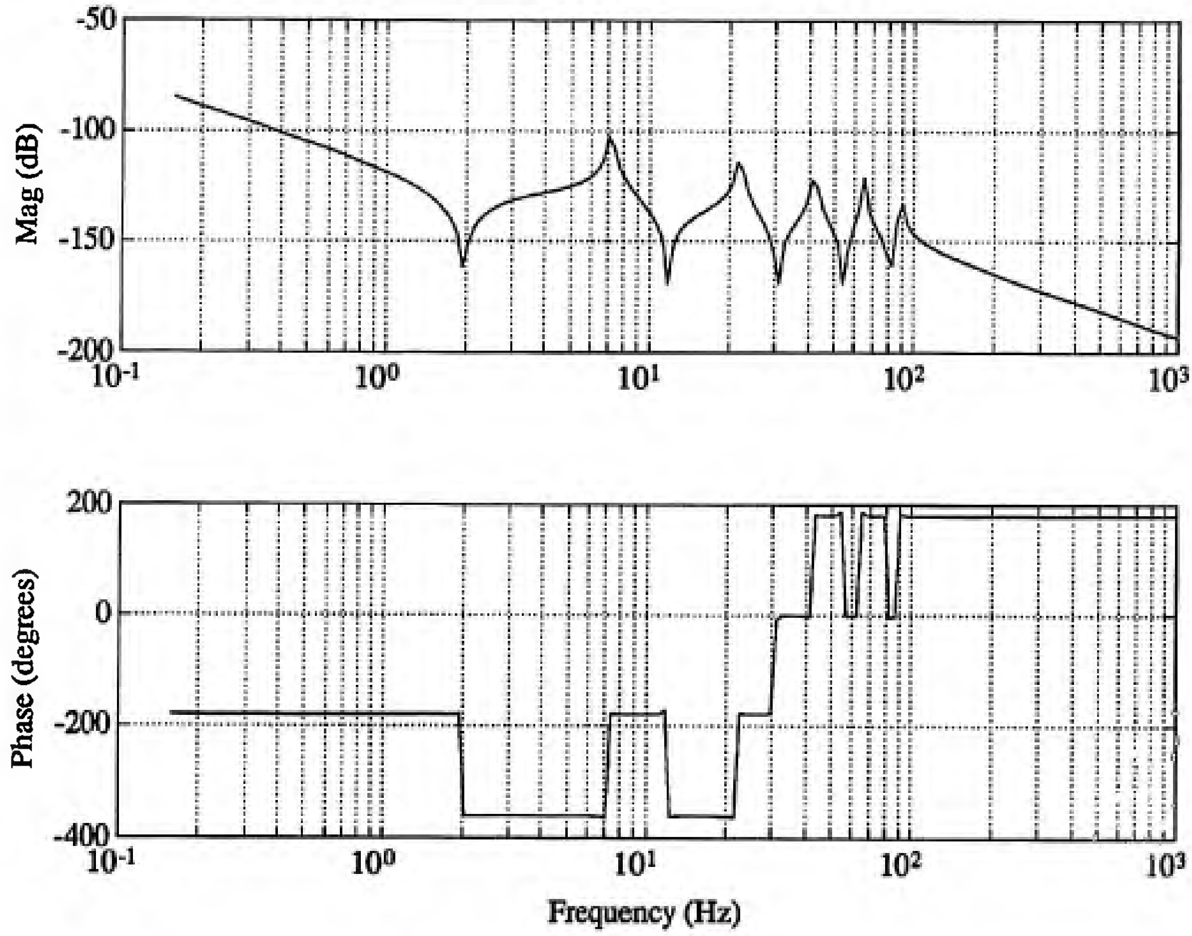

Figure 2.21: 7-DOF Flexible Support Structure Frequency Response $\theta_0(j\omega)/t_0(j\omega)$, Model#1

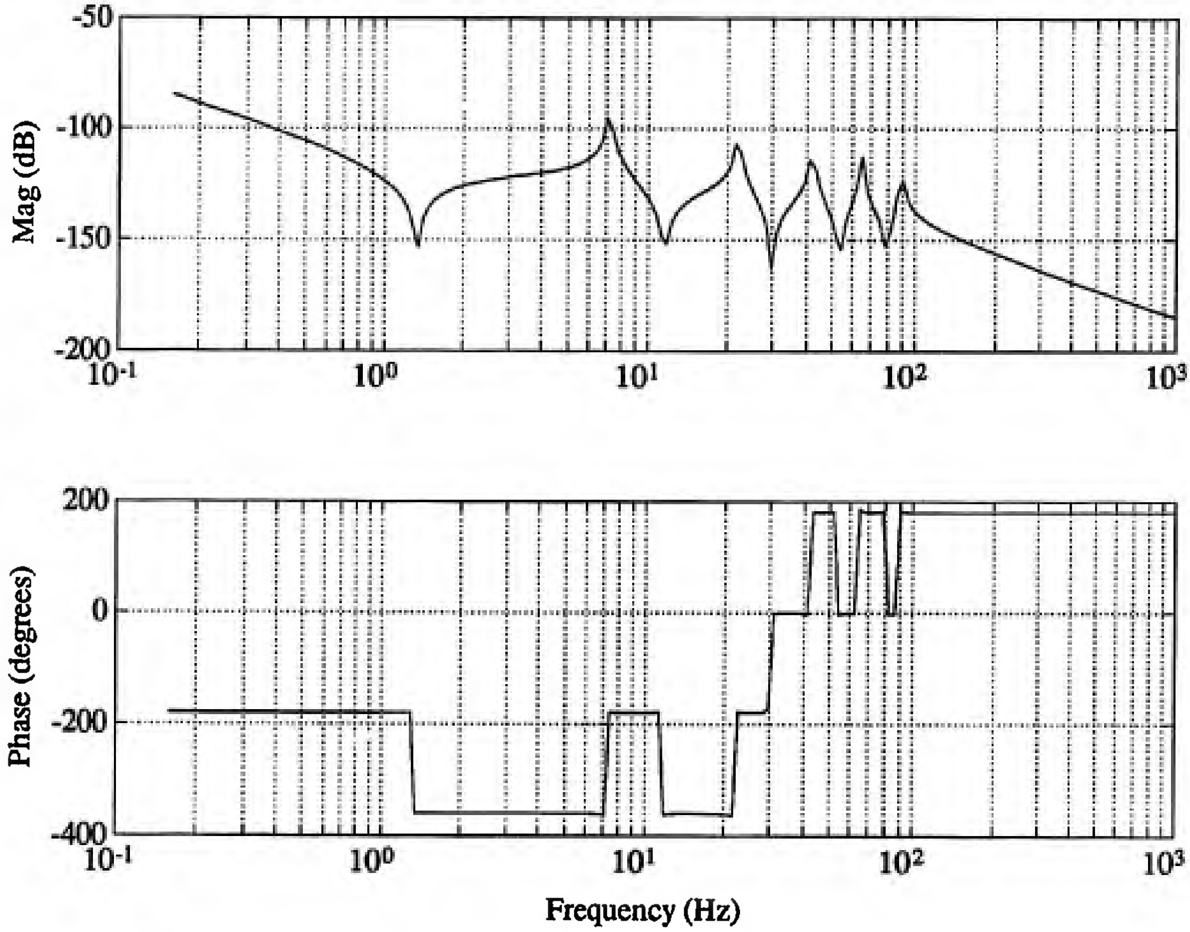

Figure 2.22: 7-DOF Flexible Support Structure Frequency Response $\theta_{20}(j\omega)/t_{20}(j\omega)$, Model#1

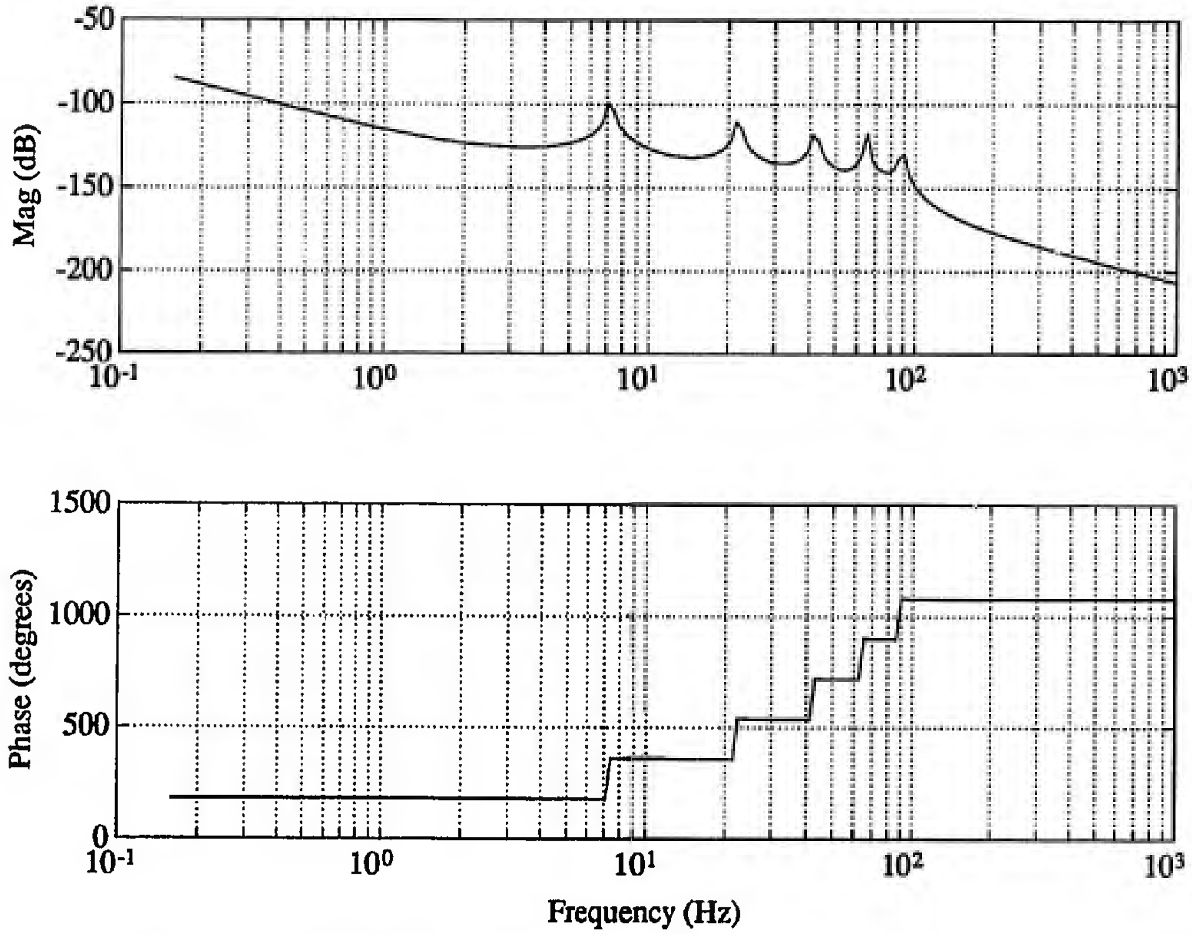

Figure 2.23: 7-DOF Flexible Support Structure Frequency Response $\theta_{20}(j\omega)/t_0(j\omega)$, Model#1

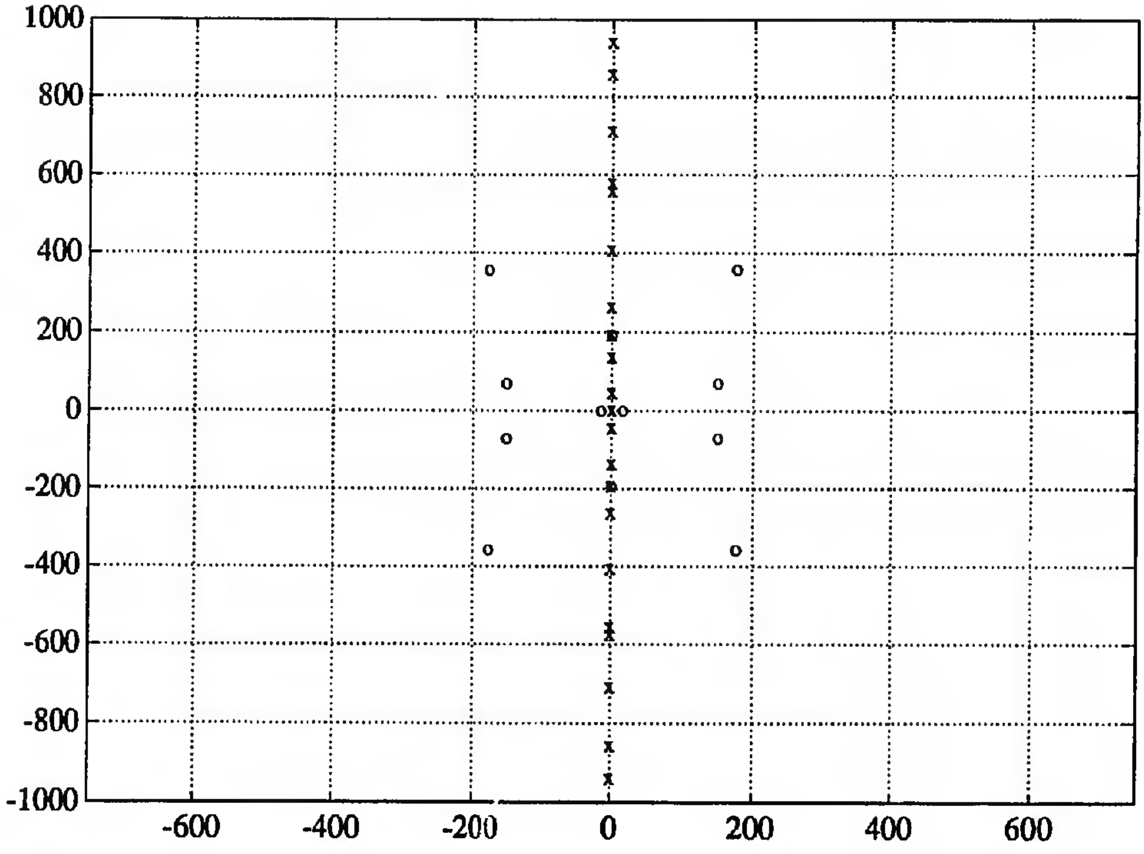

Figure 2.24: Pole-Zero Map for $\theta_{20}(s)/t_0(s)$: 6 Elastic Mode Expansion, Model#1

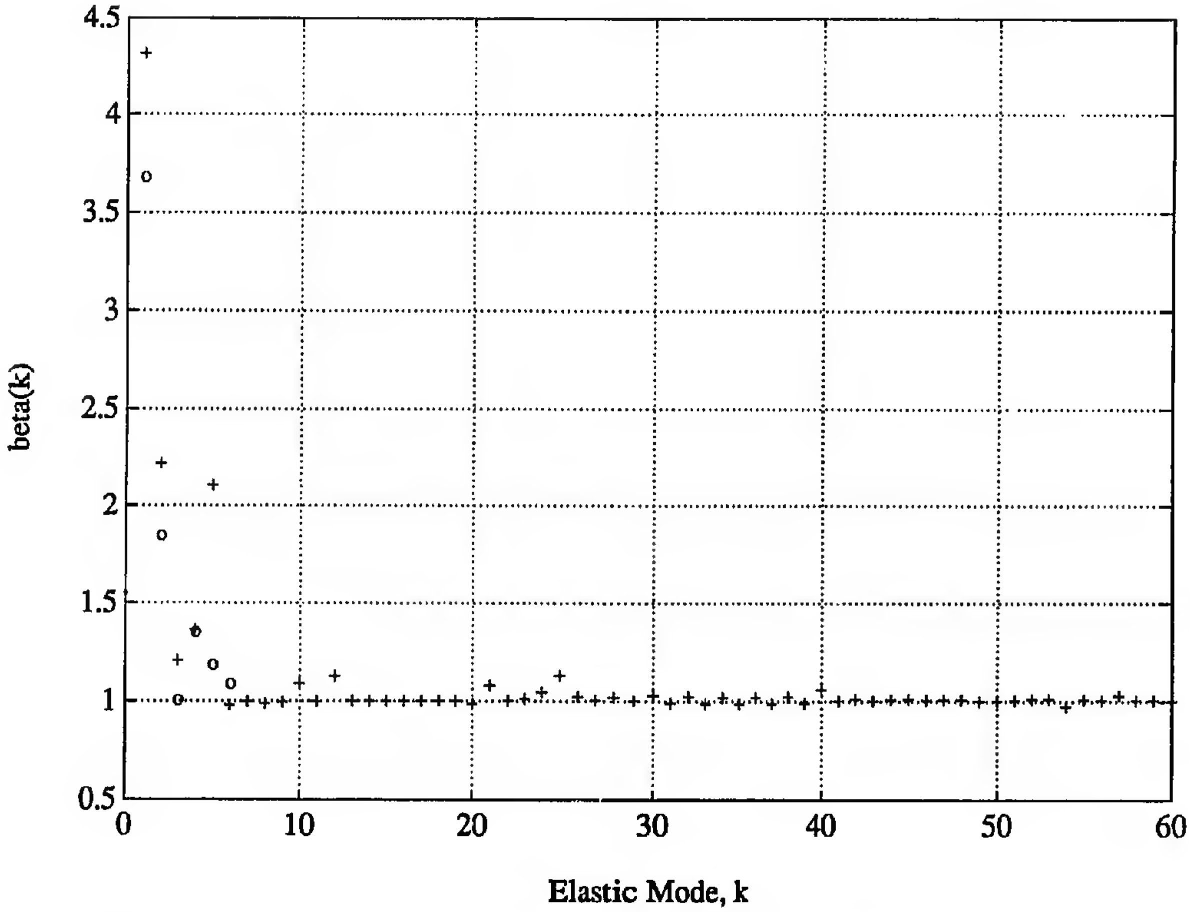

Figure 2.25: Pole-Zero Separation for $\theta_0(s)/i_0(s)$: 6 Elastic Mode Expansion (o), 60 Elastic Mode Expansion (+), Model#1

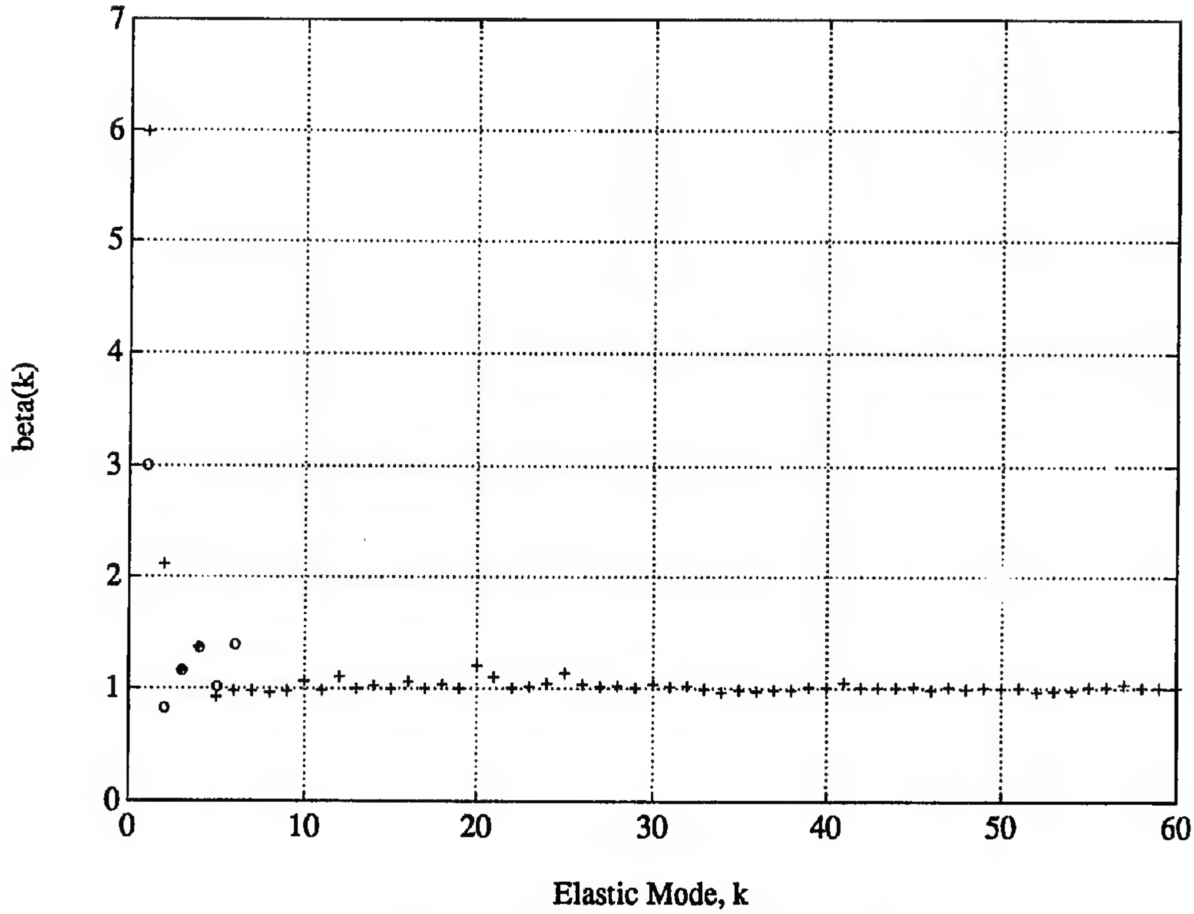

Figure 2.26: Pole-Zero Separation for $\theta_{20}(s)/t_{20}(s)$: 6 Elastic Mode Expansion (o), 60 Elastic Mode Expansion (+), Model#1

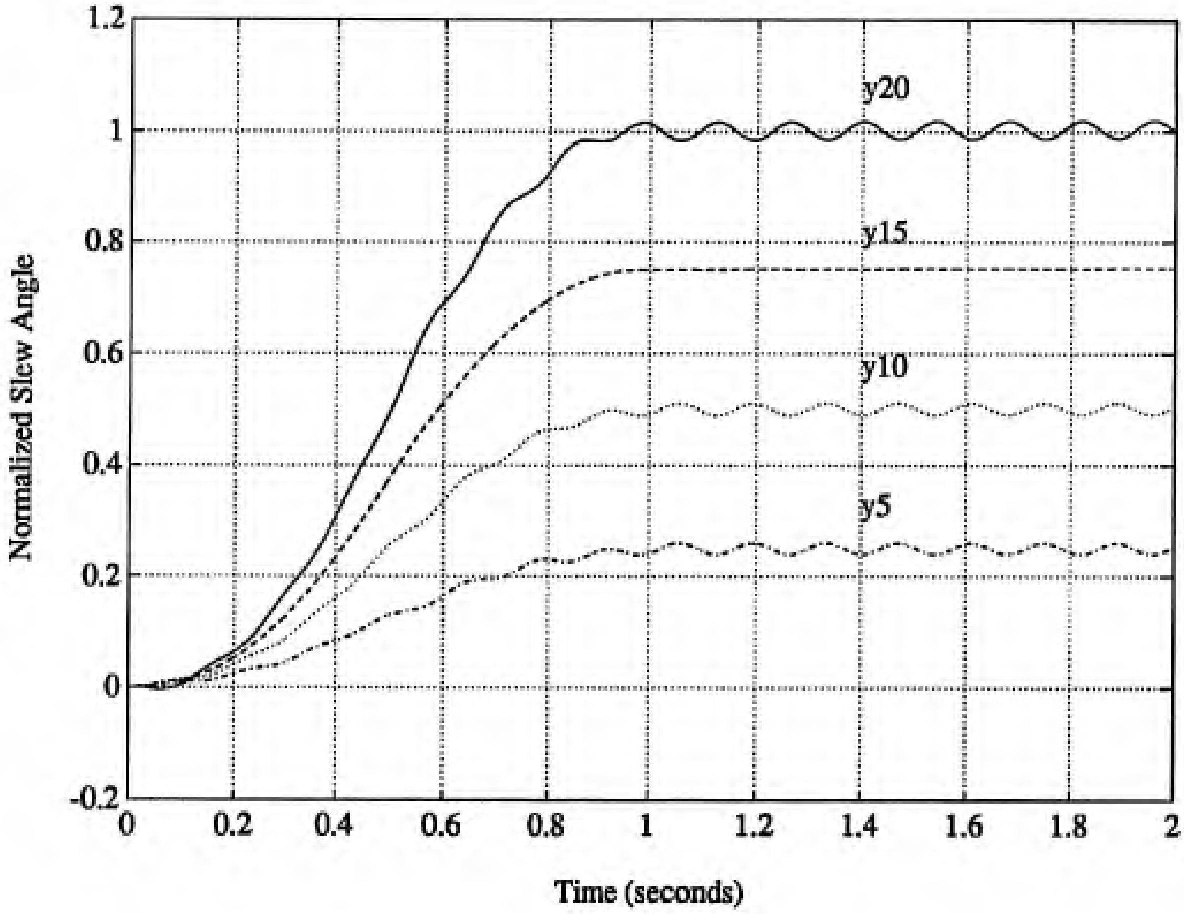

Figure 2.27: 7-DOF Flexible Support Structure Slew Response, Model#1

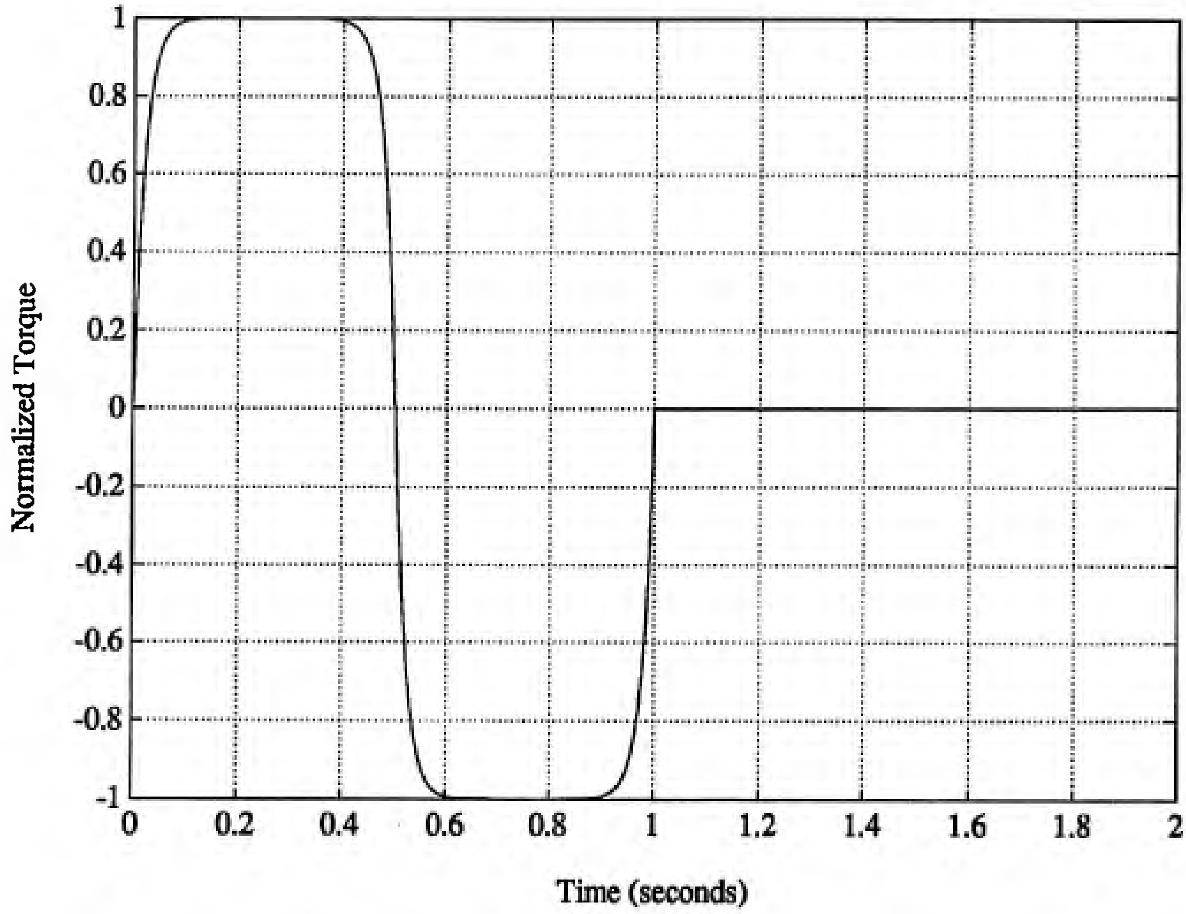

Figure 2.28: Shaped-Torque Command Applied to Flexible Support Structure, All Models

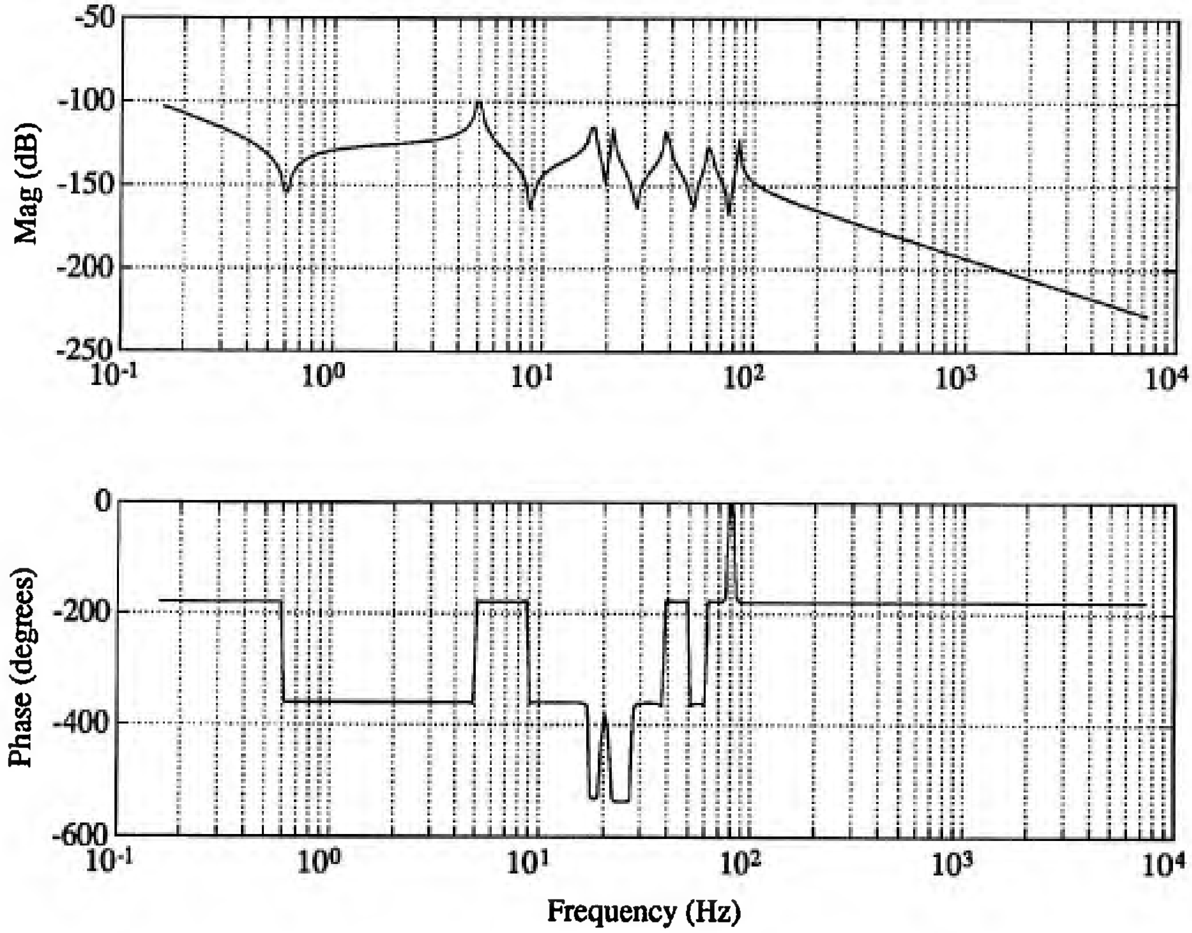

Figure 2.29: Frequency Response $\theta_0(j\omega)/t_0(j\omega)$, Mirror $\omega_n = 20(2\pi)$ rad/sec, Model#2

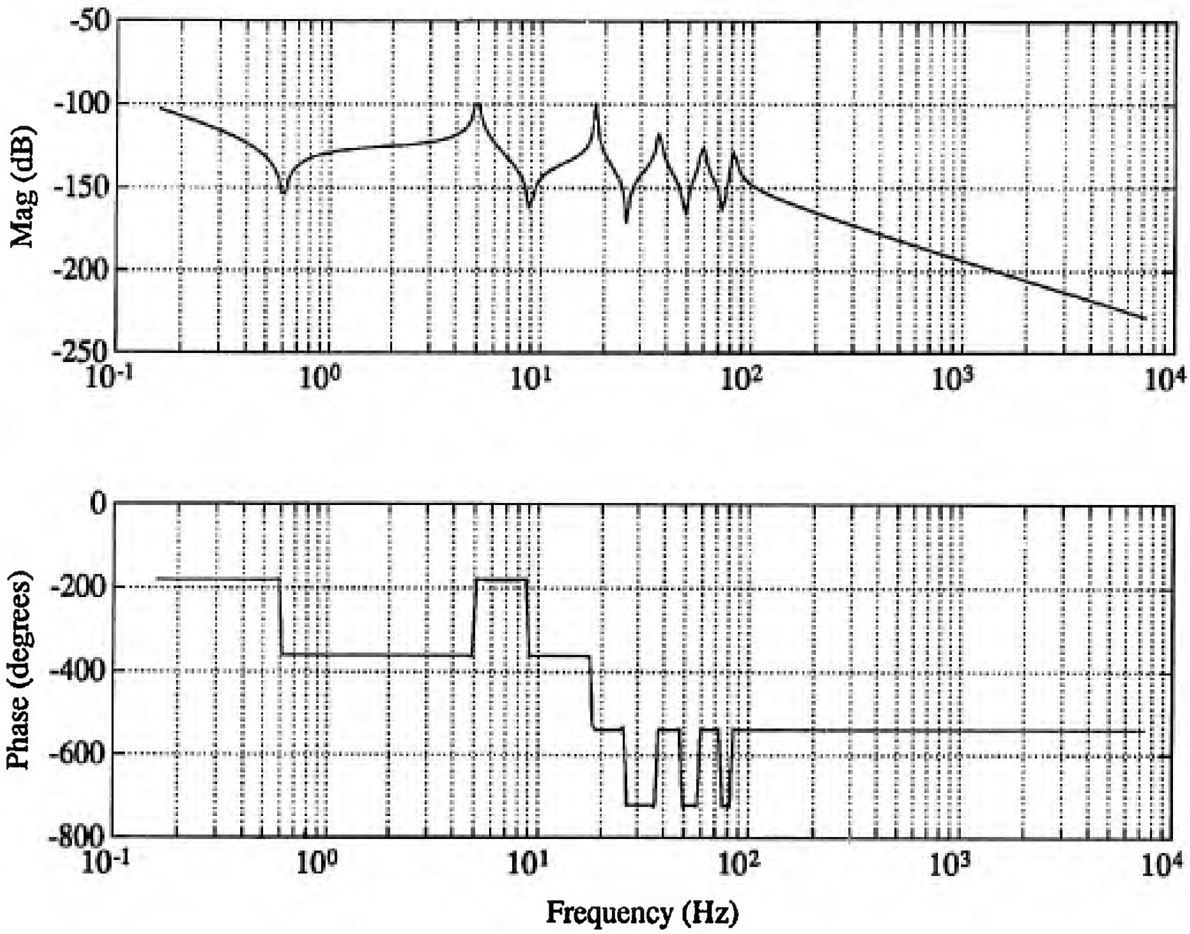

Figure 2.30: Frequency Response $\theta_0(j\omega)/t_0(j\omega)$, Mirror $\omega_n = 10,000(2\pi)$ rad/sec, Model#2

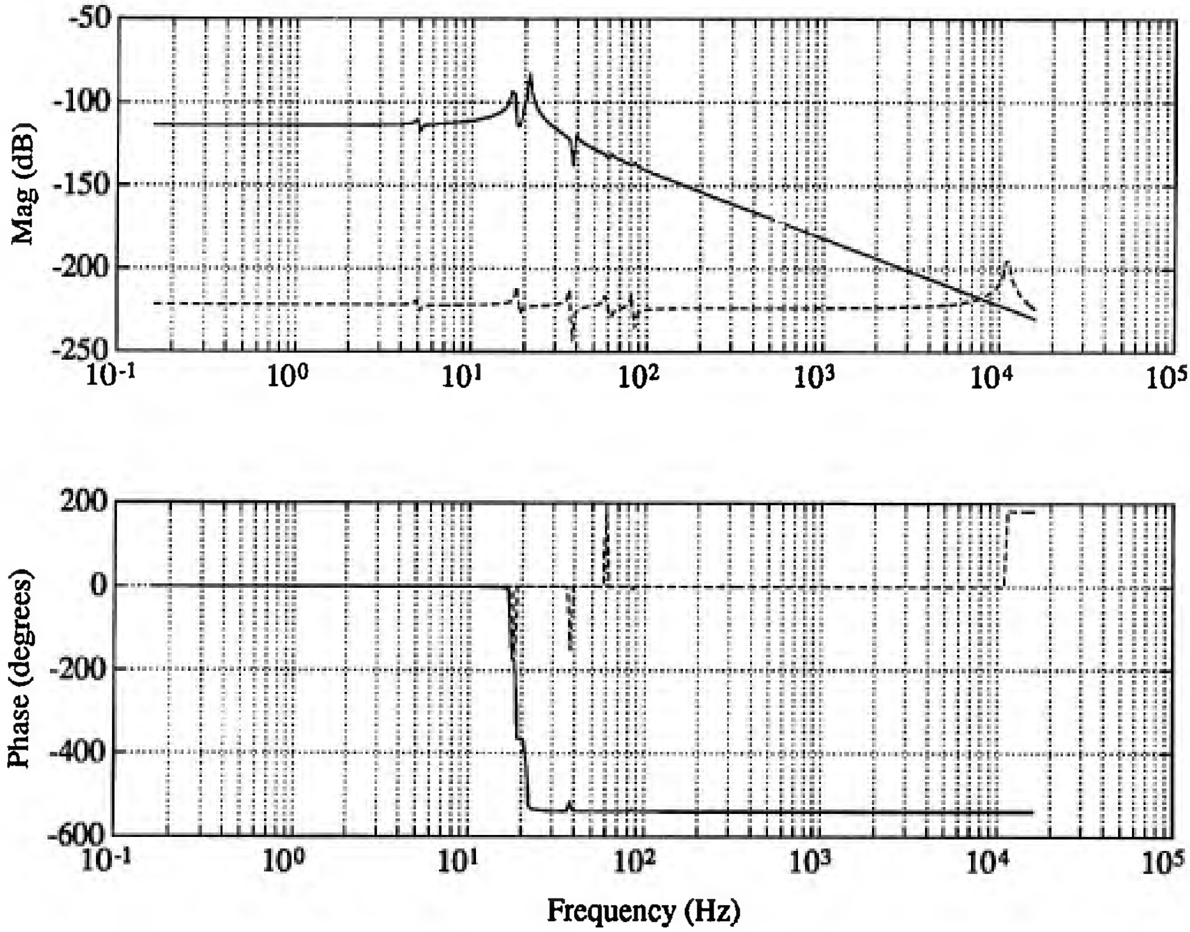

Figure 2.31: Frequency Response $\theta_m(j\omega)/t_m(j\omega)$, Mirror $\omega_n = 20(2\pi)$ rad/sec & $10,000(2\pi)$ rad/sec, Model#2

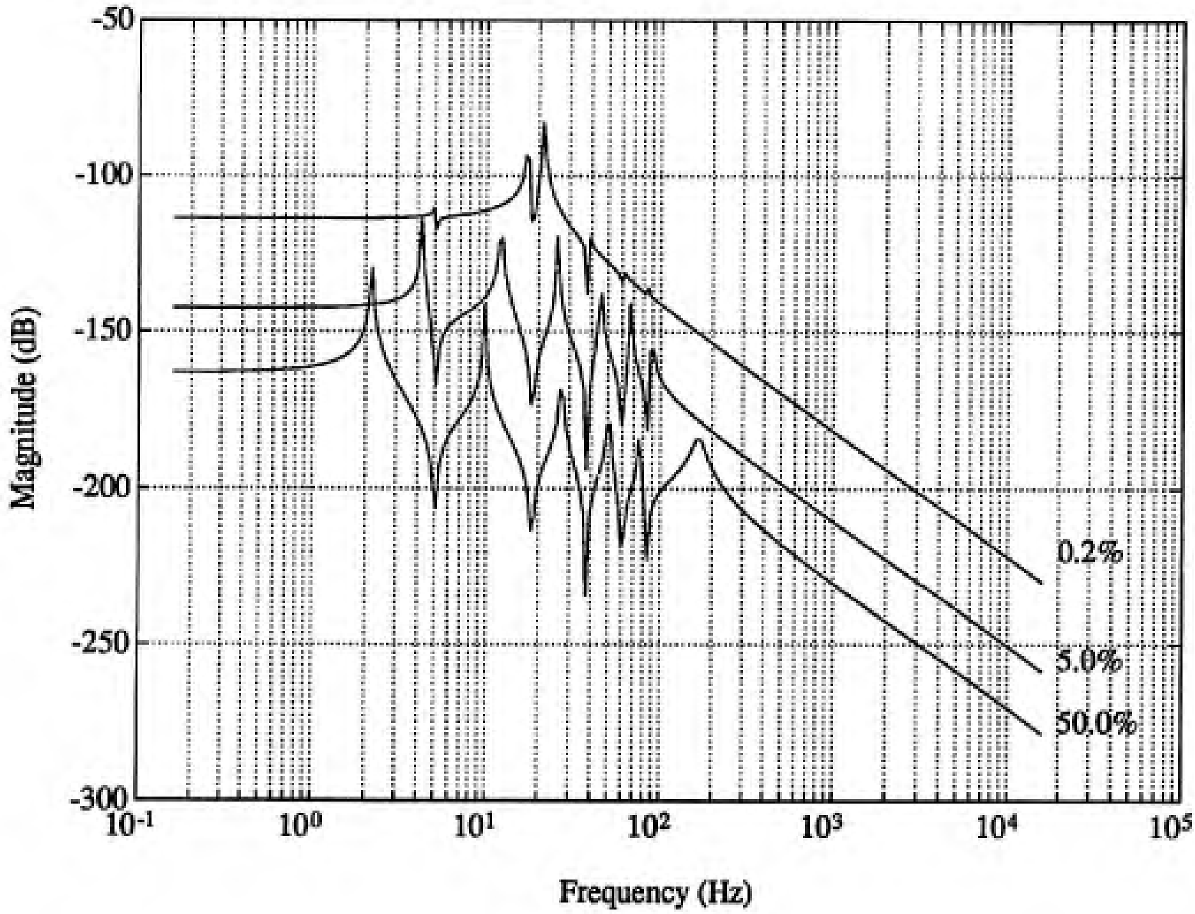

Figure 2.32: Frequency Response $\theta_m(j\omega)/t_m(j\omega)$, Mirror $\omega_n = 20(2\pi)$ rad/sec, Mirror Inertia as Percentage of Truss Inertia, Model#2

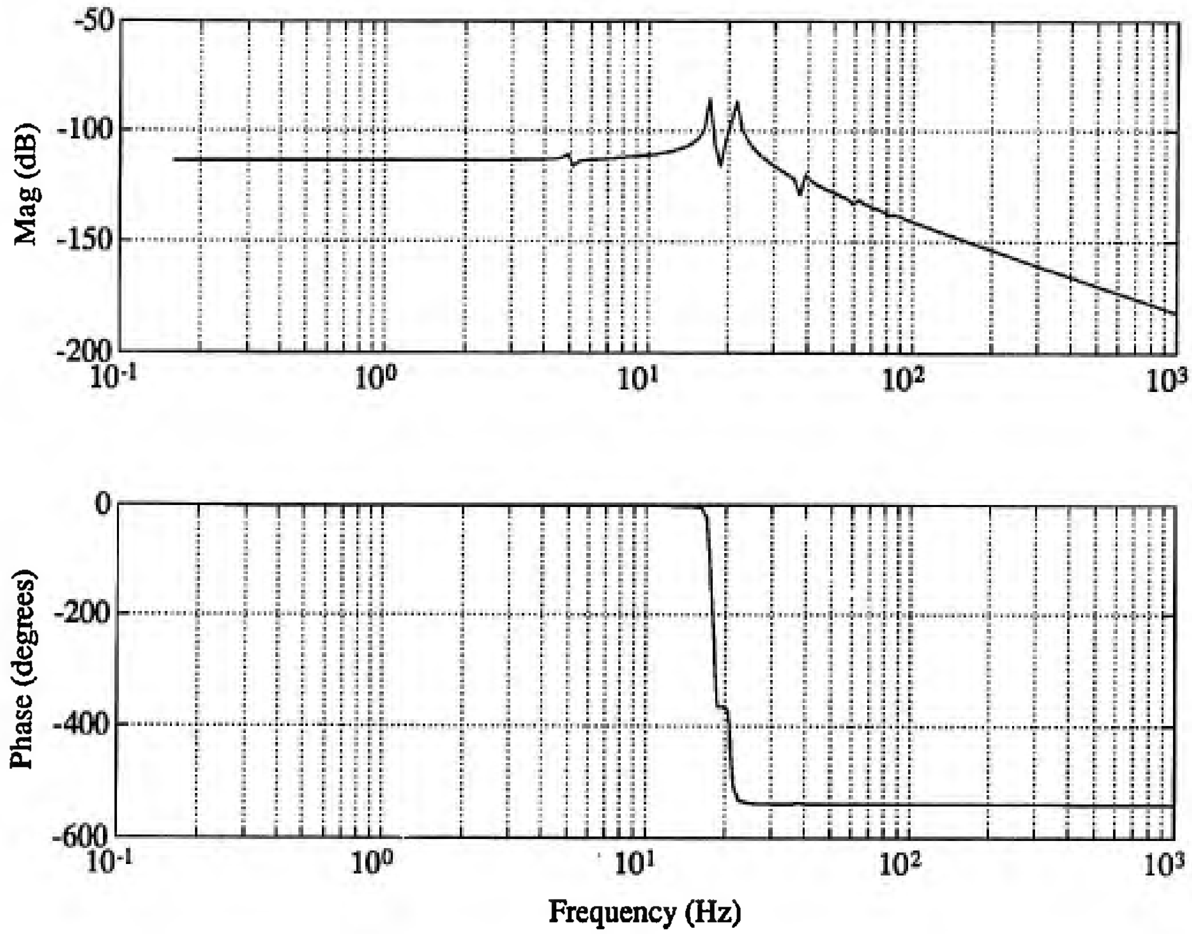

Figure 2.33: Frequency Response $\theta_m(j\omega)/t_m(j\omega)$, Mirror $\omega_n = 20(2\pi)$ rad/sec, Tip-Mounted RMA, Model#3

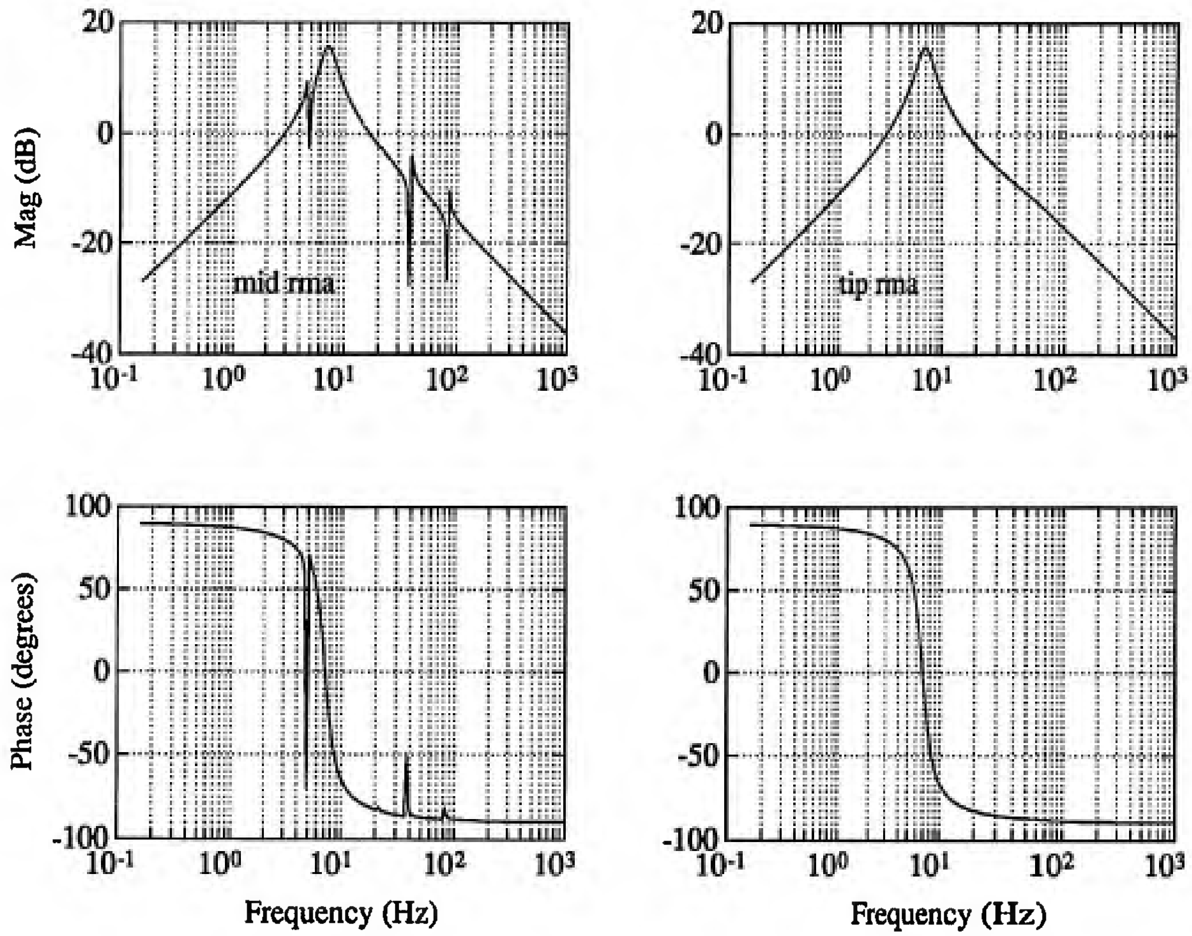

Figure 2.34: Frequency Responses $\dot{y}_{2110}(j\omega)/f_{2110}(j\omega)$ (left plots) and $\dot{y}_{2220}(j\omega)/f_{2220}(j\omega)$ (right plots), RMA mass = m_{rma}, Model#3

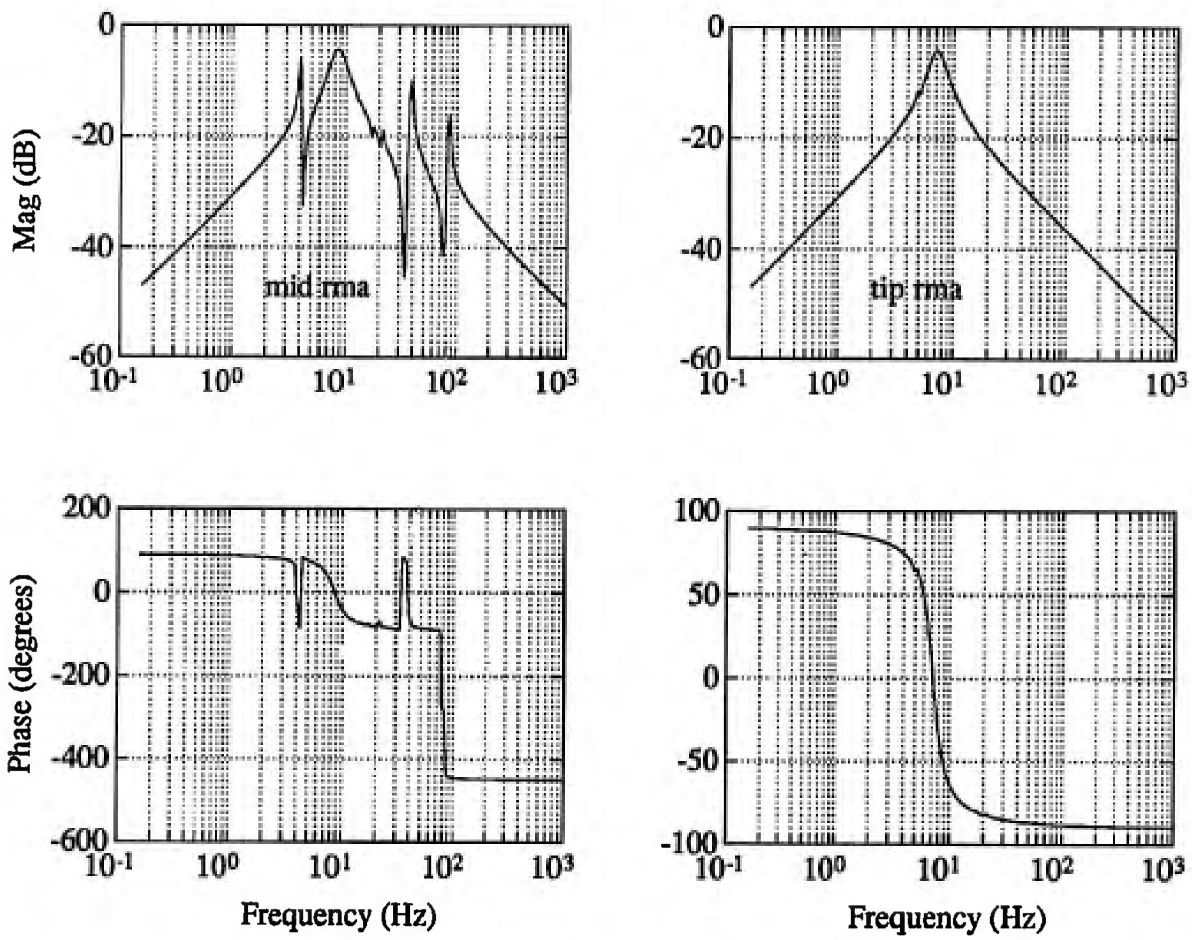

Figure 2.35: Frequency Responses $\dot{y}_{2110}(j\omega)/f_{2110}(j\omega)$ (left plots) and $\dot{y}_{2220}(j\omega)/f_{2220}(j\omega)$ (right plots), RMA mass = $10 \times m_{rma}$, Model#3

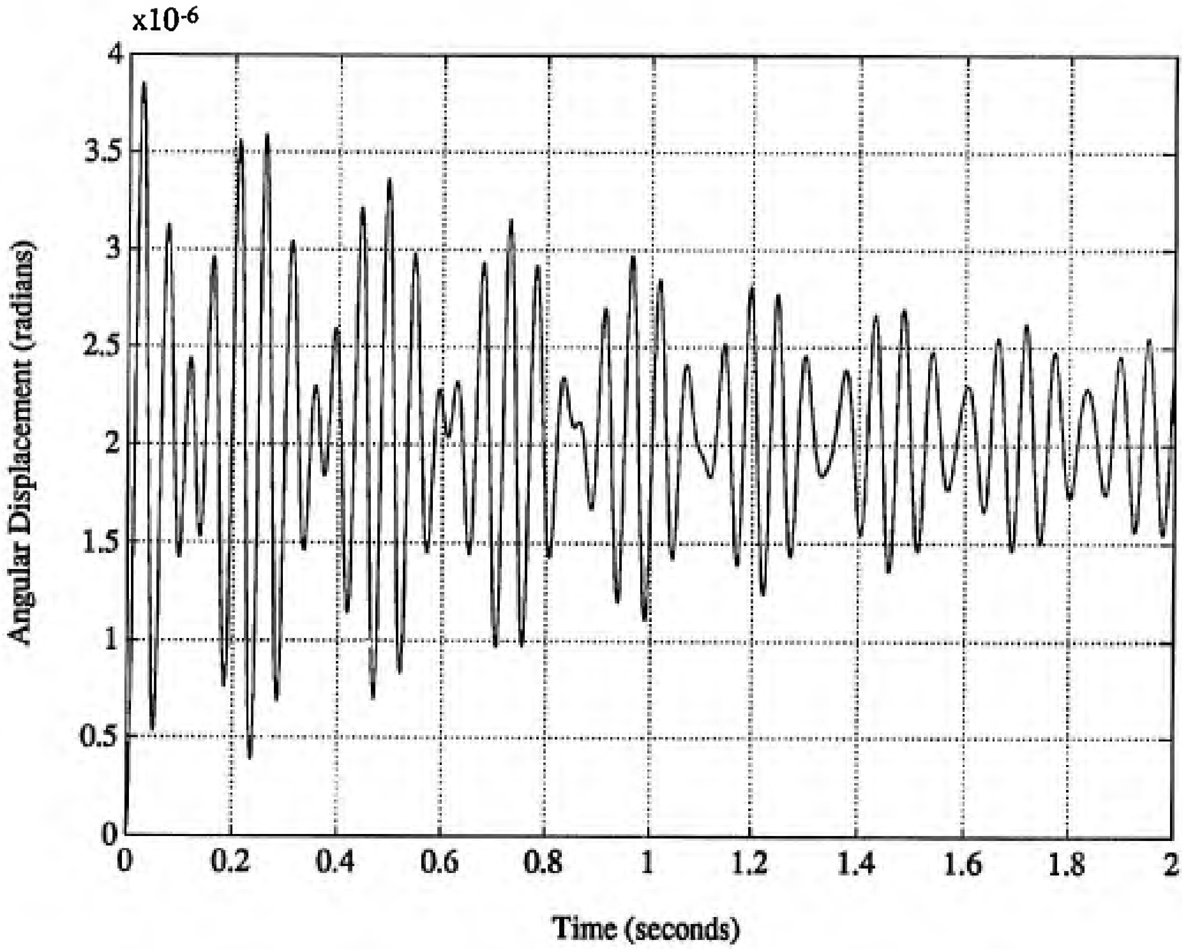

Figure 2.36: Non-Reactionless Mirror Response to Mirror Torque Step Input, Model#4

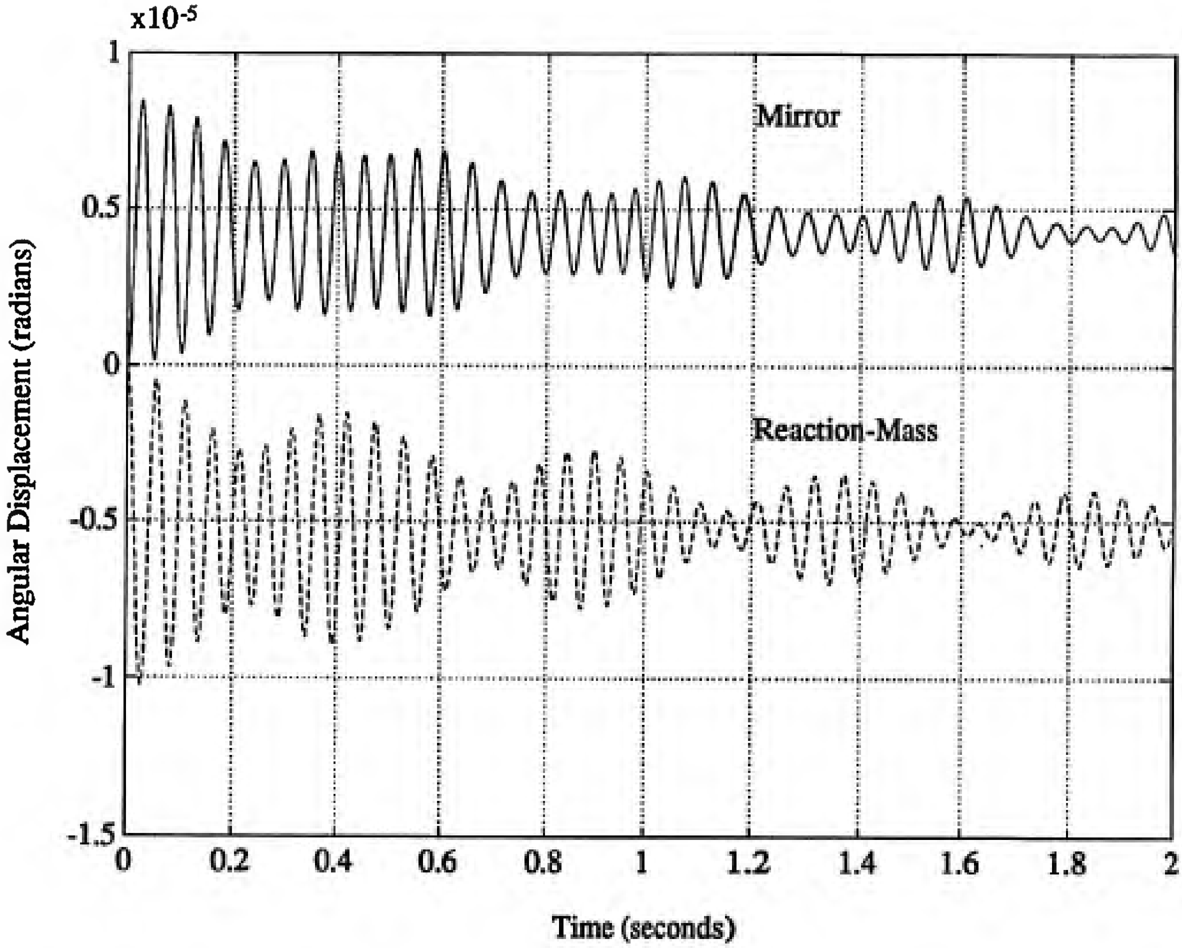

Figure 2.37: Mirror and Mirror Reaction-Mass Response to Mirror Torque Step Input, Model#4

Chapter 3

THE MODIFIED BENCHMARK PROBLEM: CONTROL-STRUCTURE INTERACTION EXPLORED

3.1 Overview

Control-Structure Interaction (CSI) phenomena present a technical challenge to the structures and controls community. Any time lightly damped flexible structures are actively controlled, the interaction between the controller and the structure being controlled can cause instabilities or critical loss of performance. Understanding the source of CSI phenomena and designing controllers to minimize the impacts are the subjects of extensive current research [3, 18, 39, 48, 49, 59]. The purpose of this chapter is to explore the CSI problem as it pertains to the flexible optical system.

3.2 Structural Flexibility Characterization

Fast pointing and large disturbance rejection are accomplished with high loop gain in the line-of-sight controller. High loop gain is limited by structural flexibility and sensor/actuator dynamics. Different types of structural flexibility impact closed-loop performance differently. Useful terminology characterizing structural flexibility, provided by Spanos [49], will be used in this research. Spanos focuses on the rigid body control of flexible structures. We extend that work to the control of a reaction actuator mounted to a flexible structure.

Finite element models of real flexible systems tend to be of large order. Transfer functions describing the dynamics between a single sensor/actuator pair include an equally large number of expansion terms, hiding the individual mode pole-zero relationships. It is these modal pole-zero relationships that characterize structural flexibility. The impact of varying structural flexibility given relatively fixed pole-zero separations on closed-loop control is best seen using single-mode models. Single-mode models of multi-mode systems are often used for initial compensator design and closed-loop stability and performance assessments. In this section we will discuss structural flexibility in the context of a single-mode model.

Rigid-Body Control

In the last three decades much has been done to treat the problem of controlling the rigid-body of a flexible structure. Gevarter [19, 20], in his treatise on basic relations on the control of flexible structures, may have been the first to use the terms 'collocation'[1] and 'non-collocation' to describe the coincidence of sensors and actuators. His work is cited by many as the source of stability guarantees for the collocated control problem using proportional plus derivative (PD) control. J.T. Spanos[49], also treating the rigid-body control of flexible structures, contributed insight to the problem by offering convenient structural flexibility classifications. In his work, Spanos begins with the basic rigid-body control transfer function describing the dynamics between a collocated or non-collocated sensor and actuator. We begin this section with that same formulation.

The single-input single-output (SISO) transfer function between a non-reaction actuator[2] at DOF i and a sensor at DOF j is

$$\frac{q_j(s)}{f_i(s)} = \sum_{k=1}^{n_r} \frac{\phi_{ik}\phi_{jk}}{s^2 + 2\zeta\omega_k s + \omega_k^2} \tag{3.1}$$

where q_j and f_i are nodal displacements (angles) and forces (torques), respectively, and the pair $\{\omega_k, \phi_k\}$ represents the n_r natural frequencies and corresponding mode shapes (normalized to unit mass), ζ is the modal damping coefficient. For a system with R rigid body modes the effective rigid body inertia J can be obtained in terms of the mode shapes as follows

$$J = \frac{1}{\sum_{k=1}^{R} \phi_{ik}\phi_{jk}} \tag{3.2}$$

---

[1] When a translation or rotational sensor occupies physically the same motion degree-of-freedom as, respectively, a force or torque actuator. The term is used in the classical sense to describe the placement of sensors and **non-reaction** actuators.

[2] Non-reaction actuators apply external forces (torques) while reaction actuators apply internal forces (torques) to the controlled structure. Momentum wheels and cold-gas jets are typically used as non-reaction actuators while reaction-mass actuators and steering mirrors are reaction actuators.

Equation 3.1 represents an exact residues model of the SISO plant and is dynamically equivalent to equation 2.36 for the j^{th} element of $\mathbf{q_r}$ and the i^{th} element of $\mathbf{f_r}$.

An appropriate single (flexible) mode model for the 'rigid-body' control problem would be

$$\frac{q_j(s)}{f_i(s)} = \frac{1}{Js^2} + \frac{\phi_{ik}\phi_{jk}}{s^2 + 2\zeta\omega_k s + \omega_k^2} \tag{3.3}$$

Simplifying equation 3.3 gives

$$\frac{q_j(s)}{f_i(s)} = \frac{1}{J}\frac{\alpha_k s^2 + 2\zeta\omega_k s + \omega_k^2}{s^2(s^2 + 2\zeta\omega_k s + \omega_k^2)} \tag{3.4}$$

where k can be any of the '$R + 1$' or greater flexible modes. If the k^{th} mode is minimum phase it can be shown that

$$\alpha_k = \frac{\omega_k^2}{\Omega_k^2} \tag{3.5}$$

where α_k is the modal participation factor and Ω_k is the zero frequency of the single-mode plant. Note that β_k of equation 2.55, which is used in section 2.5 to describe pole-zero separation in multi-mode systems, is the square root of α_k defined above. It is also important to note that Ω_k is not necessarily equal to the corresponding k^{th} exact zero frequency of the multi-mode model. Only if the exact zero frequency is known and used in equation 3.5 will equation 3.4 accurately represent the system over the frequency range of interest. If we assume constant damping throughout all flexible modes, structural flexibility is uniquely *identified* by the pair $\{\alpha_k, \omega_k\}$. In addition, structural flexibility can be uniquely *characterized* by α_k. Assuming zero damping, the single-mode model s-plane pole-zero patterns shown in figure 3.1 are possible.

In view of figure 3.1, the following definitions are provided[49].

1) An **appendage** mode is one whose zero lies on the imaginary axis of the s-plane and is smaller than its pole, or simply $\alpha_k > 1$.

2) An **in-the-loop minimum phase** mode is one whose zero lies on the imaginary axis of the s-plane and is larger than its pole, or simply $0 < \alpha_k < 1$.

3) An **in-the-loop nonmimimum phase** mode is one whose zero lies in the right half of the s-plane, or $\alpha_k < 0$.

Two conclusions can be made with regard to the rigid-body control problem, 1) collocated control results in appendage modes, though appendage modes may also occur in some non-collocated systems, and 2) Non-collocated control results in both types of in-the-loop modes [49].

With these definitions, we can characterize the structural flexibilities observed in the system frequency response plots shown in section 2.5. For example, reviewing the two collocated system frequency response plots in figures 2.13 and 2.14 with their accompanying pole-zero maps in figures 2.16 and 2.17, one can clearly see that the structural flexibility is comprised exclusively of appendage modes. Recalling that $\alpha_k = \beta_k^2$, figures 2.19 and 2.20 reveal the same information more clearly for high frequency modes. The non-collocated system shown in figures 2.15 and 2.18 is comprised of primarily in-the-loop nonminimum phase modes at low frequency. Higher frequency structural flexibility consists of a mixture of all three types.

We will extend these conclusions to the case of controlling an attached reaction actuator and show that both minimum and nonminimum phase modes can occur even in collocated systems. Of course, the term 'collocated' is really only suitable in describing the control of a non-reaction actuator. In the next section, we will introduce and define a new term 'bicollocation' which is more suitable to the control of a reaction actuator.

Reaction Actuator Control

A reaction actuator is attached to its support structure by some sort of potential energy device, such as a spring; whereas the non-reaction actuator has no such spring-like restraint. Consequently, the non-reaction actuator has but one relevant degree-of-freedom, that being the DOF at which the actuator applies its force or torque to the flexible structure. The reaction actuator, on the other hand, has three relevant degrees-of-freedom, the DOF at which the spring is attached to the flexible structure, the DOF at which the reaction actuator 'acts' onto the structure, and the DOF at which the reaction actuator 'reacts' against the structure. In addition to these degrees-of-freedom, both the non-reaction actuator and the reaction actuator control problems must consider sensor location. Therefore, the non-reaction actuator control problem has only two relevant degrees-of-freedom, whereby the terms 'collocation' and 'non-collocation' get their meaning. The reaction actuator control problem then has four relevant degrees-of-freedom. Figure 3.2 illustrates these relevant degrees-of-freedom for the reaction actuator control problem.

At this point we introduce the term 'bicollocation'. The illustration in figure 3.2 describes the four relevant degrees-of-freedom for the reaction actuator control problem. The spring attachment point is the reference DOF 'r' and is specified within the mass and stiffness matrices and therefore fixed within the structure of the modal matrix, Φ. The sensor DOF 'j' is shown in figure 3.2 as variable from s1 to s5, for this simple lumped mass system. The action and reaction DOFs are, respectively, 'i' and 'h'. Anytime $j = i$ we are collocated in the classical sense. However, with the reaction actuator control problem, there are two additional important degrees-of-freedom. Only when both $j = i$ and $r = h$ are we bicollocated. One can readily see that we can pose a non-bicollocated reaction actuator control problem and still be collocated in the classical sense. One must be very careful not to assume the stability guarantees with regard to collocated control when dealing with the case of non-bicollocation with classical collocation. In fact it will be shown later that such a collocated but non-bicollocated problem can yield nonminimum phase zeros in the reaction actuator transfer function. It will also be shown that bicollocation guarantees minimum phase zeros in the same transfer function.

The SISO transfer function between an actuator acting at DOF i and reacting against DOF h and a sensor at DOF j is

$$\frac{q_j(s)}{f_{ih}(s)} = \sum_{k=1}^{n_r} \frac{\phi_{jk}\phi_{ik} - \phi_{jk}\phi_{hk}}{s^2 + 2\zeta\omega_k s + \omega_k^2} \tag{3.6}$$

where q_j and $f_{ih} = f_i - f_h$ are nodal displacements (angles) and reactive (internal) forces (torques), respectively and the pair $\{\omega_k, \phi_k\}$ represents the n_r natural frequencies and corresponding mode shapes (normalized to unit mass), ζ is the modal damping coefficient. Note that equation 3.6 can be used to describe both bicollocated and non-bicollocated reaction actuator transfer functions. The effective rigid body inertia J for a system with R rigid body modes is now defined by

$$J = \frac{1}{\sum_{k=1}^{R} \phi_{jk}(\phi_{ik} - \phi_{hk})} \tag{3.7}$$

However, because rigid body mode shapes are constant

$$\phi_{ik} = \phi_{hk} \qquad k = 1, \ldots, R \tag{3.8}$$

and no rigid body motion results from the control of reaction (internal) forces. So,

$$\frac{q_j(s)}{f_{ih}(s)} = \sum_{k=R+1}^{n_r} \frac{\phi_{jk}\phi_{ik} - \phi_{jk}\phi_{hk}}{s^2 + 2\zeta\omega_k s + \omega_k^2} \tag{3.9}$$

Equation 3.9 represents an exact residues model of the SISO plant and is dynamically equivalent to equation 2.36 assuming that the elements of vectors $\mathbf{q}_r$ and $\mathbf{f}_r$ correspond to appropriate reaction actuator DOFs and forces.

Like the rigid body control transfer function of equation 3.3, we desire a reaction actuator control transfer function expanded to include one flexible body mode of the form

$$\frac{q_j(s)}{f_{ih}(s)} = \frac{\phi_{ja}\phi_{ia} - \phi_{ja}\phi_{ha}}{s^2 + 2\zeta_a\omega_a s + \omega_a^2} + \frac{\phi_{jk}\phi_{ik} - \phi_{jk}\phi_{hk}}{s^2 + 2\zeta\omega_k s + \omega_k^2} \tag{3.10}$$

Simplifying equation 3.10 we get

$$\frac{q_j(s)}{f_{ih}(s)} = \frac{(\varphi_a + \varphi_k)s^2 + 2(\varphi_a\zeta\omega_k + \varphi_k\zeta_a\omega_a)s + (\varphi_a\omega_k^2 + \varphi_k\omega_a^2)}{(s^2 + 2\zeta_a\omega_a s + \omega_a^2)(s^2 + 2\zeta\omega_k s + \omega_k^2)} \tag{3.11}$$

where

$$\varphi_a = \phi_{ja}\phi_{ia} - \phi_{ja}\phi_{ha}, \qquad \varphi_k = \phi_{jk}\phi_{ik} - \phi_{jk}\phi_{hk}$$

This single-mode expansion of the reaction actuator transfer function shows one set of complex conjugate poles associated with the actuator with a complex conjugate pole-zero pair associated with the flexible body mode. The single-mode model flexible mode zero frequency is defined as

$$\Omega_k^2 = \frac{(\varphi_a\omega_k^2 + \varphi_k\omega_a^2)}{(\varphi_a + \varphi_k)} \tag{3.12}$$

The modal participation factor α_k from equation 3.5 can be computed and the same criteria characterizing structural flexibility applied. Again, it is important to note that Ω_k is not necessarily equal to the corresponding k^{th} exact zero frequency of the multi-mode model. If the exact zero frequency and damping are known they can be substituted directly.

To form either of the single-mode expansion transfer functions, we can use the standard modal controllability and observability matrices to determine which modes dominate actuator dynamics. If one mode clearly dominates actuator dynamics, a single-mode approximation of the multi-mode system can be formed by setting a to the dominant actuator mode and k to any of the remaining $n_r - R - 1$ flexible body modes[3].

Assuming zero damping on both actuator and structural modes, six variations of the three basic flexibility types for the single mode reaction actuator transfer function are possible. Figure 3.3 illustrates these six pole-zero patterns. Unlike the rigid body transfer function where classical collocated control always results in appendage modes, classical collocated control on a reaction actuator transfer function can result in any of the six pole-zero configurations shown in figure 3.3–even in-the-loop nonminimum phase modes (for the non-bicollocated case).

Some generalizations regarding bicollocation vs non-bicollocation and the resulting flexible mode type can be made. Equation 3.12 can be rewritten

$$\Omega_k^2 = \left[\frac{\varphi_a}{\varphi_a + \varphi_k}\right]\omega_k^2 + \left[1 - \frac{\varphi_a}{\varphi_a + \varphi_k}\right]\omega_a^2 \tag{3.13}$$

The six flexibility types shown in figure 3.3 can be grouped in pairs (Cases I–III) according to the parameter $\varphi_a/(\varphi_a + \varphi_k)$. We can guarantee strictly minimum phase flexible modes (either appendage or in-the-loop minimum phase) if

$$0 < \frac{\varphi_a}{\varphi_a + \varphi_k} < 1 \tag{3.14}$$

which ensures an in-the-loop minimum phase mode where

$$\omega_k^2 < \Omega_k^2 < \omega_a^2 \tag{3.15}$$

or an appendage mode where

$$\omega_a^2 < \Omega_k^2 < \omega_k^2 \tag{3.16}$$

---

[3] In modally dense systems with strong inertial and/or elastic coupling, actuator dynamics may not be clearly dominated by any single mode. In such a case, single-mode expansions within a specified frequency range can be derived. Any clear distinction between actuator modes and structural modes may be lost.

Note that equation 3.14 holds only if φ_a and φ_k have the same sign. If this is the case, we can conclude that the resulting single-mode model flexibility type is guaranteed to be minimum phase. Whether this minimum phase flexible mode is appendage or in-the-loop depends on the ratio ω_a^2/ω_k^2. Unfortunately, we cannot generalize the minimum phase guarantees in terms of classical collocation. If, however, we have bi-collocated control, we can guarantee the presence of only minimum phase modes, either appendage or in-the-loop. This guarantee will be developed further in chapter 4. To illustrate this method, consider the following example.

Given $\{\omega_k, \phi_k\}$, $k = 1, \ldots, n_r$ for our full DOF model including a reaction actuator whose dynamics can be correctly described by $\{\omega_a, \phi_a\}$. The actuator 'acts' onto DOF i and 'reacts' against DOF h. The reference DOF is specified internal to the modal matrix and located at DOF r. We would like to design a controller for this reaction actuator using a sensor at DOF j. Without actually building any transfer functions in the form of equation 3.10, we can discern the character of the included flexible mode k by evaluating φ_a and φ_k. If we also know ζ_a and ζ_k we can fully evaluate the numerator of equation 3.11 thereby determining precisely the flexible mode type. Moreover, we can say that if φ_a and φ_k have the same sign, the structural flexibility will be an in-the-loop minimum phase mode if $\omega_a > \omega_k$ and an appendage mode if $\omega_a < \omega_k$. These two cases are shown in figure 2.31 for reaction actuator (steering mirror) natural frequencies of 20 Hz and 10 kHz. This figure highlights the potential problems associated with controlling mirrors with high natural frequencies attached to flexible structures. In order to evaluate the control implications of these structural flexibility types, a simple single-mode example will be formulated.

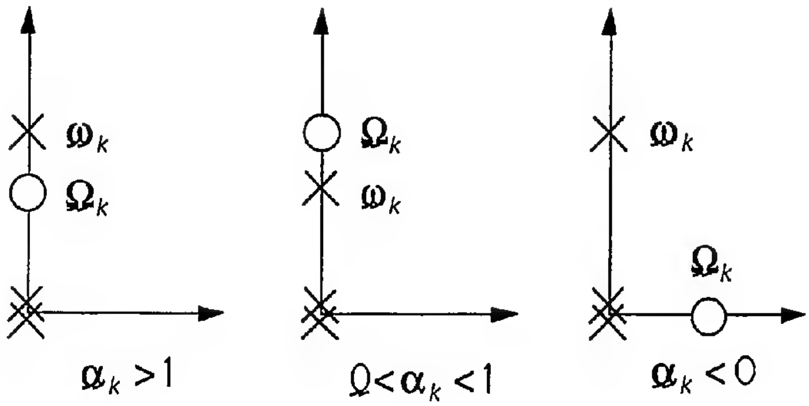

Figure 3.1: Rigid Body Control Structural Flexibility Characterizations: Pole-Zero Patterns, Appendage Mode (left), In-the-Loop Minimum Phase Mode (center), In-the-Loop Nonminimum Phase Mode (right)

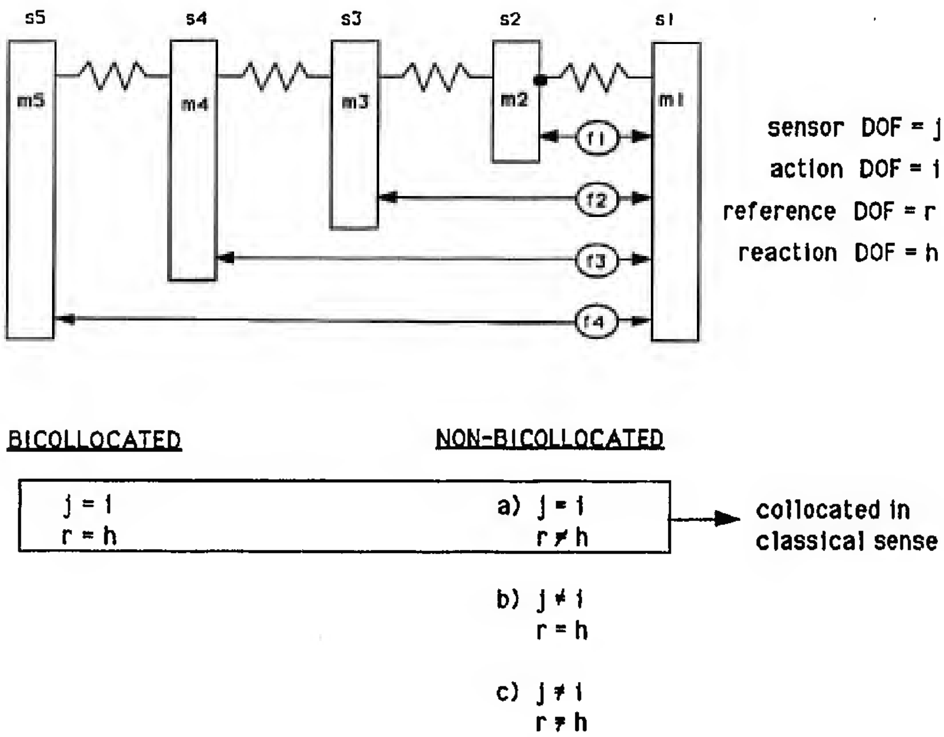

Figure 3.2: Reaction Actuator Relevant Degrees-of-Freedom: Bicollocation vs. Non-bicollocation

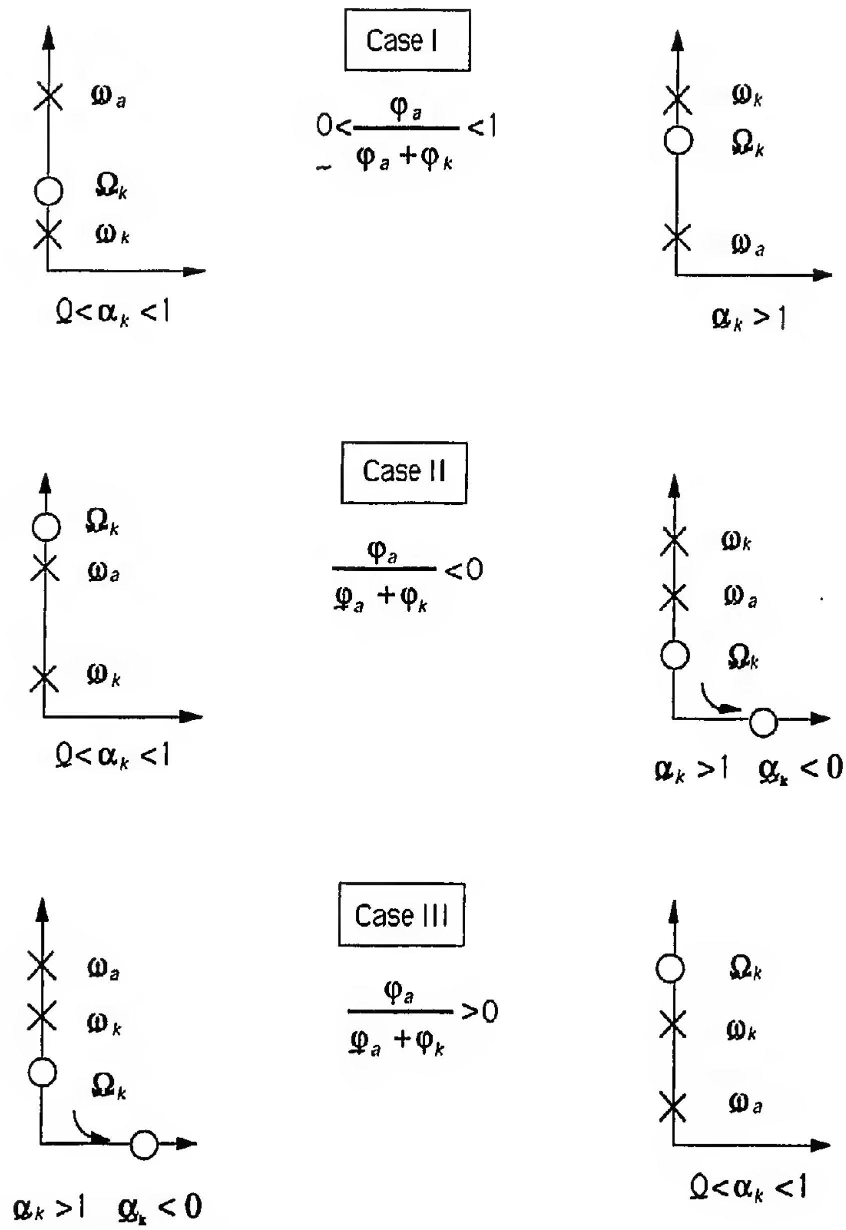

Figure 3.3: Reaction Actuator Single-Mode Model Structural Flexibility Characterizations: Pole-Zero Patterns

3.3 The Modified Benchmark Problem

The two-mass, spring-damper model, shown in figure 3.4, has been lending insight into the various aspects of the structural control problem for years. The model is so well known, it often referred to as the benchmark problem model. In recent months, the benchmark problem has been the subject for robust control research in the aerospace community [54, 7, 10, 27, 12, 43]. The model is attractive because its dynamics are relatively simple and yet representative of the dynamics in many of today's aerospace vehicles.

With simple modifications, the benchmark problem can be made to represent the fundamental dynamics of the flexible optical system developed in chapter 2. The flexible optical system model consists of 62 DOFs and 62 modes. Of the 62 modes, one represents rigid body motion about the hub, one represents the fast steering mirror motion, and the remaining 60 are flexible support structure elastic modes. The benchmark problem is modified by adding a spring-mass-damper (SMD) system, representing the fast steering mirror. Figure 3.5 illustrates the modified benchmark problem model; the SMD is emphasized with cross-hatching. The modified benchmark problem model dynamics include one rigid body mode, one lightly damped structure dominated flexible mode, and one mode dominated by the SMD. The control objective is twofold: first, reject force, displacement, and measurement noise disturbances; second, position x_a in inertial space in a prescribed amount of time using f_c. With this simplified model, CSI phenomena relevant to the flexible optical system can be studied.

3.3.1 Performance Specifications and Disturbance Models

The modified benchmark problem performance requirements and disturbance models are relevant to the high bandwidth, high precision flexible optical system. Performance is specified in two categories–jitter[4] stabilization and retargeting. The performance scenario we are modeling requires moving the optical line-of-sight α_{RET} displacement units (du) and settling to less than ε_{TOT} RMS jitter with an allowable offset error of $\pm 4\varepsilon_{TOT}$ within t_{RMS} seconds. The LOS must dwell at the new posi-

[4] The term 'jitter' is used to describe vibration in each axis of the line-of-sight.

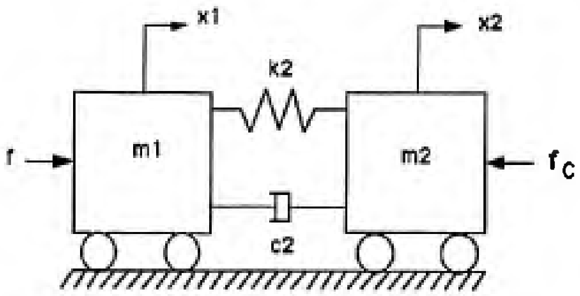

Figure 3.4: The Two-Mass Spring-Damper Model

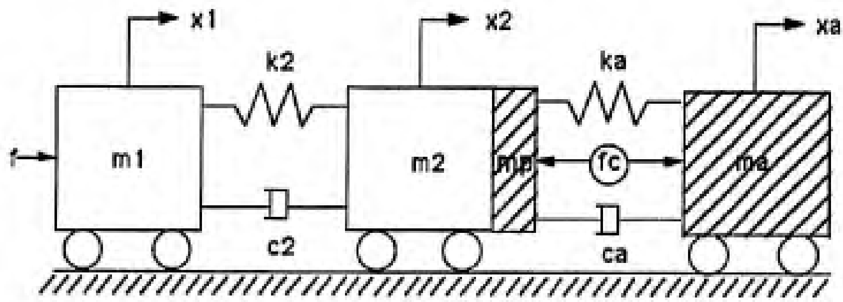

Figure 3.5: The Modified Benchmark Problem

tion inside the offset error and within the allowable RMS jitter for t_{DWELL} seconds. A total of ten retargeting cycles are required. The jitter tolerance is based upon a root-mean-square average of the three jitter (noise & disturbance) sources shown in figure 3.10. The total allowable jitter is a measure of the LOS stability (lack of vibration) required to perform its mission. Table 3.1 summarizes these requirements. The

Table 3.1: Modified Benchmark Problem Performance Requirements

Command Response Specifications	
step command, y_c	1.00 du
settling time to RMS window, t_{RMS}	0.05 seconds
dwell time in RMS window, t_{DWELL}	0.05 seconds
RMS window offset error, $y(t_{RMS}) - y_c$	
goal	0.00 du
tolerance	$\pm 400\mu$du
Error (Jitter) Budget	
Input Disturbance	*Output Error*
force, f_d	$\varepsilon_{f_d} \leq 60\mu$du RMS
displacement, x_d	$\varepsilon_{x_d} \leq 60\mu$du RMS
measurement noise, m	$\varepsilon_m \leq 60\mu$du RMS
total RMS Jitter	$\varepsilon_{TOT} \leq 100\mu$du RMS

RMS window and offset error are defined in figure 3.6. The input and resulting output power spectral density (PSD) for each disturbance listed in table 3.1 is provided in figures 3.7, 3.8, and 3.9, respectively. Input and output RMS are also provided. The force disturbance represents a mirror cooling disturbance acting directly on the mirror inertia. The displacement disturbance could be any atmospheric turbulence encountered between the mirror and the LOS sensor. Measurement noise represents spurious high frequency signals passing through the optical sensor.

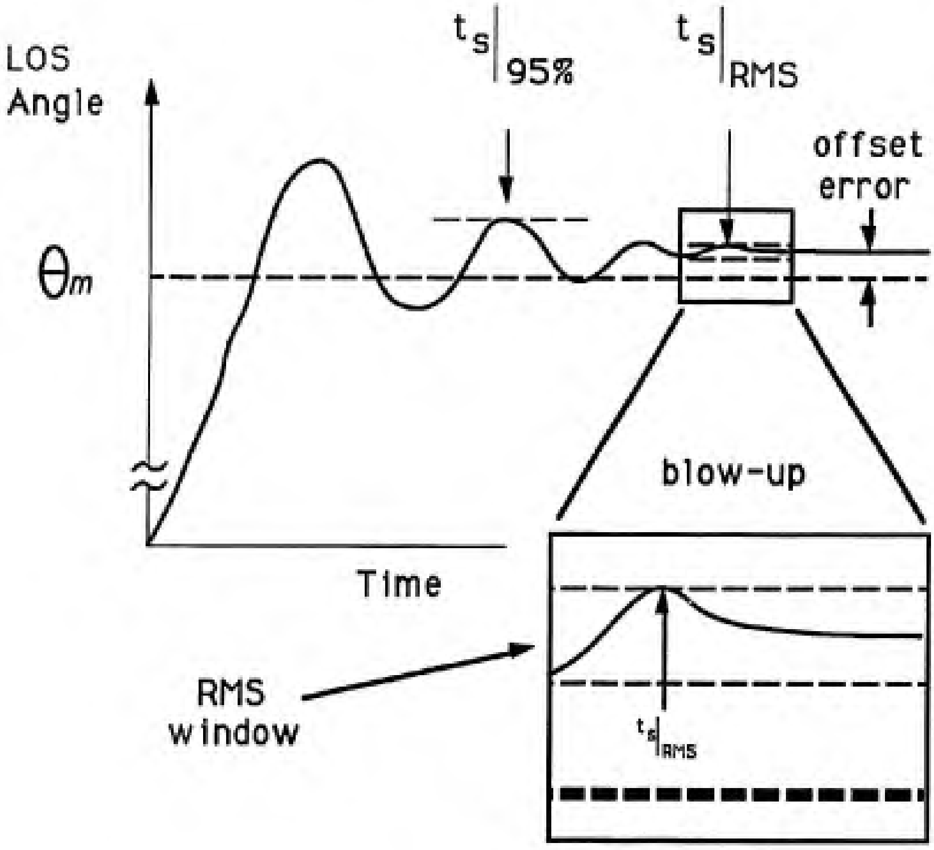

Figure 3.6: RMS Window and Offset Error

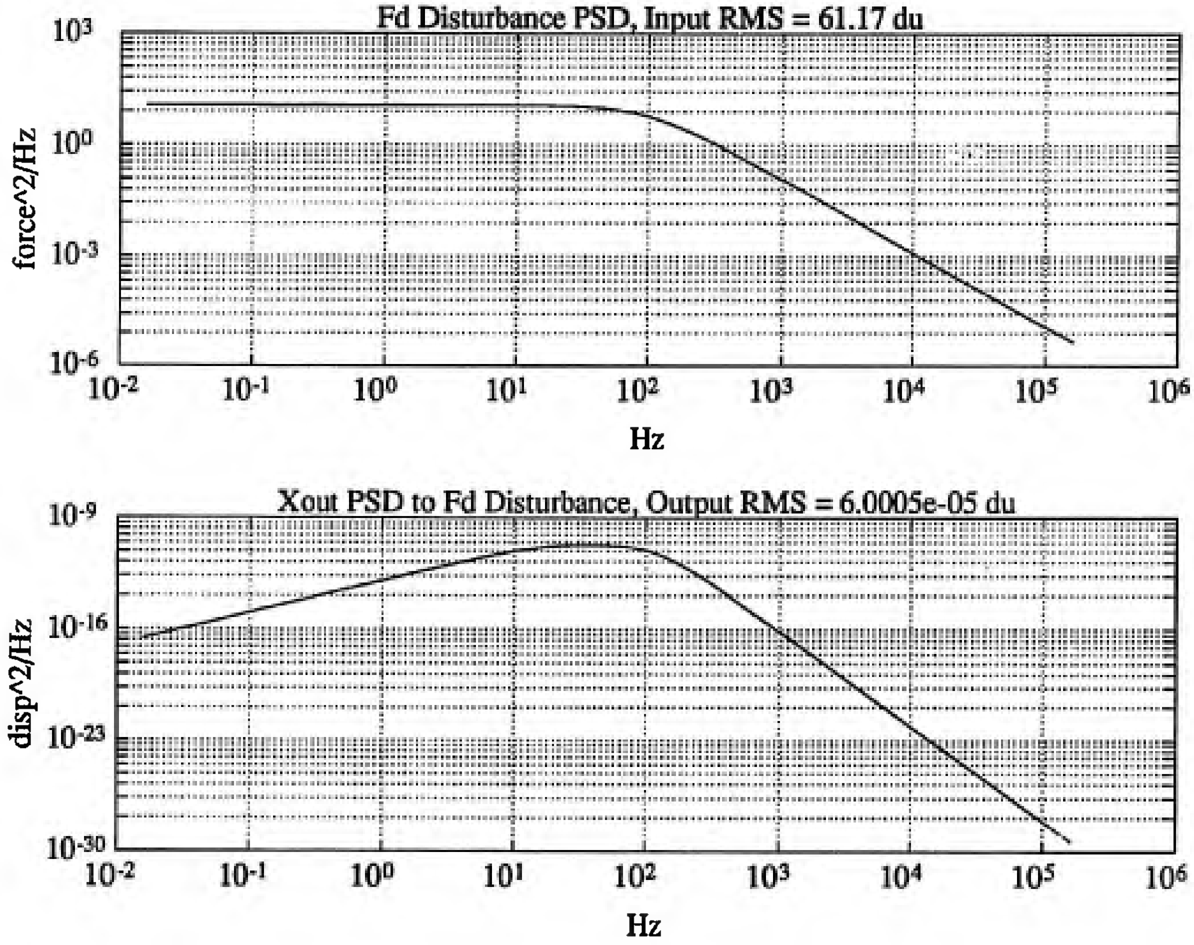

Figure 3.7: Disturbance PSD: Input Force–Output Displacement

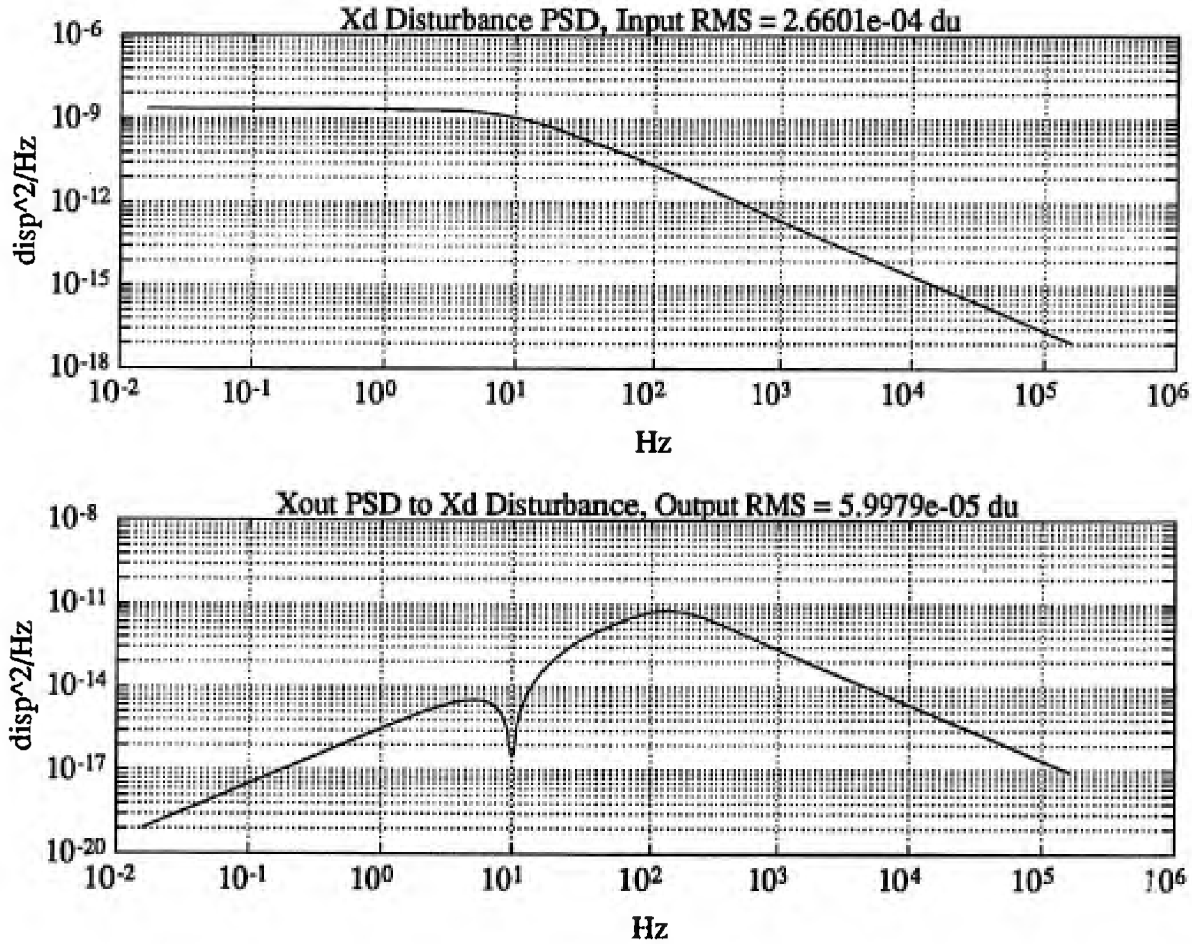

Figure 3.8: Disturbance PSD: Input Displacement–Output Displacement

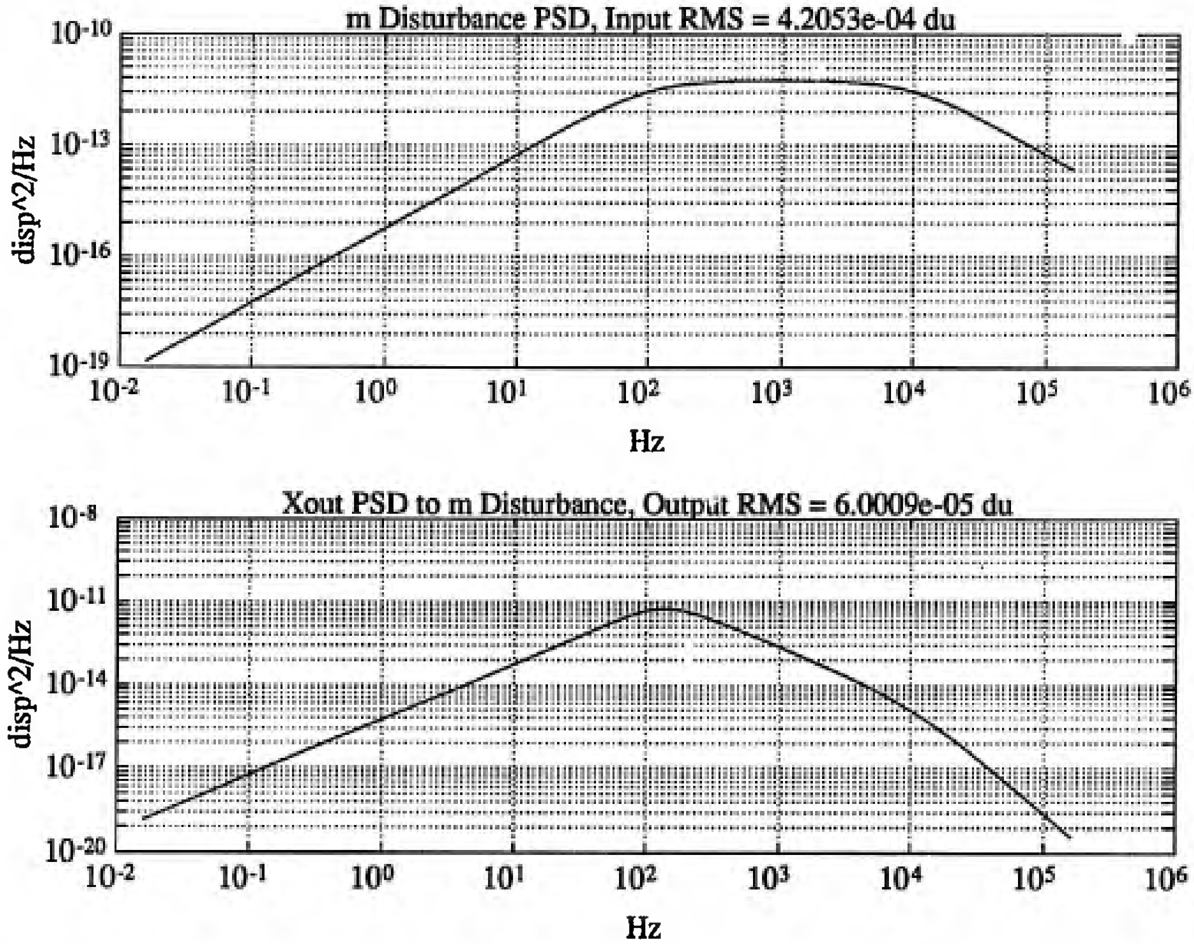

Figure 3.9: Measurement Noise PSD: Input Displacement–Output Displacement

3.3.2 The Plant and Controller Dynamics

A block diagram describing the plant and controller structure is shown in figure 3.10. The disturbance models are incorporated directly into the state space model of G(s) and are driven by unity variance gaussian white noise.

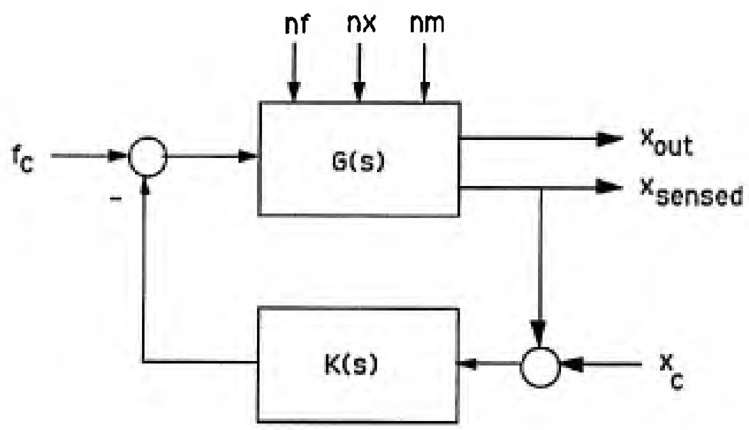

Figure 3.10: The Controlled Modified Benchmark Problem Block Diagram

The Plant

The plant consists of two independent sub-plants: the SMD and the flexible support structure. In practice, it is realistic to expect that each would be designed and built independently for later integration as a total system. The same philosophy is taken here, with interesting consequences reported. Similar to the fast steering mirror, the SMD is modeled as a lightly damped mass with a spring restoring force. For simplicity, the mass is normalized to one. The spring and damper constants are selected to reflect the SMD natural frequency. The SMD natural frequency can vary to reflect the two most common types of fast steering mirror actuators: electro-magnetic or piezo-electric. Electro-magnetic actuators deliver force while piezo-electric actuators deliver displacement. Fast steering mirrors driven by electro-magnetic actuators are characterized by low natural frequencies (10-20 Hz) while those driven by piezo-electric actuators can have natural frequencies approaching 10-20 kHz. However, structural resonances within the mirror itself may preclude taking full advantage of the high bandwidths provided by the piezo-electric actuator.

The transfer function for the uncoupled SMD, given in equation 3.17 below, is derived assuming a rigid mount. A rigid mount can be simulated by letting $m_p = \infty$ where m_p is the 'parasitic' mass associated with the SMD sub-plant shown in figure 3.5.

$$\frac{X_a(s)}{F_c(s)} = \frac{\frac{1}{ma}}{s^2 + 2\zeta_a\omega_a s + \omega_a^2} \tag{3.17}$$

where,

$$\omega_a = \sqrt{\frac{k_a}{m_a}}, \quad \zeta_a = \frac{c_a}{2\omega_a m_a}$$

The flexible support structure sub-plant, or the benchmark problem model in this case, is described by the following transfer function relations.

$$\frac{X_2(s)}{F(s)} = \frac{2\zeta_p\omega_p s + \omega_p^2}{Ms^2[s^2 + 2\zeta_p\omega_p s + \omega_p^2]} \tag{3.18}$$

$$\frac{X_2(s)}{F_c(s)} = \frac{-[\frac{M}{m_2}s^2 + 2\zeta_p\omega_p s + \omega_p^2]}{Ms^2[s^2 + 2\zeta_p\omega_p s + \omega_p^2]} \tag{3.19}$$

where,

$$2\zeta_p\omega_p = \left[\frac{M}{m_1 m_2}\right] c_2, \quad \omega_p = \sqrt{\left[\frac{M}{m_1 m_2}\right] k_2}, \quad M = (m_1 + m_2)$$

In terms of flexibility types, the non-collocated transfer function in equation 3.18 is somewhat unique in that α_2 = zero[5]. The general case of $\alpha_k = 0$ actually describes a *degenerate* in-the-loop minimum phase mode and can only occur when the single-mode expansion fully describes the system. This can happen in a lumped two-mass system like the benchmark problem, or a continuous system discretized into two degrees-of-freedom. If this is the case and if damping between the two DOFs is zero a negative real axis zero will result. For the collocated transfer function in equation 3.19, $\alpha_2 = (M/m_2) > 0$ which describes an appendage mode.

---

[5] The subscript '2' indicates that $k = 2$ or that we are looking at the 2^{nd} system mode. In this case, the first system mode is rigid-body.

When the SMD is connected to the flexible support structure, shown in figure 3.5, the SMD and support structure equations become coupled. The coupled plant can be described by the following fourth and sixth order transfer function relations. In deriving these equations of motion, $m_p = 0$, for simplicity.

$$\frac{X_a(s)}{F_c(s)} = \frac{m_1 m_2 s^2 + c_2(m_1 + m_2)s + k_2(m_1 + m2)}{a_4 s^4 + a_3 s^3 + a_2 s^2 + a_1 s + a_0} \tag{3.20}$$

$$\frac{X_2(s)}{F_c(s)} = \frac{-m_a(m_1 s^2 + c_2 s + k_2)}{a_4 s^4 + a_3 s^3 + a_2 s^2 + a_1 s + a_0} \tag{3.21}$$

$$\frac{X_1(s)}{F_c(s)} = \frac{-m_a(c_2 s + k_2)}{a_4 s^4 + a_3 s^3 + a_2 s^2 + a_1 s + a_0} \tag{3.22}$$

$$\frac{X_a(s)}{F(s)} = \frac{c_2 c_a s^2 + (c_2 k_a + c_a k_2)s + k_2 k_a}{s^2[a_4 s^4 + a_3 s^3 + a_2 s^2 + a_1 s + a_0]} \tag{3.23}$$

where,

$$a_4 = m_1 m_2 m_a$$

$$a_3 = c_2 m_a(m_1 + m_2) + c_a m_1(m_2 + m_a)$$

$$a_2 = c_2 c_a(m_1 + m_2 + m_a) + k_2 m_a(m_1 + m_2) + k_a m_1(m_2 + m_a)$$

$$a_1 = (k_2 c_a + c_2 k_a)(m_1 + m_2 + m_a)$$

$$a_0 = k_2 k_a(m_1 + m_2 + m_a)$$

The flexible mode in each of the transfer functions of equations 3.20–3.23 are all minimum phase. The specific *type* of structural flexibility depends upon the parameters φ_a and φ_k which are functions of the mass, damping, and stiffness factors. The denominator roots of equations 3.20–3.23 reveal an interesting trend in the movement of the SMD and flexible mode frequencies. When the flexible support structure and SMD natural frequencies are fixed and the actuated mass m_a increases with respect to the flexible support structure masses m_1 and m_2, significant inertial coupling between the two sub-plants occurs and the two sub-plant mode frequencies and damping coefficients diverge. Figure 3.11 shows this divergence as a function of mass ratio μ where

$$\mu = \frac{m_a}{m_1 + m_2} \tag{3.24}$$

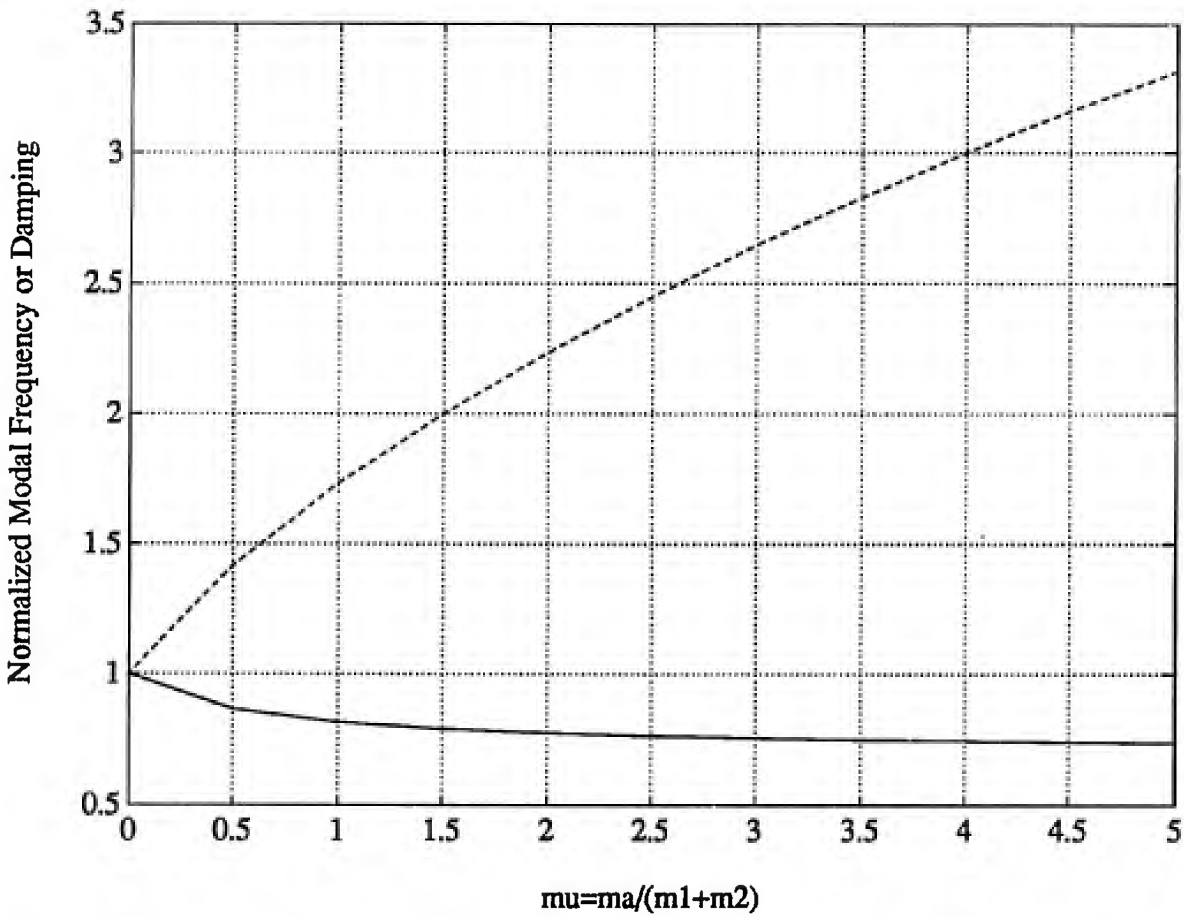

Figure 3.11: Tip Mass Effect on Modal Frequency and Damping

The divergence of system mode frequencies can pose some interesting stability and/or performance problems, especially since controllers for fast steering mirrors are generally designed under a 'rigid' rather than 'flexible' support structure assumption. For example, consider an actuated mass comprising 70% of the total system mass. This equates to a mass ratio μ of 2.33, which increases the frequency of the SMD dominated mode by a factor of nearly 2.3. Controllers tuned to the rigidly supported SMD using notch filters, for example, may destabilize the coupled system or deliver degraded performance.

Note that the numerator zeros of equations 3.20–3.23 are not functions of m_a. Consequently, as m_a increases and the system poles diverge, the system zeros remain fixed. It is this pole-zero 'spreading' that adversely contributes to CSI instabilities in certain structural modes. This issue will be further examined in section 3.4.

The Controller

Due to the zero steady-state offset error goal and the relatively slow and lightly damped nature of the SMD, a PID controller is selected. The SMD natural frequency (w_a) and damping coefficient (ζ_a), described by equation 3.17, were set to 10 Hz and .01 respectively with actuated mass $m_a = 1$. Using a simple pole placement technique the controller parameters were selected to achieve the performance requirements outlined in table 3.1. The controller transfer function is

$$K(s) = K\left[\frac{k_d s^2 + k_p s + k_i}{s}\right] \tag{3.25}$$

where,

$$K = 1300, \quad k_d = 1, \quad k_p = 600, \quad k_i = 50000$$

Controller parameters were selected under the assumption that the SMD is mounted to a rigid rather than flexible body. Design under this 'rigid' support structure assumption is quite common in practice [36, 34, 49, 15].

3.4 Closed-Loop Analysis: The Rigid Controller on the Flexible Structure

Actual performance for the PID controlled SMD under 'rigid' support is provided in table 3.2. SMD characterization and performance plots are provided in figures 3.13–3.16. The sensitivity and complimentary sensitivity functions graphically depict how disturbances pass through the closed loop system. The *output* disturbance PSDs and RMS values shown in figures 3.7, 3.8, and 3.9 are direct consequences of the accompanied *input* disturbance PSDs convolved with the appropriate sensitivity or complimentary sensitivity function. For simplicity, the input disturbance RMS levels were determined to force the resulting SMD output RMS levels to meet performance requirements. Figure 3.14 shows the locus of closed loop roots as forward loop gain, K, is varied from 0 to 1300. Figure 3.16 shows the output response $X_{out}(t)$ for the commanded ten engagement square wave $X_c(t)$[6]. Enlargements of the first and ninth engagements show $X_{out}(t)$ entering the offset error tolerance band of $\pm 400\mu$du with less than 100μdu jitter.

To examine the CSI phenomena, the SMD is mounted to the flexible support structure in the manner shown in figure 3.12. Four case studies are presented describing CSI effects ranging from critical performance degradation to system instability. In each case the total system mass is held constant ($m_1 + m_2 + m_a = 1.44$) with $m_a = 1.0$ rendering a mass ratio $\mu = 2.33$. Damping coefficients ζ_p and ζ_a were set to .1% and 1% of critical, respectively. The SMD natural frequency w_a is constant at $10(2pi)$ rad/sec (10 Hz) with $k_a = 3947.84$. In cases 1–4 k_2 is varied to represent 'soft' versus 'stiff' flexible support structures. The resulting support structure natural frequency w_p, defined by equations 3.18 and 3.19 are 1 Hz, 10 Hz, 100 Hz, and 500 Hz, for cases 1–4 respectively. These four case studies allow us to examine the CSI effects due to structural resonances less than, equal to, and greater than the actuator natural frequency, and both less than and greater than the SMD control loop crossover frequency. Simulated jitter stabilization performance for the four contolled benchmark model case studies is summarized in table 3.4.

Flexibility types can be estimated from the pair $\{\omega_k, \phi_k\}$ assuming zero damping. In these four case studies, φ_a and φ_k are of the same sign thereby defining the resulting structural flexibility as either an appendage or in-the-loop minimum phase mode.

---

[6] See figure 3.10.

Table 3.2: Spring-Mass-Damper (SMD) Under Rigid Support: Simulated Performance

Command Response Performance	
step command, y_c	1.00 du
settling time to RMS window, t_{RMS}	0.042 seconds
dwell time in RMS window, t_{DWELL}	0.058 seconds
RMS window offset error, $y(t_{RMS}) - y_c$	0.00 du
Error (Jitter)	
Input Disturbance	*Output Error*
force, f_d	$\varepsilon_{f_d} \leq 60\mu$du RMS
displacement, x_d	$\varepsilon_{x_d} \leq 60\mu$du RMS
measurement noise, m	$\varepsilon_m \leq 60\mu$du RMS
total RMS Jitter	$\varepsilon_{TOT} \leq 100\mu$du RMS

Interchanging mode 'a' with 'k', which can occur when w_a and w_p are closely spaced, simply changes the flexibility type from appendage to in-the-loop minimum phase or vice versa without affecting the estimate of fundamental pole-zero structure. Table 3.3 summarizes the structural flexibility parameters and the resulting flexibility types for each case.

Case 1: ($w_a = 10(2\pi)$ rad/sec and $w_p = 1(2\pi)$ rad/sec)

In this case the SMD is mounted to a less massive, 'soft' flexible support structure. The forward loop frequency response is shown in figure 3.19. As predicted in the coupled system equation 3.20 the system zeros are equal to the poles of the flexible support structure (benchmark problem sub-plant) defined in equation 3.19. The pole-zero separation is a function of the mass ratio μ. A larger mass ratio equates to wider pole-zero separation. The root locus plots in figures 3.20 and 3.21 show that the flexible mode is potentially unstable but in this case gain stabilized. Often times, the course granularity on a Bode plot hides pertinent stability information in the vicinity of the 0dB line. For this reason a Bode plot is generated (figure 3.22) with

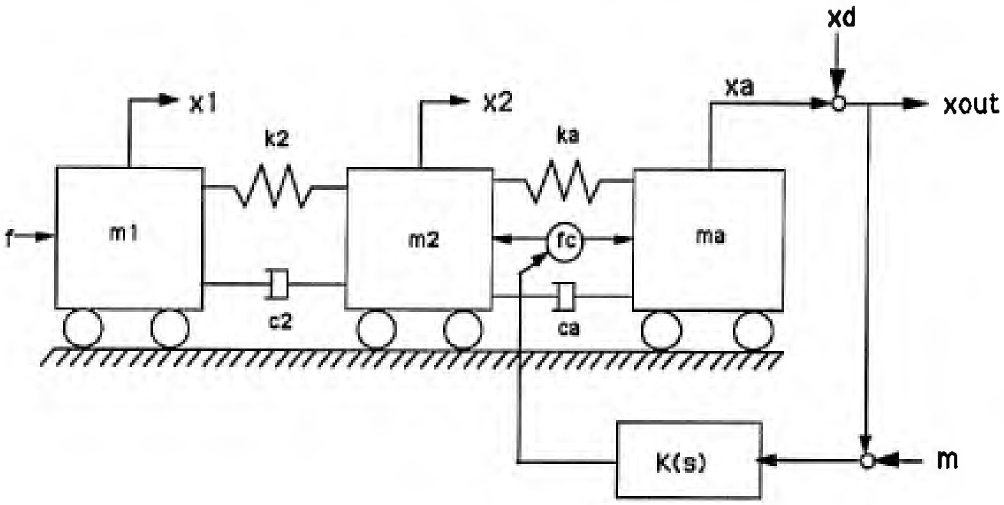

Figure 3.12: The Modified Benchmark Problem Controller Architecture

Table 3.3: Case Study Structural Flexibility Summary

Case	$\frac{\varphi_a}{\varphi_a+\varphi_k}$	α_k	Type
1	.9993	.5897	In-the-Loop Minimum Phase
2	.9167	.5455	In-the-Loop Minimum Phase
3	.9760	1.0235	Appendage Mode
4	.9990	1.0009	Appendage Mode

finer granularity around the frequency of potential instability. A Nyquist plot in the same frequency range (figure 3.23) verifies system stability. A comparison between the SMD and modified benchmark closed loop frequency response plots is provided in figure 3.24. Command response performance loss is revealed in the curves provided in figure 3.25. Table 3.4 shows the source of jitter stabilization performance loss to be ε_{f_d}. Figure 3.26 compares the three appropriate disturbance rejection transfer functions (sensitivity functions) for the SMD and the Case 1 modified benchmark problem. The top left curves verify that the low frequency support structure flexible mode amplifies low bandwidth force disturbance f_d. Output jitter due to displacement disturbance x_d and measurement noise m are not significantly different from the SMD.

Case 2: ($w_a = 10(2\pi)$ rad/sec and $w_p = 10(2\pi)$ rad/sec)

The support structure here is less massive but of comparable stiffness. The coincidence of the two natural frequencies at 10 Hz creates coupling that prevents clear distinction between the SMD and flexible structure modes. Consequently, the resulting flexibility type can be described as either in-the-loop minimum phase or appendage. The forward loop frequency response is shown in figure 3.27. The magnitude plot suggests a gain stabilized flexible mode, however, root locus plots (figures 3.28 and 3.29) show that in fact the structural flexibility is unstable, albeit slow. As with case 1, finer granularity about the zero frequency is required, this time revealing a clear drop in magnitude below 0dB (figure 3.30) and an unstable excursion through the unit circle (figure 3.31). A comparison between the SMD and modified benchmark closed loop frequency response plots is provided in figure 3.32. Command response performance loss is revealed in the curves provided in figure 3.33. Jitter stabilization results were not obtained because the closed loop system is unstable.

Case 3: ($w_a = 10(2\pi)$ rad/sec and $w_p = 100(2\pi)$ rad/sec)

The SMD is mounted to a less massive but more stiff support structure. The two subplant natural frequencies are separated enough to allow a clear distinction between SMD and structural flexibility modes, yet still below the SMD control loop crossover frequency of approximately 230 Hz. The forward loop frequency response is shown in figure 3.34. The structural flexibility type is clearly an appendage mode and, under the existing control law, not a potential cause of CSI instability. It should be noted, however, that unmodeled sensor dynamics or filters designed to attenuate noise or prevent aliasing in digital implementation can introduce sufficient phase lag at an appendage mode causing instability to occur. A root locus plot magnified around the 100 Hz flexible mode (figure 3.35) verifies a stable flexible mode that induces significant output vibration. The closed loop frequency response plot in figure 3.36 shows the structural resonance at a point of near maximum amplification on the command response magnitude plot. Figure 3.37 highlights the critical CSI induced performance loss. The resulting oscillation is clearly outside the allowable

$\pm 400\mu$du offset error band and nearly two orders of magnitude greater than the required RMS jitter stability. As with Case 1, support structure flexibility amplifies force disturbance f_d outside the jitter budget.

Case 4: ($w_a = 10(2\pi)$ rad/sec and $w_p = 500(2\pi)$ rad/sec)

In this case the support structure natural frequency is beyond the SMD control loop crossover frequency. The forward loop frequency response, shown in figure 3.38, barely reveals the presence of the structural flexibility. In most applications, a flexible mode with this high a frequency would not pose significant problems, however with our severe performance requirements, structural resonances beyond loop crossover can (and do) cause significant output vibration. The command response shown in figure 3.40 reveals an interesting source of vibration attenuation between the first and ninth engagements. Figures 3.41– 3.43 show the sequence of ten engagements and lend some insight into the source of this vibration attenuation. The vibration amplitude is minimum in the seventh engagement and begins to grow again through the tenth suggesting modulation (or beating) between high frequencies in the command signal and the 500 Hz structural flexibility. When the command signal becomes aperiodic (more likely in a real retargeting scenario) modulation is not necessarily reinforced with each engagement and attenuation over many engagements is not likely to occur.

Table 3.4: Modified Benchmark Problem: Jitter Stabilization Performance

	RMS Residual Jitter (μdu)			
Model	ε_{f_d}	ε_{x_d}	ε_m	ε_{TOT}
SMD	60.005	59.984	60.001	103.92
Case 1	7956.6	58.732	59.828	7957.1
Case 2	*Unstable System*			
Case 3	79.245	60.409	59.674	116.15
Case 4	61.005	59.368	59.924	104.41

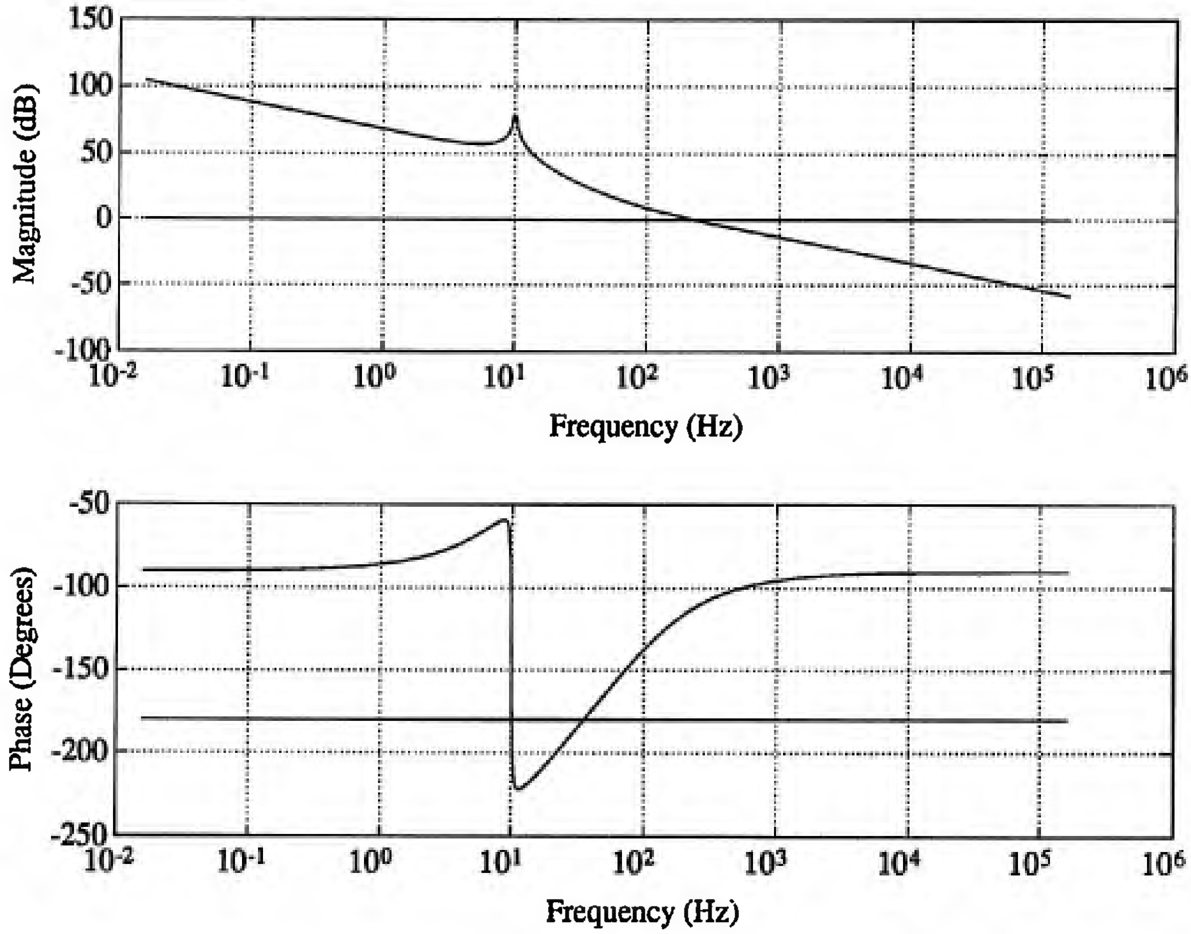

Figure 3.13: Forward Loop Frequency Response: Rigidly Supported Spring-Mass-Damper (SMD)

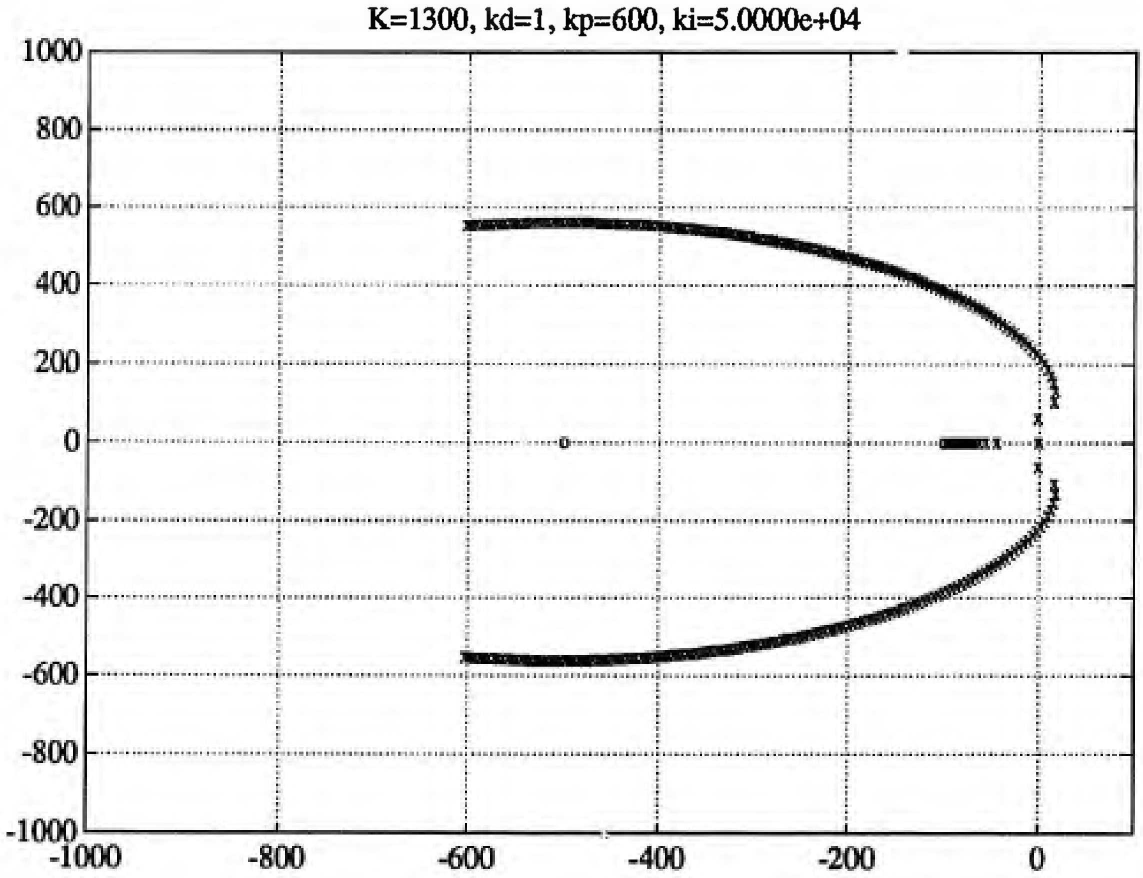

Figure 3.14: Loci of Closed Loop Roots: Rigidly Supported Spring-Mass-Damper (SMD)

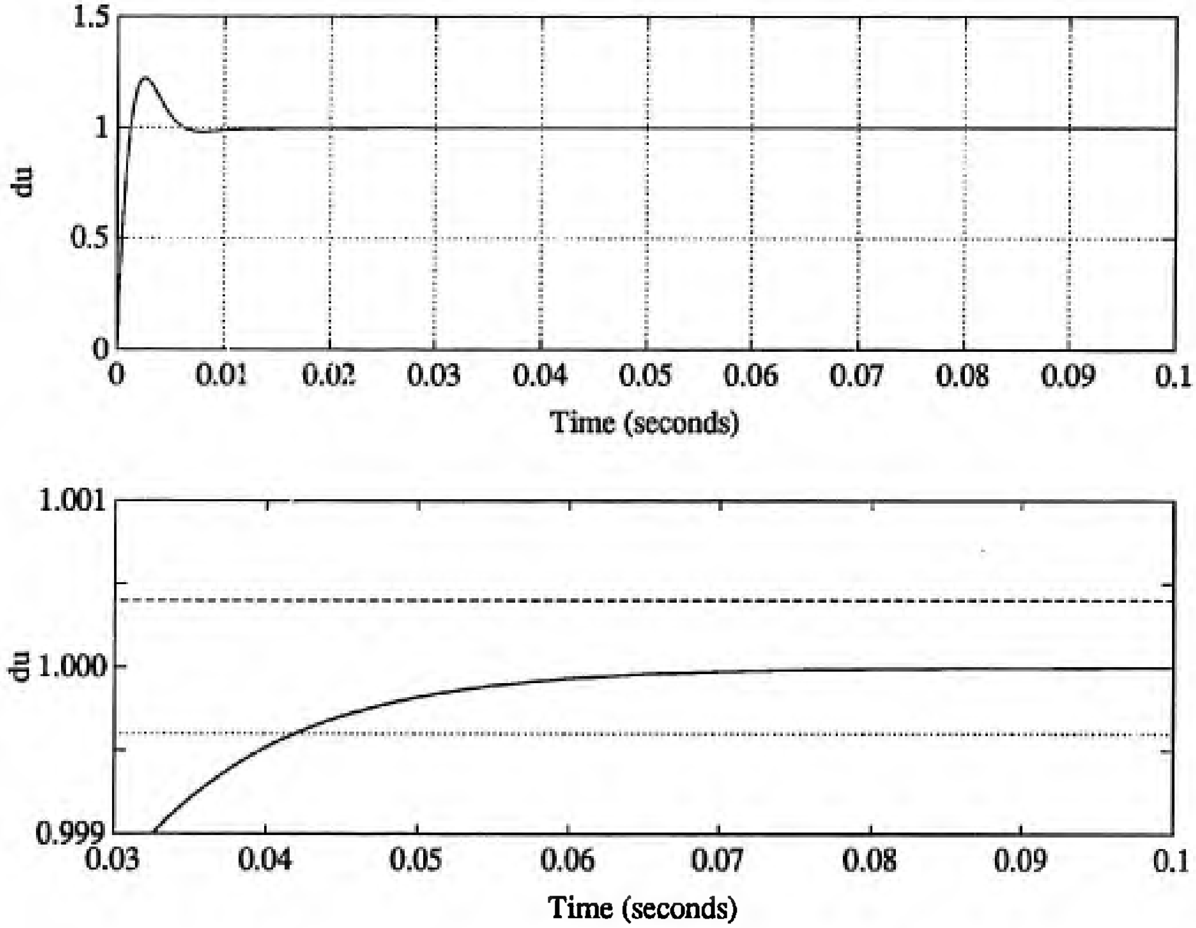

Figure 3.15: Output Step Response: Rigidly Supported Spring-Mass-Damper (SMD)

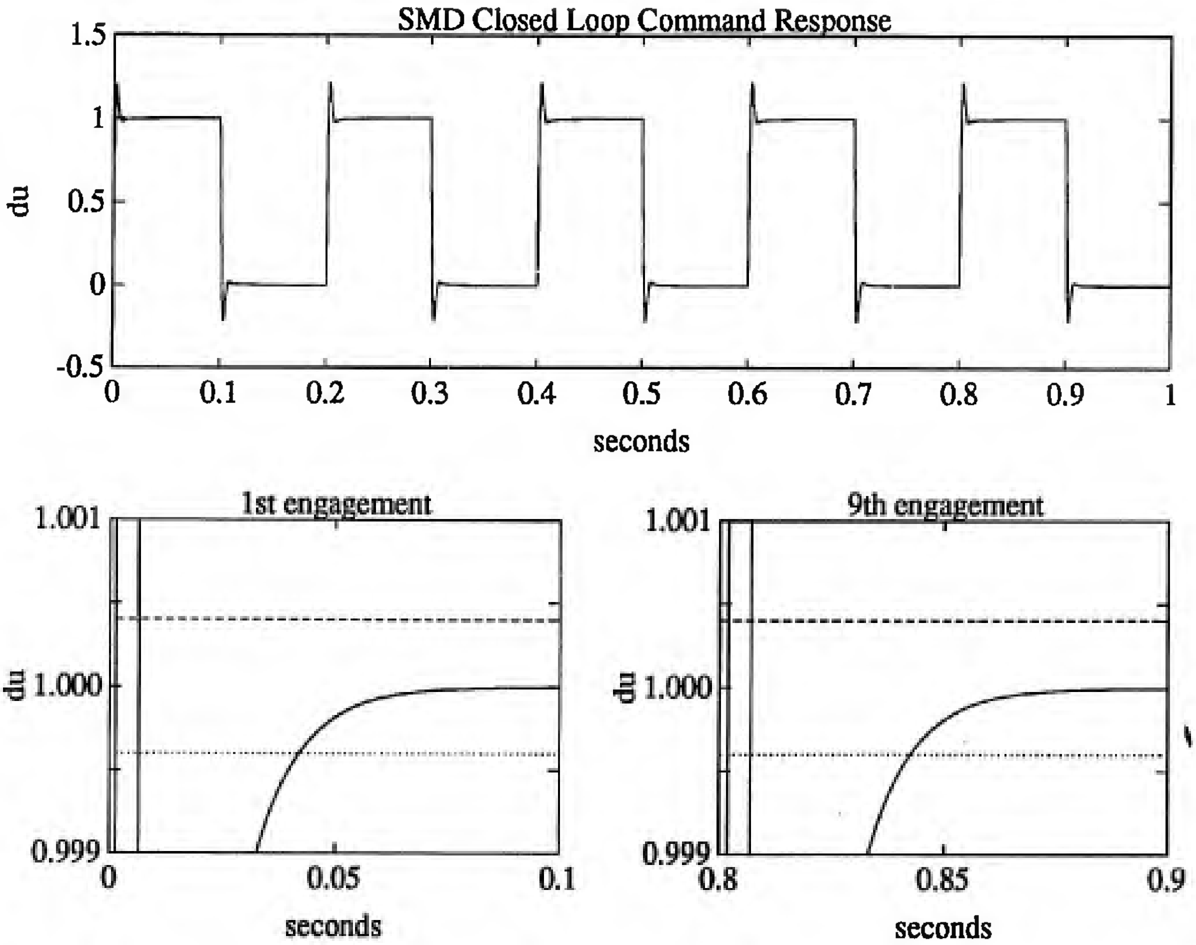

Figure 3.16: Command Response: Rigidly Supported Spring-Mass-Damper (SMD); Ten Engagement Sequence (top), First Engagement (bottom left), Ninth Engagement (bottom right)

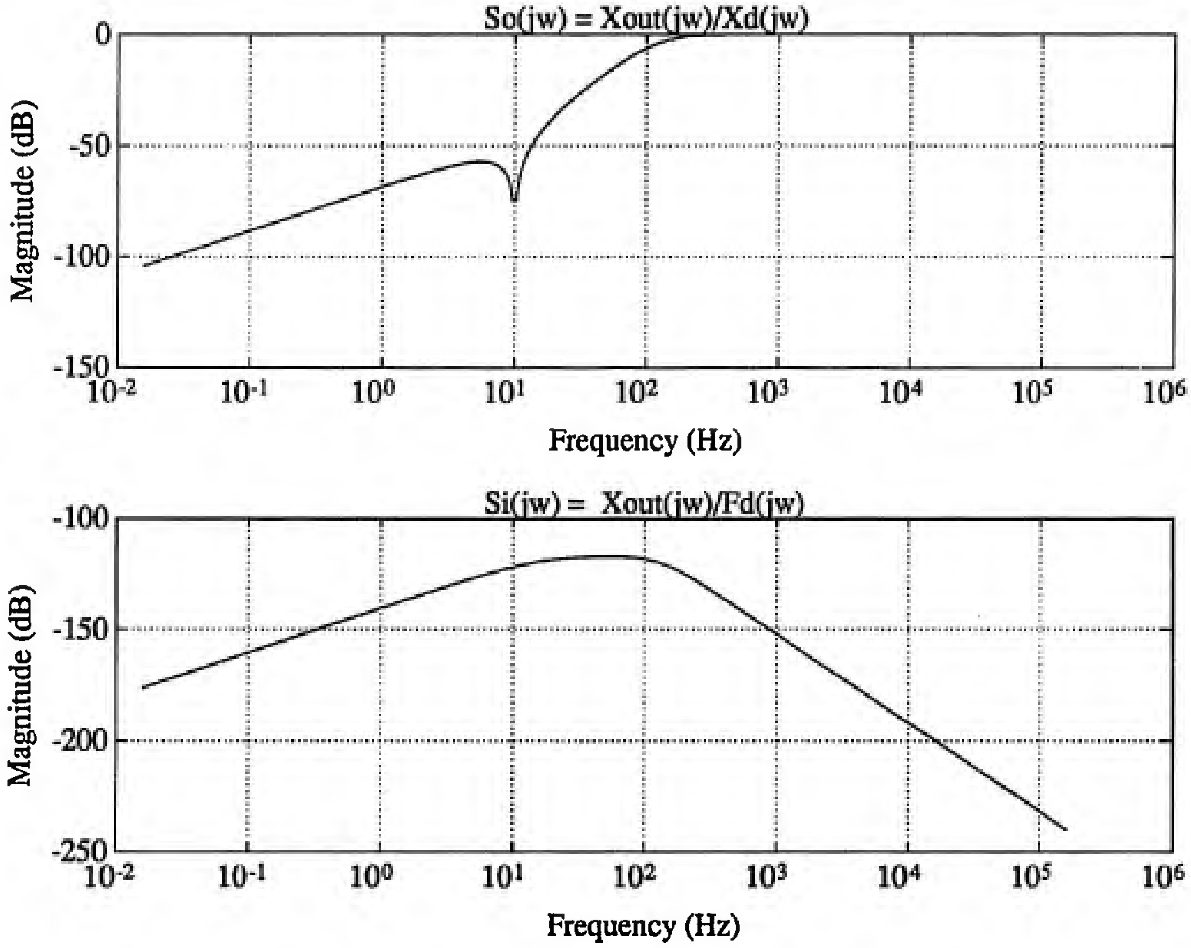

Figure 3.17: Disturbance Rejection Frequency Responses: Rigidly Supported Spring-Mass-Damper (SMD); Output Sensitivity Function (top), Input Sensitivity Function (bottom)

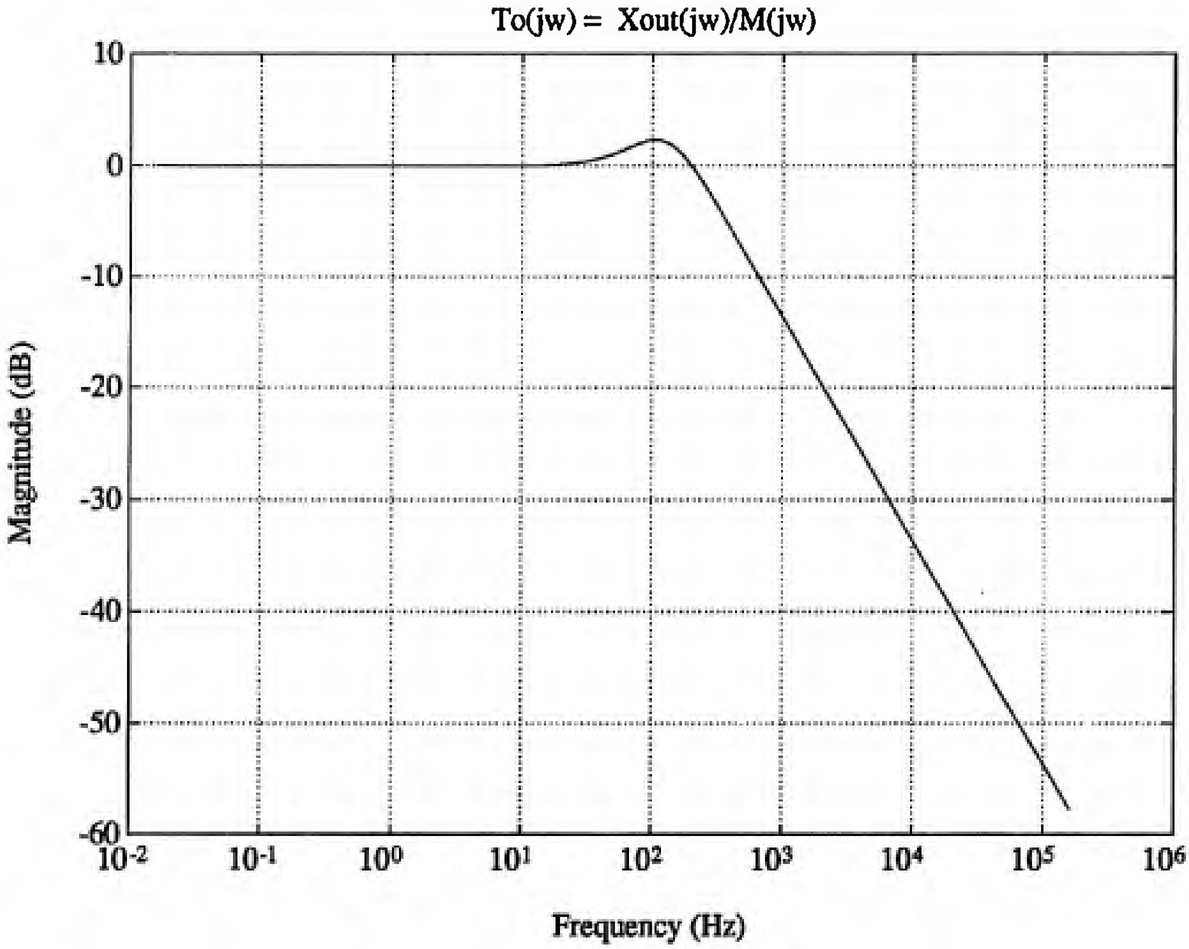

Figure 3.18: Noise Rejection Frequency Response (Complimentary Output Sensitivity Function): Rigidly Supported Spring-Mass-Damper (SMD)

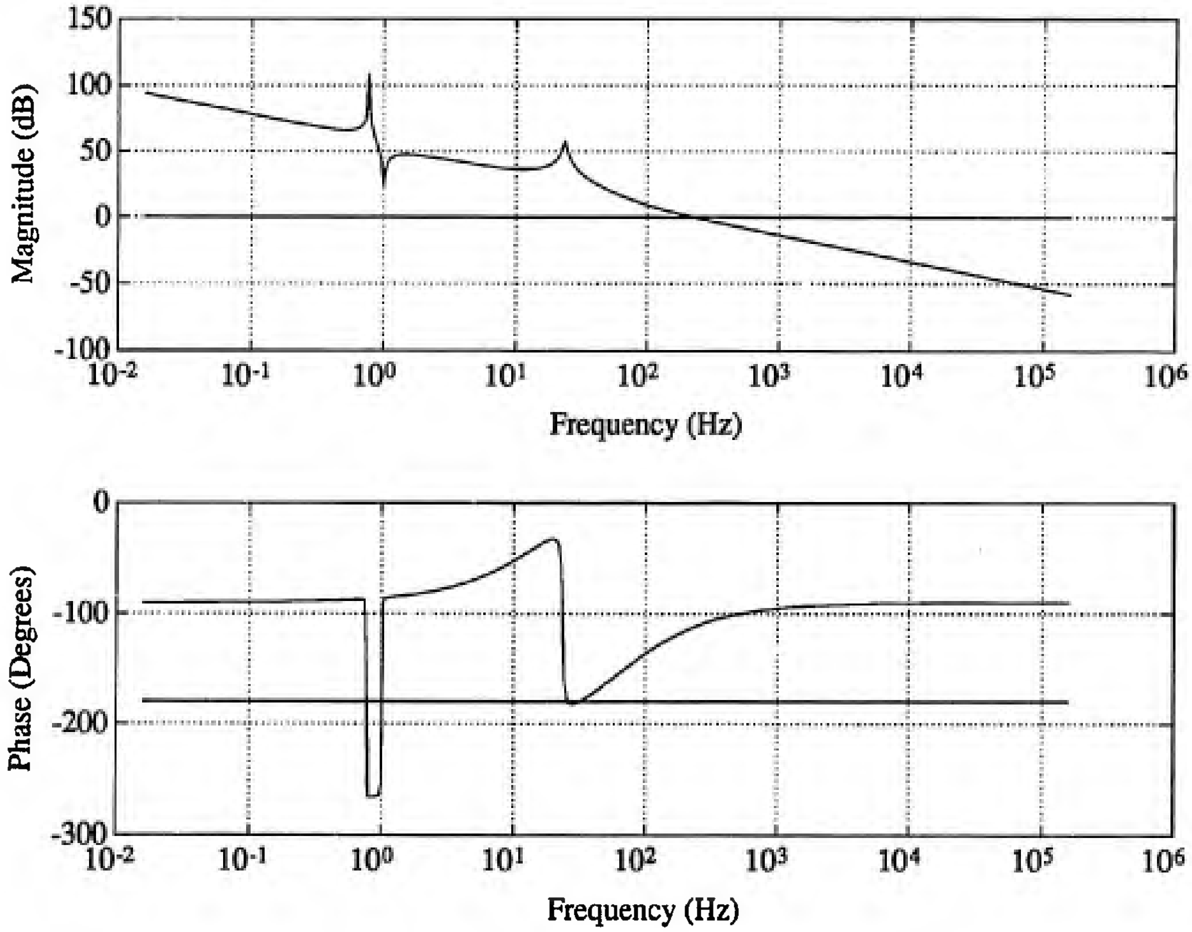

Figure 3.19: Forward Loop Frequency Response: Case 1

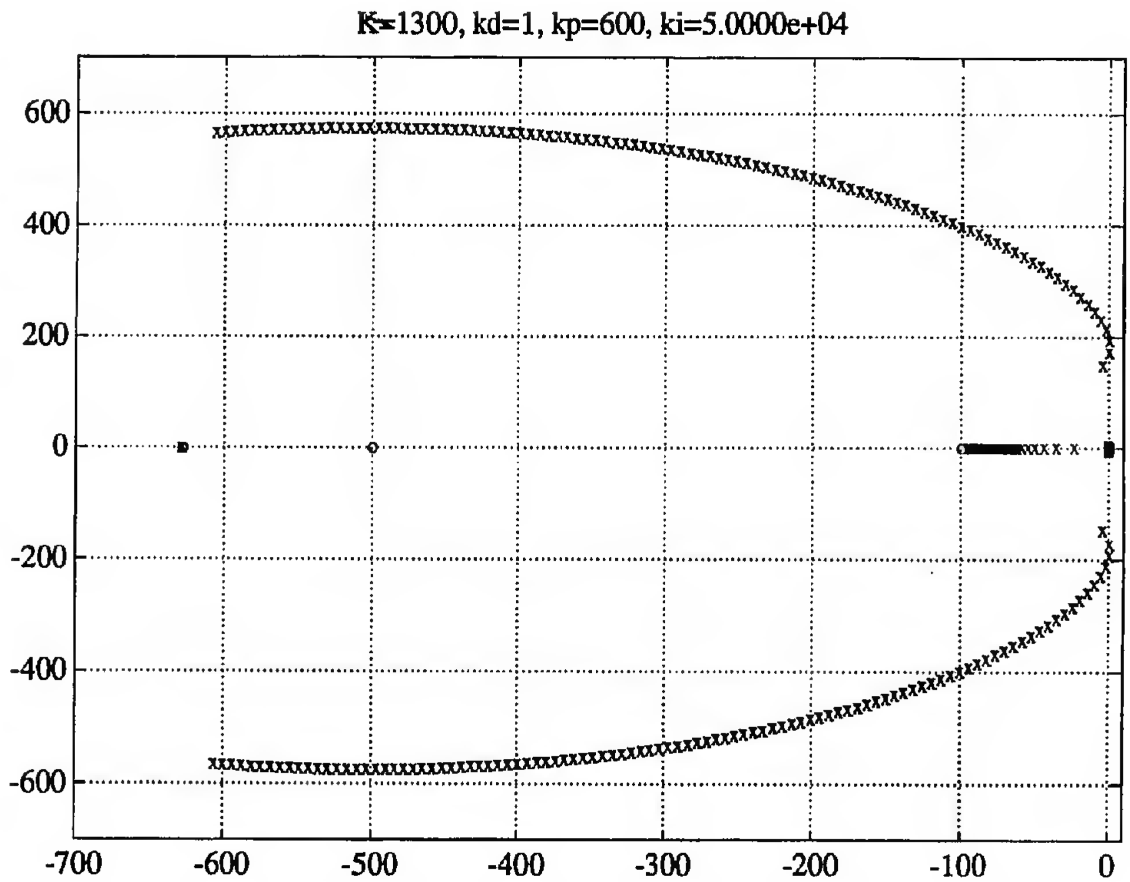

Figure 3.20: Loci of Closed Loop Roots: Case 1

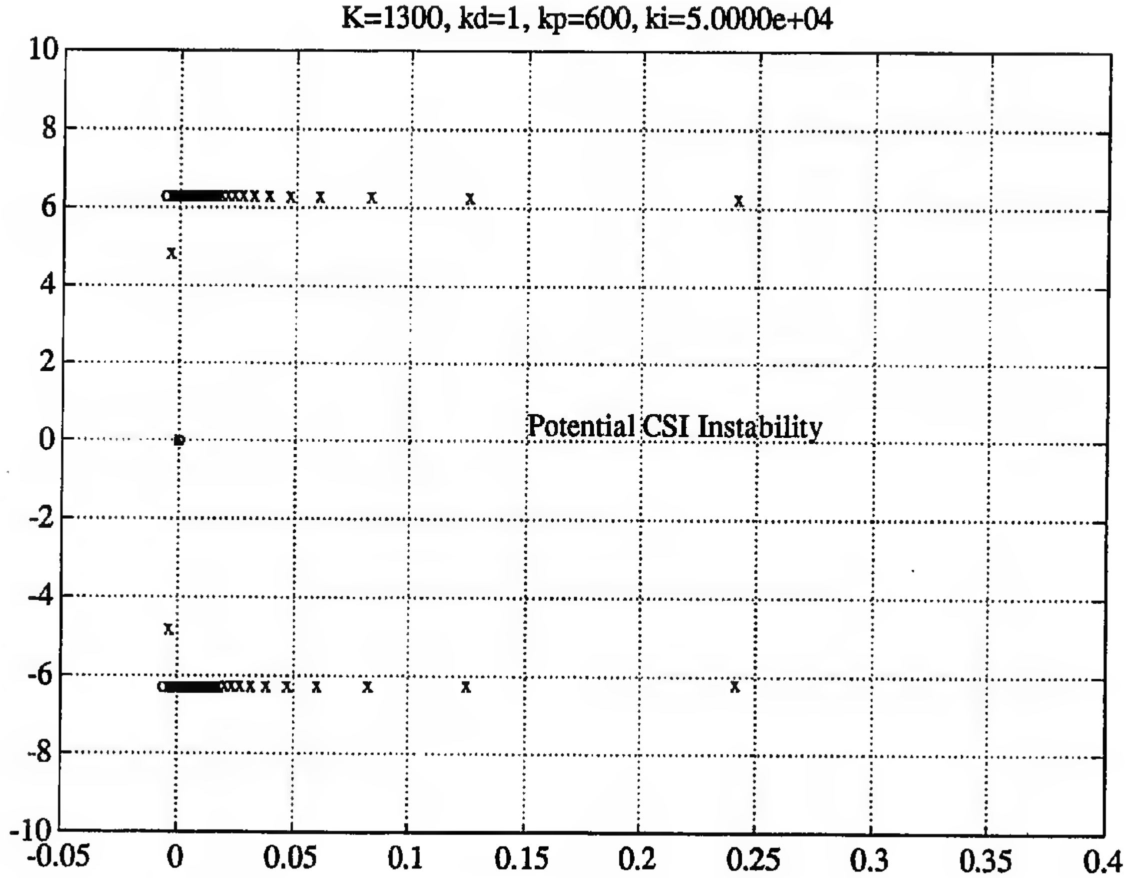

Figure 3.21: Loci of Closed Loop Roots (Magnified at Structural Flexibility): Case 1

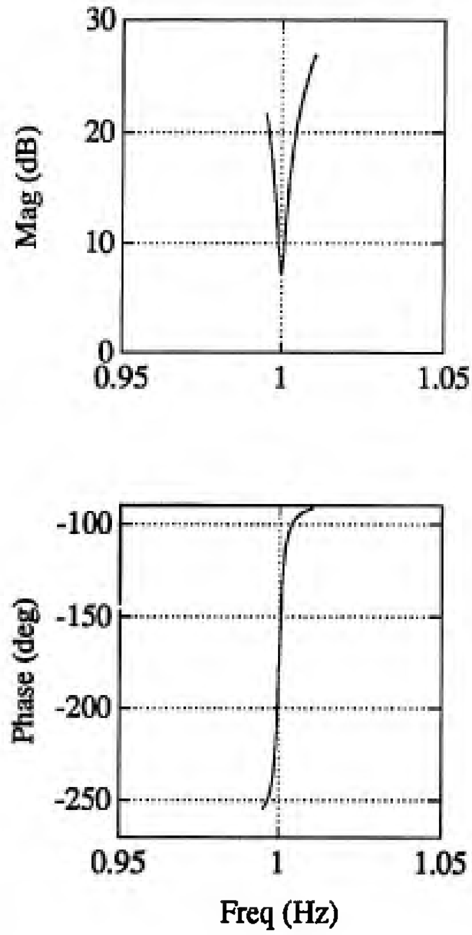

Figure 3.22: Forward Loop Frequency Response (Magnified at Potential Instability): Case 1

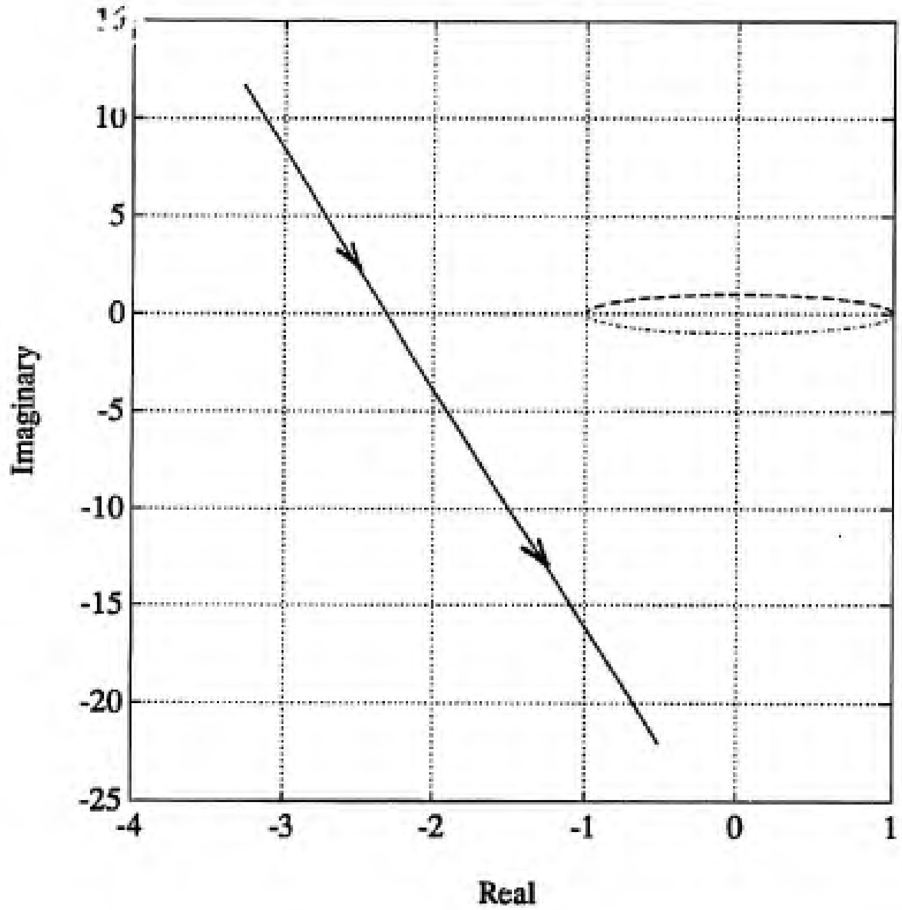

Figure 3.23: Nyquist Plot in Region of Potential Instability: Case 1

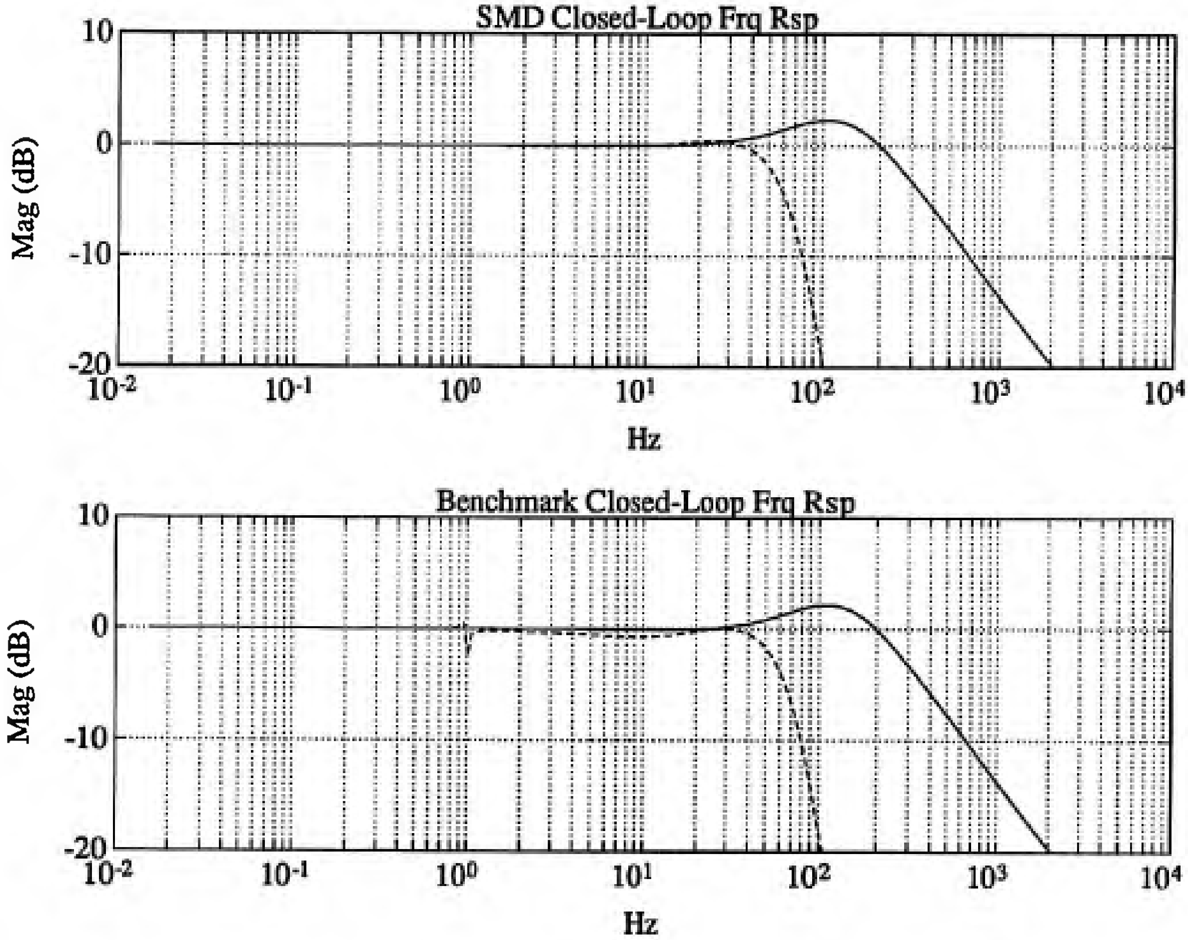

Figure 3.24: Closed Loop Frequency Response Plots, SMD versus Modified Benchmark: Case 1

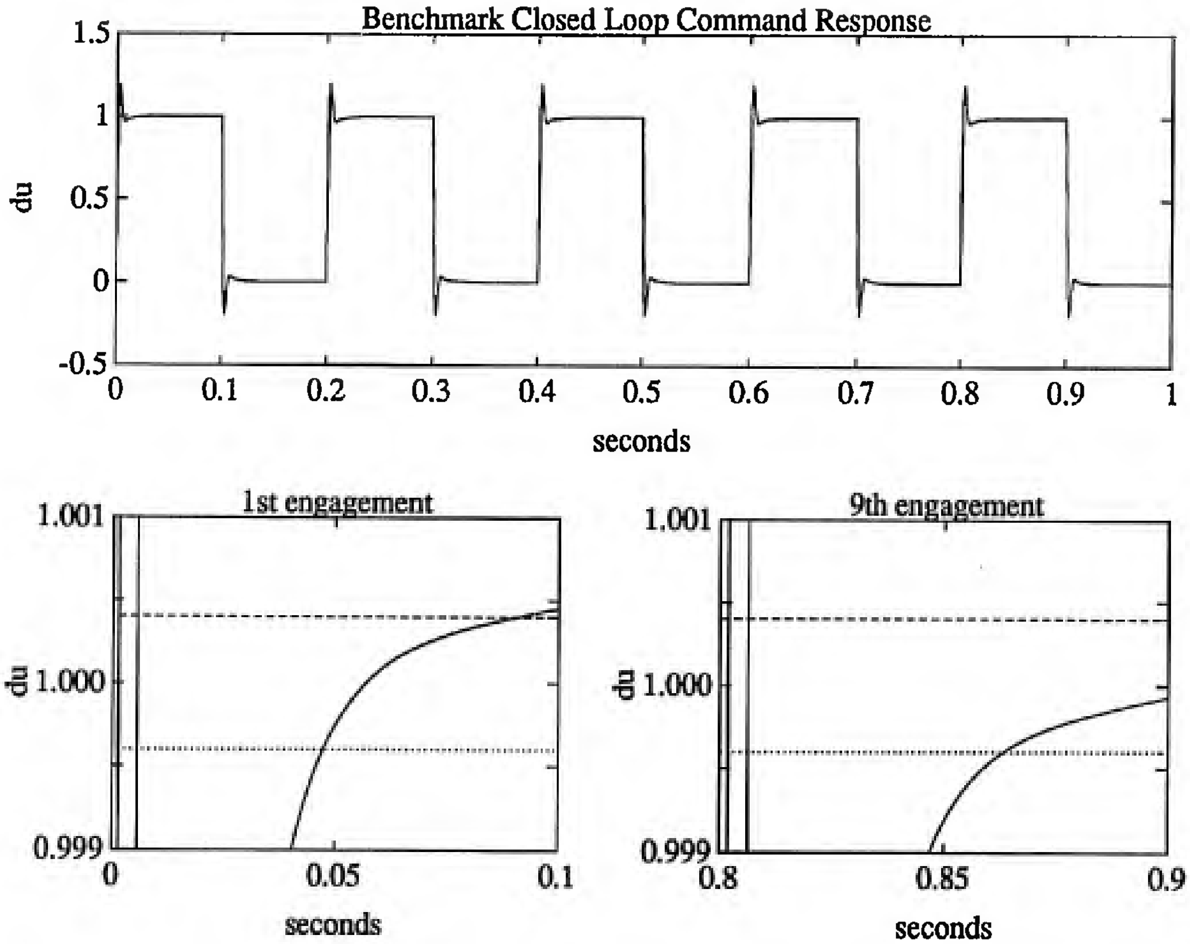

Figure 3.25: Command Response Curves: Case 1

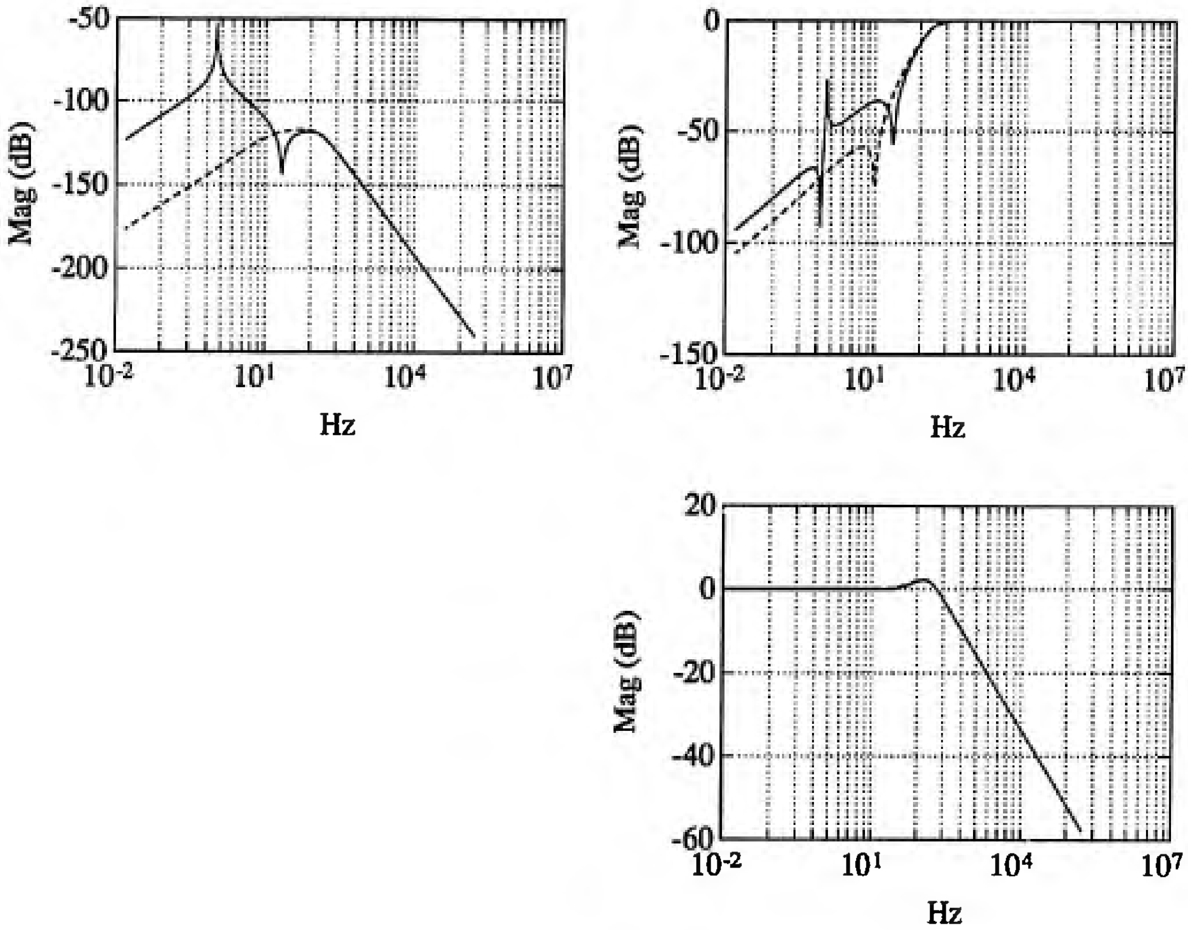

Figure 3.26: Disturbance Rejection Frequency Responses:Modified Benchmark Model, Case 1 (solid) vs. SMD (dashed); Input Sensitivity Function (top left), Output Sensitivity Function (top right), Output Complimentary Sensitivity Function (bottom right)

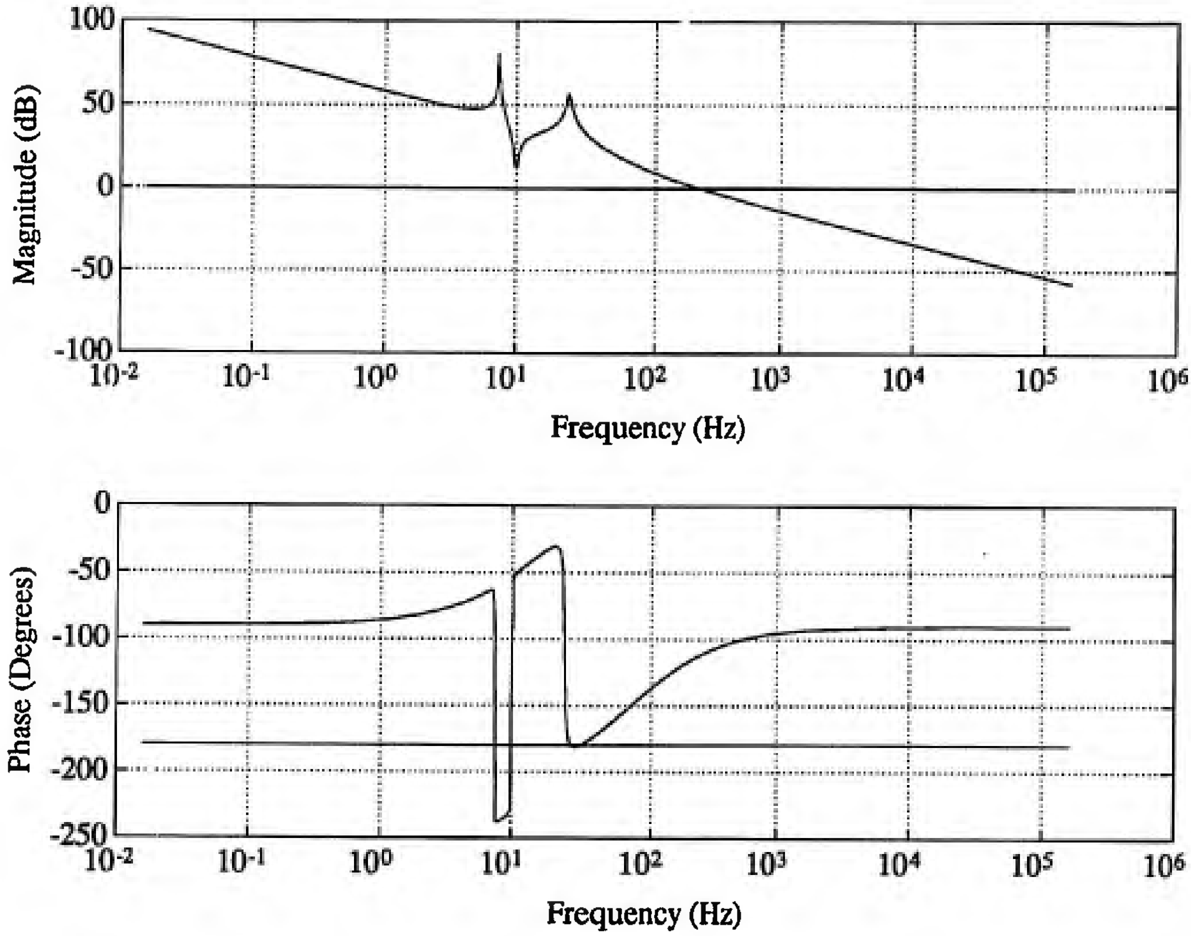

Figure 3.27: Forward Loop Frequency Response: Case 2

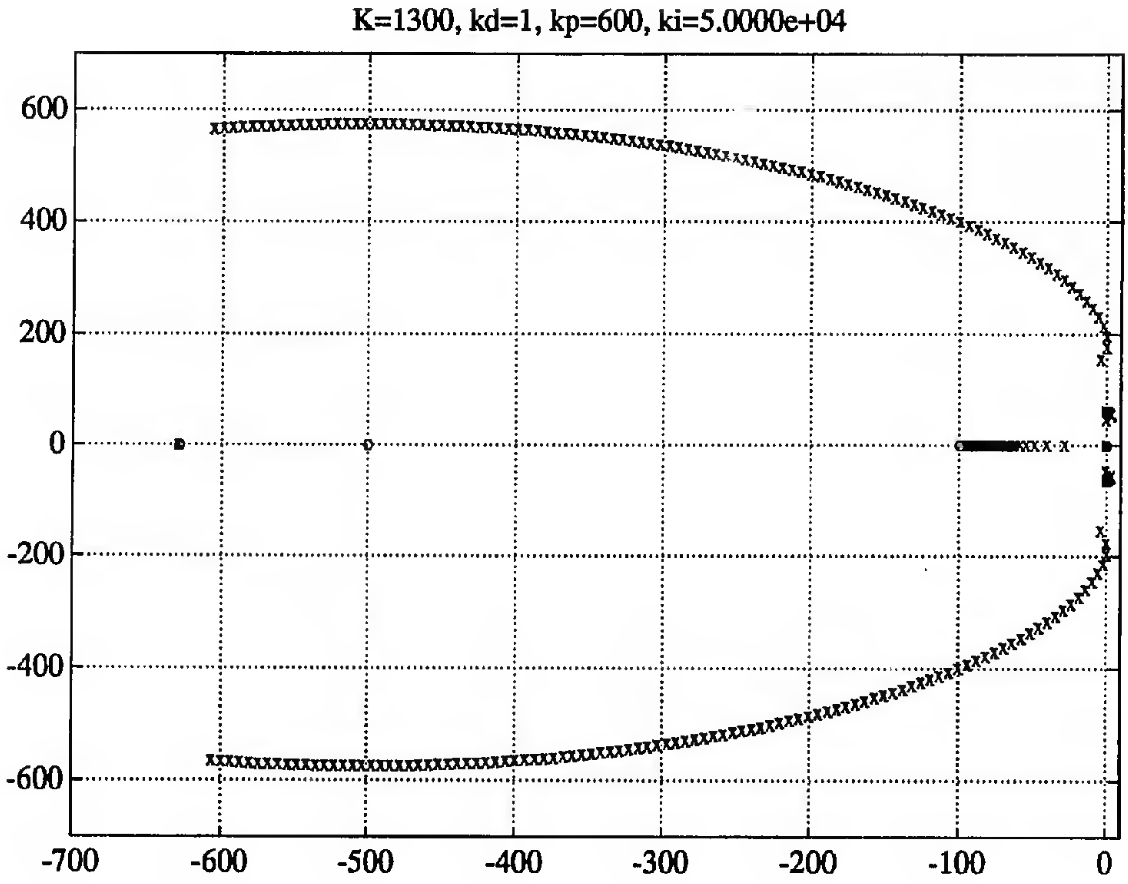

Figure 3.28: Loci of Closed Loop Roots: Case 2

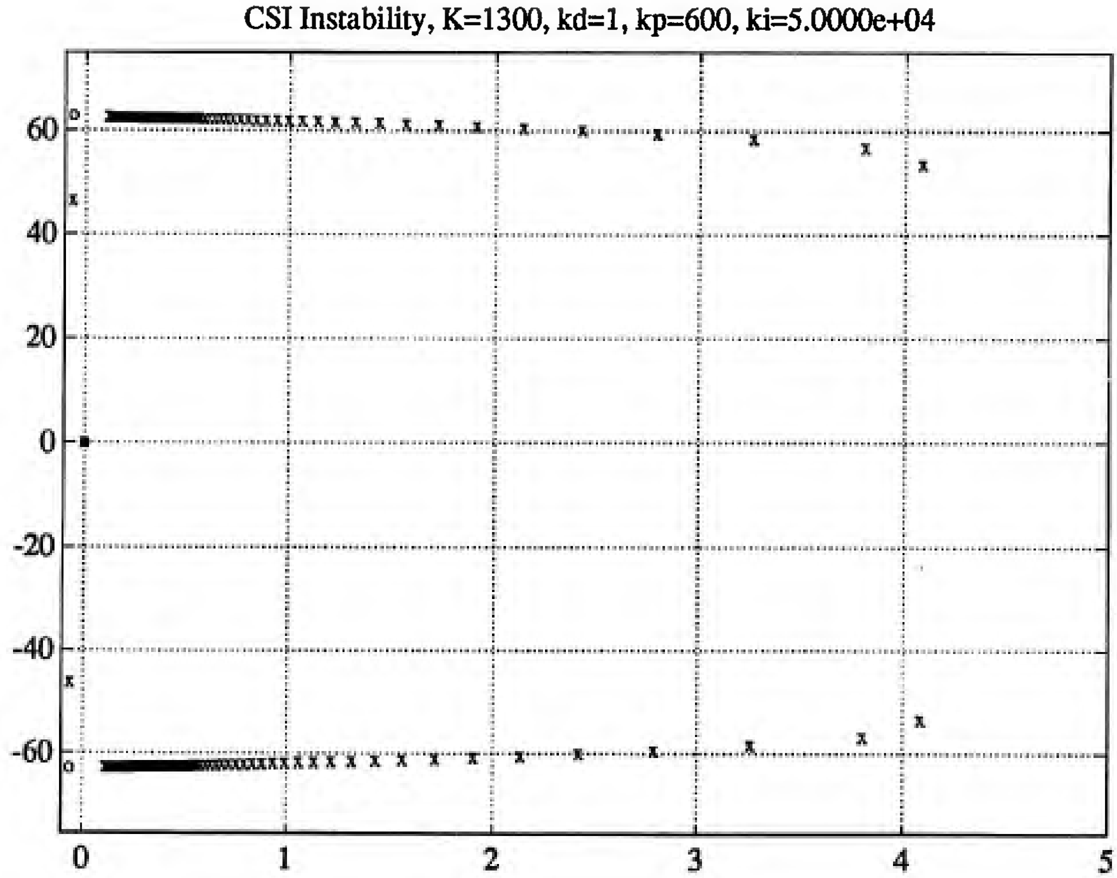

Figure 3.29: Loci of Closed Loop Roots (Magnified at Structural Flexibility): Case 2

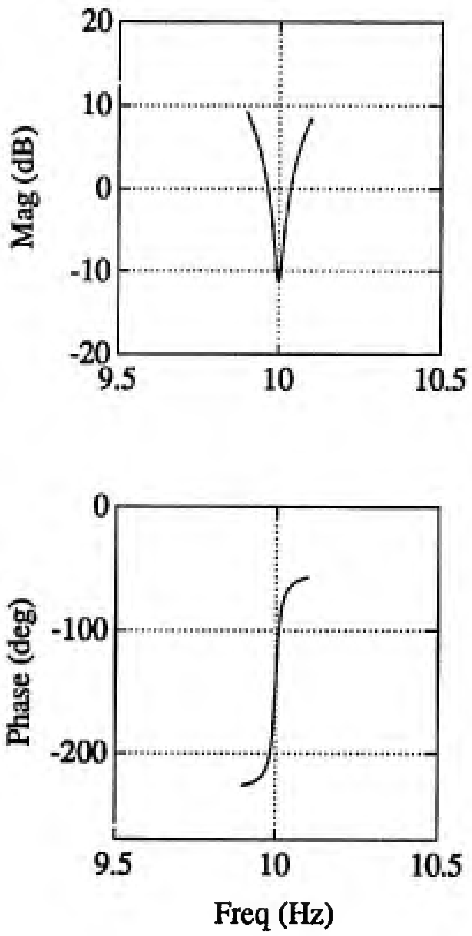

Figure 3.30: Forward Loop Frequency Response (Magnified at Potential Instability): Case 2

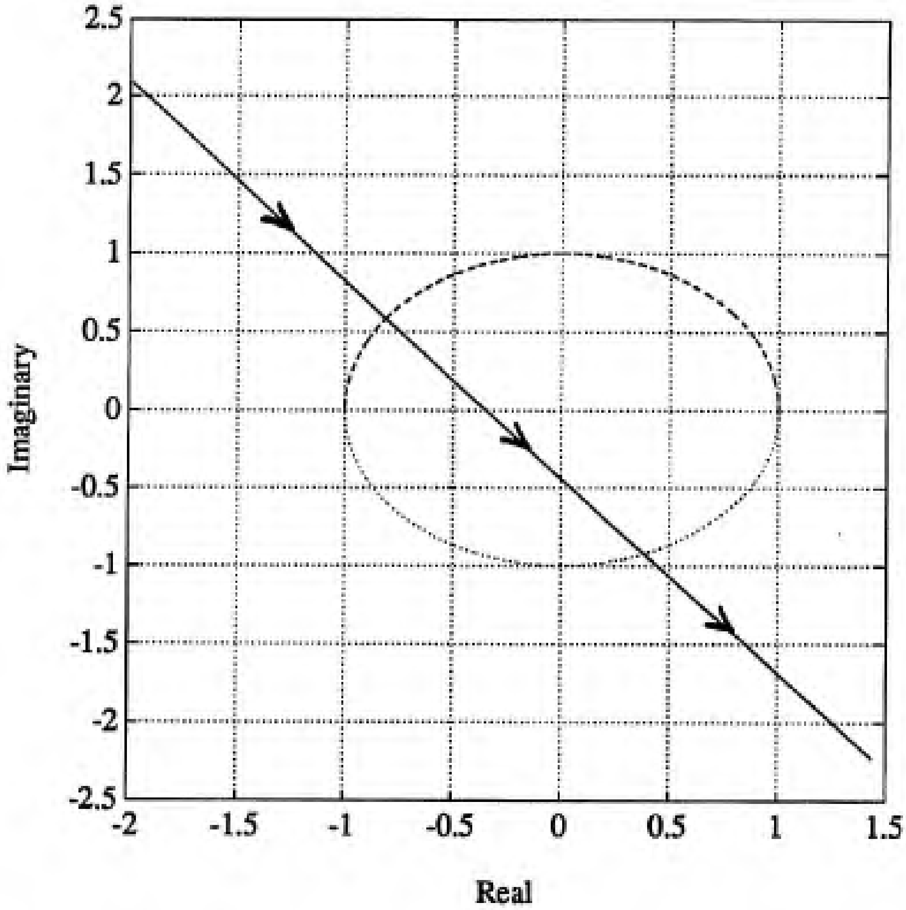

Figure 3.31: Nyquist Plot in Region of Potential Instability: Case 2

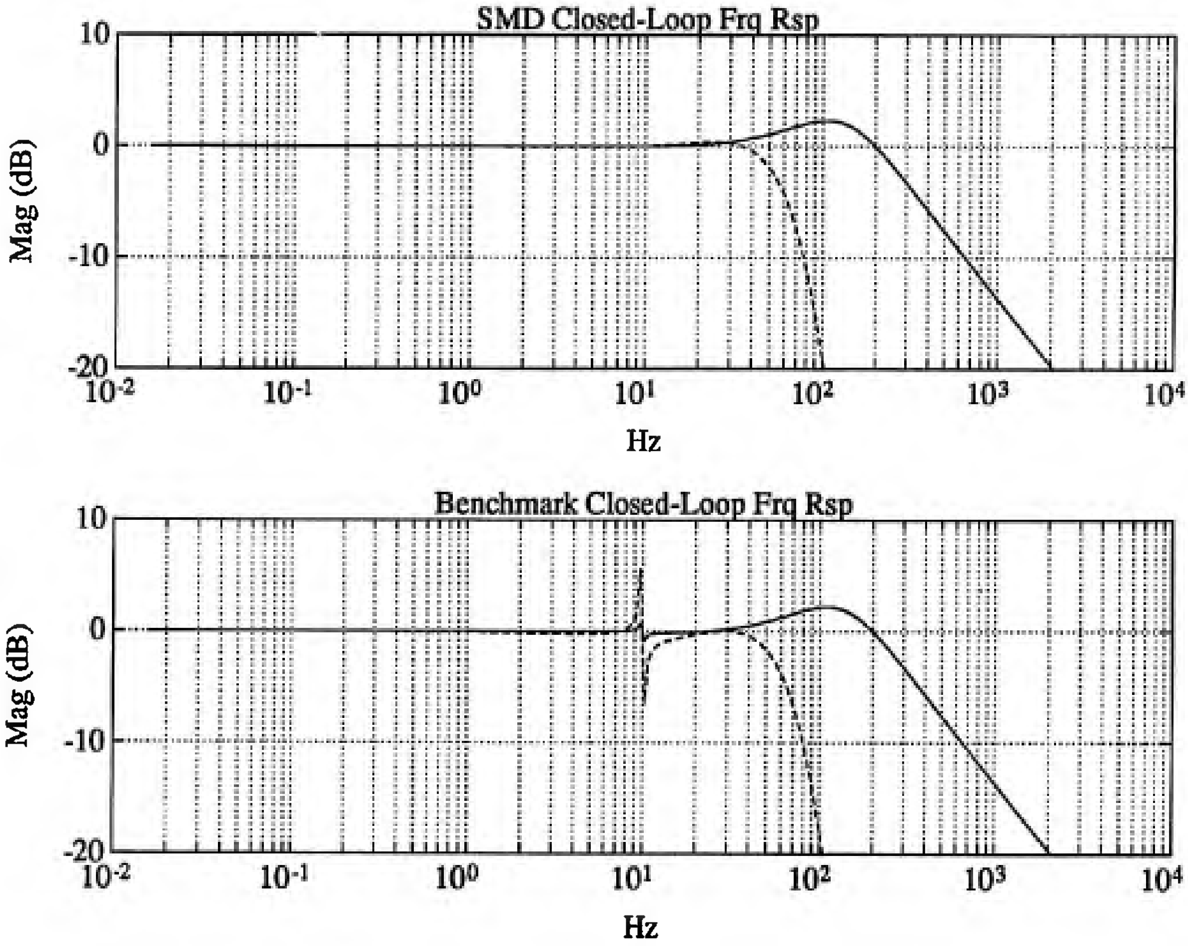

Figure 3.32: Closed Loop Frequency Response Plots, SMD versus Modified Benchmark: Case 2

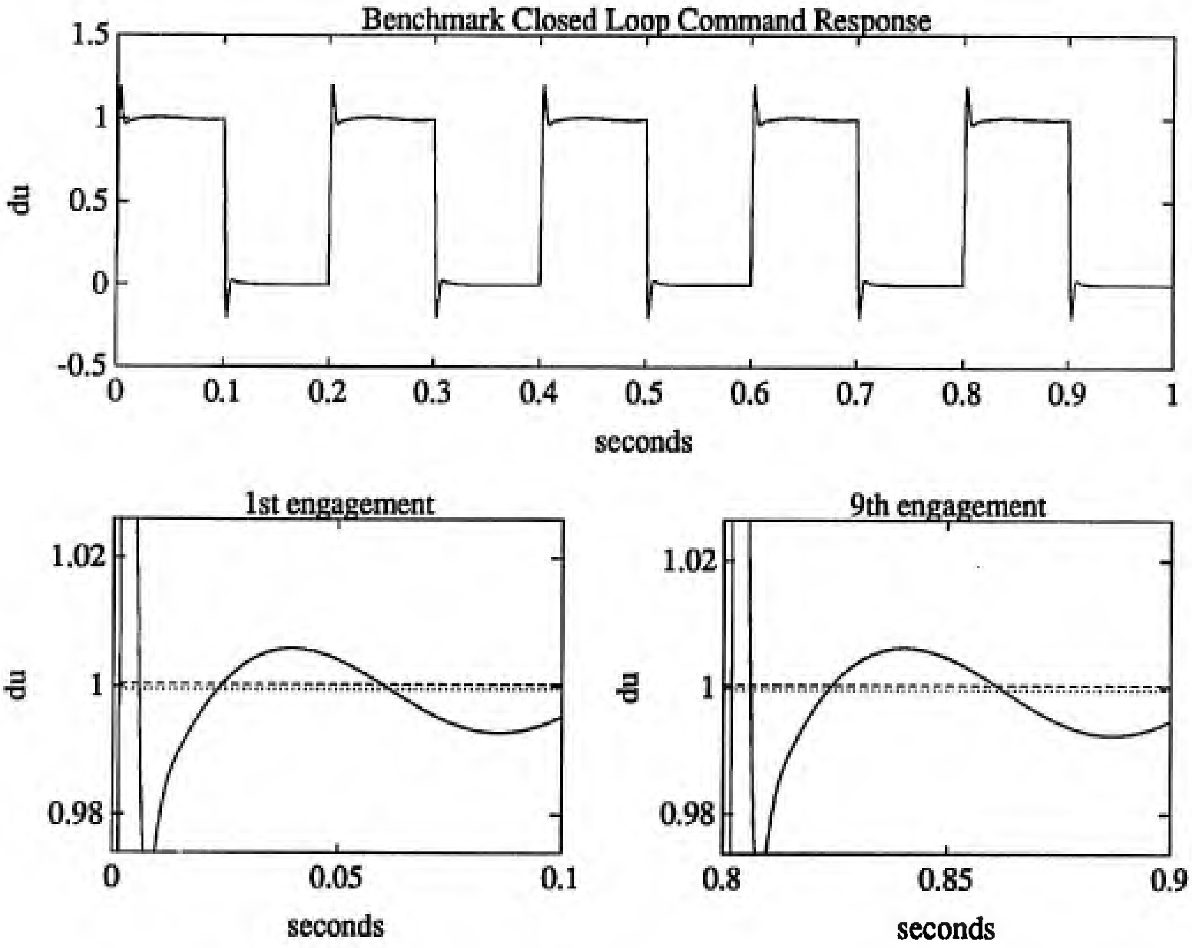

Figure 3.33: Command Response Curves: Case 2

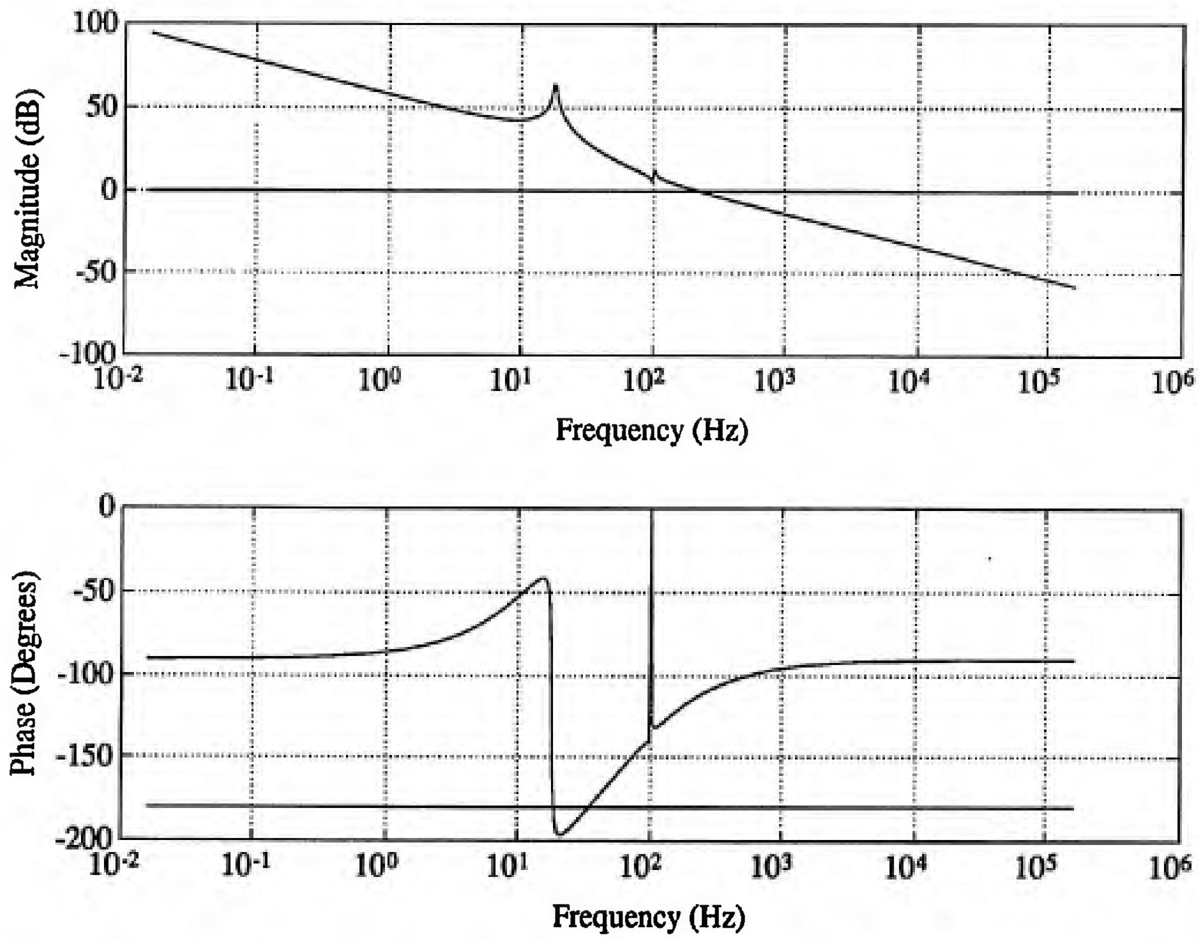

Figure 3.34: Forward Loop Frequency Response: Case 3

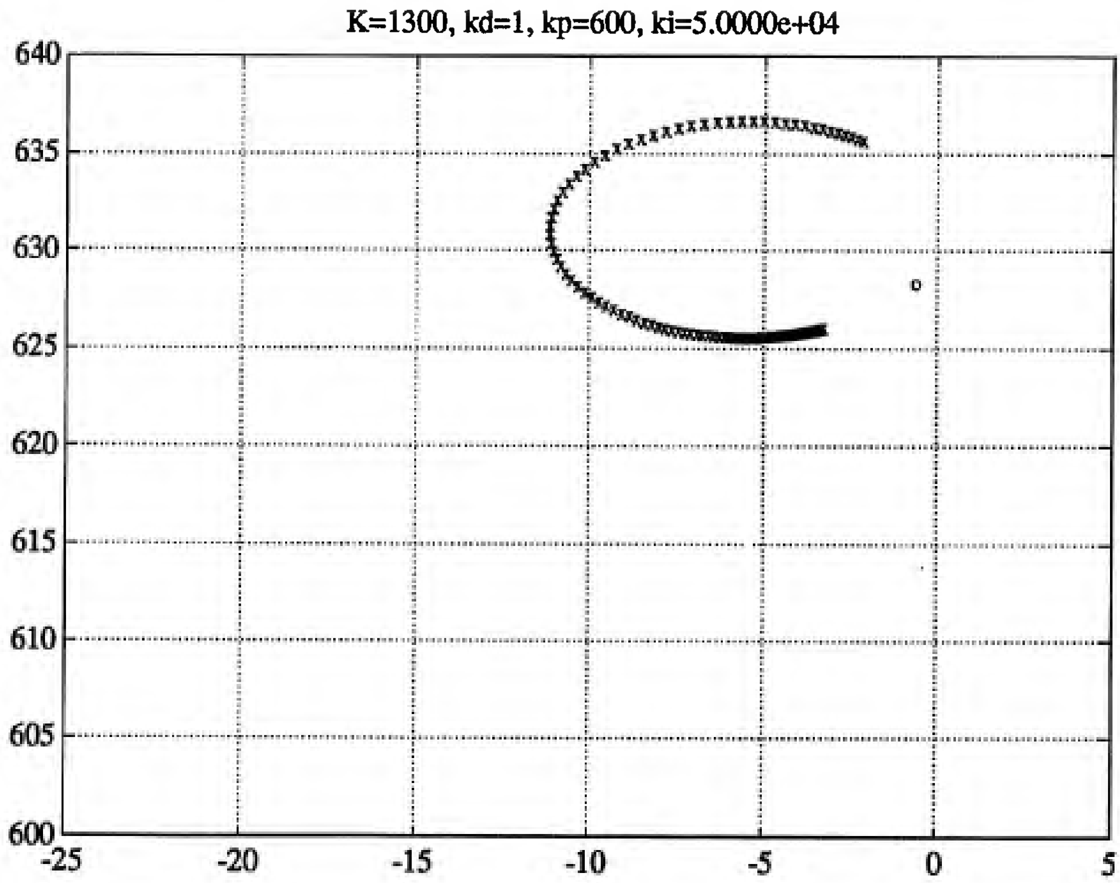

Figure 3.35: Loci of Closed Loop Roots (Magnified at Structural Flexibility): Case 3

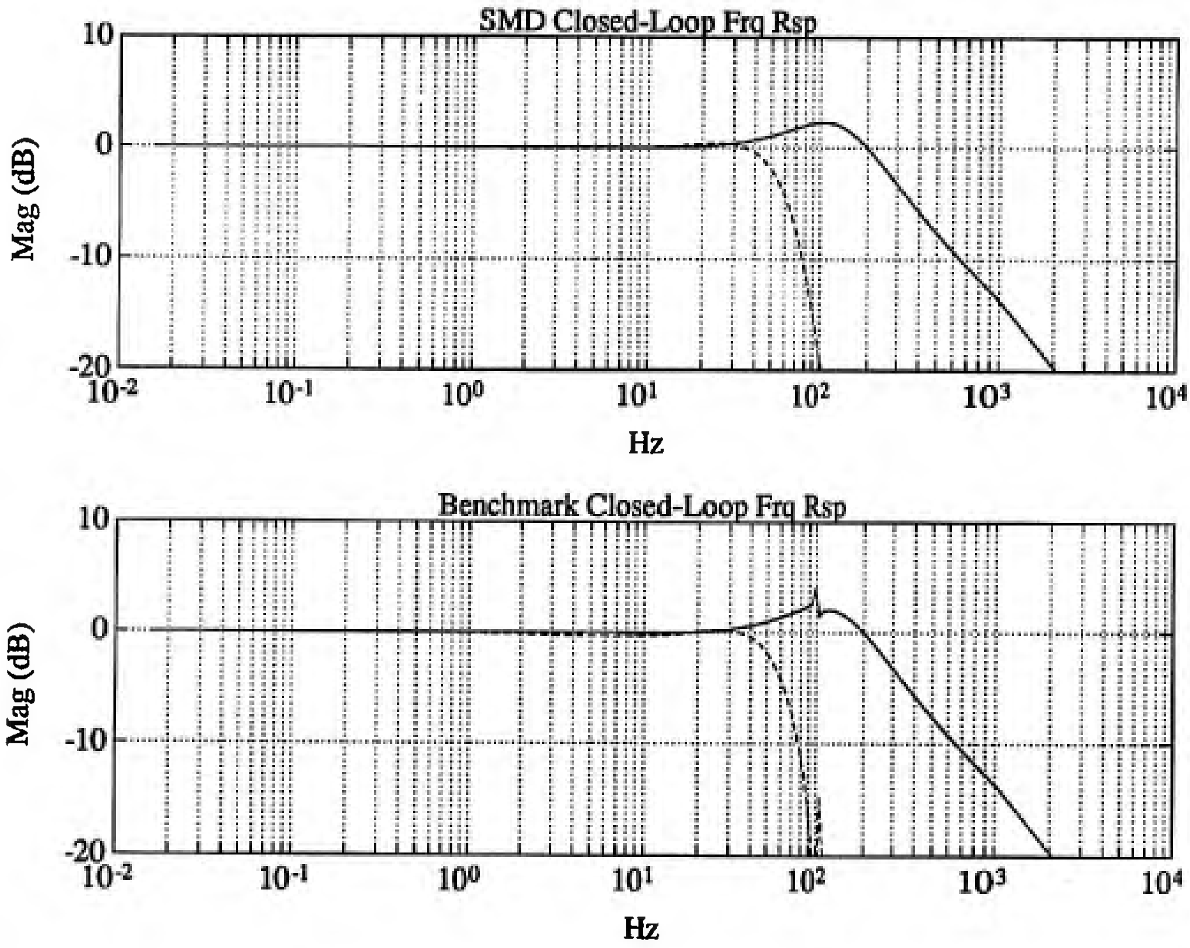

Figure 3.36: Closed Loop Frequency Response Plots, SMD versus Modified Benchmark: Case 3

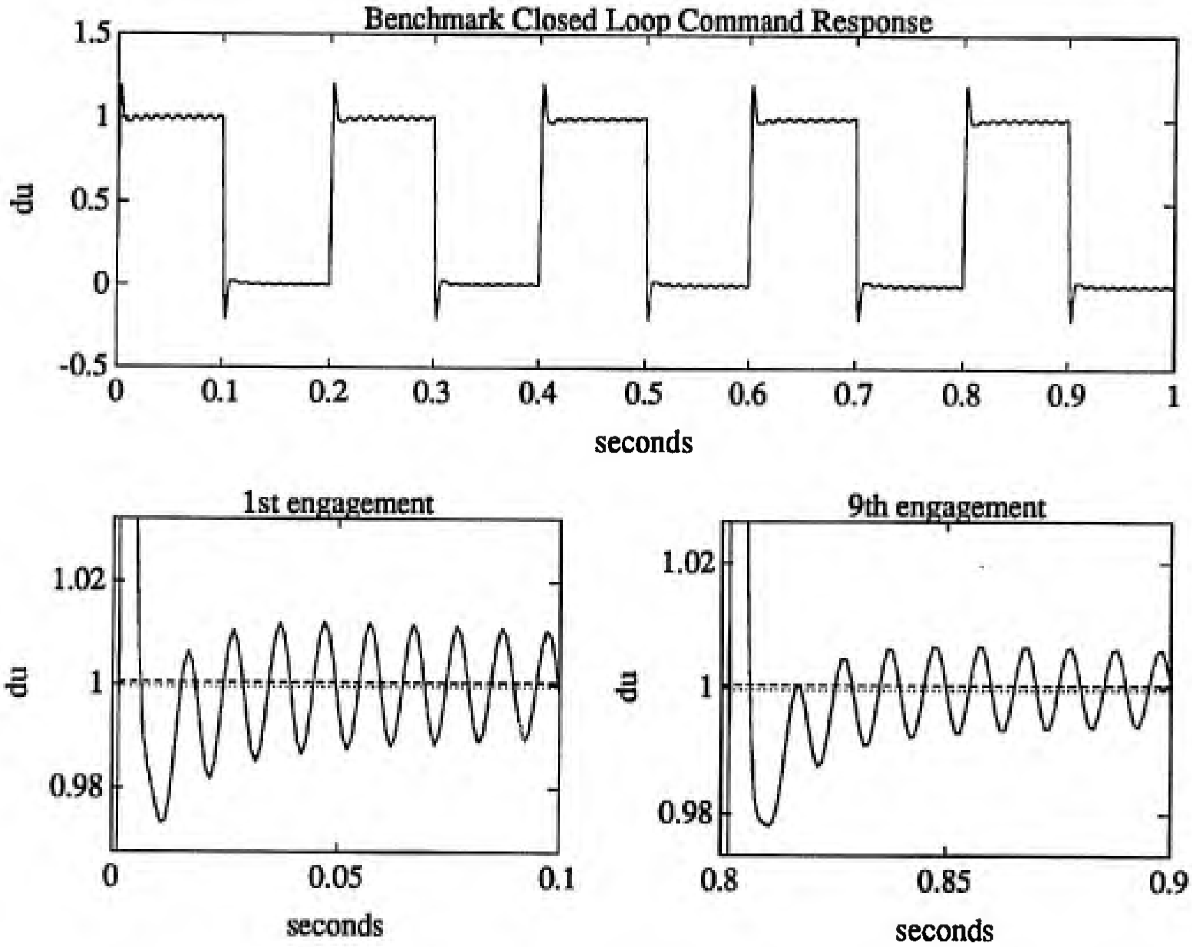

Figure 3.37: Command Response Curves: Case 3

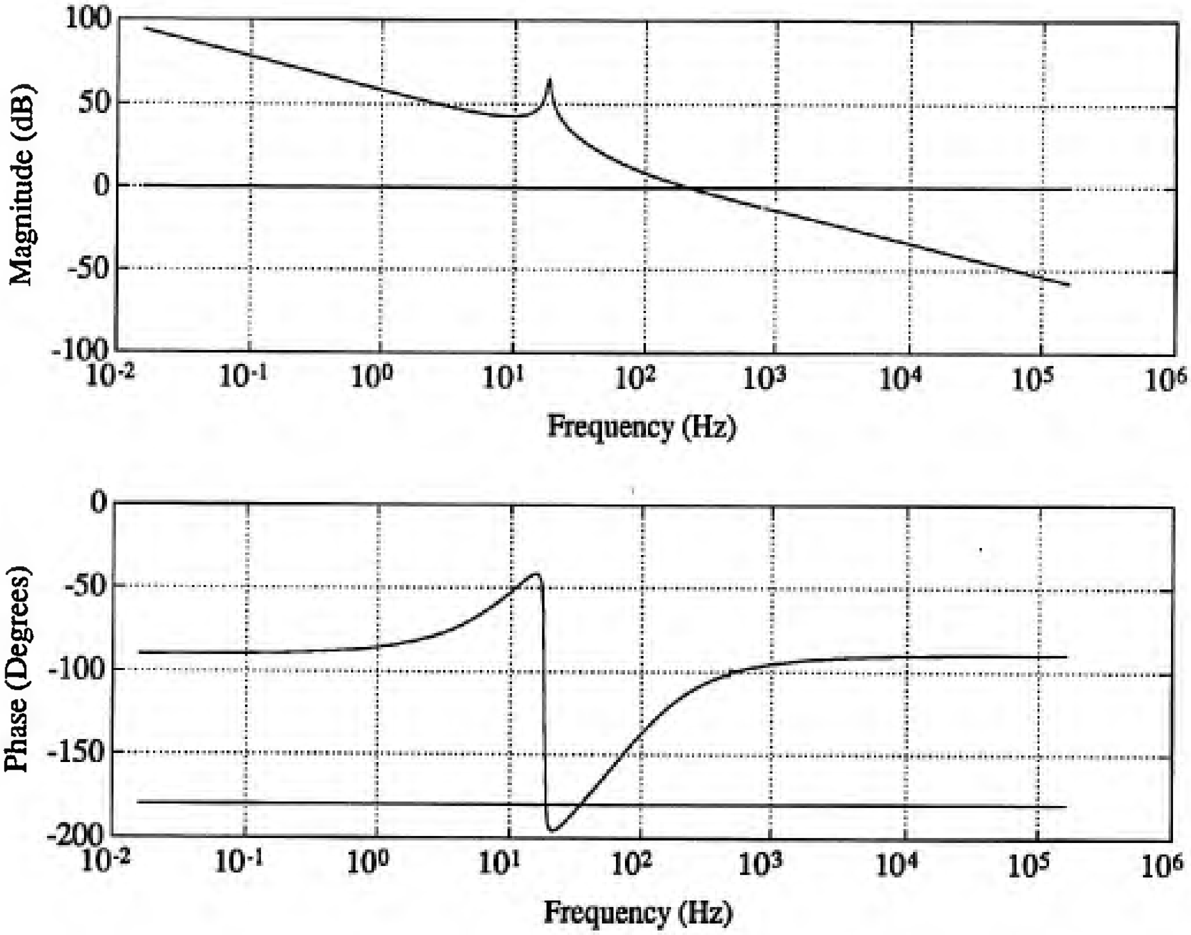

Figure 3.38: Forward Loop Frequency Response: Case 4

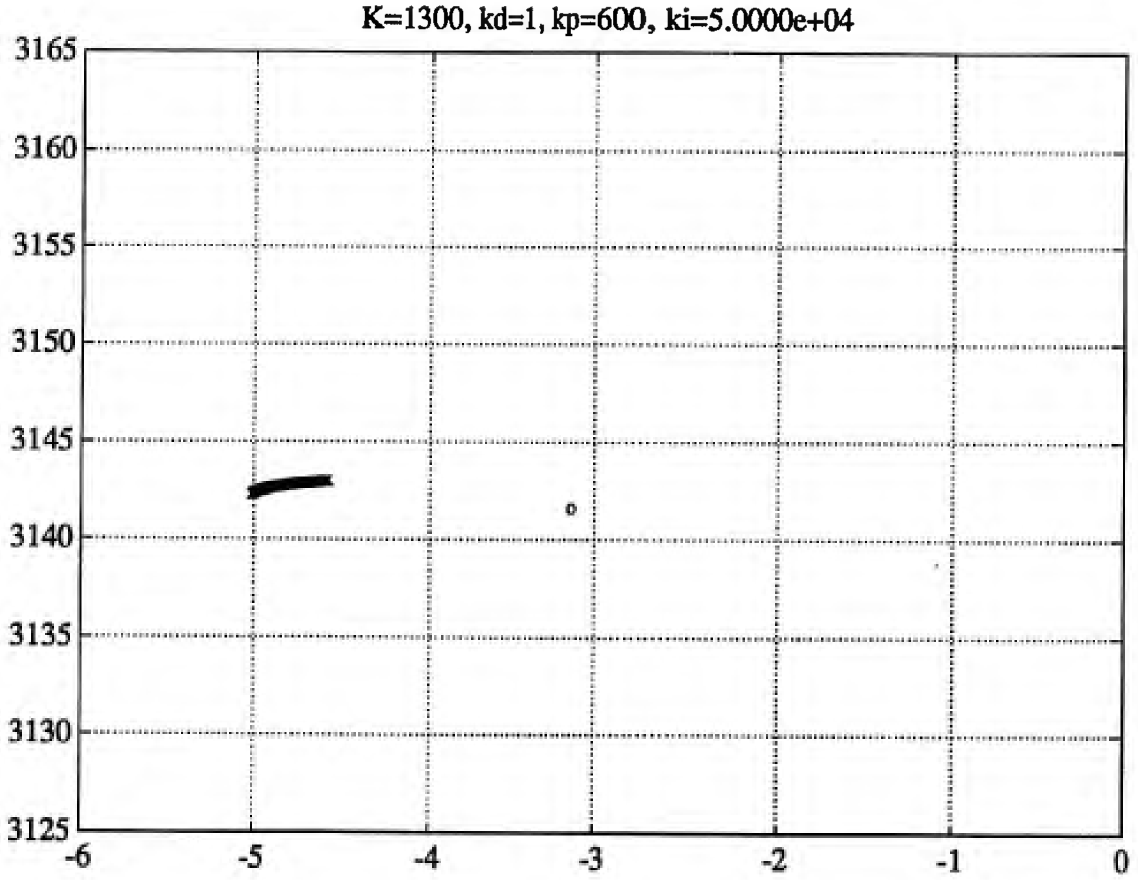

Figure 3.39: Loci of Closed Loop Roots (Magnified at Structural Flexibility): Case 4

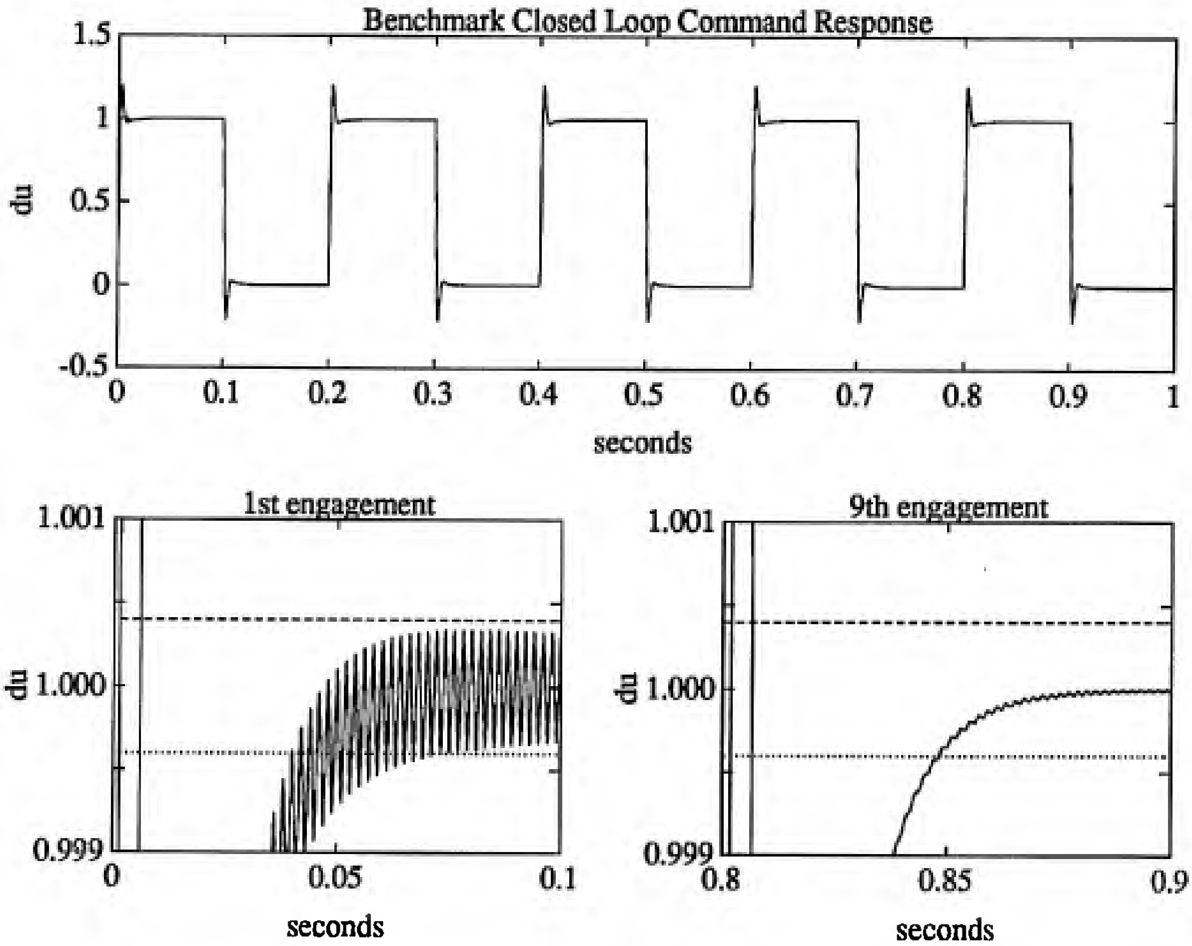

Figure 3.40: Command Response Curves: Case 4

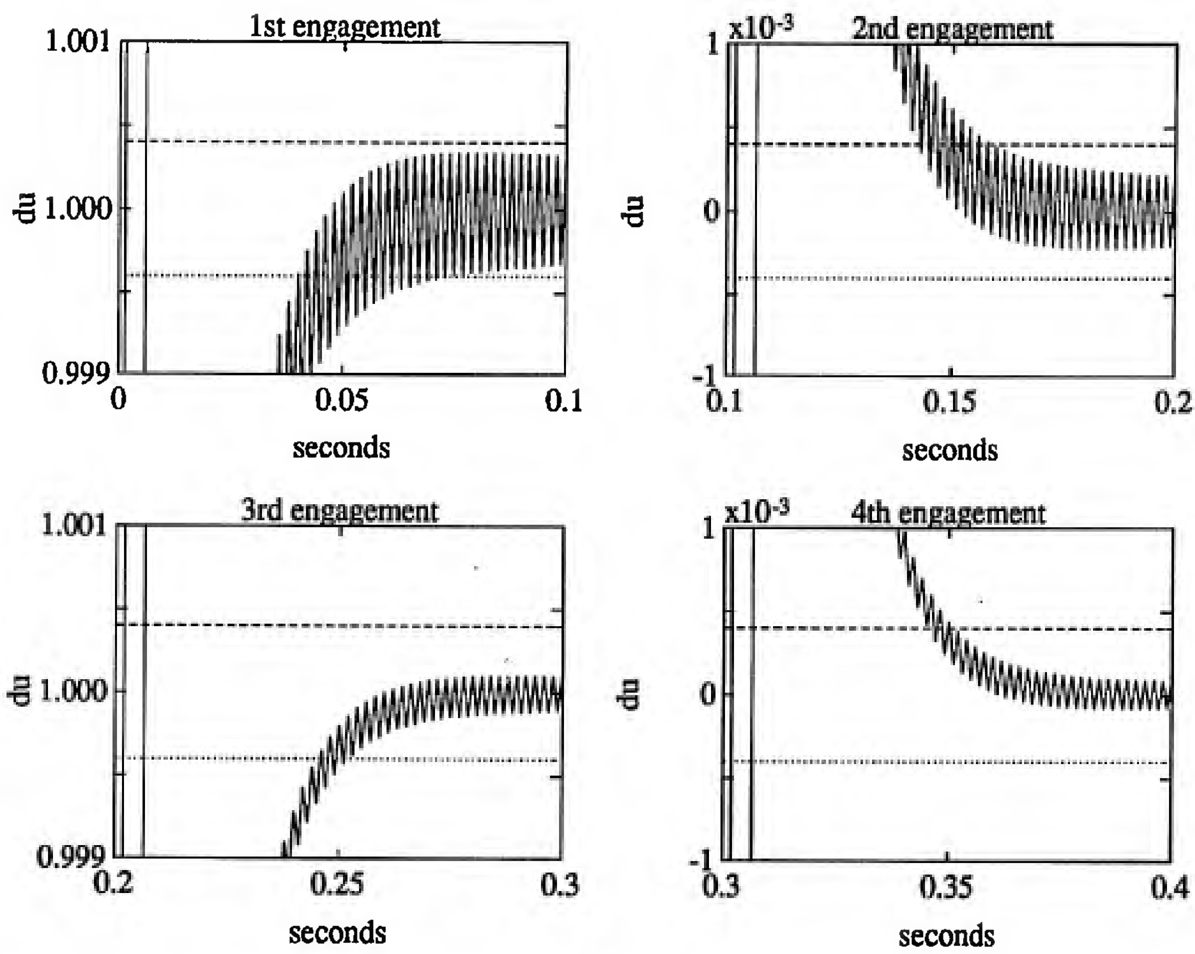

Figure 3.41: Command Response Curves: Case 4, First Through Fourth Engagements (clockwise from top left)

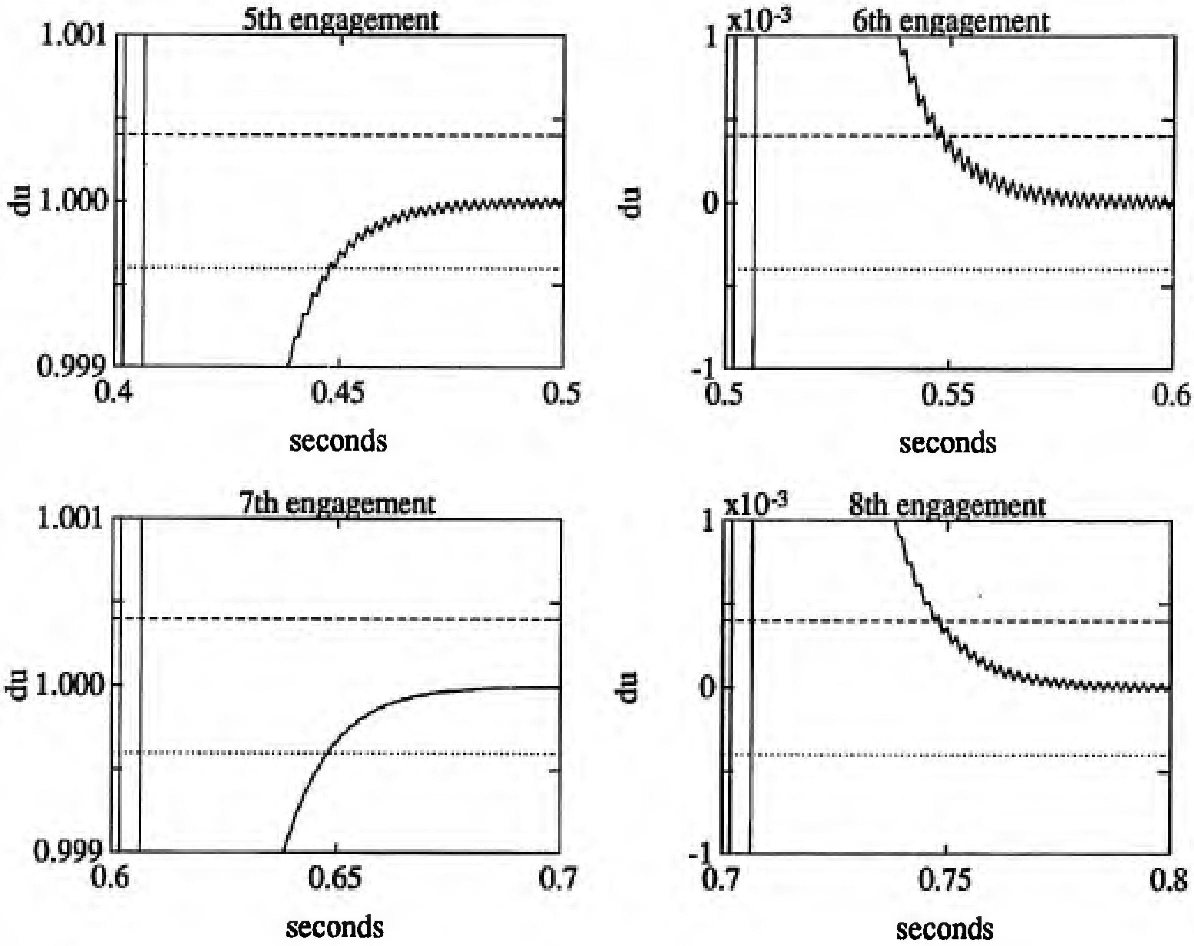

Figure 3.42: Command Response Curves: Case 4, Fifth Through Eighth Engagements (clockwise from top left)

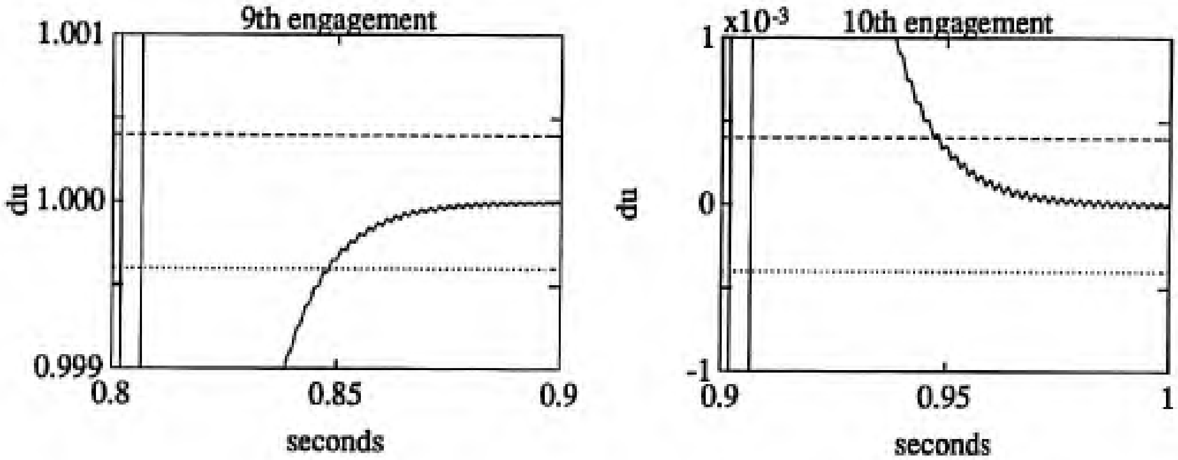

Figure 3.43: Command Response Curves: Case 4, Ninth (left) and Tenth (right) Engagements

3.5 *Summary of Findings*

We have introduced the concept of bicollocation with regard to the control of reaction actuators attached to flexible support structures. We describe the differences between bicollocation, non-bicollation, classical collocation, and classical non-collocation.

We have developed a method of classifying structural flexibility for the single-mode reaction actuator model. This method is particularly useful for sparse modal systems with wide separation between the natural frequency of the reaction actuator and the support structure flexible modes. We have verified that both appendage and in-the-loop minimum phase modes can occur with bicollocated reaction actuator control that is collocated in the classical sense, unlike the rigid-body control problem where collocated control guarantees only appendage modes.

We have formulated a simple example demonstrating the control-structure-interaction phenomena for the reaction actuator control problem resembling the fast steering mirror control problem for the flexible optical system. This modified benchmark problem evaluates the control-structure-interaction phenomena with respect to support structure flexibility. Controller performance requirements were specified resembling the high bandwidth, high precision flexible optical system line-of-sight control problem. Command response and disturbance rejection requirements simulate small angle rapid retargeting and line-of-sight jitter stabilization.

Significant findings from the modified benchmark problem analysis include:

1) The presence and degree of the control-structure-interaction phenomena is a function of the inertial coupling between the reaction actuator and the flexible support structure.

2) 'Rigidly supported' bicollocated reaction actuator controller designs applied to flexible structures will cause significant control-structure-interaction phenomena including severe performance degradation and possible closed loop instability.

3) Support structure in-the-loop minimum phase modes with frequencies below the reaction actuator natural frequency are gain stabilized modes. Very light modal damping and/or high loop gain may destabilize these modes.

4) Support structure appendage modes with frequencies between the reaction actuator natural frequency and the control loop crossover frequency are phase stabilized modes. Unmodeled sensor dynamics, noise attenuation filters, or anti-aliasing filters

may destabilize these modes.

5) Support structure appendage modes with frequencies greater than the control loop crossover frequency are both gain and phase stabilized modes and can severly degrade closed-loop performance.

6) Support structure flexibility adversely effects the ability of the reaction actuator control loop to reject force disturbances.

Single-mode analysis using the modified benchmark problem model has given significant insight into the type and severity of control-structure-interaction phenomena present in reaction actuator control loops mounted on flexible support structure. In the next chapter we analyze the multi-mode problem in the context of line-of-sight control on flexible optical systems.

Chapter 4

HIGH BANDWIDTH HIGH PRECISION CONTROL OF A MULTIMODE FLEXIBLE OPTICAL SYSTEM

4.1 Overview

In chapter 3 we discussed the control-structure-interaction phenomena associated with high bandwidth high precision control of a reaction actuator mounted to a single-mode flexible structure. We discovered CSI phenomena ranging from instabilities to performance degradation depending upon support structure flexibility. In this chapter we will extend the single-mode analyses to the multimode flexible optical system model developed in chapter 2. The controller performance for the modified benchmark problem specified in chapter 3 will be the same for the flexible optical system. In this chapter the reaction actuator will be referred to as the reaction steering mirror or simply the mirror.

4.2 Control-Structure-Interaction Terminology and Parameters Applicable to the Multimode Flexible Optical System

The type of control-structure interaction and the degree to which stability and performance are affected are functions of the inertial and elastic coupling between the steering mirror and the flexible support structure and the location of the steering mirror natural frequency with respect to the flexible support structure natural frequencies. If we assume the relative location of natural frequencies of both the steering mirror and the flexible support structure is predetermined we can show directly the relationship between inertial and elastic coupling and control-structure-interaction. For comparison purposes the inertial and elastic coupling between the steering mirror and the support structure is varied by holding the steering mirror natural frequency constant while varying the mirror inertia. Consequently as mirror inertia increases, so does mirror stiffness. The steering mirror inertia is varied from small to large values with respect to the local support structure inertia at the mirror attachment or reference point J_{ref}. As mirror inertia and stiffness increase with respect to support structure inertia and stiffness, inertial and elastic coupling increase. Increasing mirror inertia and stiffness while holding it's natural frequency constant simulates the case where all physical and dynamical characteristics of the mirror are fixed and the support structure inertia and stiffness are uniformly decreased. We can then assertain the CSI impact due to making the support structure lighter and less stiff.

Before proceeding, we will define five parameters: mirror inertia, reference inertia, modal inertia, modal reaction inertia and effective modal reaction inertia. In these definitions, the modal matrix ϕ is normalized to the system mass matrix M such that

$$\phi^T M \phi = I \tag{4.1}$$

giving

$$\phi^T K \phi = \mathrm{diag}(\omega_k^2) \tag{4.2}$$

where K is the system stiffness matrix and ω_k is the vector of natural frequencies. The pair $\{\phi_k, \omega_k\}$ represent the coupled system with both steering mirror and flexible support structure dynamics. The pair $\{\tilde{\phi}_k, \tilde{\omega}_k\}$ represent only the flexible support structure dynamics.

Mirror inertia J_m is simply the inertia of the steering mirror and can be determined from the mass normalized modal matrix ϕ as follows

$$J_m = \frac{1}{\sum\limits_{k=1}^{n} \phi_{ik}^2} \tag{4.3}$$

where the inertial mirror angle θ_m is the i^{th} system degree-of-freedom. If θ_m is not a system degree-of-freedom explicitly, but instead the *relative* mirror angle θ_{mref} is the i^{th} system degree-of-freedom such that $\theta_{mref} = \theta_m - \theta_{ref}$ with θ_{ref} being the angle at the support structure attachment point and the h^{th} system degree-of-freedom, then the mirror inertia is determined by

$$J_m = \frac{1}{\sum\limits_{k=1}^{n} [\phi_{ik} + \phi_{hk}]^2} \tag{4.4}$$

The support structure attachment point is the point on the support structure where the steering mirror is mounted. The **reference inertia** J_{ref} is an approximation of the inertia at a specific location on the flexible structure and can be viewed as a local resistance to inertial (total) mirror torque. J_{ref} can also be determined from the mass normalized modal matrix as follows

$$J_{ref} = \frac{1}{\sum_{k=1}^{n} \phi_{hk}^2} \tag{4.5}$$

where the support structure attachment point angle θ_{ref} is degree-of-freedom h. For a uniform structure, J_{ref} is constant at each common degree-of-freedom (i.e. rotational degrees-of-freedom will share the same value of local inertia and translational degrees-of-freedom will share the same value of local mass). Both mirror inertia and reference inertia are physical quantities and can be physically related to hardware [1].

Modal reaction inertia J_k, on the other hand, is a 'perceived' inertia and is not in general related to a physical inertia. The modal reaction inertia is a function of mirror dynamics as well as both sensor and actuator locations. Since we are dealing with reaction actuators, it is also a function of the 'action' and 'reaction' locations. If we have a sensor at degree-of-freedom j and an actuator acting on degree-of-freedom i and reacting against degree-of-freedom h, the modal reaction inertia is defined as

$$J_k = \frac{1}{\phi_{jk}(\phi_{ik} - \phi_{hk})} \tag{4.6}$$

Large J_k suggests that either the k^{th} mode is unobservable and the sensor at or near a k^{th} mode node or undisturbable and mirror does not have enough inertia to disturb the k^{th} mode. Of course, both of these possibilities could occur simultaneously. Note that $J_k = \infty$ for rigid-body modes which means that the system exhibits infinite resistance to rigid body motion. The system cannot be moved as a rigid body using reaction actuators. Modes that are dominant in off-axis degrees-of-freedom are also characterized by large J_k. Conversely, if J_k is small, the k_{th} mode is more disturbable

[1] It is common for a reaction actuator to react against the structure at the same point (degree-of-freedom) as it is referenced to the structure. If such an arrangement is not possible (i.e. the reference and reaction degrees-of-freedom differ), the reference inertia will no longer have any physical relationship to the system.

by total mirror inertial torque. If a mode is disturbable by the mirror then increasing mirror inertia equates to increasing the pole-zero separation in that mode. As we concluded in chapter 3, increased pole-zero separation is the mechanism by which CSI performance degradation and instabilities occur.

Effective modal reaction inertia $\bar{J}_k$ is defined by normalizing the modal reaction inertia with the mirror inertia

$$\bar{J}_k = \frac{J_m}{J_k} \tag{4.7}$$

where

$$\sum_{k=1}^{n} \bar{J}_k = 1.000 \tag{4.8}$$

Effective modal reaction inertia is a normalized measure of the mirror's effectiveness in disturbing a particular mode[2]. Effective modal reaction inertia is useful in comparing modal disturbability of systems with different steering mirror characteristics. It will also be shown that effective modal reaction inertia is a reasonable prediction of closed-loop inertial mirror angle spectral density for systems with small mirror inertia.

Modal inertia $\tilde{J}_k$ is a measure of the flexible structure's resistance to external torques. Modal inertia is similar to modal reaction inertia applied to the uncoupled system. Instead of being a measure of modal participation from reaction actuation, modal inertia is a measure of modal participation from non-reaction actuation. Consequently, rigid-body inertia can be determined from the mass normalized modal matrix associated with the flexible support structure dynamics $\tilde{\phi}$. If we have a sensor at degree-of-freedom j and an non-reaction actuator at degree-of-freedom i, the modal inertia is defined as

$$\tilde{J}_k = \frac{1}{\tilde{\phi}_{jk}\tilde{\phi}_{ik}} \tag{4.9}$$

Modal inertia can also be thought of as a measure of modal susceptibility to pole-zero separation ultimately brought about by increases in reaction actuator inertia. It will be shown that modal inertia is also useful in identifying salient features of the coupled system dynamics.

---

[2] Effective modal reaction inertia may be more properly termed effective reaction mirror inertia since we are dividing mirror inertia by modal reaction inertia. Both definitions are valid in communicating modal disturbability.

4.3 Multimode Flexible Optical System Dynamics

In this section, the transfer function from mirror torque input to inertial mirror angle for the mirror attached to a flexible support structure will be developed. Damping will be assumed zero for simplicity. We will develop transfer functions from two different approaches in an attempt to highlight the usefulness of the parameters defined in the previous section.

Using equation 3.6 with the $n+1$ degree-of-freedom coupled system represented by the pair $\{\phi_k, \omega_k\}$ we have

$$\frac{\Theta_m(s)}{T_m(s)} = \sum_{k=1}^{n+1} \frac{1}{J_k(s^2+\omega_k^2)} \tag{4.10}$$

where $T_m(s)$ is better described as $T_{m20}(s)$ and the modal reaction inertia J_k is defined as

$$J_k = \frac{1}{\phi_{\theta_m k}(\phi_{\theta_m k} - \phi_{\theta_{20} k})} \tag{4.11}$$

Equation 4.10 is an exact residues transfer function of the steering mirror supported by and coupled to a flexible structure. By examining the transfer function in this form we can see directly how each of the $n+1$ modes participate in the inertial mirror response to a reaction torque input. Note that as mirror inertia increases, pole-zero separation occurs in only the disturbable modes. We can use the effective modal reaction inertia $\bar{J}_k$ to predict the degree to which disturbable mode pole-zero separation will occur. $\bar{J}_k$ will also be shown to be a reasonable measure of the resulting line-of-sight jitter spectral density for systems with small mirror inertias.

Figures 4.1–4.8 show the relationship between $\bar{J}_k$ and β_k for the 62 degree-of-freedom flexible optical system where β_k is defined by equation 2.55. The mirror mass was held constant as mirror inertia increased, consequently the system zeros remain fixed. When pole-zero separation occurs, the pole either increases or decreases away from the fixed zero depending on the *type* of structural flexibility (i.e. in-the-loop or appendage). Structural flexibility type also depends on the location of the mirror natural frequency. In each successive figure the mirror natural frequency in fixed at 20 Hz while mirror inertia is increased from 0.002% of total support structure inertia J_{truss} (about 45% J_{ref}) to 20% of J_{truss} (about 4500 times J_{ref}). In these figures, the first mode is the rigid-body mode with zero effective modal reaction inertia. The fifth mode is the mirror mode, at least in the figures representing small inertial and elastic coupling. When the mirror inertia is small with respect to support structure inertia, or more precisely, the local reference inertia J_{ref}, effective modal reaction inertia $\bar{J}_k$ is nearly unity. This means that the mirror is effective in disturbing (controlling) only that particular mode. As mirror inertia increases, the magnitude of $\bar{J}_k$ increases in other disturbable modes. As $\bar{J}_k$ increases its magnitude at any individual mode decreases such that equation 4.8 holds. Note that because mirror natural frequency is held constant increasing mirror inertia results in increasing mirror stiffness which eventually dominates coupled system stiffness and $\bar{J}_{n+1}$ eventually goes to unity. In the limit, as mirror inertia and stiffness go to infinity, the entire system goes to a pinned-fixed configuration. This appears to have the effect of reducing $\bar{J}_k$ and therefore the system disturbability for the first n system modes. However, this apparent reduction in $\bar{J}_k$ for $k = 1 \ldots n$ is merely a consequence of our normalization procedure and does not reflect a decrease in system disturbability. In fact, system instability can occur long before $\bar{J}_{n+1}$ reaches unity.

To summarize, we have found that modal inertia $\tilde{J}_k$ is a good measure of the uncoupled flexible support structure's susceptibility to modal disturbability. We can, therefore, use modal inertia as a design variable when trying to design a flexible structure that will support some type of reaction actuator operating in a closed loop. Different materials or structural configurations will invariably affect the magnitude of the modal inertias and therefore modal disturbability.

Modal reaction inertia J_k was shown to be a measure of pole-zero separation within the coupled system. As mirror inertia and stiffness increased, so did modal reaction inertia with respect to the fixed flexible support structure. As modal inertia increased, pole-zero separation increased at disturbable modes. Of course, pole-zero separation is the mechanism by which control-structure-interaction adversely effects ones controller. Modal reaction inertia, therefore, can also be used as a design variable within a combined controls-structures design methodology. Unlike modal inertia, which is a function only of the support structure dynamics, modal reaction inertia accounts for flexible support structure dynamics, reaction actuator dynamics, and the coupling between the two.

Modal reaction inertia can also be used as a first cut measure of closed-loop behavior of uncompensated high frequency flexible modes. If a high frequency flexible mode is uncompensated, we can assume that its open and closed loop pole-zero separations are approximately equal. Knowing the open loop pole-zero separation via the modal reaction inertia, we can simply apply knowledge regarding the location of the particular flexible mode with respect to the compensated loop (i.e. take account of loop shaping, roll-offs, etc.) and predict the resulting closed loop contribution due to that mode.

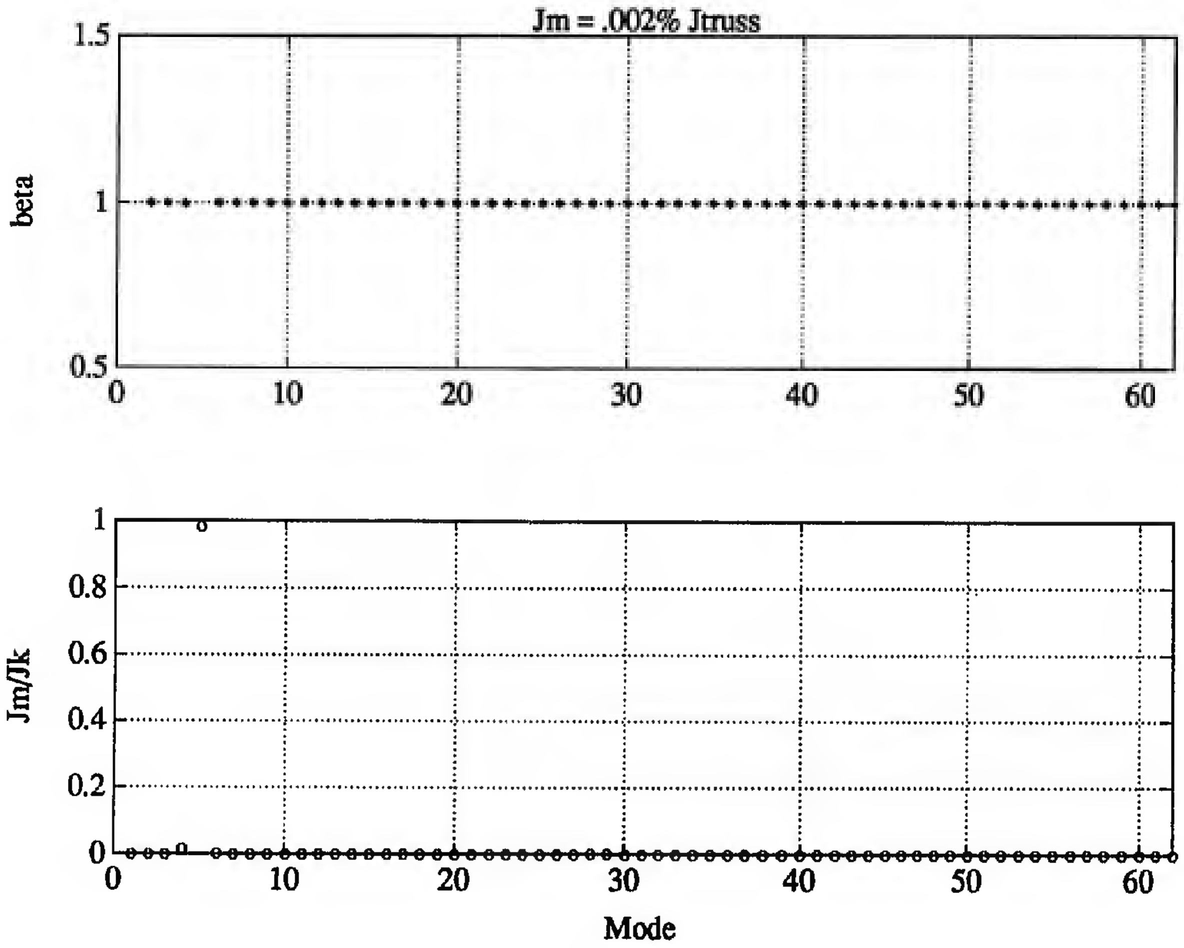

Figure 4.1: Pole-Zero Separation vs. Effective Modal Reaction Inertia: $J_m = 0.002\%$ J_{truss}

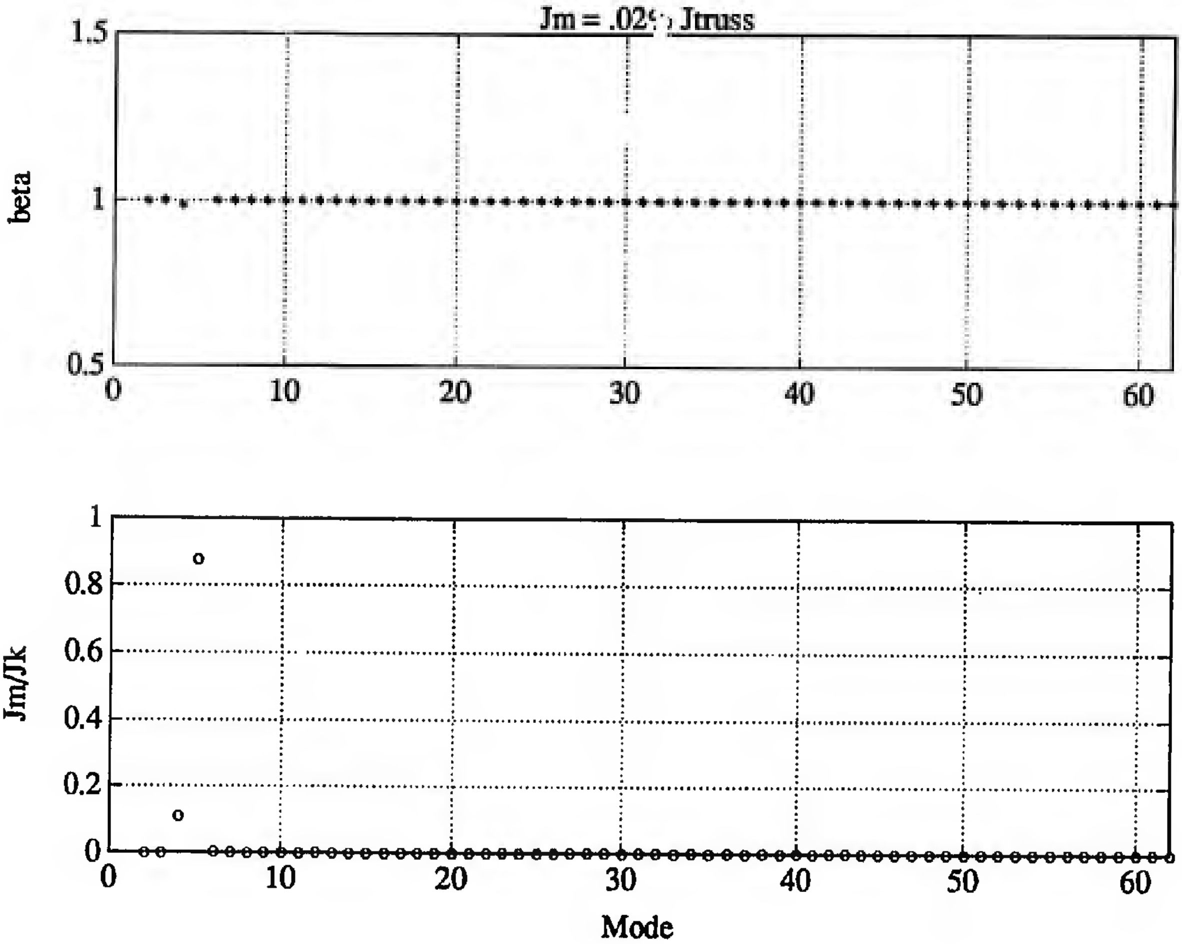

Figure 4.2: Pole-Zero Separation vs. Effective Modal Reaction Inertia: $J_m = 0.02\%$ J_{truss}

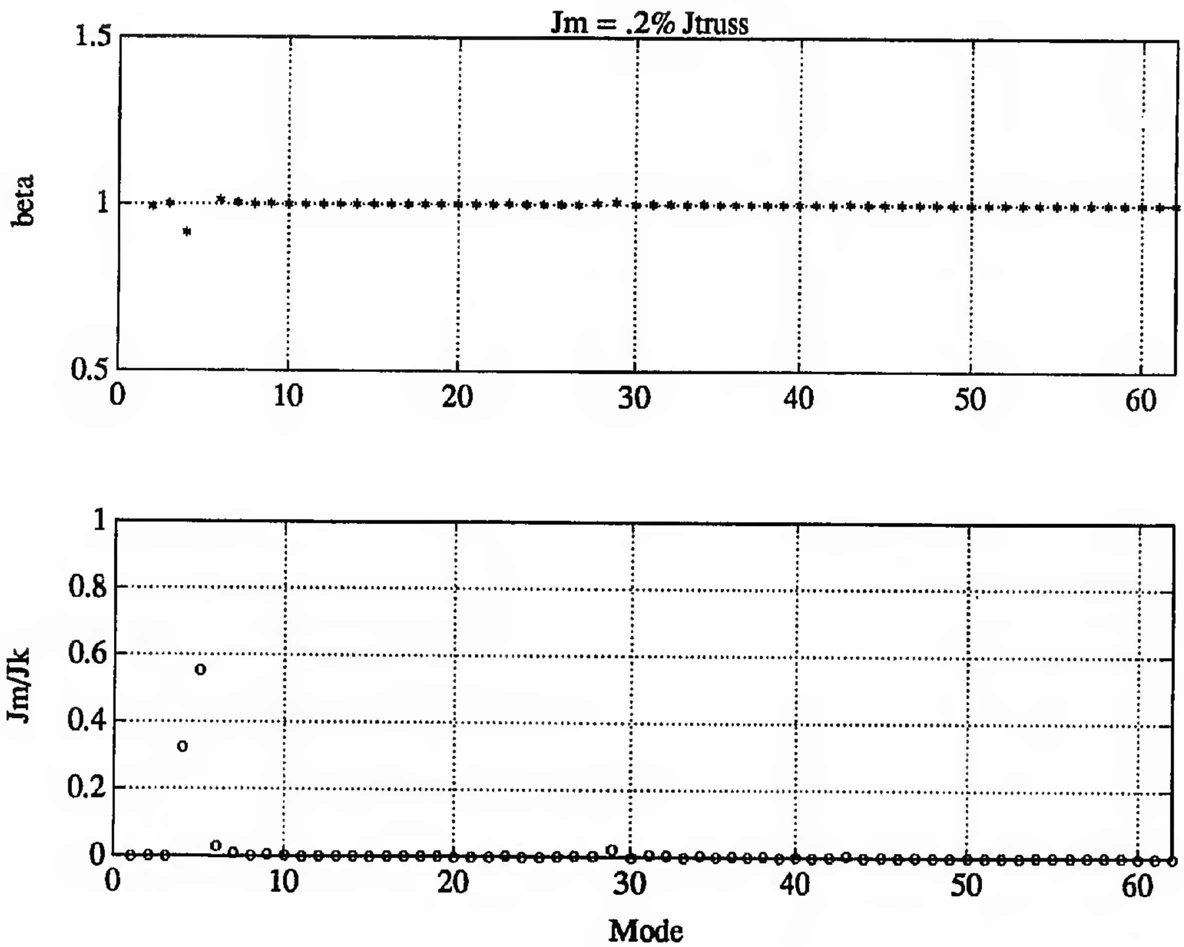

Figure 4.3: Pole-Zero Separation vs. Effective Modal Reaction Inertia: $J_m = 0.2\%$ J_{truss}

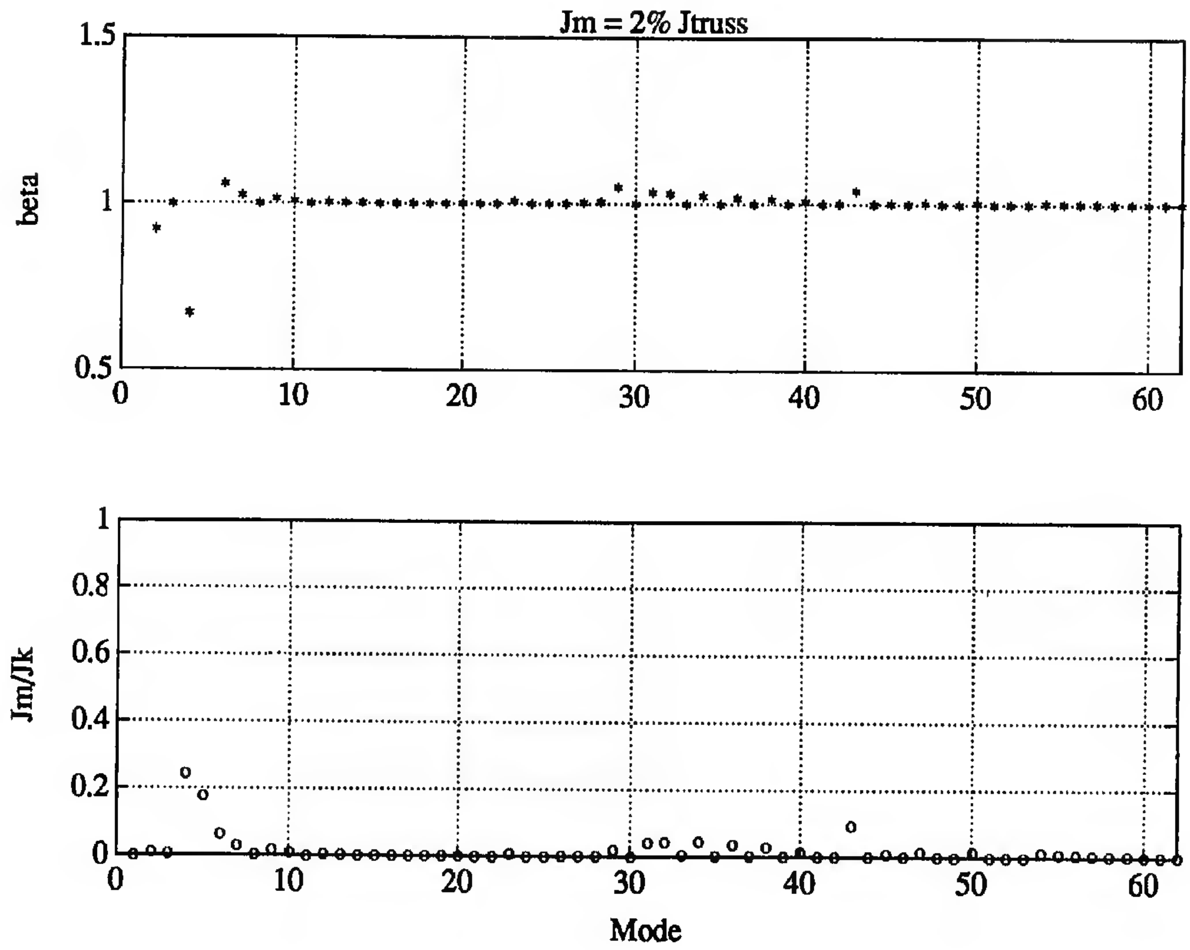

Figure 4.4: Pole-Zero Separation vs. Effective Modal Reaction Inertia: $J_m = 2\%$ J_{truss}

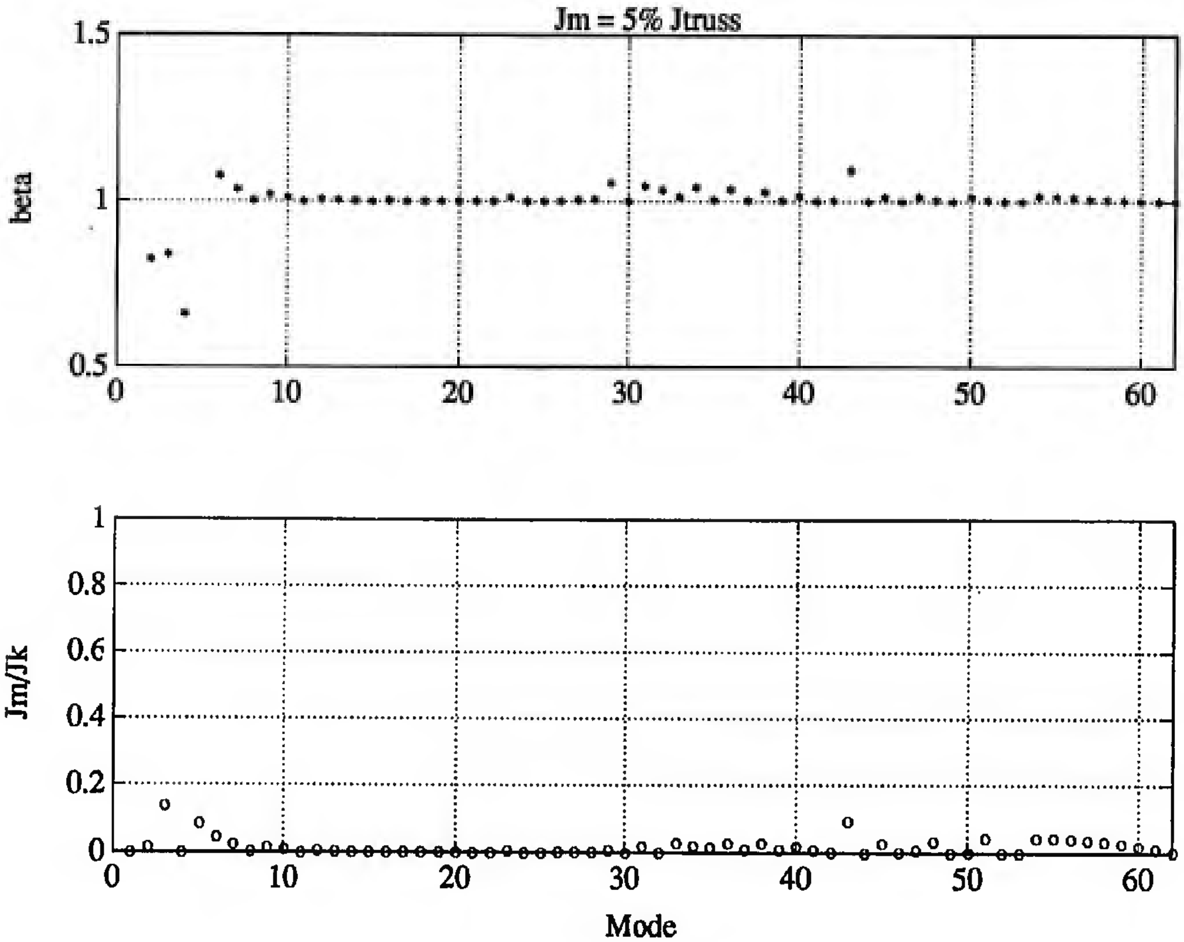

Figure 4.5: Pole-Zero Separation vs. Effective Modal Reaction Inertia: $J_m = 5\%$ J_{truss}

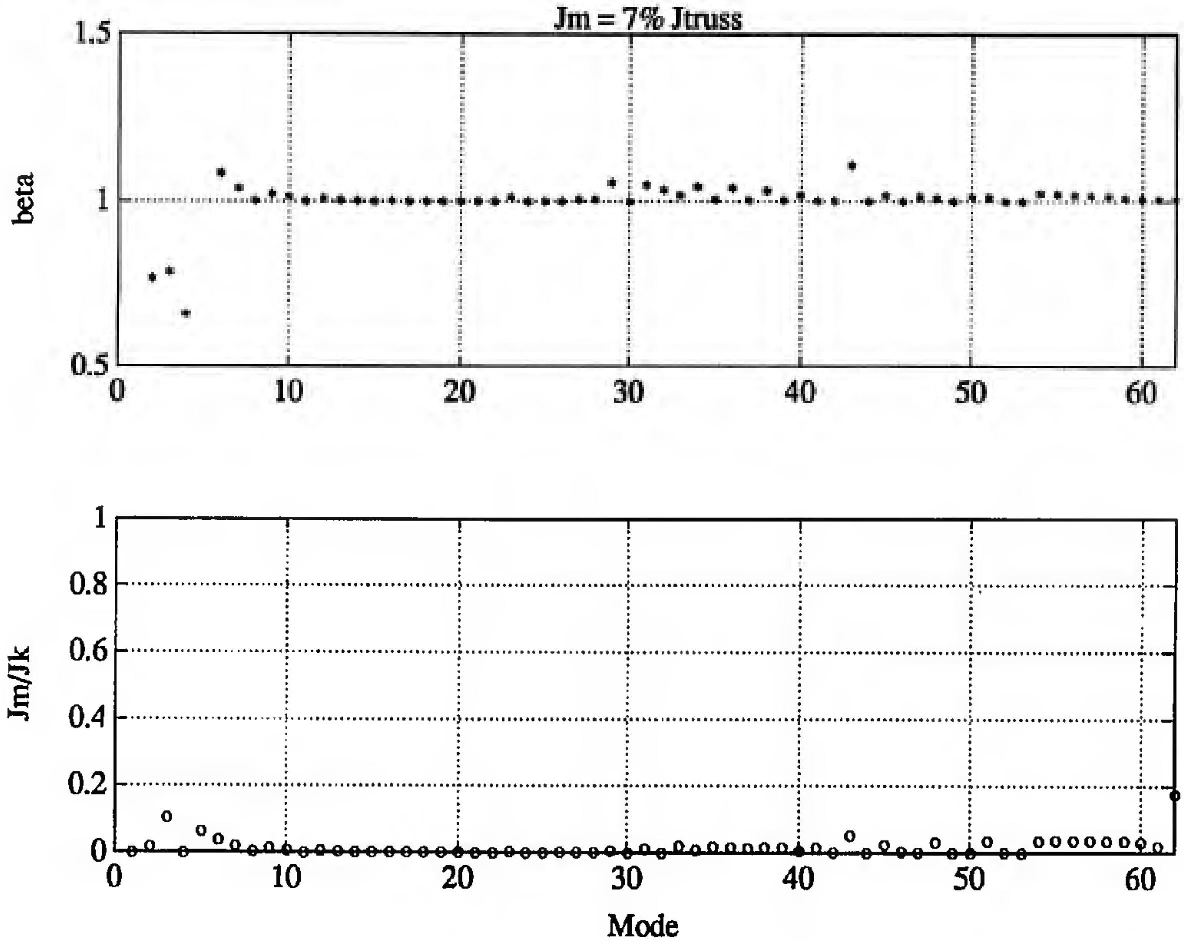

Figure 4.6: Pole-Zero Separation vs. Effective Modal Reaction Inertia: J_m = 7% J_{truss}

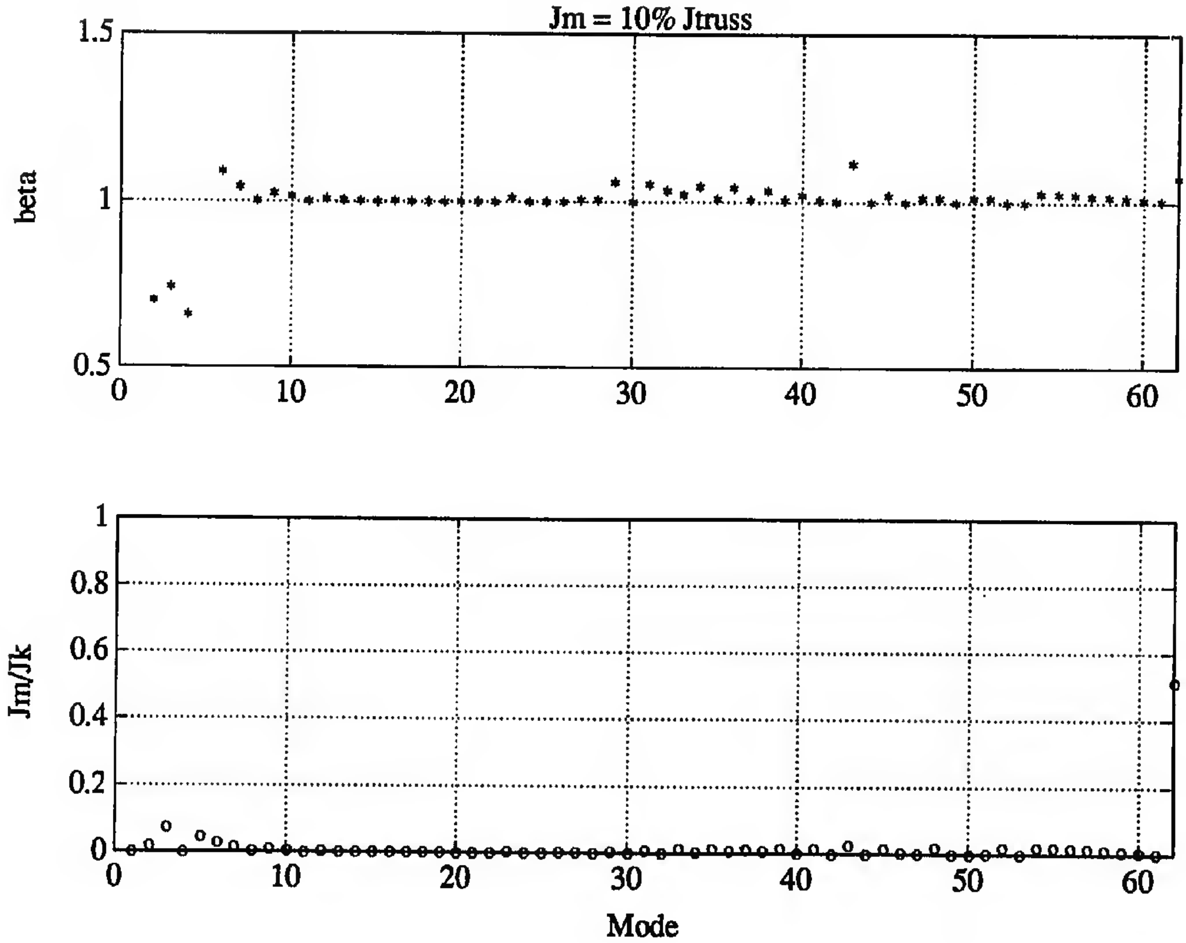

Figure 4.7: Pole-Zero Separation vs. Effective Modal Reaction Inertia: J_m = 10% J_{truss}

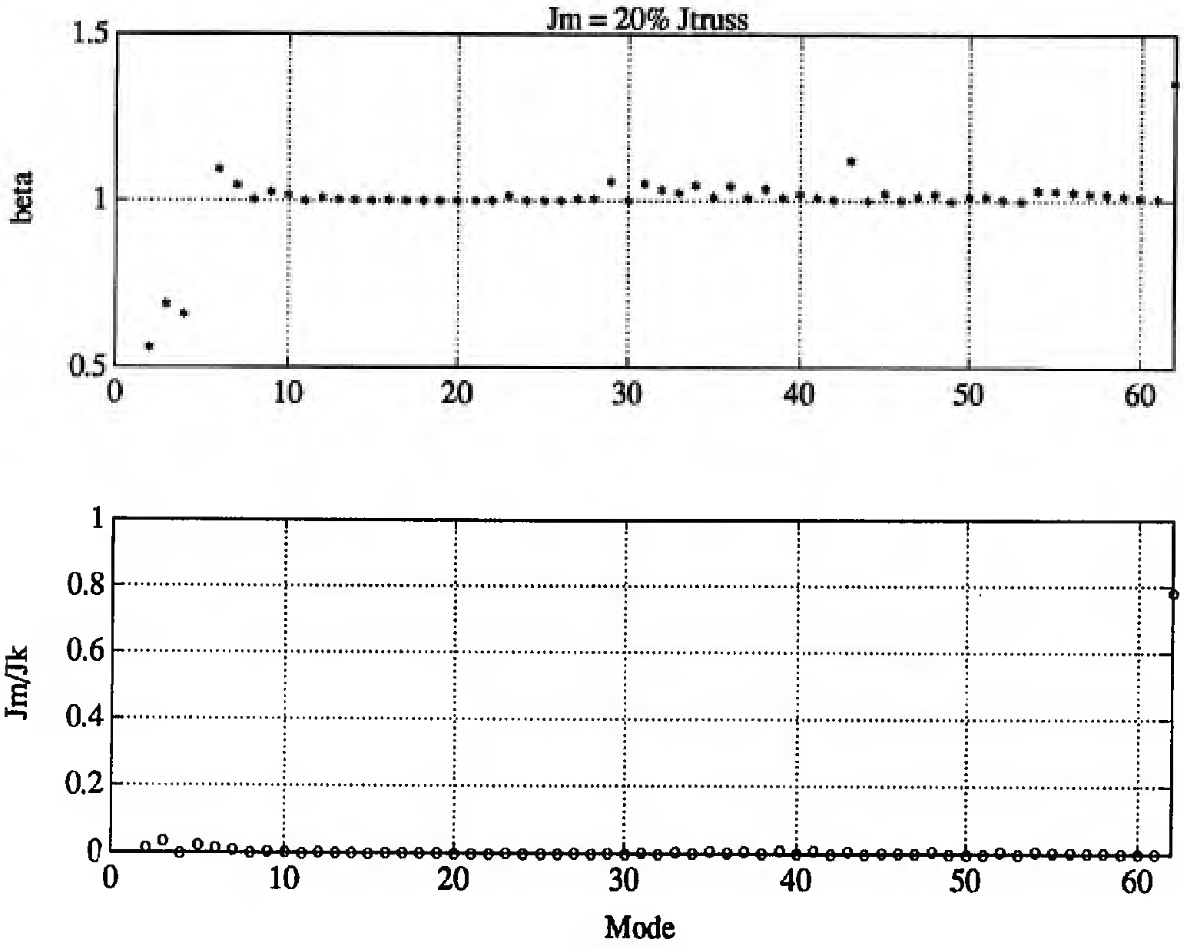

Figure 4.8: Pole-Zero Separation vs. Effective Modal Reaction Inertia: J_m = 20% J_{truss}

Thus increasing mirror inertia increases modal disturbability and pole-zero separation in an increasing number of modes. The figures also show that for modes below the mirror natural frequency (20 Hz), the poles decrease in frequency while for modes above the mirror natural frequency, the poles increase in frequency. By examining the mirror transfer function in the form of equation 4.10, we gain an understanding of system behavior in terms of its effective modal reaction inertia.

By deriving the same mirror transfer function from another approach, we will see clearly why the system zeros remained fixed even as both inertial and elastic coupling between the mirror and structure increase. The equation of motion for the steering mirror coupled with the flexible support structure is

$$J_m \ddot{\theta}_m(t) = t_m(t) - k_m[\theta_m(t) - \theta_{ref}(t)] \tag{4.12}$$

where k_m is the mirror spring constant, t_m is the applied mirror torque, and $\theta_{ref}(t)$ is the angle at the structure attachment point. In the Laplace domain equation 4.12 can be written

$$\Theta_m(s)[J_m s^2 + k_m] = T_m(s) + k_m \Theta_{ref}(s) \tag{4.13}$$

Using equation 3.1, the n degree-of-freedom uncoupled flexible structure can be described as

$$\Theta_{ref}(s) = \left[\sum_{k=1}^{n} \frac{\tilde{\phi}_{theta_{ref}k} \tilde{\phi}_{theta_{reac}k}}{s^2 + \tilde{\omega}_k^2} \right] T_{reac}(s) \tag{4.14}$$

If we assume the mirror is referenced to the structure at the same point at which it reacts against the structure (i.e. bicollocated control, ref=reac or r=h), then

$$\Theta_{ref}(s) = \left[\sum_{k=1}^{n} \frac{\tilde{\phi}^2_{theta_{ref}k}}{s^2 + \tilde{\omega}_k^2} \right] T_{ref}(s) \tag{4.15}$$

where the modal inertia $\tilde{J}_k$ is defined as

$$\tilde{J}_k = \frac{1}{\tilde{\phi}^2_{theta_{ref}k}} \tag{4.16}$$

The mirror and flexible structure are coupled by requiring the total mirror inertia to react into the reference degree-of-freedom

$$T_{ref}(s) = -J_m s^2 \Theta_m(s) \tag{4.17}$$

Substituting equations 4.17 and 4.14 into equation 4.13 we get

$$\frac{\Theta_m(s)}{T_m(s)} = \frac{1}{J_m s^2 + k_m + k_m J_m \left[\sum_{k=1}^{n} \frac{1}{\tilde{J}_k(s^2 + \tilde{\omega}_k^2)}\right] s^2} \tag{4.18}$$

Rewriting equation 4.18 we can obtain

$$\frac{\Theta_m(s)}{T_m(s)} = \frac{\frac{1}{J_m}\left[\prod_{k=1}^{n} \tilde{J}_k(s^2 + \tilde{\omega}_k^2)\right]}{[s^2 + \omega_m^2]\left[\prod_{k=1}^{n} \tilde{J}_k(s^2 + \tilde{\omega}_k^2)\right] + s^2 k_m \sum_{p=1}^{n}\left[\prod_{k=1}^{n} \tilde{J}_k(s^2 + \tilde{\omega}_k^2)\right]_{p \neq k}} \tag{4.19}$$

Equation 4.19 is the transfer function between mirror torque and inertial mirror angle for a bicollocated reaction mirror. The transfer function describes a bicollocated reaction actuator because the torque acts onto the mirror inertia while the sensor senses the inertial mirror angle (j=i) and the torque reacts against the reference degree-of-freedom (ref=react or r=h). There are several interesting features of this bicollocated mirror transfer function. First, notice that the system zeros are the poles of the uncoupled flexible support structure transfer function of equation 4.15 and independent of mirror stiffness or inertia. Assuming our uncoupled flexible structure is asymptotically stable, herein lies the guarantee for strictly minimum phase transfer function zeros for the bicollocated case. We also notice that as modal inertia $\tilde{J}_k$ goes to zero for every mode k, the mirror transfer function simplifies to its 'rigidly supported' form. Figure 4.9 describes the susceptibility of each of the 61 uncoupled flexible support structure modes to pole-zero separation. In this figure, the reciprocal of the modal inertia $1/\tilde{J}_k$ is plotted for each system mode. Modes associated with low values of the reciprocal have high modal inertia and are not likely to be disturbed. Equation 4.19 can be further reduced to

$$\frac{\Theta_m(s)}{T_m(s)} = \frac{\frac{1}{J_m}\prod_{k=1}^{n}(s^2 + \tilde{\omega}_k^2)}{\prod_{k=1}^{n+1}(s^2 + \omega_k^2)} \tag{4.20}$$

which reveals the simple form of the transfer function where the coupled system zeros are the uncoupled system poles.

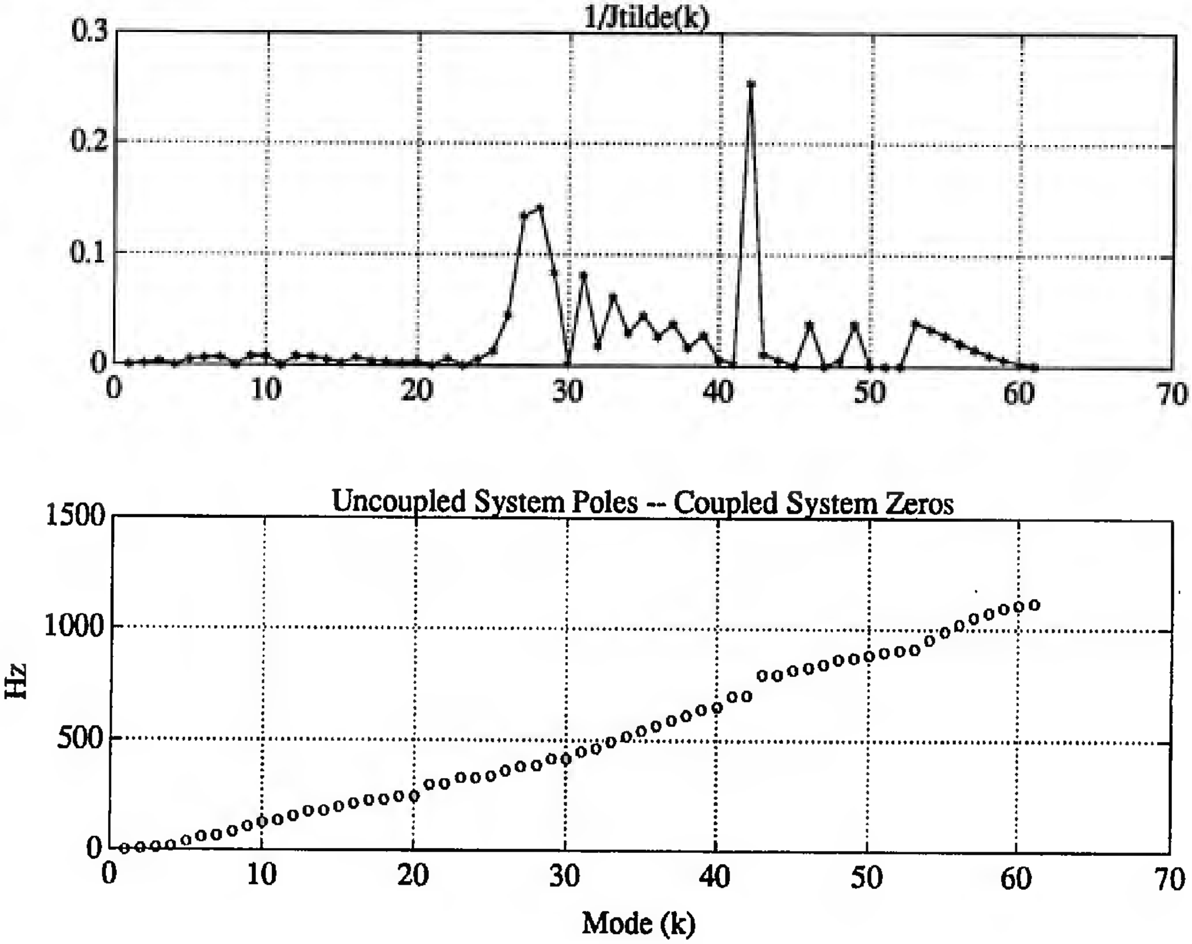

Figure 4.9: Modal Susceptibility to Pole-Zero Separation for the Uncoupled Flexible Support Structure

Using the same type formulation, we can derive the transfer function for the non-bicollocated reaction mirror. To do so, we first recognize that equation 4.17 describes the total opposing torque from the reaction mirror into the flexible structure. To allow for non-bicollocation, we must rewrite equation 4.14 to account for the fact that the reaction torque enters the structure at other than the reference degree-of-freedom.

$$\Theta_{ref}(s) = \left[\sum_{k=1}^{n} \frac{\tilde{\phi}_{theta_{ref}k}\tilde{\phi}_{theta_{ref}k}}{s^2+\tilde{\omega}_k^2}\right] T_{ref}(s) + \left[\sum_{k=1}^{n} \frac{\tilde{\phi}_{theta_{ref}k}\tilde{\phi}_{theta_{reac}k}}{s^2+\tilde{\omega}_k^2}\right] T_{reac}(s) \quad (4.21)$$

where, for the undamped case, $T_{reac}(s) = -T_m(s)$ and $T_{ref} = k_m(\Theta_m(s) - \Theta_m(s))$. Substituting these expressions into equation 4.21 yields

$$\frac{\Theta_m(s)}{T_m(s)} = \frac{\frac{1}{J_m}\left\{\prod_{k=1}^{n} \tilde{J}_{rrk}(s^2+\tilde{\omega}_k^2) + k_m\left[\Sigma\Pi_{rrk} - \prod_{k=1}^{n}\left(\frac{\tilde{J}_{rrk}}{\tilde{J}_{rhk}}\right)\Sigma\Pi_{rhk}\right]\right\}}{[s^2+\omega_m^2]\left[\prod_{k=1}^{n} \tilde{J}_{rrk}(s^2+\tilde{\omega}_k^2)\right] + s^2 k_m \sum_{p=1}^{n}\left[\prod_{k=1}^{n} \tilde{J}_{rrk}(s^2+\tilde{\omega}_k^2)\right]_{p\neq k}} \quad (4.22)$$

where

$$\tilde{J}_{rrk} = \frac{1}{\tilde{\phi}_{rk}\tilde{\phi}_{rk}} \quad (4.23)$$

$$\tilde{J}_{rhk} = \frac{1}{\tilde{\phi}_{rk}\tilde{\phi}_{hk}} \quad (4.24)$$

$$\Sigma\Pi_{rrk} = \sum_{p=1}^{n}\left[\prod_{k=1}^{n} \tilde{J}_{rrk}(s^2+\tilde{\omega}_k^2)\right]_{p\neq k} \quad (4.25)$$

$$\Sigma\Pi_{rhk} = \sum_{p=1}^{n}\left[\prod_{k=1}^{n} \tilde{J}_{rhk}(s^2+\tilde{\omega}_k^2)\right]_{p\neq k} \quad (4.26)$$

The non-bicollocated transfer function shown in equation 4.22 does not offer the same minimum phase zero guarantees as with the bicollocated transfer function of equation 4.21. When inertial and elastic coupling between the reaction mirror and the flexible support structure becomes significant, equation 4.22 will give nonminimum phase zeros. A sufficient condition for the presence of nonminimum phase zeros for a single-mode expansion of the first flexible mode is given as follows.

$$\tilde{\omega}_1^2 < k_m\left[\frac{1}{\tilde{J}_{rh1}} - \frac{1}{\tilde{J}_{rr1}}\right] \quad (4.27)$$

It is difficult to establish sufficient conditions for the presence of nonminimum phase zeros using equation 4.22 for any arbitrary mode k as the validity of such results depends upon the proper summation of modal inertias in the numerator. It is important to remember, however, that the single-mode expansion developed in chapter 3 (equation 3.11) is valid for both the bicollocated and non-bicollocated cases and can therefore with the appropriate assumptions can be used to predict the presence of nonminimum phase zeros in the non-bicollocated transfer function.

4.4 Line-of-Sight Control Using the Fast Steering Mirror

The strategy for examining the impact of CSI on stability and performance is similar to that of the modified benchmark problem of chapter 3. The key difference lies in the tradeoff parameters. The modified benchmark problem stability and performance studies were performed with a fixed mass ratio and varying single-mode flexibilities. Thus we were able to ascertain CSI effects as a function of flexible mode location. For the multimode flexible optical system, flexible modes already span a large frequency spectrum. CSI effects are therefore studied as a function of varying mass (inertia) ratio. To accomplish this, we will first design the steering mirror controller based upon the rigid support structure assumption. Because the performance requirements are similar as with the modified benchmark problem, the same proportional-integral-derivative control law will be assumed[3]. Loop gain is selected to obtain an open-loop crossover frequency of 230 Hz ($\omega_c = 230$ Hz) achieving the desired closed-loop bandwidth of 300 Hz ($\omega_b = 300$ Hz). The mirror and controller are then coupled to a reduced 7 degree-of-freedom flexible support structure model with the first seven elastic modes retained. Closed-loop stability and performance are evaluated as mirror inertia and stiffness increase in proportion with respect to those of the support structure.

Before proceeding with the closed-loop analysis we will examine the general form of the closed-loop undamped inertial mirror angle command response transfer function $\Theta_m(s)/\Theta_{m_c}(s)$. The closed-loop block diagram is shown in figure 4.10. The plant is described by equation 4.20 and the controller by $K(s) = KN_c(s)/D_c(s)$. Plant

[3] An aft-to-fore body disturbance source is considered for the multimode flexible optical system that was not considered for the modified benchmark problem.

disturbances f_d, f_h, m, and θ_d represent mirror cooling flow torque, aft-to-fore body disturbance torque, line-of-sight sensor measurement noise, and optical line-of-sight angular disturbance, respectively. The closed-loop transfer function is of the form

$$\frac{\Theta_m(s)}{\Theta_{m_c}(s)} = \frac{G(s)K(s)}{1+G(s)K(s)} \tag{4.28}$$

Substituting equation 4.20 into equation 4.28 we obtain

$$\frac{\Theta_m(s)}{\Theta_{m_c}(s)} = \frac{\frac{K}{J_m}N_c(s)\prod_{k=1}^{n}(s^2+\tilde{\omega}_k^2)}{D_c(s)\prod_{k=1}^{n+1}(s^2+\omega_k^2)+\frac{K}{J_m}N_c(s)\prod_{k=1}^{n}(s^2+\tilde{\omega}_k^2)} \tag{4.29}$$

which is equivalent to

$$\frac{\Theta_m(s)}{\Theta_{m_c}(s)} = \frac{\frac{K}{J_m}N_c(s)\prod_{k=1}^{n}(s^2+\tilde{\omega}_k^2)}{\prod_{k=1}^{n+1+n_c}(s^2+\hat{\omega}_k^2)} \tag{4.30}$$

where n_c is the order of the controller and $\hat{\omega}_k^2$ are the closed-loop system poles. For a flexible system with small mirror inertia, flexible modes are nearly pole-zero cancelled. This means that the residues for each flexible mode are very small and nearly equal to their open-loop values. Thus, for small mirror inertias we can use the effective modal reaction inertia as a reasonable measure of closed-loop inertial mirror jitter. We will see the relationship between effective modal reaction inertia and inertial mirror command response in the following section.

Figures 4.11–4.14 are forward loop frequency response plots with mirror inertia varying from 0.02% to 20% of support structure inertia J_{truss}[4]. The pole-zero separations seen in these figures are verified in figures 4.2, 4.3, 4.4, and 4.8. Root loci plots for these four configurations are provided in figures 4.15–4.16. The loci reveal unstably interacting flexible modes for the two higher mirror inertia configurations. It is important to note that the controller is collocacted in the classical sense and

[4] Notice the ambiguities in the phase plots as pole-zero separation decreases. It appears that even todays sophisticated software cannot determine the correct phase change for very lightly damped modally dense systems.

unstably interacts with these flexible modes. Figure 4.17 shows mirror response to a five engagement retargeting scenario. A controller operating on a mirror with inertia as small as 2% support structure inertia is shown to induce system instability. Further evaluation of LOS jitter as a function of small reacting mirror inertia will follow. Jitter stabilization results are summarized in table 4.1. To keep the total line-of-sight jitter requirement ε_{TOT} at 100 μdu RMS with four disturbance sources, the jitter budget for any one disturbance source is limited to 50 μdu RMS. Residual output

Table 4.1: Flexible Optical System: Jitter Stabilization Performance

$J_m\%$	*RMS Residual Jitter (μdu)*				
	ε_{f_d}	ε_m	ε_{θ_d}	ε_{f_h}	ε_{TOT}
≈ 0.00	50.000	50.000	50.000	50.000	100.00
0.02	50.114	49.998	49.942	4483.5	4484.3
0.20	0.0621	49.999	49.926	4632.7	4633.2
2.00	*Unstable System*				
20.0	*Unstable System*				

jitter due to sensor measurement noise m is relatively unaffected by mirror to flexible structure inertia and stiffness coupling. This is to be expected with optical sensing devices with high pass noise characteristics as modeled in this research. Line-of-sight disturbance θ_d effects behave similarly though due to the very low pass disturbance model. Output jitter from the two force (torque) disturbances is affected oppositely. As mirror inertia and stiffness increase, the relative support structure inertia and stiffness decrease acting as an isolator (absorber) for the torque disturbance f_d. On the other hand, output jitter due to aft-to-fore body disturbance f_h is more sensitive to the increased low frequency pole-zero separation caused by the increased inertial and elastic coupling. This result suggests that systems with larger mirror inertias create a more challenging aft-to-fore body isolator design problem.

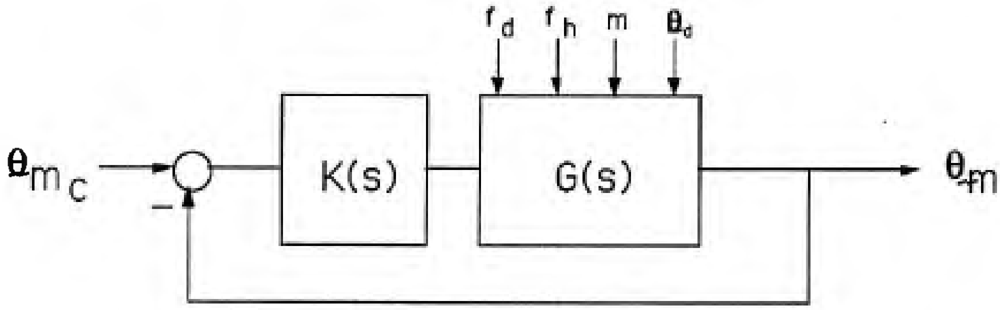

Figure 4.10: Mirror Command Response Block Diagram

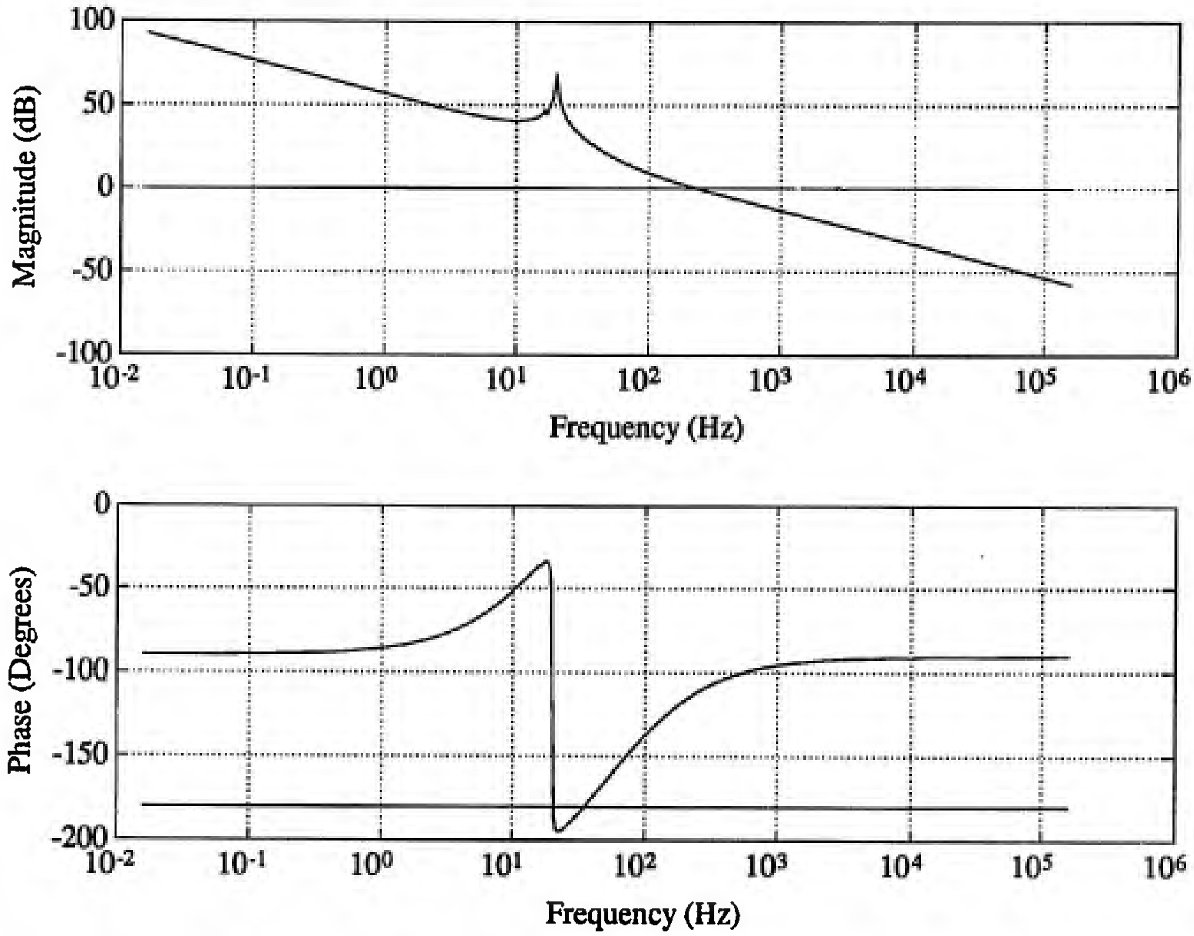

Figure 4.11: Forward Loop Frequency Response, J_m =0.02% J_{truss}

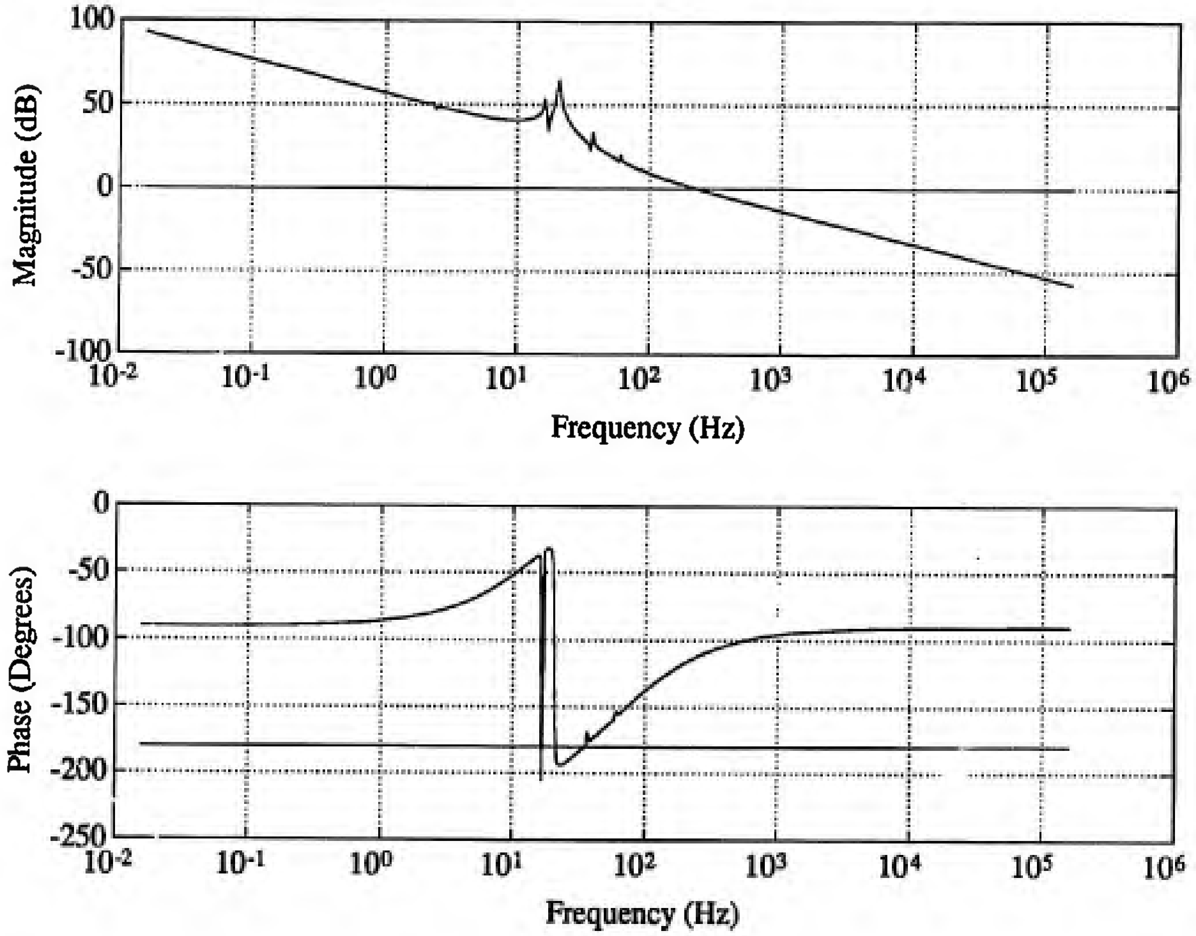

Figure 4.12: Forward Loop Frequency Response, J_m =0.2% J_{truss}

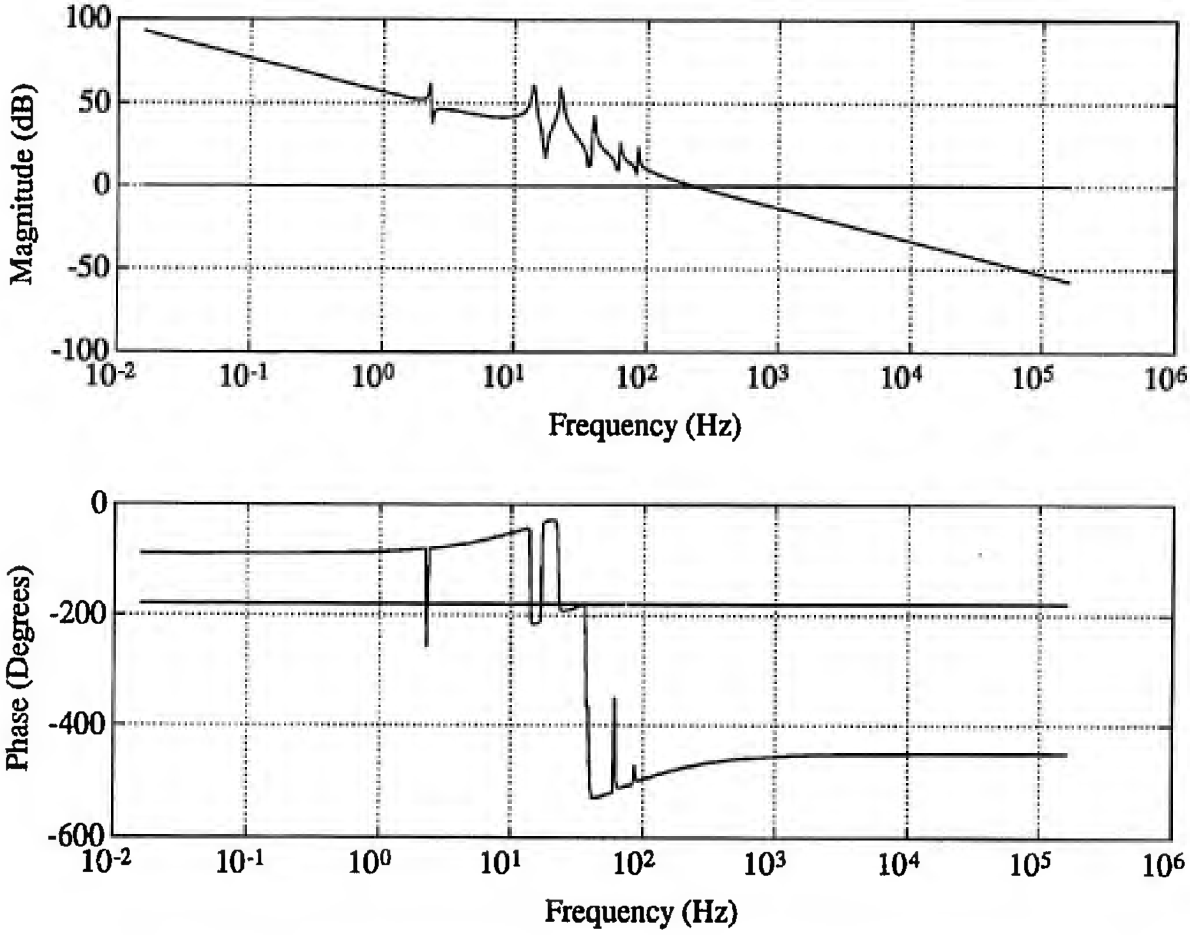

Figure 4.13: Forward Loop Frequency Response, J_m =2.0% J_{truss}

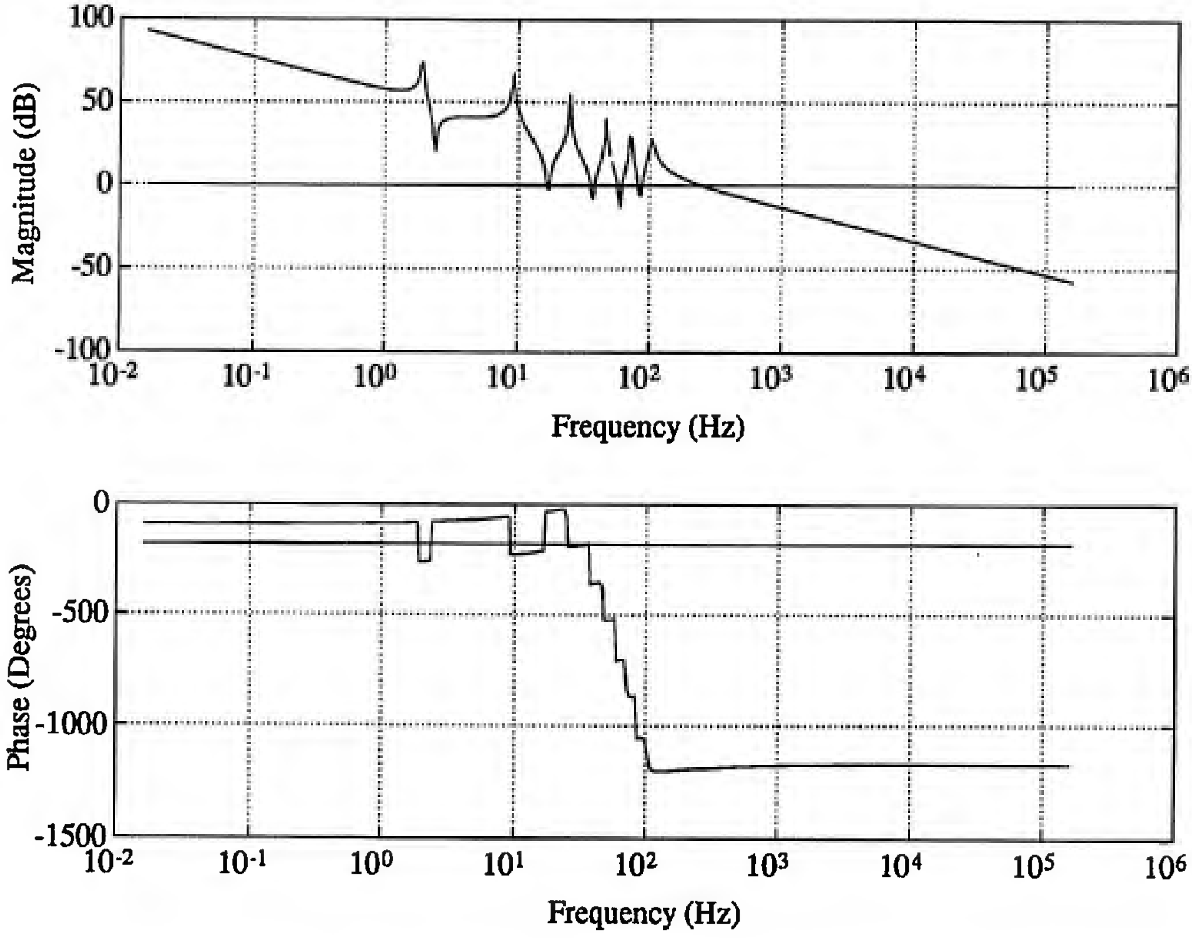

Figure 4.14: Forward Loop Frequency Response, J_m =20.0% J_{truss}

4.5 *Reactionless Steering Mirror Control*

Residual line-of-sight jitter is a function of inertial and elastic coupling between the mirror and its flexible support structure. In fact, enlarging the top left plot from Figure 4.17 shows that even with $J_m = 0.02\%\ J_{truss}$ LOS vibration stability is not achieved. The obvious question is just how small must the mirror inertia be with respect to its support structure before LOS jitter is within performance requirements? As mentioned earlier, the key parameter is not mirror inertia as a percentage of total support structure inertia but rather as a percentage of its local reference inertia. For example, if we construct the support structure such that the mirror attachment point has significant inertia compared to the mirror itself, we would see an increase in modal inertia and corresponding increases in effective modal reaction inertias resulting in less modal disturbability. However, unless we uniformly increase the structure's inertia, we will pay severe penalties in the large angle slew task (assuming the mirror attachment point is not coincident with the slewing center-of-mass). Of course uniform increases in structure inertia mean more total system mass with its own set of problems. Mirror mass and mirror attachment point location are also critical design parameters. It seems that the ideal design scenario is a uniformly light support structure constructed with maximum stiffness. Mirror inertia is designed small with respect to support structure inertia. One way of reducing the 'effective' mirror inertia is to design it reactionless. Reactionless mirrors have been built demonstrating less than ten percent torque leakage, making them ninety percent reactionless. If our analysis shows that mirror inertia of one percent results in tolerable LOS vibration from command response, then a ninety percent reactionless mirror with $J_m = 10\%$ J_{truss} should suffice[5]. With the reactionless mirror in mind, we examine the case where $J_m = 0.002\%\ J_{truss}$. Figure 4.18 shows the response to a step command for the 0.002% case. The enlargement on the bottom half of the figure shows that indeed the residual LOS jitter from the command step lies within performance requirements. However, when we use the same LOS controller with the full 62-DOF model, we see residual LOS vibration outside jitter bounds. This result highlights the need to verify

[5] This is only a crude approximation of allowable mirror inertia. To be more accurate, separate account must be taken of mirror versus reaction-mass component mismatches including inertia, spring restoring force constants, and most importantly actuator force constants[36].

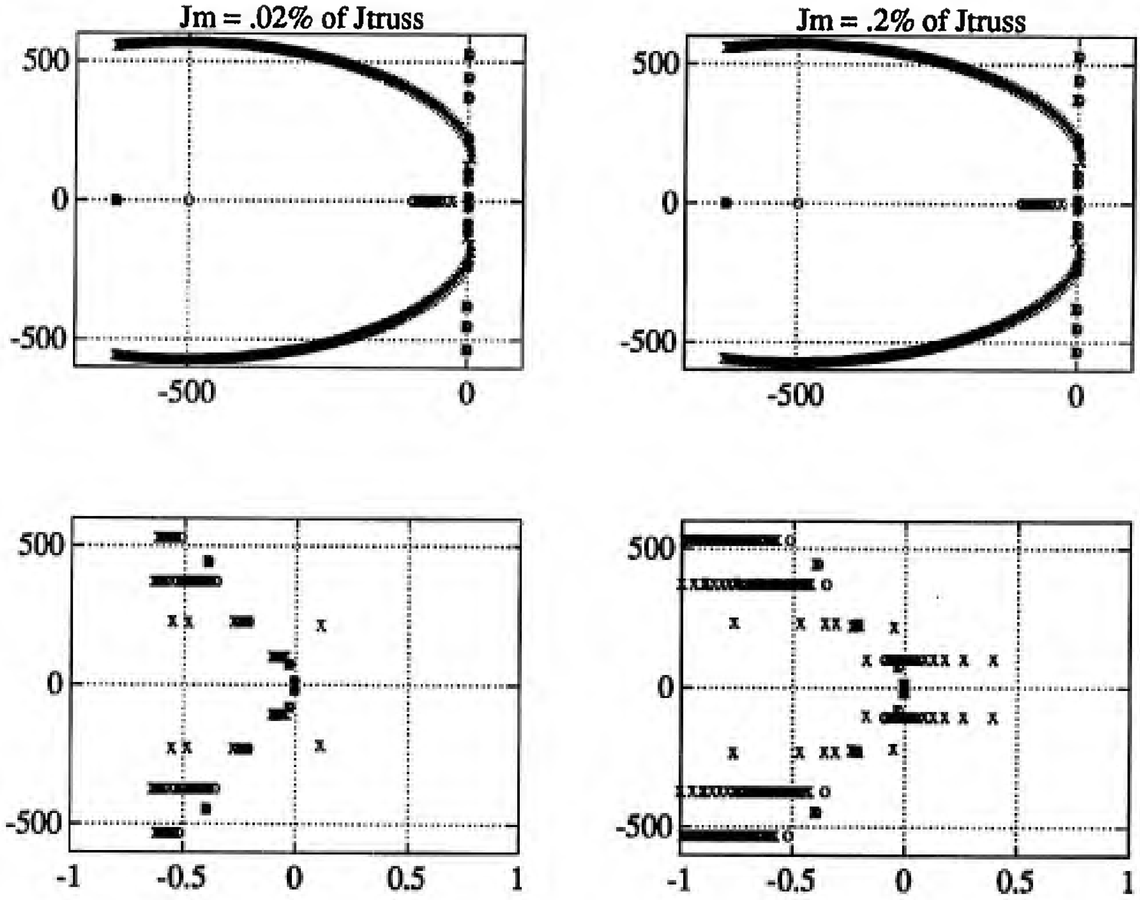

Figure 4.15: Loci of Closed Loop Roots, J_m =0.02% J_{truss} (left), J_m =0.2% J_{truss} (right)

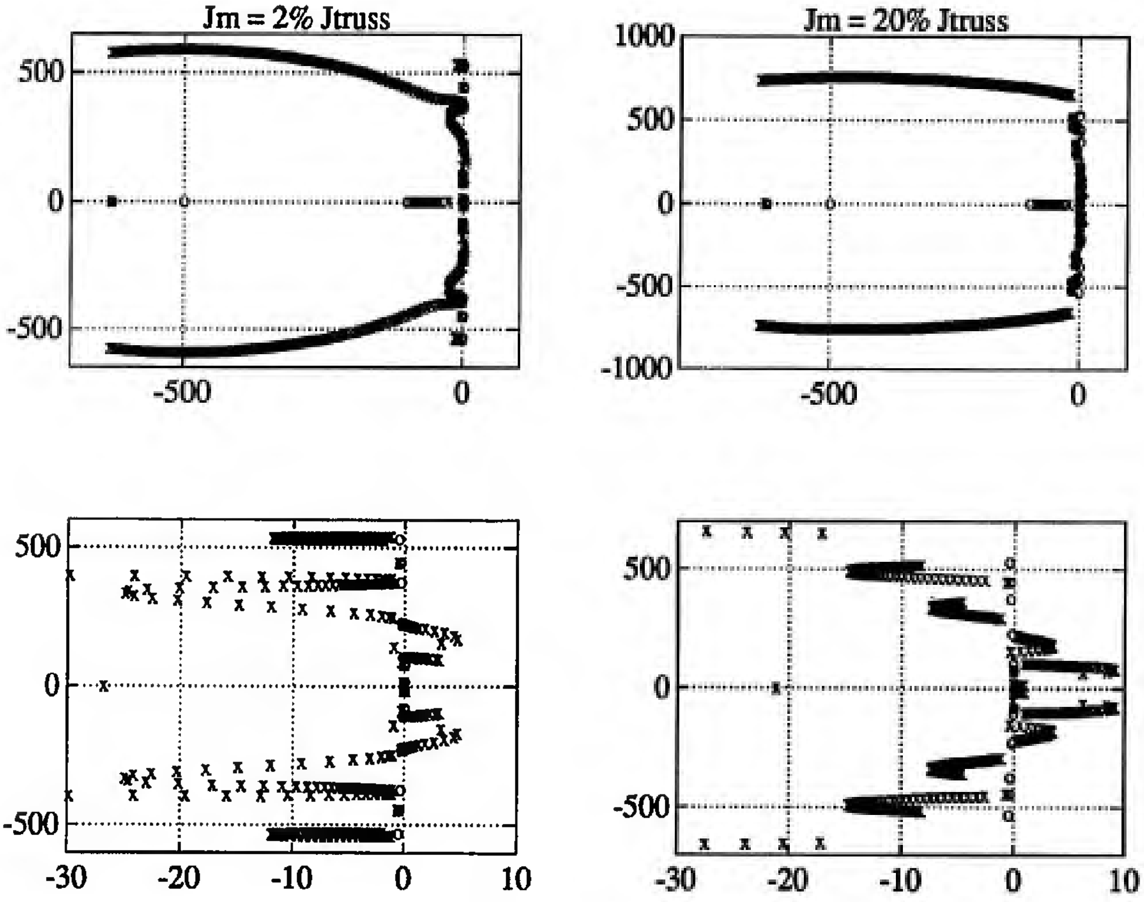

Figure 4.16: Loci of Closed Loop Roots, J_m =2.0% J_{truss} (left), J_m =20.0% J_{truss} (right)

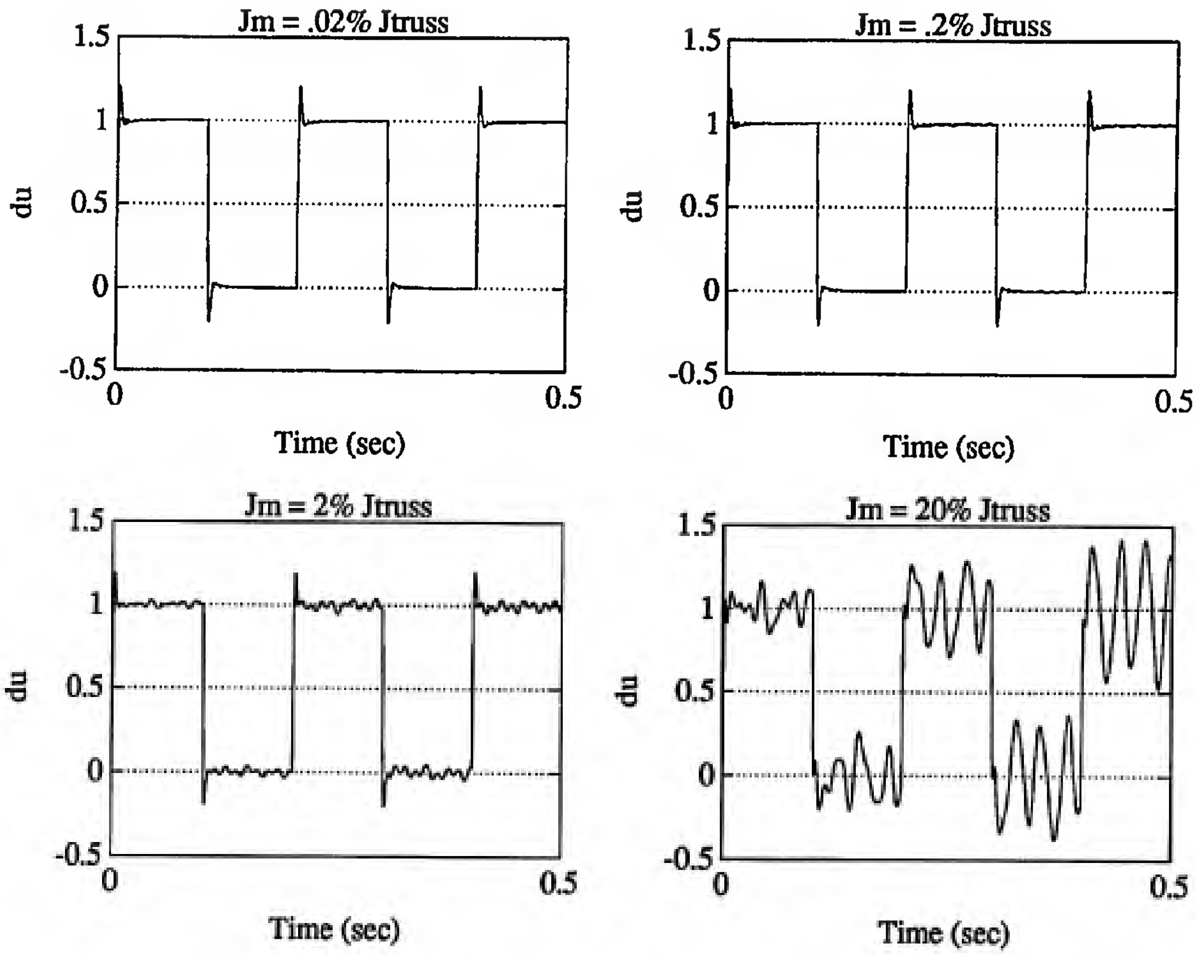

Figure 4.17: Mirror Angle Command Response, J_m =0.02% J_{truss} (top left), J_m =0.2% J_{truss} (top right), J_m =2.0% J_{truss} (bottom left), J_m =20.0% J_{truss} (bottom right)

controller performance simulations on as high an order 'truth' model as is feasible. Figures 4.19 and 4.20 are the forward loop frequency response and the step response for the LOS controller operating on the 62-DOF system. An examination of the frequency content of the step response again shows high participation from modes just under 400 Hz. Since these frequencies are beyond our closed-loop bandwidth, command response jitter requirements can be met simply with an appropriately ordered roll-off filter. Note however that this amounts to high frequency gain stabilization and does not necessarily benefit disturbance rejection. Residual jitter with frequency content inside the loop bandwith is absent in this example strictly as a consequence of the relatively large modal reaction inertias associated with modes with those frequencies. This is a result of our particular flexible structure and is not guaranteed.

If we re-examine the case where $J_m = 0.02\%\ J_{truss}$ using the full order system, we will see the relationship between the effective modal reaction inertia and output spectral density. Figures 4.21 and 4.22 are the resulting forward loop frequency response and the step response plots. In figure 4.23 we show a crude power spectral density of the output LOS response. The data is only a rough estimate of the actual power spectral density as we used a limited record length with no averaging. The inverse effective modal reaction inertia is plotted in figure 4.24. A comparison of overall shape and regions of significant energy between figures 4.23 and 4.24 reveals the usefullness of the *open-loop* effective modal reaction inertia in predicting (conservatively) the resulting output power spectrum. For systems with large mirror inertia, this technique tends towards less reasonable comparisons because the pole-zero separations shown in equation 4.30 become too far removed from their open-loop values. We see the beginnings of this in figures 4.25 and 4.26 for the case where $J_m = 2.0\%\ J_{truss}$. The increased inertial and elastic coupling results in increased modal coupling and energy being spread into a wider spectrum of disturbable modes.

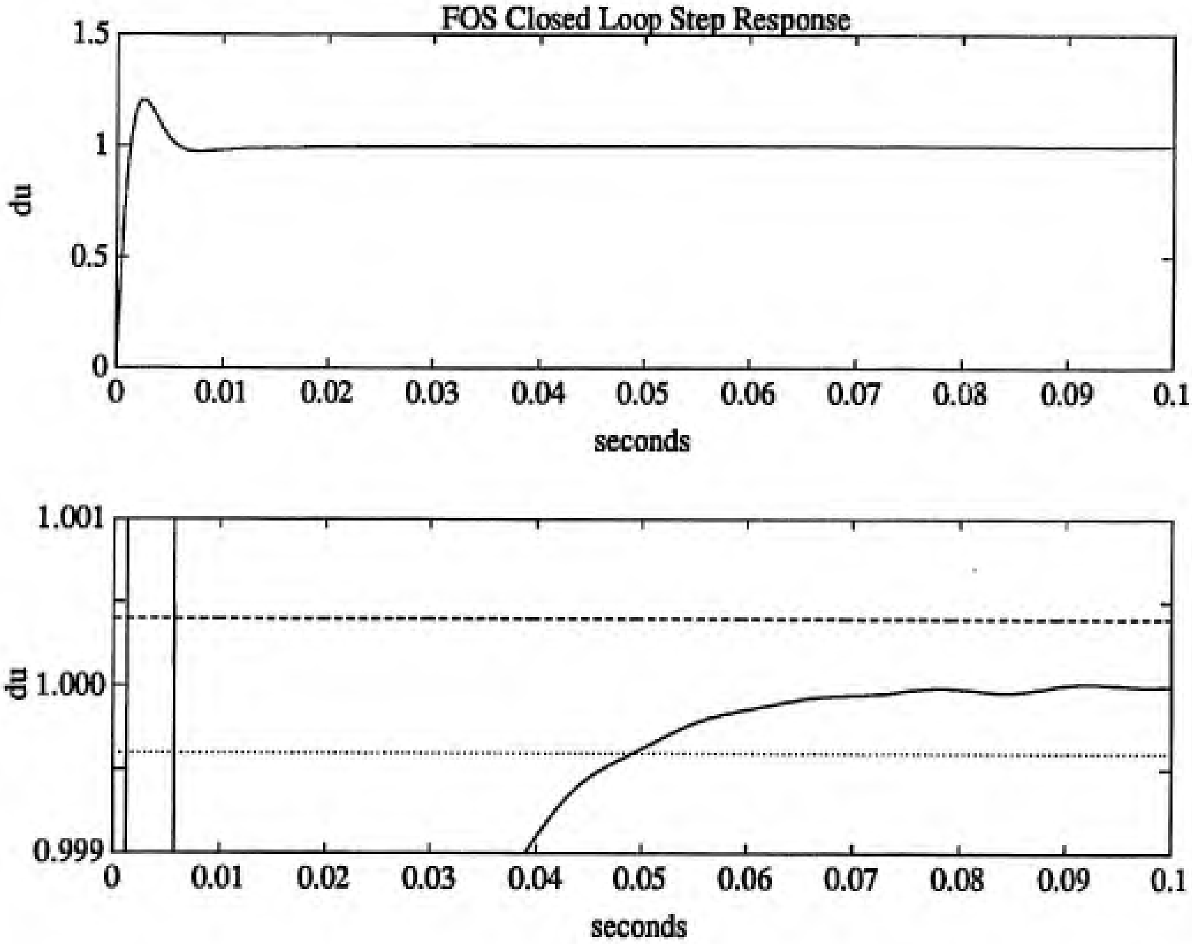

Figure 4.18: θ_m Response to Step in θ_{m_c}, 8-DOF Model, J_m =0.002% J_{truss}

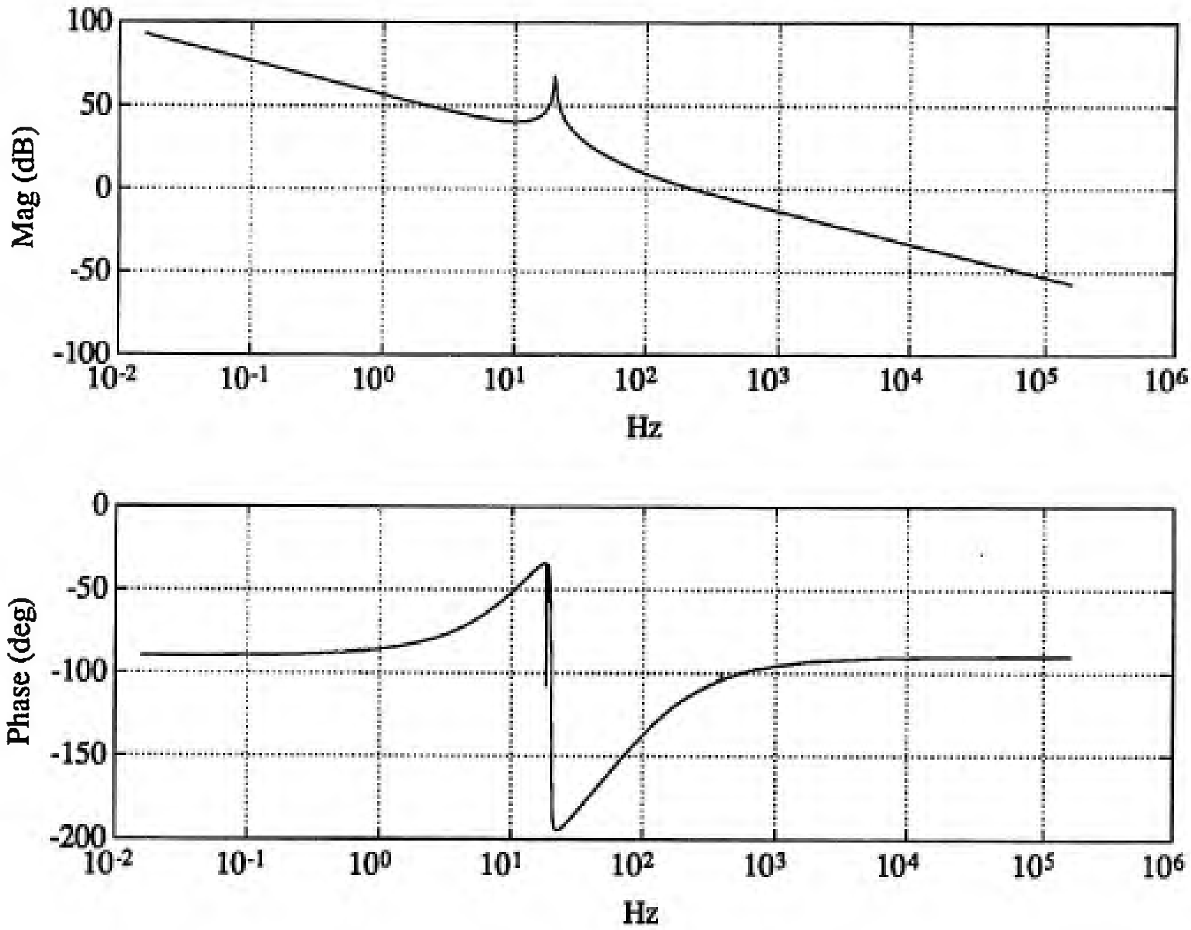

Figure 4.19: Forward Loop Frequency Response, J_m =0.002% J_{truss}

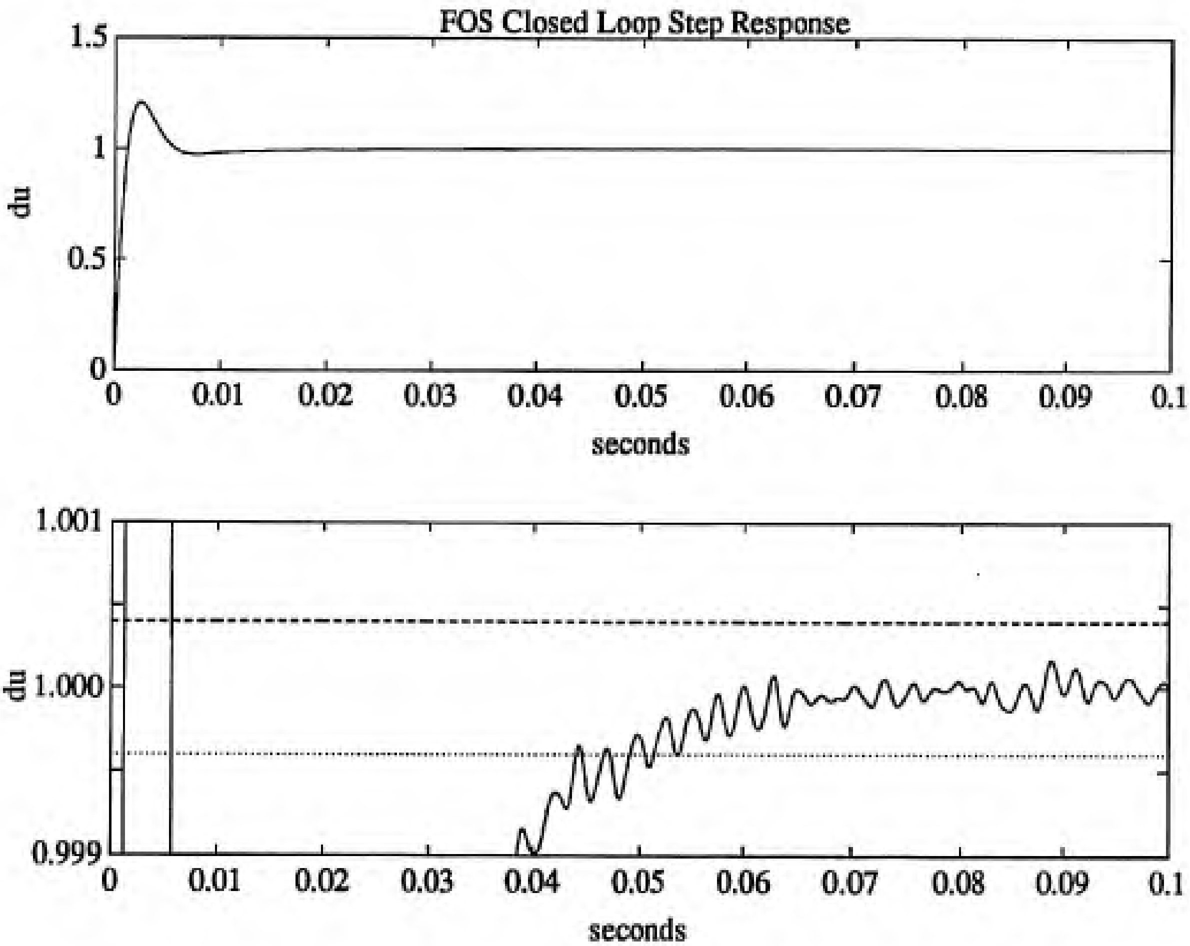

Figure 4.20: θ_m Response to Step in θ_{m_c}, 62-DOF Model, J_m =0.002% J_{truss}

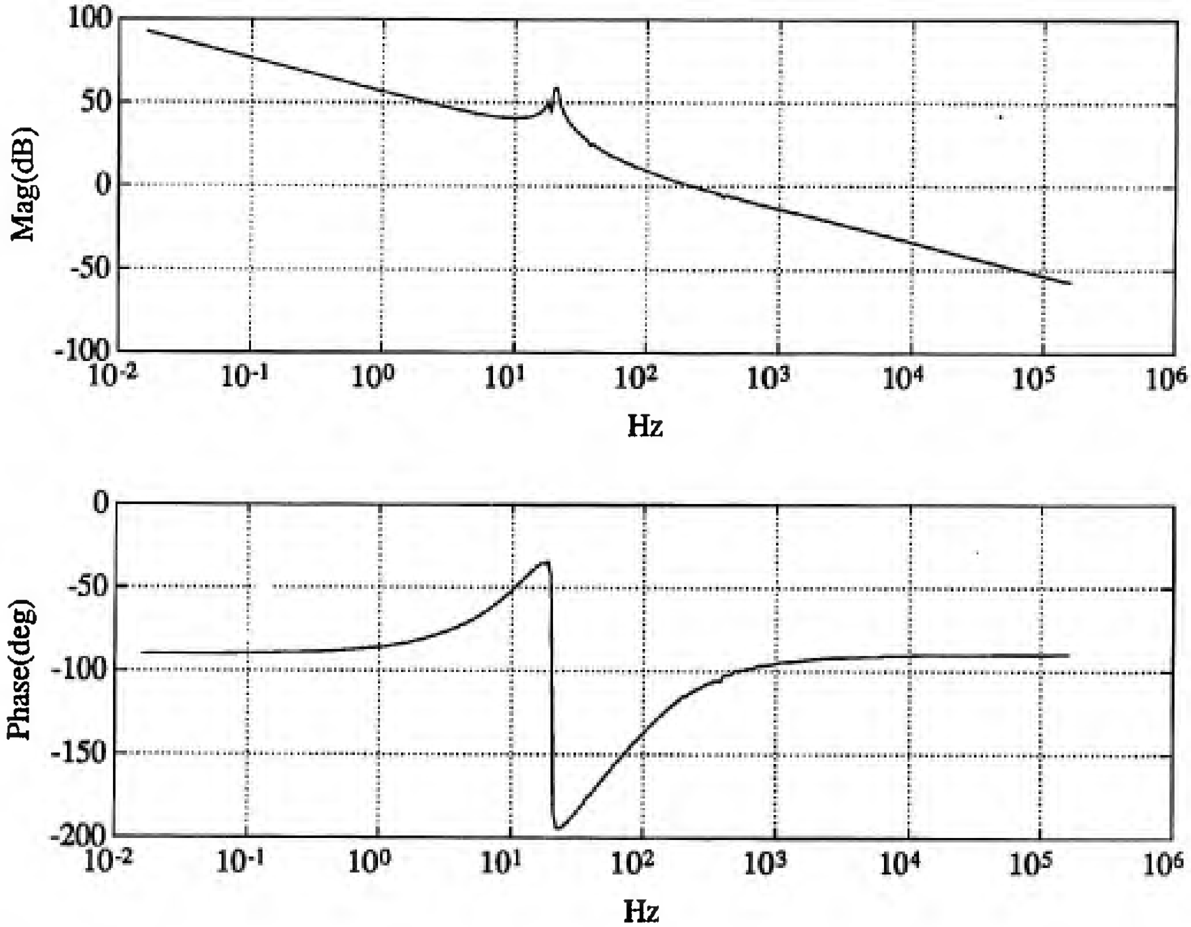

Figure 4.21: Forward Loop Frequency Response, J_m =0.02% J_{truss}

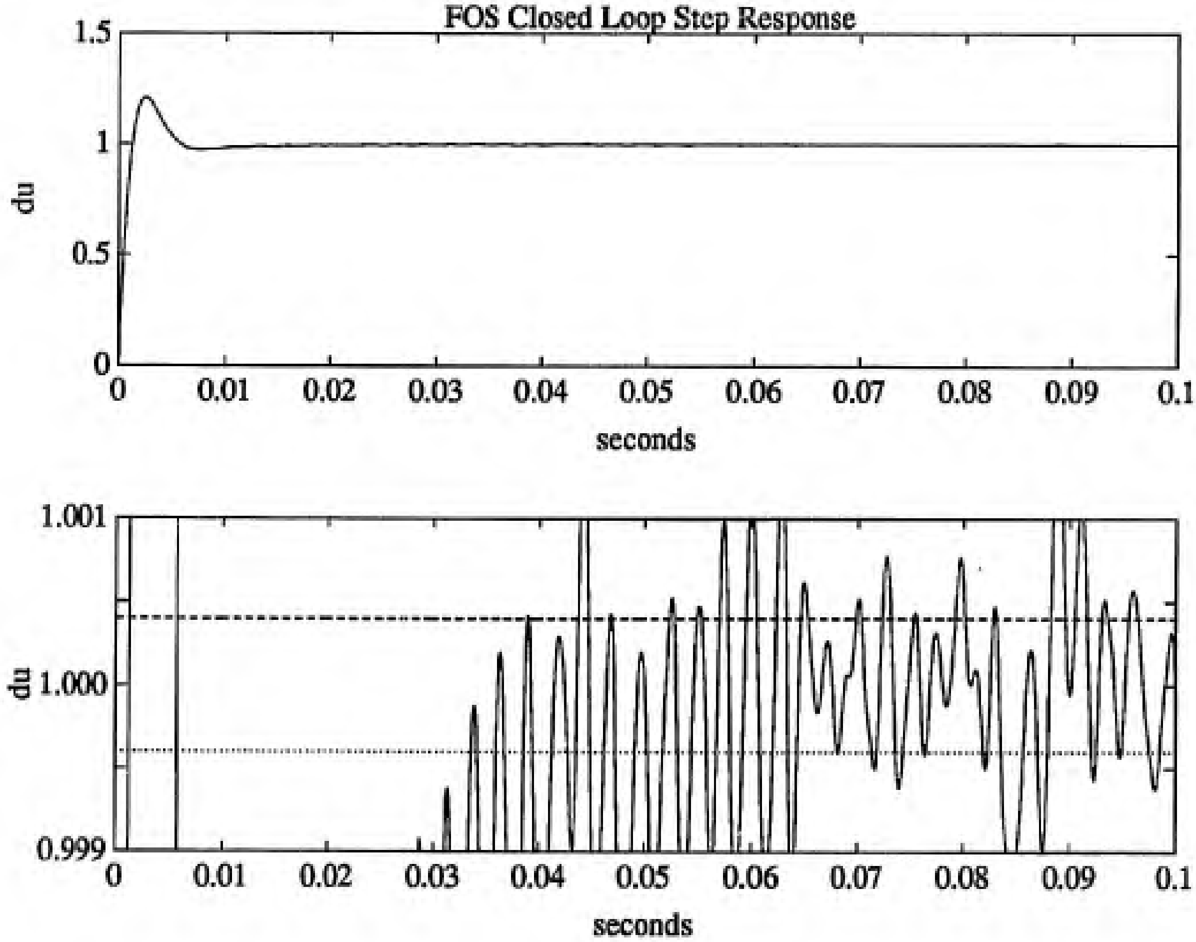

Figure 4.22: θ_m Response to Step in θ_{m_c}, 62-DOF Model, J_m =0.02% J_{truss}

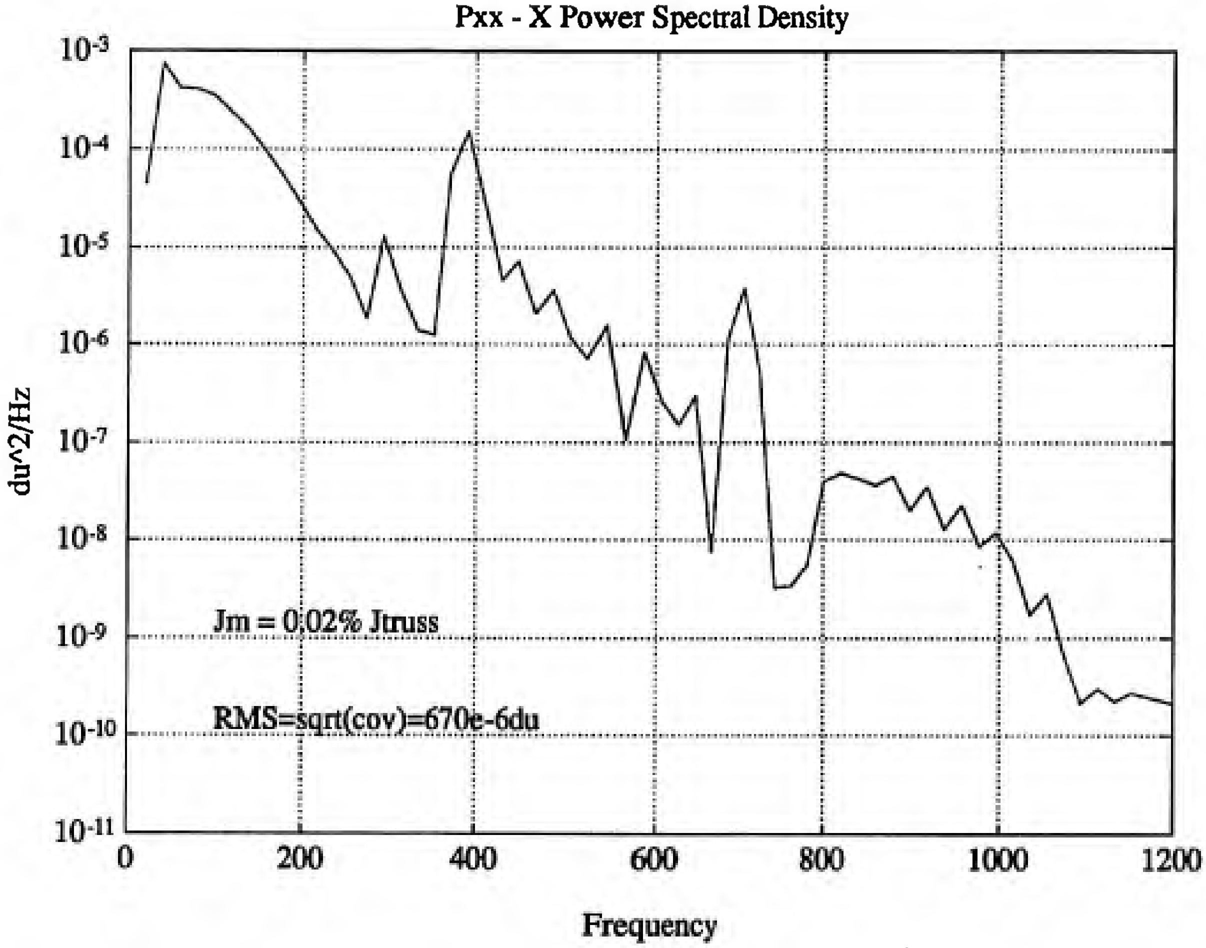

Figure 4.23: θ_m Step Response Power Spectral Density, J_m =0.02% J_{truss}

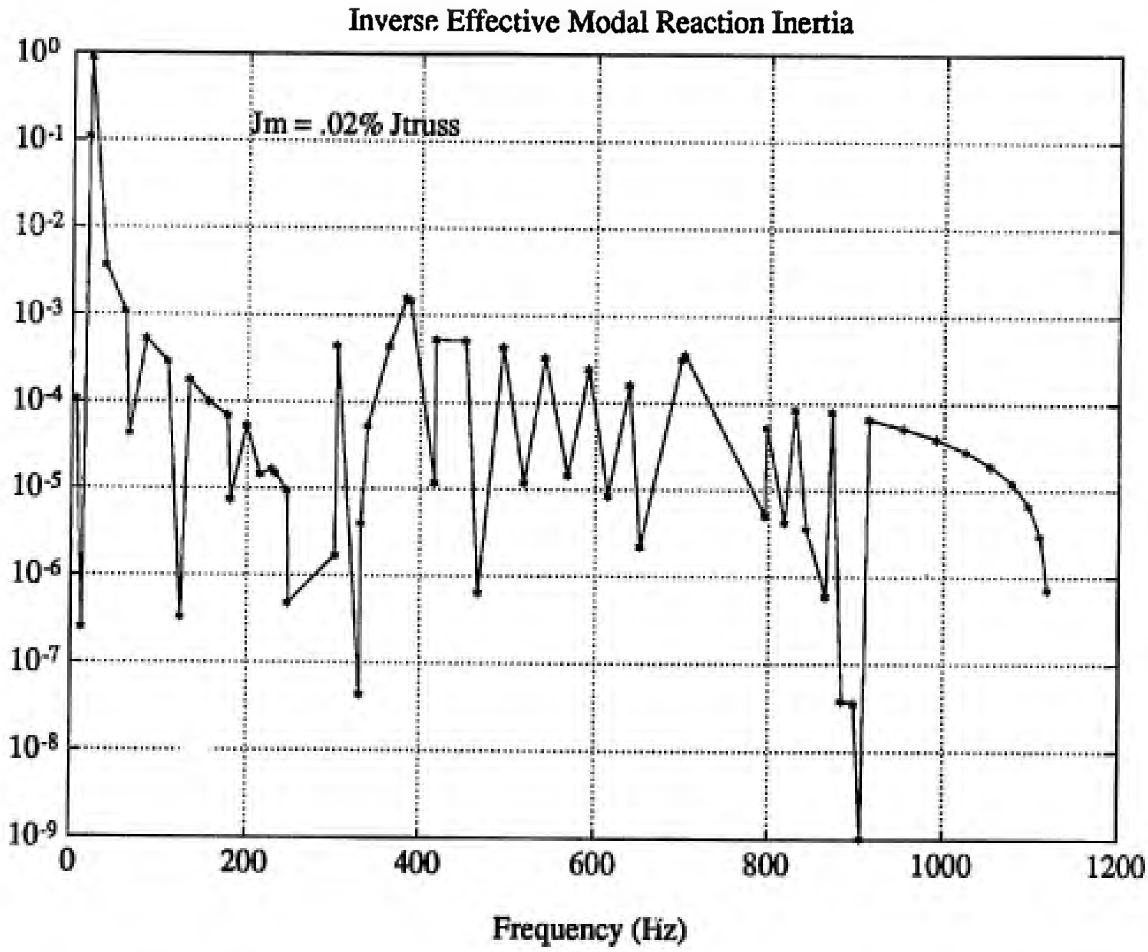

Figure 4.24: Inverse Effective Modal Reaction Inertia $1/\bar{J}_k$, J_m =0.02% J_{truss}

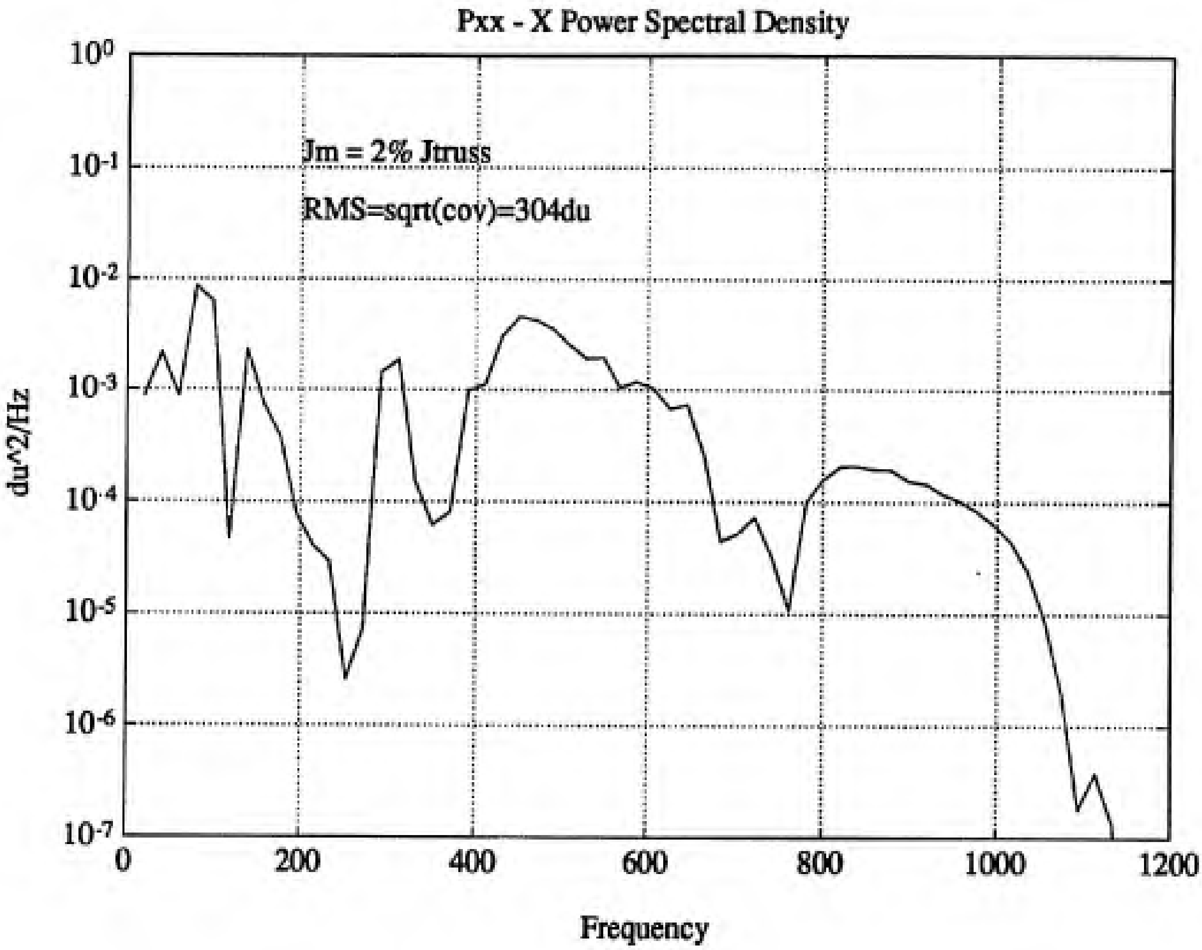

Figure 4.25: θ_m Step Response Power Spectral Density, J_m =2.0% J_{truss}

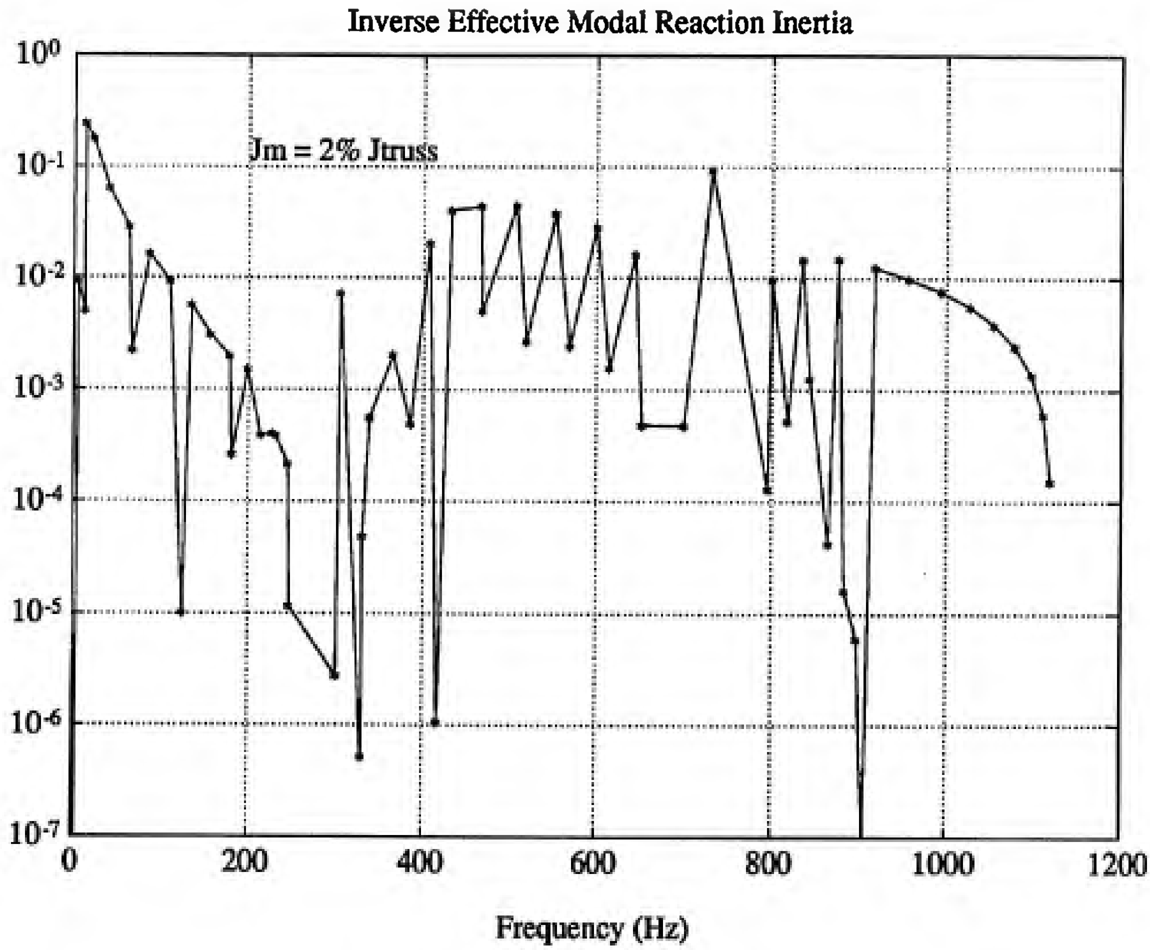

Figure 4.26: Inverse Effective Modal Reaction Inertia $1/\bar{J}_k$, J_m =2.0% J_{truss}

4.6 Summary of Findings

In this chapter, we have extended the control-structure-interaction analyses from the single-mode to the multimode flexible support structure. We have shown that very small degrees of inertial and elastic coupling between the flexible support structure and the reaction actuator, which for many applications would be considered negligible, induces performance limiting control-structure-interaction. We have shown modal inertia $\tilde{J}_k$ to be a measure of the uncoupled flexible structure's susceptibility to modal disturbability. We have introduced three new system parameters, reference inertia J_{ref}, modal reaction inertia J_k, and effective modal reaction inertia $\bar{J}_k$ as useful both in identifying and quantifying the extent to which these interaction occur in any given structure. Perhaps most importantly, we have verified that as with the single-mode models in chapter three, control-structure-interaction can lead to critical performance degradation and/or system instabilities *even with bicollocated control, collocated in the classical sense.*

Chapter 5

CONCLUSIONS

5.1 Summary

This research is to the best of our knowledge the first attempt to describe, in both a qualitative and quantitative manner, the degree to which control-structure-interaction phenomena effect stability and performance of high bandwidth high precision flexible optical systems. We have developed a multimode planar model representative of a simple flexible optical system. We used this model to simulate certain aspects of the flexible optical system mission, namely the small angle rapid line-of-sight repositioning and line-of-sight stabilization against a variety of disturbances.

In this thesis, we have examined the effect of control-structure-interaction on both of these mission aspects using the single flexible mode modified benchmark model and the multimode planar model. We used the single-mode model to examine control-structure-interaction effects as a function of the location of the flexible mode with respect to steering mirror natural frequency. We used the multimode model to examine control-structure-interaction effects as a function of inertial and elastic coupling between the steering mirror and the flexible support structure.

The single most significant result of this research is the introduction and definition of bicollocated reaction actuator control and its resulting minimum phase guarantees. Another significant finding is that, contrary to the commonly accepted view, collocated control (collocated in the classical sense) can induce closed-loop instabilities if the reaction actuator is non-bicollocated. The common view that collocated control always results in a stable closed-loop system was formulated with respect to the problem of controlling the rigid-body in the presence of appendage flexibilities using a proportional-derivative (PD) control law. In this context the assertion is correct–collocated control results in a stable system so long as unmodeled loop dynamics are not present. However, when controlling a reaction actuator, bicollocation or non-bicollocation must be considered. A classical collocated reaction actuator controller can be non-bicollocated and as such, can have nonminimum phase zeros in the plant transfer function. No proportional plus derivative control law is absolutely robust against nonminimum phase zeros. We also showed that a bicollocated reaction actuator proportional-integral-derivative (PID) controller can unstably interact with any flexible mode residing at a frequency below the natural frequency of the reaction actuator depending upon the degree of inertial and elastic coupling between the actuator and its flexible support structure. This research also reveals the difficulty in meeting very high precision, line-of-sight jitter requirements when the steering mirror is free to react against its flexible support structure. Reactionless steering mirrors may not be 'reactionless' enough to totally alleviate these control-structure interactions.

Line-of-sight jitter stabilization is also affected by control-structure-interaction. We have shown that the presence of low frequency structural modes in a high bandwidth control loop increase the amount of line-of-sight jitter from both mirror cooling and aft-to-fore body torque disturbances. We have also shown that high inertial and elastic coupling between the steering mirror and the flexible support structure decreases line-of-sight jitter from mirror cooling but increases that due to aft-to-fore body disturbances. This is primarily a function of the pole-zero spreading induced by the high inertial and elastic coupling.

To better understand the control-structure-interaction phenomena as it relates to the flexible optical system, we have extended the work of J.T. Spanos[49] to the case of controlling a reaction actuator on a multimode system. We have developed a method of classifying the type of structural flexibility for the reaction actuator system thereby allowing us to examine, on a single-mode basis, the control-structure-interaction effects due to any of these flexibility types.

We have shown the conventional modal inertia to be a measure of a flexible structure's susceptibility to modal disturbability and consequently to pole-zero separation. We have defined two new mulitmode system parameters, modal reaction inertia and effective modal reaction inertia, and used them to predict control-structure-interaction effects on the control of a reaction actuator coupled to a flexible support structure. In this thesis these parameters were used to analyze system performance. These same parameters can be used as design variables in the structures-control optimization problem.

5.2 *Directions for Future Work*

We see two possible directions for future work: 1) development of the theory and application of bicollocated and non-bicollocated reaction actuator control and, 2) multidisciplinary structures-optics-controls design optimization.

Reaction Actuator Control

In this research, we introduced the concept of bicollocated and non-bicollocated reaction actuator control. We developed the guarantee for minimum phase zeros with bicollocated control and provided a sufficient condition for the existence of nonminimum phase zeros in the first flexible mode in a single-mode expansion. But more can be done. For example, one might pursue minimum phase zero guarantees in terms of bounds on modal inertia or modal reaction inertia for the non-bicollocated control of the reaction actuator. It would also be interesting to investigate the usefulness of a physically implementable nonminimum phase filter–which is exactly what a non-bicollocated reaction actuator provides. We understand the usefulness of second order nonminimum phase filters in the control of flexible structure modes [53]. Perhaps some utility can be found for such a filter implemented in hardware rather than electronically or digitally.

Multidiscipinary Optimization

As a result of this research, obvious questions arise concerning the ability of high bandwidth high precision systems to perform their missions with only post-regard for inherent control-structure-interactions in the line-of-sight controller design. The normal procedure in designing a line-of-sight controller is to initially exclude most or all the flexible modes. Compensation for troublesome modes is designed in an ad-hoc fashion using trial and error with engineering judgement. Multivariable controllers are designed using reduced order models with, at best, bounded uncertainties in high frequency modes. Both of these methods will result in exceedingly high order controllers for the type of systems studied in this research–a system with greater than ten or twenty structural modes inside the closed-loop bandwidth extending to frequencies higher than theory allows us to accurately predict with a model. We have pointing requirements that are not only very demanding but require large potentially massive pointing mirrors, gimbals, etc. Should CSI phenomena critically impinge upon the performance of these type systems, the response will likely be in efforts spent in noise cancellation, image motion compensation, or possibly active structural vibration suppression. These techniques have proven successful in the past, albeit for systems with much less stringent performance requirements. This research leads us to the conclusion that such high bandwidth high precision line-of-sight controllers are best designed concurrently optimizing the structure and controller to minimize interaction between the two.

The structural parameters defined in chapter 4–modal inertia, modal reaction inertia, mirror inertia, and reference inertia, can be integral elements or even design variables in such an optimization scheme. For example, we know that CSI effects on the control of the reaction actuator can be reduced if reference inertia is increased. However, arbitrary increase in reference inertia will undoubtedly interfere with other performance criteria such as large angle rigid body slew. A uniform increase in modal inertia will tend to make the flexible support structure more undisturbable but may also prohibitively increase total system mass. The list of tradeoffs is endless, however, the structural parameters defined in this research can provide at least intermediate if not primary criteria for the successful design of high bandwidth high precision flexible optical systems.

A multidisciplinary optimization problem formulation can include any level of complexity. For example, we can see at least four disciplines involved: structure, structural dynamics, optics, and controls. The optimization problem might be formulated as constrained or unconstrained using both static and dynamic objective functions. The design descriptors can be either pre-assigned or variable and might span all four disciplines. Some examples of design descriptors pertinent to the multidisciplinary optimization of the flexible optical system are:

Structures and Structural Dynamics

1) Configuration or shape of the flexible support structure
2) Mass, stiffness (element material, size, and shape)
3) Natural frequencies, damping
4) Modal inertia, modal reaction inertia, reference inertia

Reaction Actuators

1) Number of actuators
2) Location on the flexible support structure
3) Mass, stiffness, natural frequency, damping (reaction actuator dynamics)
4) Optical sensitivity (optical actuators only)

Controls

1) Architecture
2) Connectivity
3) Order
4) Gains
5) Transfer function coefficients
6) Controller model parameters

A low level optimization scheme might involve only a small subset of the descriptors on this list. For example, the overall design configuration may be pre-assigned. The flexible support structure configuration and shape as well as the number of reaction actuators and their locations might be fixed. We may allow support structure element size and shape as well as reaction actuator dynamics to be design variables. Whatever the specific problem formulation, we can envision advantages in overall system performance if the flexible optical system is designed as a total system instead of in sequence as a series of individual sub-systems.

For whatever the reason, complex systems in the field or close to being placed in the field are designed and implemented primarily sequentially. Perhaps the expense and expediency of the development, testing, and deployment makes these systems less likely candidates for such a multidisciplinary optimization procedure. Only when system performance cannot be met with the design techniques currently in use, will it such a procedure likely find its place in the design of real systems. The high bandwidth high precision flexible optical system may be such a system.

BIBLIOGRAPHY

[1] Aubrun, J. N. Theory of the Control of Structures by Low-Authority Controllers. *Journal of Guidance, Control, and Dynamics*, Vol 3, No 5, September-October 1980, pp 444-451.

[2] Aubrun, J. N. Performance Analysis of the Segment Alignment Control System for the Ten Meter Telescope. *Automatica*, Vol 24, No 4, 1988, pp 437-453.

[3] Aubrun, J. N., Lorell, K. R. Demonstration of the Controls/Structure Interaction Phenomena Using the ASCIE Testbed. Presented at the *American Controls Conference, San Diego, CA*, May 1990.

[4] Balas, M. J. Direct Velocity Feedback Control of Large Space Structures. *Journal of Guidance, Control, and Dynamics*, Vol 2, No 3, May-June 1979, pp 252-253.

[5] Barbieri, E., Özgüner, Ü. Unconstrained and Constrained Mode Expansions for a Flexible Slewing Link. *Journal of Dynamic Systems, Measurement, and Control*, Vol 110, December 1988, pp 416-421.

[6] Barbieri, E., Özgüner, Ü., Yurkovich, S. Vibration Compensation in Optical Tracking Systems. *Journal of Guidance, Control, and Dynamics*, Vol 12, No 4, July-August 1989, pp 585-592.

[7] Byrns, E. V., Calise A. J. Fixed Order Dynamic Compensation for the H_2/H_∞ Benchmark Problem. *Proceedings of the 1990 American Control Conference, San Diego, CA*, May 1990, pp 963-965.

[8] Cannon, R. H. and Rosenthal, D. E. Experiments in Control of Flexible Structures with Noncolocated Sensors and Actuators. *Journal of Guidance, Control, and Dynamics*, Vol 7, No 5, September-October 1984, pp 546-553.

[9] Carrier, A. Modeling and Shape Control of a Segmented-Mirror Telescope. PhD Dissertation, Stanford University, March 1990.

[10] Chiang, R. Y., Safonov, M. G. H^∞ Robust Control Systhesis for an Undamped, Non-colocated Spring-Mass System. *Proceedings of the 1990 American Control Conference, San Diego, CA*, May 1990, pp 966-967.

[11] Chiarappa, D. J., and Claysmith, C. R. Deformable Mirror Surface Control Techniques. *Journal of Guidance, Control, and Dynamics*, Vol 4, No 1, January-February 1981, pp 27-34.

[12] Collins, E. G., and Berstein, D. S. Robust Control Design for a Benchmark Problem Using A Structured Covariance Approach. *Proceedings of the 1990 American Control Conference, San Diego, CA*, May 1990, pp 970-971.

[13] Dougherty, H. Space Telescope Pointing Control System. *Journal of Guidance, Control, and Dynamics*, Vol 5, No 4, July-August 1982, pp 403-409.

[14] Duke, J. P., Webb, S. B., and Vu H. Optimal Passive Control of Multi–Degree of Freedom Systems Using a Vibration Absorber. *Proceedings of the 1990 AIAA Guidance, Navigation, and Control Conference, Portland, OR*, August 1990, pp 1657-1663.

[15] Ebbesen, L., et al. High Bandwidth Beam Steering. Air Force Weapons Laboratory, Air Force Systems Command, Kirtland AFB,NM, 87117-6008, AFWL-TR-85-02, Vol. 1, June 1986.

[16] Founds, D. Joint Optics Structures Experiment (JOSE). *Proceedings of the First NASA/DoD Control/Structures Interaction Technology Conference, Norfolk, VA*, NASA CP 2447 part II, November 1986, pp 591-602.

[17] Garcia E., and Inman, D. J. Modeling of Actuator-Structure Interaction in the Slewing of Flexible Structures. *Proceedings of the 1990 American Control Conference, San Diego, CA*, May 1990, pp 1962-1968.

[18] Garcia, J. G. Stability of an Actuated Mirror on a Flexible Structure as a Function of Mass and Structural Damping. M.S. Thesis, MIT, Cambridge, MA. June 1990.

[19] Gevarter, William B. Attitude Control of a Flexible, Spinning, Toroidal Manned Space Station. PhD Dissertation, Stanford University, 1965.

[20] Gevarter, William B. Basic Relations for Control of Flexible Vehicles. *AIAA Journal*, Vol 8, No 4, April 1970.

[21] Hallauer, W. L. MAPMODES User's Guide. *Private Publication*, 2 February 1989.

[22] Hallauer, W. and Lamberson, S. Experimental Active Vibration Damping of a Plane Truss Using Hybrid Actuation. *Proceedings of the 30th Structures, Structural Dynamics and Materials Conference, Mobile, AL*, April 1989, pp 80-90.

[23] Hughes, R. O. Conceptual Design of Pointing Control Systems for Space Station Gimballed Payloads. *Proceedings of the AIAA Guidance, Navigation, and Control Conference, New York, NY*, June 1986.

[24] Jones, C.D. Space Telescope Optics. *Optical Engineering*, Vol 18, May 1979, pp 273-280.

[25] Laura, P.A., Pombo, J.L., and Susemihl, E. A. A Note on the Vibrations of a Clamped-Free Beam With a Mass at the Free End. *Journal of Sound and Vibrations*, Vol 37, No 2, pp 161-168.

[26] Ly, U. A Design Algorithm for Robust Low Order Controllers. PhD Dissertation, Stanford University, 1982.

[27] Ly, U. Robust Control Design Using Nonlinear Constrained Optimization. *Proceedings of the 1990 American Control Conference, San Diego, CA*, May 1990, pp 968-969.

[28] Martin, G. D. and Bryson, A. E. Attitude Control of a Flexible Spacecraft. *Journal of Guidance, Control, and Dynamics*, Vol 3, January-February 1980, pp 37-41.

[29] Meirovitch, L. *Analytical Methods in Vibrations*, Macmillan, New York, 1967.

[30] Meirovitch, L. *Computational Methods in Structural Dynamics*, Sijthoff & Noordhoff, The Netherlands, 1980.

[31] Meirovitch, L. *Elements of Vibration Analysis*, 2nd ed. New York, McGraw-Hill Book Co., 1986.

[32] Miller, D. W. and Crawley, E. F. Theoretical and Experimental Investigation of Space–Realizable Inertial Actuation for Passive and Active Structural Control. *Journal of Guidance, Control, and Dynamics*, Vol 11, No 5, September-October 1988, pp 449-458.

[33] Morine, L. A. Zenith Star: A Structural Control Challenge. *Third NASA/DoD Control/Structures Interaction Technology Conference, San Diego, CA*, NASA CP 3041, January 1989, pp 17-29.

[34] Neal, R. D. Rapid Retargeting and Precision Pointing (R2P2) Simulator Delivery Order Ten Final Technical Report. *Final Technical Report-Covering the period 16 April, 1990 - 30 October, 1990, Contract No. DASG60-87-D-0244*, Report MCR-90-627, 13 November, 1990.

[35] Ogata, K. *Modern Control Engineering*, Englewood Cliffs, NJ, Prentice-Hall, Inc. 1970.

[36] Pluim, R. Beamwalk Mirror System Analysis. *Ball Aerospace Internal Document*, May 1988.

[37] Przemieniecki, J. S. *Theory of Matrix Structural Analysis*, McGraw-Hill Book Co., 1968.

[38] Quinn, R. D. and Meirovitch, L. Maneuver and Vibration Control of SCOLE. *Journal of Guidance, Control, and Dynamics*, Vol 11, No 6, November-December 1988, pp 542-553.

[39] Quinn, R. D. and Yunis, I. Control-Structure Interactions of Freedom's Solar Dynamic Modules. *Proceedings of the 1990 AIAA Guidance, Navigation, and Control Conference, Portland, OR*, August 1990, pp 79-88.

[40] Ramakrishnan, J., Byun, K. W., Skelton, R., and Cossey, D. F. ASTREX Controller Design: OVC and OCC Approach. *Presented at the 4th NASA/DOD Control/Structures Interaction Technology Conference, Orlando, FL*, November 1990.

[41] Rao, S. S., Pan, T. S., and Venkayya, V. B. Modeling, Control, and Design of FLexible Structures: A Survey. *Applied Mechanics Review*, Vol 43, No 5, Part 1, May 1990, pp 99-117.

[42] Redding, D. C. and Chien T. T. Space-Stabilized Beam Pointing for a Bifocal Satellite Experiment. *12th Annual AAS Guidance and Control Conference, Keystone, CO*,AAS 89-032, February 4-8, 1989.

[43] Rhee I., and Speyer, J. L. Application of a Game Theoretic Controller to a Benchmark Problem. *Proceedings of the 1990 American Control Conference, San Diego, CA*, May 1990, pp 972-973.

[44] Safonov, M. G., Laub, A. J., and Hartmann, G. L. Feedback Properties of Multivariable Systems: The Role and Use of the Return Difference Matrix. *IEEE Transactions on Automatic Control*, Vol AC-26, No 1, February 1981, pp 47-65.

[45] Schaechter, D. B. Hardware Demonstration of Flexible Beam Control. *Journal of Guidance, Control, and Dynamics*, Vol 5, No 1, January-February 1982', pp 48-53.

[46] Schaechter, D. B. Optimal Local Control of Flexible Structures. *Journal of Guidance, Control, and Dynamics*, Vol 4, No 1, January-February 1981, pp 22-26.

[47] Shaw, G. O. and Vu, H. V. Modal Analysis and Active Vibration Control of a System of a Cantilever Beam and A Reaction Mass Actuator. *Proceedings of the 1990 AIAA Guidance, Navigation, and Control Conference, Portland, OR*, August 1990, pp 73-78.

[48] Silverberg, L. M., and Park, S. Interactions Between Rigid-Body and Flexible-Body Motions in Maneuvering Spacecraft. *Journal of Guidance, Control, and Dynamics*, Vol 13, No 1, January-February 1990, pp 73-81.

[49] Spanos, J. T. Control-Structure Interaction in Precision Pointing Servo Loops. *Journal of Guidance, Control, and Dynamics*, Vol12, No 2, March-April 1989, pp 256-263.

[50] Thompson, R. C. Predicting Accelerometer Errors In Ground-Based Testing of Large Flexible Structures. *Presented at the 1990 AIAA Astrodynamics Conference, Portland, OR*, August 1990.

[51] Vincent, T. L., Lin, Y. C., and Joshi, S. P. Positioning and Active Damping of Flexible Beams. *Journal of Guidance, Control, and Dynamics*, Vol 13, No 4, July-August 1990, pp 714-724.

[52] Webb, S. B., and Turcotte, J. S. Analysis of a Passively Tuned Actuator. *Proceedings of the 1990 AIAA Guidance, Navigation, and Control Conference, Portland, OR*, August 1990, pp 1664-1672.

[53] Wie, B., and Byun K. New Generalized Structural Filtering Concept for Active Vibration Control Synthesis. *Journal of Guidance, Control, and Dynamics*, Vol12, No 2, March-April 1989, pp147-154.

[54] Wie, B., and Bernstein D. S. A Benchmark Problem for Robust Control Design. *Proceedings of the 1990 American Control Conference, San Diego, CA*, May 1990, pp 961-962.

[55] Williams, T. Transmission-Zero Bounds for Large Space Structures, with Applications. *Journal of Guidance, Control, and Dynamics*, Vol12, No 1, January-February 1989, pp 33-38.

[56] Williams, T. and Juang, J. N. Pole/Zero Cancellations in Flexible Structures. *Journal of Guidance, Control, and Dynamics*, Vol 13, No 4, July-August 1990, pp 684-690.

[57] Yocum, J. F., and Slafer, L. I. Control System Design in the Presence of Severe Structural Dynamics Interactions. *Journal of Guidance and Control*, Vol 1, No 2, March-April 1978, pp 109-116.

[58] Yuan, J. S. and Stieber, M. E. Robust Beam Pointing and Attitude Control of a Flexible Spacecraft. *Journal of Guidance, Control, and Dynamics*, Vol 9, March 1973, pp 22-27.

[59] Zimmerman, D. C. and Inman, D. J. On the Nature of the Interaction Between Structures and Proof-Mass Actuators. *Journal of Guidance, Control, and Dynamics*, Vol 13, No 1, January-February 1990, pp 82-88.

VITA

Kenneth Wayne Barker

[redacted]

Education:

United States Air Force Academy, B.S. Aeronautical Engineering, 1979

Massachussetts Institute of Technology, M.S., Aerospace Engineering, 1982

University of Washington, Ph. D., Aerospace Engineering, 1991